

DENSITY-FUNCTIONAL THEORY FOR *f*-ELECTRON SYSTEMS: THE α - γ PHASE TRANSITION IN CERIUM



MAX-PLANCK-GESellschaft

Dissertation

zur Erlangung des Grades

Doktor der Naturwissenschaften (Dr. rer. nat.)

eingereicht im Fachbereich Physik
der Freien Universität Berlin

Vorgelegt in Juli 2013 von

Marco Casadei

Diese Arbeit wurde von November 2008 bis Juli 2013 am Fritz-Haber-Institut der Max-Planck-Gesellschaft in der Abteilung Theorie unter Anleitung von Prof. Dr. Matthias Scheffler angefertigt.

1. Gutachter: Prof. Dr. Matthias Scheffler
2. Gutachter: Prof. Dr. Felix von Oppen

Tag der Disputation: 21 Oktober 2013

Hierdurch versichere ich, dass ich in meiner Dissertation alle Hilfsmittel und Hilfen angegeben habe und versichere gleichfalls auf dieser Grundlage die Arbeit selbstständig verfasst zu haben.

Die Arbeit habe ich nicht schon einmal in einem früheren Promotionsverfahren verwendet und ist nicht als ungenügend beurteilt worden.

Berlin, 18 Juli 2013

ABSTRACT

Rare earths are technologically important and scientifically highly interesting elements. The description of the volume collapse exhibited by some *rare earth* metals poses a great challenge to density-functional theory (DFT) since local/semi-local functionals (LDA/GGA) only partially capture the associated phase transitions. In this work this problem is approached by treating all electrons at the same quantum mechanical level, using both hybrid functionals (e.g. PBE0 and HSE06) and exact-exchange plus correlation in the random-phase approximation (EX+cRPA). The performance of recently developed beyond RPA schemes is also assessed.

The isostructural α - γ phase transition in cerium is the most studied. The exact exchange contribution in PBE0 and HSE06 is crucial to produce two distinct solutions that can be associated with the α and γ phases. The two solutions emerge in bulk as well as in cluster calculations. Most notable is their presence in the cerium dimer. However, quantitative agreement with the extrapolated phase diagram requires EX+cRPA. So far the EX+cRPA correction can only be applied to cerium clusters and not to the bulk. A cluster of 19 atoms cut from the fcc crystal structure (the same that characterizes the α and γ phases) was therefore determined as representative. (EX+cRPA)@PBE0 for Ce₁₉ provides good agreement with the extrapolated transition pressure to zero temperature. We predict that a pressure induced phase transition should exist at or close to zero. A finite temperature phase diagram can be drawn in reasonable agreement with experiment by adding entropic effects.

The cerium neighbors are also studied: lanthanum, which has no f electrons, praseodymium, with three f electrons and a volume collapse, and neodymium, with four f electrons and no volume collapse. Multiple solutions are also present for these f electron elements, confirming the importance of exact-exchange for f electron systems.

ZUSAMMENFASSUNG

Seltene Erden sind technologisch wichtige und wissenschaftlich höchst interessante Elemente. Die Beschreibung des Volumenkollapses den einigen Seltenen Erden aufweisen stellt eine grosse Herausforderung an die Dichte-Funktional-Theorie (DFT) dar, weil lokale/semilokale Funktionale (LDA/GGA) nur teilweise die damit verbundenen Phasenübergänge erfassen. In dieser Arbeit wird dieses Problem durch die Beschreibung aller Elektronen auf der gleichen quantenmechanischen Ebene behandelt, wobei Hybridfunktionale (zB. PBE0 und HSE06) und exakter-Austausch plus Korrelation in der Random-Phase Approximation (EX+cRPA) zum Einsatz kommen. Die Nützlichkeit von Methoden, die über RPA hinausgehen wird ebenfalls bewertet.

Hauptaugenmerk wird auf den isostrukturellen α - γ Phasenübergang in Cerium gelegt. Der Beitrag vom exakten Austausch in PBE0 und HSE06 ist entscheidend um zwei unterschiedliche Lösungen zu generieren, die jeweils der α und γ Phase zugeordnet werden können. Die beiden Lösungen entstehen sowohl unter periodischen Randbedingungen als auch bei Cluster Rechnungen. Bemerkenswerterweise tritt eine zweifache Lösung bereits beim Cerium Dimer auf. Allerdings erfordert eine quantitative Übereinstimmung mit dem extrapolierten Phasendiagramm EX+cRPA. Da sich bislang die EX+cRPA Korrektur einer Anwendung unter periodischen Randbedingungen entzieht, werden Cerium Cluster studiert. Es zeigt sich, dass ein Cluster von 19 Atomen der aus der FCC-Kristallstruktur (jener, der die α und γ Phasen charakterisiert) repräsentativ ist. (EX+cRPA)@PBE0 für Ce19 liefert eine gute Übereinstimmung mit dem auf Nulltemperatur extrapoliert Übergangsdruck. Unsere Ergebnisse sagen wir einen Druck-induzierten Phasenübergang in der Nähe des Nullpunktes voraus. Unter Berücksichtigung von entropischen Effekten kann ein Phasendiagramm bei endlichen Temperaturen ermittelt werden, welches in guter experimenteller Übereinstimmung ist.

Die Cerium Nachbarn werden ebenfalls untersucht: Lanthan, das keine f -Elektronen besitzt, Praseodym mit drei f -Elektronen und das ebenfalls einen Volumskollaps aufweist, und Neodym, mit vier f -Elektronen und ohne Volumskollaps. Auch hier für diese Elemente werden mehrdeutige Lösungen gefunden, welches die Bedeutung des exakten Austausches für die Beschreibung von f -Elektronensystemen bekräftigt.

CONTENTS

Abstract	V
Zusammenfassung	VII
Contents	IX
Introduction	1
I Background: experiments and theory	5
1 Rare earths and Cerium	7
1.1 Lanthanides and actinides	7
1.2 Rare earth metals and volume collapse	9
1.3 Cerium α - γ phase transition	11
1.4 Theoretical models for the α - γ phase transition	24
1.5 Cerium clusters	32
1.6 Summary	34
2 Theoretical Methods for Electronic Structure Calculations	35
2.1 The many-body problem	35

2.2	Hartree-Fock Theory	38
2.3	Density-Functional Theory	40
2.4	Exchange-Correlation Functionals	45
2.5	Orbital-dependent approaches	49
2.6	Hybrid functionals	56
2.7	Many-Body Perturbation Theory	59
II	<i>Ab initio</i> description of the α-γ transition in cerium	67
3	Previous <i>Ab initio</i> studies of the α-γ transition	69
4	<i>First principle</i> calculations for cerium systems	75
4.1	Computational settings	75
4.2	Convergence of the SCF cycle	76
4.3	Multiple solutions	79
5	Cerium dimer	83
5.1	Local and semi-local functionals: LDA and PBE	84
5.2	(EX+cRPA)@PBE	86
5.3	Hartree-Fock	89
5.4	Hybrid functionals: PBE0	90
5.5	Fraction of exact-exchange	94
5.6	(EX+cRPA)@PBE0	95
5.7	Beyond RPA methods	99
5.8	Summary	101
6	Cerium clusters	103

6.1	PBE and PBE0	104
6.2	EX+cRPA: the α - γ phase transition	111
6.3	Summary	115
7	Cerium bulk	117
7.1	Hybrid functionals and the α and γ phases	117
7.2	Spin unpolarized results	127
7.3	Magnetic properties	133
7.4	Role of Exact-exchange	137
7.5	Summary	140
8	Phase diagram for the α-γ transition	143
8.1	Toward the bulk	144
8.2	Finite temperature	146
8.3	Summary	157
9	Beyond cerium	159
9.1	Hybrid functional calculations for La, Pr, and Nd	160
9.2	Many-body functional calculations of the dimers: La ₂ , Pr ₂ , and Nd ₂	167
9.3	Summary	173
10	Summary and Outlook	175
10.1	The α - γ phase transition	175
10.2	Future directions	177
	Appendices	181
A	Crystal structures	183

B Computational details	185
B.1 Numerical atom centered orbitals	185
B.2 Basis set superposition error	188
B.3 Convergence with respect to the basis set	190
B.4 Convergence with respect to the frequency points	193
B.5 <i>k-point</i> convergence	194
Publications	197
Curriculum Vitæ	199
Acknowledgements	205
Bibliography	207

INTRODUCTION

In winter in Berlin, the snow lays thick on the ground. As winter comes to an end, the temperature increases. We will watch the snow melt away, but few of us will think twice about it. Likewise, we never wonder about ice melting in our cocktail or water becoming steam when we boil it for *pasta*.

Phase transitions are a familiar part of our everyday lives, and yet we do not consider them as direct proof of the microscopic nature of matter. We do not normally ask, “Why does water in its liquid form spread into the air in the form of steam as it approaches $T=100^{\circ}\text{C}$?” The answer is not simple. Nowadays, we understand this process in terms of the balance between the system’s internal energy and its entropy. These quantities are macroscopic observables which ultimately represent the arrangement and motion of electrons and nuclei in a macroscopic body in thermodynamic equilibrium

During a phase transition, a system alters some physical properties, often discontinuously, in response to changes in certain external conditions, such as temperature or pressure. Some have speculated that the universe itself originated from a succession of phase transitions. It possessed a large number of symmetries in its hot and primitive state and cooled with symmetry-breaking phase transitions; these transitions developed order and led to matter, made of electrons, protons, neutrons and so on.

Cerium metal has its own special phase transition. Cerium belongs to the *lanthanide* elements, which are included among *rare earth elements*. The rare earth elements are the “Wild West” of the natural elements. This group was discovered relatively recently compared to the other elements –starting from 1794– and has since

attracted the scientific community's attention. Even though rare earth elements already have applications in several fields – from nuclear power and weapons to medical tools, from communication technology to catalysis – their properties and behavior are not fully understood.

The rare-earth elements are characterized by the presence of localized f electrons at high energy. With only one $4f$ electron, cerium is the most studied of the rare earth elements. At ambient pressure and above room temperature cerium behaves like a normal metal. Its volume gradually decreases under compression or as the temperature is lowered, but at room temperature and 1 atm, it suddenly collapses by around 15%. This is the well-known α - γ phase transition. This transition, the magnetic properties of the metal are modified, but the lattice structure is preserved. This indicates that the volume collapse is not due to a displacement of the atoms.

Numerous experimental and theoretical studies have investigated the α - γ phase transition, but a consensus concerning the driving mechanism of the volume collapse has not yet been reached. The most prevalent explanations are based on models, which involve the f electrons as main actors. Notable are the Mott transition [1] and the Kondo volume collapse [2, 3], to which a quadrupolar alignment of the charge density [4] has been added recently. No overwhelming evidence has emerged in favor of one or another model. Overall, the transition could be very complex and different mechanisms may cooperate.

In this context, theoretical *ab initio* approaches provide a unique perspective. Beginning with the fundamental laws of physics (i.e., from *first principles*) *ab initio* approaches seek solutions to the equations of quantum mechanics without any prior assumptions. This cannot be done analytically even for very simple systems, and computational techniques and numerical algorithms come to our aid. A never-ending search for the right balance between the approximations introduced in the problem and the computational tractability makes *ab initio* methods an extremely active area of research.

Many authors studied the α - γ phase transition with *ab initio* methods. However, none of the previous studies has been able to describe the structural properties of both phases within a single theoretical framework. This has introduced doubts about the quantum nature of the transition, posing the question whether the volume

collapse could survive at zero temperature or not.

In this thesis, I approach the α - γ phase transition in Ce in view of newly-developed *first principle* methods. Using *hybrid functionals* and the *random-phase approximation*, I show that the volume collapse survives at zero temperature, and both the α and γ phases can be described within a single theoretical framework. Moreover, I provide evidence that the finite temperature behavior of the phase transition is obtainable beginning with the ground state structural and energetic properties of the two phases. These findings are extended to other lanthanide elements.

The thesis is organized into two parts. In Part I, Chapter 1 reports on the experimental evidence of the α - γ phase transition and previous theoretical studies of the volume collapse. Chapter 2 summarizes theoretical methods important for understanding this work. Part II presents *ab initio* studies of the α - γ phase transition. Chapter 3 summarizes previous works. Chapter 4 describes relevant computational details and techniques. In Chapter 5, local and semi-local functionals (LDA and PBE) and hybrid functional (PBE0 and HSE06) calculations for the cerium dimer are presented. Exact-exchange combined with correlation in the random-phase approximation (EX+cRPA) is also computed for the dimer based on the PBE and PBE0 results. The outcome of *renormalized second order perturbation theory* (rPT2) is also discussed. Next, in Chapter 6 cerium clusters are studied with the same approaches, and in Chapter 7 bulk results are presented for the LDA, PBE, PBE0 and HSE06 functionals. Finally, the cerium phase diagram, reported in Chapter 8, is established based on the (EX+cRPA)@PBE0 results. Chapter 9 is dedicated to other lanthanide elements, namely lanthanum, praseodymium and neodymium, for which hybrid functional and EX+cRPA calculations are reported. Chapter 10 discusses insights that emerged during the course of this research and potential future developments.

I BACKGROUND: EXPERIMENTS AND THEORY

1 RARE EARTHS AND CERIUM

1.1 LANTHANIDES AND ACTINIDES

Rare earth elements distinguish themselves from all other elements by the presence of partially filled $4f$ and $5f$ orbitals. *Rare* has historical origins, because those elements were discovered and analyzed relatively late. Their presence in the earth crust is however significant, as illustrated in Figure 1.1, and some of them are even more abundant than commonly used metals. Unlike the other elements in the periodic table, which share much of their chemical properties among columns, the *rare earths* are arranged in rows according to their physical characteristics, and are divided in two subgroups: *lanthanides* and *actinides*.

Lanthanides are soft metals of silvery color and have partially filled $4f$ orbitals. The only exception is lanthanum that, even if it does not possess any f electrons, still shows physical properties characteristic for the all row. In lanthanum a $5d$ orbital becomes occupied before a $4f$ one. Lanthanum shares This anomaly only with cerium. The latter has peculiar characteristics linked to the presence of only one $4f$ electron in addition to the $5d$ filled state, and will be the main subject of the present study. The f orbitals have an energy that is comparable to the outer $6s$ and $5d$ electrons, but are strongly localized around the core (Figure 1.3). Therefore, they shield the outer states ($6s$ and $5d$) from the nucleus. As they fill up across the series the screening of the outer electrons becomes increasingly important, leading to a decrease of atomic volume along the row, that is generally known as *lanthanide contraction*.

Actinides are marked by the presence of filled $5f$ orbitals. They are dense

metals and are characterized by radioactive behavior. Only three actinide elements, out of the fourteen total, can be found in nature. The others, after uranium, can be synthesized as nuclear products. The existence of transuranium elements was first suggested by Enrico Fermi in 1934 and marked the beginning of *rare earth* research. While the first lanthanides were already discovered in the eighteenth century, a real interest in their properties only developed with the advent of nuclear fission, that lead to the development of nuclear power and nuclear weapons.

Nowadays actinides are still actively studied for nuclear applications, such as medical tools, weapons, and as fuel in nuclear reactors. Lanthanides on the other hand are used for a wide range of applications. The high probability of electronic transitions between the $4f$ states makes them suitable for optoelectronic applications, such as lasers, fluorescent materials, and optical-fibers for communication systems. They are also added in sunglasses and lenses in order to deflect ultraviolet and infrared radiation. Moreover, they are suitable for explosives and, e.g., lighter flints, because they are highly reactive and burn easily when exposed to air. In compounds the range of applicability grows further. Lanthanide oxides are used in superconductors, magnets, electronic polishers, batteries, etc. Other applications emerge in medicine, where lanthanides are used as anti-tumor agents and in kidney dialysis. For example gadolinium is employed in magnetic resonance imaging as a contrasting agent, and europium compounds are used in molecular genetics to mark specific strands of DNA. Cerium finds application as a catalytic converter for the reduction of CO emissions in diesel fuels, in the coloring of glasses and enamels, in steel manufacturing for the reduction of free oxygen and sulfur, etc. Its oxides are particularly important for the photo-stability of pigments, are used as components of glass polishing powders and are employed as hydrocarbon catalyst in self cleaning ovens.

Although the properties of the lanthanide and actinide elements have been investigated in depth only after the discovery of the first transuranium element, they have become increasingly important for practical use. Nevertheless the behavior of *rare earths* is still far from being fully understood. Despite the diverse range of properties that industry and experimental physicists are able to harness, some of their peculiar characteristics remain unexplained and somehow mysterious. The best of all examples is the *volume collapse* that is present in some of the lanthanide

and actinide elements [5] and continues to intrigue researchers from several fields of modern physics.

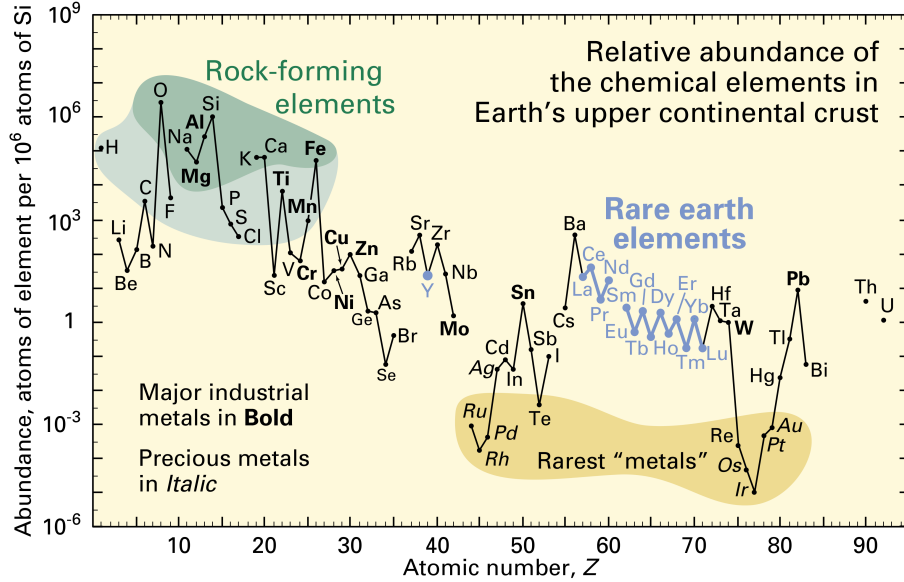


Figure 1.1: Abundance of the chemical elements in earth's upper continental crust as a function of atomic number. Major industrial metals are labeled in bold, while precious metals in italic. From Ref. [6].

1.2 RARE EARTH METALS AND VOLUME COLLAPSE

Under compression, or by lowering temperature, some of the *rare-earth* metals display an unusual behavior. In general, the lanthanides follow a structural change that goes from hexagonal closed packed (hcp) to double hexagonal closed packed (dhcp), to face centered cubic (fcc) and then to some distorted fcc structures, like distorted fcc (dfcc) and α -uranium (α -U)¹. But more interestingly a number of trivalent lanthanides undergo a first-order phase transition, when temperature is decreased or pressure increased, that is accompanied by a volume collapse and a change in magnetic properties [7]. Such phase transitions were observed in the actinides series too [8]. The most interesting elements in this regard are cerium (Ce), with a volume

¹See Appendix A for a schematic representation of the different structures.

collapse of 15% at room temperature [9, 10], praseodymium (Pr), with 9% [11, 12, 13], gadolinium (Gd), with 5% [14], and dysprosium (Dy), 6% [15].

The volume collapse is evident in the room temperature pressure-volume curves of Figure 1.2, where data for the first six elements with f electrons are reported. While the symbols indicate the structural change, the thick gray horizontal lines for Ce, Pr and Gd mark the jump in volume. For instance, praseodymium displays an abrupt change of the unit cell volume when transforming from the d-fcc structure to the α -U one. Cerium shows the same behavior between two fcc phases that have different magnetic properties. An isostructural phase transition accompanied by a volume collapse is a very special and unexpected property for materials in general, but even unique among metals and will be extensively examined in the next section.

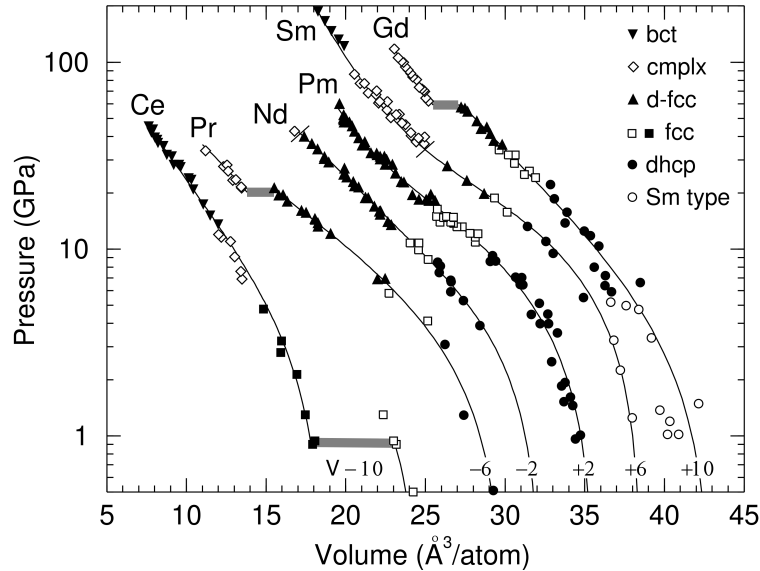


Figure 1.2: Pressure-volume data for Ce, Pr, Nd, Pm, Sm, Gd. Different symbols identify different crystal structures, while lines are guides to the eye. The volume collapse is marked with orizontal thick lines. Under the label “cmplx” several closed packed structures are included that are not further specified here. For clarity, the data and curves are shifted in volume by the numbers (in $\text{\AA}^3/\text{atom}$) shown at the bottom of the Figure. From Ref. [5].

The mechanism of such an anomalous volume collapse was extensively discussed in the past [16, 17, 1, 2], but has not been fully understood. After first attempts from different perspectives, the general opinion has converged towards a mechanism connected to a change in the behavior of the $4f$ electrons [18]. As already mentioned,

and depicted in Figure 1.3, the f electrons are found with a much higher probability in regions close to the nucleus than the $6s$ and $5d$ ones, and at the same time they are very close in energy to them. A direct proof of this can be found in the way in which orbitals are filled up along the lanthanide series. While La has one $5d$ electron, Ce accommodates one electron in the $5d$ orbitals and one in the $4f$ ones, so that the f electron appears before the $5d$ shell is fully filled. The next is Pr, which loses the $5d$ electron and switches to a configuration with three $4f$ occupied orbitals². The next element in which a $5d$ state is added again is found at the end of the series.

The energy of the f electrons with respect to the valence electrons, together with their spatial distribution, gives rise to intricate phenomena such as, for example, the *lanthanides contraction* (see Section 1.1). The theoretical speculations around the nature of the volume collapse lead to the common understanding that an abrupt change in $4f$ electron correlation, mediated or not by the s and d electrons, would happen under compression and the f orbitals would turn from a localized state in the low-pressure, high-temperature regime, to a bonding-like state in the high-pressure one. The terms “itinerant” and “localized” are often used to describe the nature of the electrons in the low and the high volume phases. But these labels are only pictorial, as the description of the f states and the reasons of their abrupt change in behavior from one phase to the other are still a matter of debate. The suppositions around the mechanism of the transition will be discussed in Section 1.4, where it will become more clear that a deep understanding of the intuitive *localization-delocalization* concept permeates the extensive investigations of the f electron metals, representing for instance one of the biggest challenges for electronic structure theory nowadays, and, quite important here, a strong motivation for this thesis.

1.3 CERIUM α - γ PHASE TRANSITION

Cerium was discovered by the Swedish chemists Jöns Jacob Berzelius and Wilhem von Hisinger and independently by Martin Heinrich Klaproth, a German chemist, in

²It is interesting to note that there is no element in the periodic table with nominally two $4f$ electrons.

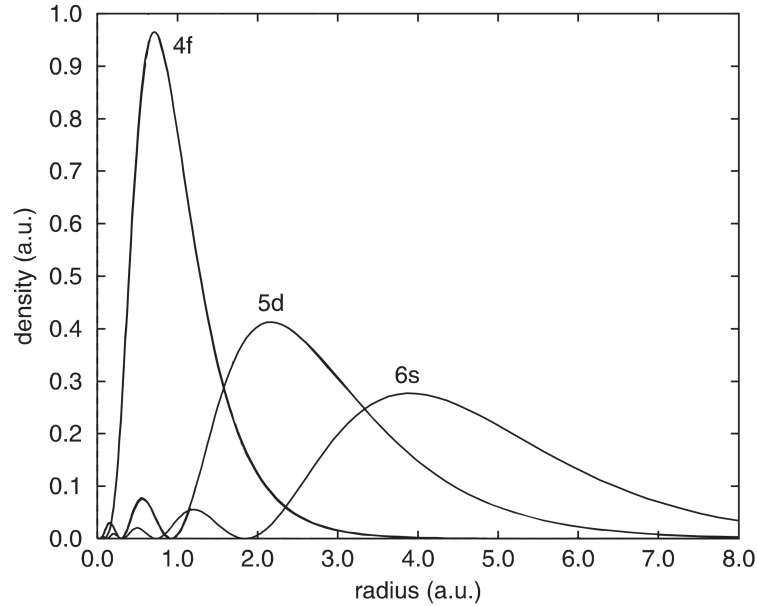


Figure 1.3: Radial densities of the $4f$, $5d$, and $6s$ valence shells in atomic cerium from Dirac-Hartree-Fock calculations. From Ref. [19].

1803. It is the most abundant *rare earth* element and one of the most fascinating members of the periodic table. Cerium is a malleable and ductile metal and its phase diagram, shown in Figure 1.4, counts seven known distinct solid regions. The different phases exhibit various crystal and magnetic structures. Some phases, like the high pressure α' phase, display superconductivity.

Cerium has 58 electrons. It is the second element in the lanthanide row and has one $4f$ electron. Its atomic orbital configuration is $6s^2 5d^1 4f^1$ in the ground state. The presence of a single $4f$ electron makes cerium a case study for the understanding of all f electron systems.

In the phase diagram the low-pressure, high-temperature β and γ phases, display closed packed dhcp and fcc crystal structures, and a localized magnetic moment that is close to the value of the free atom [9], $1 \mu_0$. In the β phase antiferromagnetic order arises below 300 K [21]. The α phase is also found in an fcc configuration in the interval $0 \leq T \leq 200$, but with a magnetic susceptibility that is essentially temperature independent –in contrast to the other two phases. This implies that there is no localized magnetic moment. At high pressures, the superconducting α'

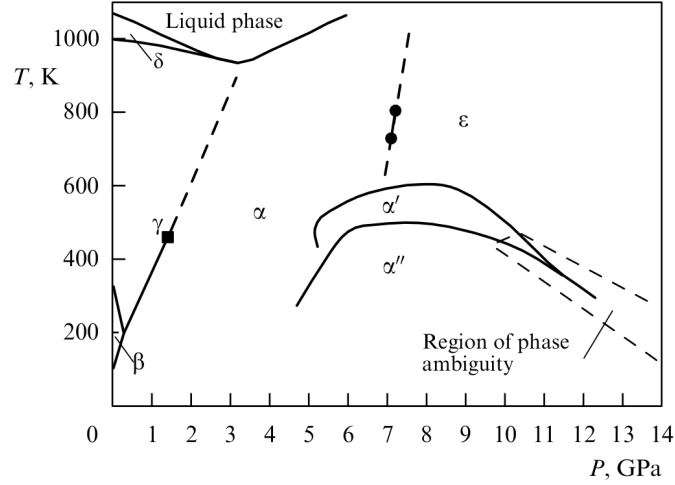


Figure 1.4: Cerium metal: phase diagram. Regions α , γ : face-centered cubic (fcc); β : double hexagonal close packed (dhcp); δ : body-centered cubic (bcc); α' : α -U structure, C-centered (based) orthorhombic; α'' : monoclinic; ϵ : body-centered tetragonal (bct); upper region: liquid. CP denotes the critical point. From Ref. [20].

phase appears, accompanied by two other phases with complex –i.e. monoclinic and body-centered tetragonal– crystal structure. The δ phase, squeezed between the γ region and the liquid state, has a body-centered cubic (bcc) crystal structure.

Despite the richness of the cerium phase diagram, the most known and distinctive feature remains the so called α - γ phase transition: At room temperature and pressure of around 1 GPa, the γ phase collapses into the denser α phase with a volume change of 15% [9]. One key feature of this first order phase transition is that the crystal structure is preserved (fcc in both states) despite the volume collapse, and the magnetic properties of the two phases are different. First order isostructural phase transitions with a volume collapse are very unusual, even for lanthanides and actinides where, as mentioned in Section 1.2, a volume collapse can occur, but it is accompanied by a structural change. Also distinctive is the presence of a solid-solid critical point at pressure $p_c \simeq 1.5$ GPa and temperature $T_c \simeq 480$ K [9]. At the other extreme, the α - γ phase transition ends in a triple point, where the β phase appears at low temperatures and low pressures. When the γ transforms to the β phase no appreciable volume collapse is found and the γ and β regions display similar magnetic properties. The collapse emerges instead when β -Ce turns to α -Ce. The γ - β transition is similar to the one in lanthanum, where no f -electrons

are present but the fcc phase transforms to the dhcp phase upon cooling. A possible explanation is that the γ - β transition is a shear transformation dictated by the d electrons, whereas the f electrons drive the γ - α and β - α phase transitions.

Hysteresis effects play an important role in the transitions between the γ , β and α regions and complicate the study of the different phases. Two structures can easily coexist, therefore phase identification methods like magnetism or conductivity measures are not suited for the problem and diffraction techniques are usually employed. A temperature-pressure diagram that takes account of hysteresis contributions is reported in Figure 1.5. In the following paragraphs a description of the physical properties of α - and γ -Ce will be provided, for a better understanding of the α - γ phase transition, along with an overview of the experiments that were performed until the present time. As close neighbor to the two phases, properties for β -cerium will also be discussed whenever relevant.

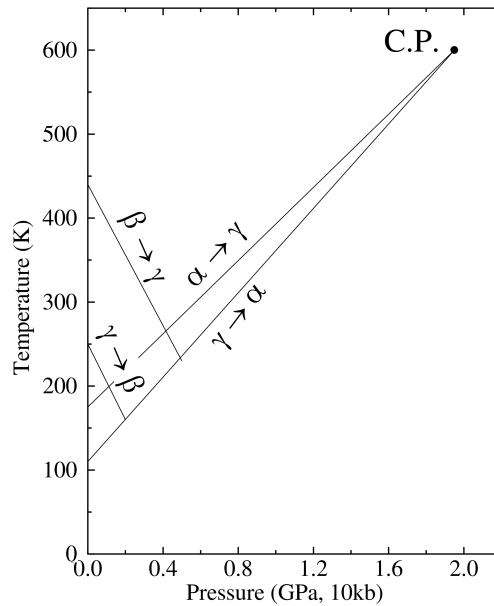


Figure 1.5: Non-equilibrium phase diagram of cerium. Arrows indicate the transition direction: $\gamma \rightarrow \alpha$, transition boundary for the γ to α transformation; $\alpha \rightarrow \gamma$, transition boundary for the α to γ transformation; $\gamma \rightarrow \beta$, boundary for the γ to β transformation; $\beta \rightarrow \gamma$, boundary for the β to γ transformation. From Ref. [9].

1.3.1 NUMBER OF f ELECTRONS

The first estimation of the number of $4f$ electrons in the α and γ phases was provided by Gustafson *et al.* [22] by means of positron annihilation. When a positron is placed into a metal it annihilates with a conduction electron emitting a photon. By measuring the lifetime of the positron and the angular correlation of the resulting photon it is possible to derive the number of conducting electrons and their momentum distribution. Results from positron annihilation measurements showed no change in the number of f electrons going from one phase to the other. This invalidated the early hypothesis that the f electron would be promoted to d or s states. The results were then partially confirmed by Compton scattering and neutron scattering measurements [23, 24], which found $\langle n_f \rangle \simeq 1$ for γ -Ce and $\langle n_f \rangle \simeq 0.8$ for α -Ce. In the latter study the authors also claimed to have evidence, from spectral response analysis, for a localized nature of the f electrons in the α phase, suggesting the presence of Kondo³ physics in the system and estimated the Kondo temperature to be around 2000 K.

1.3.2 MAGNETISM

The magnetic susceptibility of α -Ce as a function of temperature and pressure has been measured by several authors [25, 26, 27]. All studies agreed that the α phase is essentially a Pauli paramagnet. That means the susceptibility of the material is weak and reflects that of conduction band electrons. However, the value of the susceptibility is 4.5 times higher than the expected Pauli susceptibility calculated from heat capacity results.

The γ phase of cerium is also a paramagnet. The magnetic susceptibility obeys however the Curie-Weiss law, as indicated by early studies [28, 21, 29]. In 1995 Naka *et al.* [30] measured the magnetic susceptibility of cerium as a function of temperature and external magnetic field and deduced that the γ phase susceptibility follows the expression

$$\chi(T) = \chi_0 + \frac{C_\gamma}{T - \theta_p}, \quad (1.1)$$

³See Section 1.4 for an introduction to Kondo physics.

where χ_0 is a constant susceptibility, C_γ the Curie constant and θ_p the paramagnetic Curie temperature, confirming the Curie-Weiss law. The pressure dependence of χ_0 was found to be small ($\chi_0 = 1.18 \times 10^{-4}$ emu/mol), and comparable to the one of lanthanum, which has no f electrons. The value of θ_p (-57 K), on the other hand, varied strongly with pressure, determining a suppression of the susceptibility with increasing pressure [30].

To interpret the change in magnetic properties across the α - γ phase transition the following *localization-delocalization* process is typically invoked. In γ -cerium the $4f$ electron would reside close to the nucleus. It would be unpaired and therefore display spin degrees of freedom. In the α phase, on the other hand, the f electron would be delocalized, hybridized with other f electrons or with conduction states that would screen its spin. In this picture the discrepancy from the ideal Pauli paramagnetism in the α phase could be attributed to a Stoner exchange enhancement arising from a non-complete delocalization of the $4f$ states and a persistence of localized magnetic moments. Stoner suggested in 1934 that an attractive contribution $E_{ex} = -I/4(N_\uparrow - N_\downarrow)^2$ (where N_\uparrow and N_\downarrow are the number of spin up and down electrons, respectively, and I is a material dependent parameter) should be considered in order to describe the effect that localized electrons, when close to each other, prefer to align their spin in opposite directions. Following this procedure the usual Pauli susceptibility of a metal χ_p is increased according to the expression

$$\chi = \frac{\mu_B}{1 - IN(E_F)}\chi_p \quad (1.2)$$

where $N(E_F)$ is the density of states at the Fermi level.

The susceptibility of the β -phase also follows the Curie-Weiss law showing an antiferromagnetic ordering of the local moments. The β and γ phases have often been associated with each other mainly on the base of this difference with respect to α -Ce. This follows following the hypothesis that in both phases the $4f$ electron should be *localized*, and the *delocalization* of the f states would drive both the γ - α and β - α volume collapse. In 2005, however, a study from Murani *et al.* [31] argued that the magnetic form factor measured in neutron scattering would correspond to a Ce^{3+} electronic configuration in all three phases, suggesting a persistence of the f electron *localization* in α -Ce too. While there is a fair agreement on the observed

magnetic properties of cerium, the debate on the existence of an experimental proof for the *localization-delocalization* process is still ongoing and a consensus has not been reached.

1.3.3 ELECTRICAL RESISTIVITY/CONDUCTIVITY.

Resistivity measurements for α -Ce are found in a number of studies by different authors [32, 26, 33, 34, 35] but, as it is often the case for cerium, the results are conflicting. The main dispute is whether the resistivity would follow a “ T^2 ” dependence at low temperature or not. A T^2 dependence is typical for metals with exchange enhancement –see previous section–, and is expected as a consequence of spin fluctuations in the low temperature regime [36]. A second expected feature for exchange enhancement, the departure from a T law at higher temperature [37], was not observed in any experiment. The discrepancy between different studies could be attributed to the incomplete transformation from β - to α -cerium in some samples, but no definitive conclusion has been reached. In the pressure range close to the α' , α'' phase ($\simeq 2.0$ GPa), α -Ce is superconducting at extremely low temperatures ($\simeq 20$ mK), as emerges in high pressure studies [38].

The electrical resistivity of β -Ce has been measured by Gshneidner *et al.* [39] and Burgardt *et al.* [40] from 300 to 100 K. The temperature dependence of the resistivity is unusual. It decreases slightly between 300 K and 50 K, and then drops suddenly below 20 K. The effect could not be explained by existing models for metals. The authors noted that the high temperature resistivity could be fitted to a Kondo model⁴ for scattering of conduction electrons from magnetic impurities. The rapid drop would then be connected to a quenching of Kondo scattering by the magnetic ordering in β -Ce. The electrical resistivity in γ -Ce was found to display nearly the same temperature dependence as that of β -Ce, in the temperature range of stability, but reduced by around 10%. Below 100 K however the γ transforms to the α phase, and no information could be provided. Similarities between the two phases would suggest that γ -Ce may also exhibit Kondo scattering, however no further analysis is found in the literature.

⁴See Section 1.4 for an introduction to the Kondo physics.

In 2001 Van der Eb *et al.* [41] studied the optical properties of cerium using ellipsometry and grazing incidence reflectometry. They observed significant changes in the optical conductivity, the dynamical scattering rate, and the carrier effective mass between α - and γ -cerium. In γ -Ce the charge carriers showed a large scattering rate in the far infrared and a carrier mass characteristic of $5d$ band electrons. In the α -Ce, a Fermi-liquid frequency-dependent scattering rate was obtained, with an effective mass of the carries about twenty times that of an electron: three times larger than in the γ phase.

1.3.4 SPECTRAL PROPERTIES - OCCUPIED STATES

It has already emerged in the previous paragraphs that the valence electronic structure of cerium has been a subject of uncertainty and controversy for a long time. In this regard photoemission spectroscopy (PES) has been the most applied experimental technique in characterizing the α and γ phases, because it gives direct access to the electronic structure of materials. Numerous experimental studies have been carried out by means of photoelectron spectroscopy [42, 43, 44, 45, 46, 47, 48], X-ray absorption [49], X-ray photoemission spectroscopy [50, 51, 52], and inverse photoelectron spectroscopy for the unoccupied states [52, 46, 53]. The reason for the remarkable amount of studies can be found in the difficulty to extract the $4f$ component from the spectra. As a consequence, the contribution of the f states is ambiguous. The main subject of debate has been if $4f$ electrons are present at the Fermi level (E_F), and if yes, whether they would show distinctive features of Kondo physics, as e.g. a clear peak at the Fermi level. In fitting the data to the Kondo model, however, neither a simple one-electron band nor a pure core-level description of the f states suits the case of cerium, and the processing of the results strongly influences their interpretation [54]. Moreover, electron spectroscopies are highly surface sensitive and this further complicates the understanding of the bulk properties of cerium, where the surface is believed to be of a γ nature even in the α phase [47].

Early measurements of the α and γ phase were performed in 1984 by Jensen *et al.* [55] by means of angle resolved photoemission spectroscopy on cerium crystals. The authors observed the presence of two main peaks, one at the Fermi level and

one at around 2 eV binding energy. Several other experiments followed and in 1992 Liu *et al.* made a first attempt to reconcile all the available results in a unique framework [46]. Nowadays the results obtained in 1991 by Weschke *et al.* [44] are generally taken as the reference for the cerium PES spectra. In previous studies, two spectra taken with incident photon energies of He I and He II ($h\nu = 21.2$ eV and $h\nu = 40.8$ eV respectively) were subtracted in order to extract the bulk contribution of the emission. Weschke *et al.* instead, being aware of the fact that low photon energy emission carries a big contribution from the valence band electrons and it is surface sensitive, performed resonant photoemission measurements at incident photon energies of $h\nu = 120$ eV and $h\nu = 884$ eV, the $4d \rightarrow 4f$ and $3d \rightarrow 4f$ energy resonances, respectively. The outcome, shown in Figure 1.6, confirmed the presence of the two main peaks, and a splitting of the peak next to the Fermi level, that the authors assigned to spin orbit splitting.

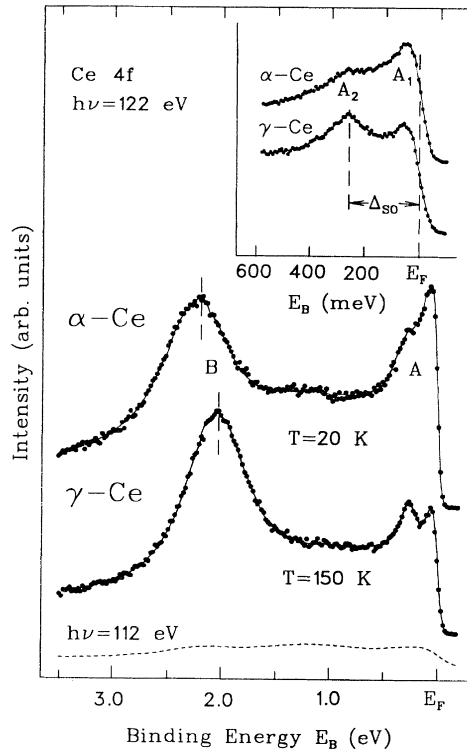


Figure 1.6: $4d \rightarrow 4f$ resonant photoemission spectra of γ - and α -Ce. The inset shows the region close to the Fermi level. The total energy resolution is 40 meV. The splitting of peak A is evidenced in the inset. For comparison a normalized off-resonance spectrum of α -Ce metal is included. From Ref. [44].

1.3.5 SPECTRAL PROPERTIES - UNOCCUPIED STATES

Only few inverse photoemission spectroscopy (IPES) studies are available for cerium. This is unfortunate, because the main part of the $4f$ states resides above the Fermi level. Nevertheless, some results were acquired by Wuilloud *et al.* [52] from a sample of polycrystalline cerium undergoing a temperature driven α - γ phase transition, and by Grioni *et al.* [53], who performed resonant inverse photoemission spectroscopy (RIPES) on thin films.

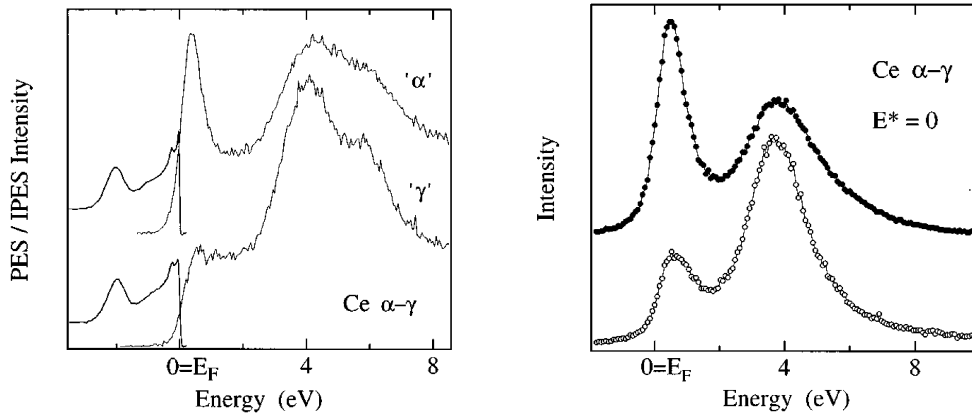


Figure 1.7: Left: combined PES and IPES spectra for the α and γ phases from Weschke *et al.* [44] and Wuilloud *et al.* [52]. The spectra are characterized by a three peak structure, typical for cerium. Right: RIPES spectra of α -Ce (solid symbols) and γ -Ce (empty symbols) measured at the maximum of the high energy peak resonance by Grioni *et al.* [53].

The combination of IPES results from Wuilloud *et al.* and PES data from Weschke *et al.* [44] is shown in Figure 1.7. What emerges is a significant difference between the spectra of the α and γ ⁵ phase near the Fermi level. The basic structure of all spectra is similar. It shows three peaks located at around -2 eV, the Fermi level, and 4 eV. The largest difference is in the central peak, and is even more pronounced than observed in photoemission spectroscopy. As in the PES studies the authors associated this behavior with a Kondo resonance emerging from the hybridization of f and conduction states. However, we will show in Section 1.4 that this is not the only explanation. The results from Grioni *et al.*⁶ confirm the observation of

⁵The γ phase was measured at room temperature and the α phase at 80 K. The pressure was kept at 1×10^{-11} Torr for the whole experiment.

⁶The γ phase was measured at 300 K and the α phase at 20 K. The pressure was kept at

Wuilloud *et al.*, but, even if the two spectra are similar, the one from Grioni *et al.* has an increased spectral weight at the Fermi level and displays a contribution to the peak at E_f also in the γ phase.

In 2004 Dallera *et al.* [56] and Rueff *et al.* [57] performed bulk-sensitive x-ray absorption (XAS), resonant x-ray emission (RXES) and resonant inelastic x-ray scattering (RIXS) measurements, confirming the presence of the three-peak structure in the spectra. As already observed in IPES, the estimated ratio between the peak at high energy and the one at the Fermi level has a sharp drop across the α - γ transition.

1.3.6 SYMMETRY CHANGE

In 2008 and 2011 two studies from Lipp *et al.* [58] and Decremps *et al.* [59] analyzed the volume collapse in cerium using high precision x-ray diffraction techniques. The two studies agree on the isomorphism of the α - γ phase transition, excluding a change from the fcc to distorted-fcc structure that is observed in other lanthanides. They performed measurements from room temperature up to 600-800 K, and confirmed the presence of a solid-solid critical point at $T_c \simeq 460$ K and $p_c \simeq 1.5$ GPa. The results from Decremps are presented in Fig. 1.8. They show a clear hysteresis region. The inset displays the different contributions to the free energy that are derived from the experimental data.

Based on previous theoretical works [4, 62, 63] that propose a change in symmetry between the α and γ phases, in 2010 Tsvyashchenko *et al.* [64] measured the electric field gradient (EFG) of ^{111}Cd probe nuclei in solid Ce using time-differential perturbed angular correlation spectroscopy (TDPACs). TDPACs is a nuclear spectroscopy method in which the electric quadrupole hyperfine interaction (QHI) is determined by introducing $^{111}\text{In}/^{111}\text{Cd}$ probe nuclei into the sample under examination. From the QHI, the EFG can be directly obtained at a lattice site and the nuclear quadrupole frequency can be determined. Tsvyashchenko *et al.* found that the value of EFG in the α phase is four times larger than in the γ phase. The results were interpreted as evidence for quadrupolar electronic charge-density ordering in the α phase and symmetry lowering in the γ - α transition. In this case

1×10^{-10} Torr for the whole experiment.

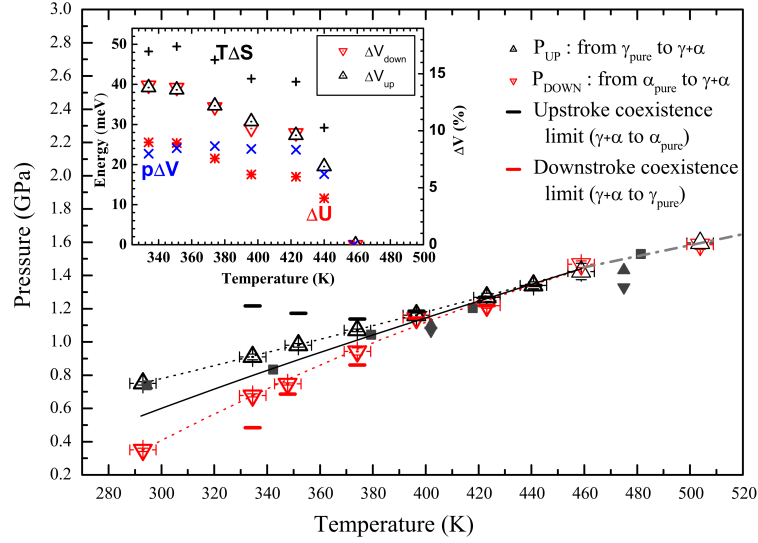


Figure 1.8: Pressure vs temperature phase diagram of cerium with hysteresis effects (dotted lines, as guides for the eye). Black solid curve: thermodynamic transition line. Filled squares: data from reference [58]. Filled triangles: data from reference [60]. Inset: temperature dependence of the volume collapse (right scale, triangles) and energetic terms (left scale). From Ref. [59]. The energetic terms are obtained using the continuity of the Gibbs free energy at the transition and the Clausius-Clapeyron relation as described in Ref. [61] and Section 1.3.7.

the nuclei would remain in face-centered cubic structure in both phases, but the symmetry of the α phase would be lower than the symmetry of the fcc crystal. The underlying mechanism and the implications of this outcome will become clear later and will be explained in Section 1.4.5.

1.3.7 ENTROPIC CONTRIBUTIONS

The role of entropy in the α - γ phase transition was first pointed out by Amadon *et al.* [61] in 2006. Based on experimental data, the authors gave an estimation of the change in Gibbs free energy considering the internal energy (here ΔE , for consistency with the authors), as well as entropic ($T\Delta S$) and volume ($p\Delta V$) contributions. Taking dp/dT and ΔV from experiments, they derived the different terms using the Clausius-Clapeyron relation

$$\frac{dp}{dT} = \frac{\Delta S}{\Delta V} \quad (1.3)$$

and the continuity of the Gibbs free energy

$$\Delta E - T\Delta S + p\Delta V = 0. \quad (1.4)$$

The results are reported in Figure 1.9. Very similar conclusions were reached later by Decremps *et al.* [59] (Figure 1.8). Noticing that at room temperature entropic effects dominate, the authors concluded that a study of only the electronic properties of the system would not be sufficient for understanding the driving mechanism of the transition.

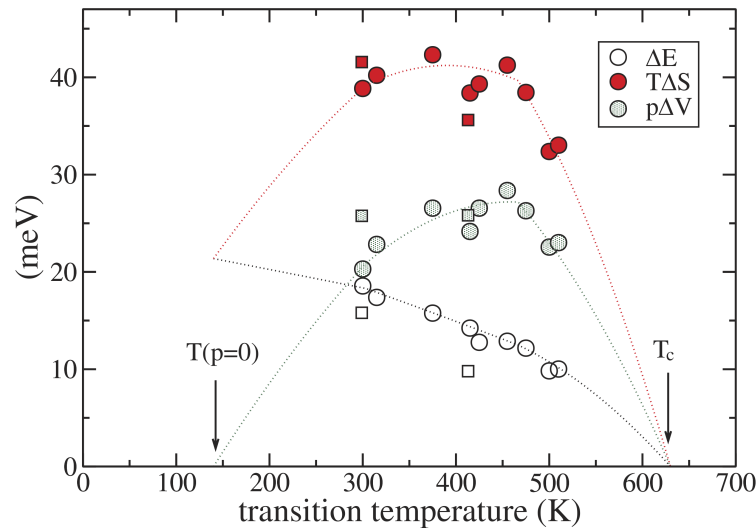


Figure 1.9: Variation of different contributions to the entropy between the α and γ phases across the transition (dotted lines are extrapolations based on the exact limit at T_c). From Ref. [61]. The data are compiled from experimental values taken from [60] (circles) and [65] (squares).

The entropic change across the transition includes two different contributions, that arise from both lattice and electronic degrees of freedom. The role of phonons in the α and γ phases was estimated in several studies. In 2004, high-pressure X-ray and neutron diffraction measurements on polycrystalline cerium by Jeong *et al.* [66] suggested a vibrational contribution $\Delta S_{\text{vib}}^{\gamma-\alpha} \approx 0.75 k_B$ –at room temperature–, that would account for half of the energy change across the transition. The value agreed with earlier estimations of $\Delta S_{\text{vib}}^{\gamma-\alpha}$ [9] but was in contradiction with the inelastic neutron scattering results of Manley *et al.* on a $\text{Ce}_{0.9}\text{Th}_{0.1}$ alloy [67], where the

change in entropy was suggested to be negligible. Further analysis was provided by ultrasonic investigations [68, 69], where the vibrational contribution to the total entropy change was estimated to be on the order of 15%, and by a combined high-pressure and high-temperature X-ray diffraction study [58], which suggested $\Delta S_{\text{vib}}^{\gamma-\alpha} / \Delta S_{\text{tot}}^{\gamma-\alpha} \approx 50\%$. Both values refer to room temperature. In 2011, Krisch *et al.* [70] provided results based on inelastic X-ray scattering. The lattice contribution to the phase transition was found to be around $0.33 k_{\text{B}}$. Using the Clausius-Clapeyron relation $dP/dT = \Delta S_{\text{tot}}^{\gamma-\alpha} / \Delta V^{\gamma-\alpha}$, this would account for around $\approx 50\%$ of the entropy variation.

Despite this uncertainty, one thing is clear: phononic degrees of freedom account for only half of the energy change at most; the other half has to be of electronic nature. This motivates the effort that is put in to the study of the f electrons. A deep understanding of the f electron behavior would clarify the driving mechanism of the α - γ transition. Several theoretical models have been formulated, and are presented in the next section. Starting from the very basics of quantum mechanics, *ab initio* calculations are used to investigate materials from a different perspective than model studies. The *ab initio* study of cerium will be the main subject of this thesis.

1.4 THEORETICAL MODELS FOR THE α - γ PHASE TRANSITION

The nature of the transformation in cerium metal from the γ to the α phase has been a matter of debate for a long time and different theories have been applied to understand its behavior. In general, the intuitive picture of $4f$ electrons undergoing a *localization-delocalization* process has always been prevalent, but the mechanism that would drive this change has been connected to different scenarios and still no conclusion has been reached. In the following, we will provide a summary of the most important theoretical models.

1.4.1 PROMOTIONAL MODEL

In 1947 and 1950 Pauling [16] and Zacharisen [17] suggested independently that the *localization-delocalization* process in cerium could be connected to a *promotion* of $4f$ electrons to the conduction band, $(5d6s)^3 4f^1 \rightarrow (5d6s)^4 4f^0$. The model accounts for the large volume collapse because the $4f$ electron in α -Ce would no longer shield the valence electrons from the nuclear charge and therefore make them more tightly bound, reducing the volume in the process. Simultaneously, the promotion would transform the solid from trivalent to tetravalent and the magnetic moment connected with the $4f$ electrons would be lost. An extension of this picture was given by Ramirez and Falicov [71], who included the Coulomb interaction between the localized f states and the conduction band states in the model, and Coqblin and Blandin (1968) [72], who added a compensation of the spin of the $4f$ electron by the conduction electrons with increasing pressure.

The models fit some experimental observations, but were eventually abandoned when new findings emerged. In particular positron-annihilation experiments (see Section 1.3.1) suggested that the $4f$ orbitals would not change their occupation much across the transition ($1.0 \rightarrow 0.8$). Moreover, the *promotional model* would require the $4f$ level to lie very close to the Fermi energy, so that the energy needed to promote the $4f$ electron would be on the order of the energy gain in the phase transition. This is in contradiction with photoemission experiments, which place the $4f$ states at around 2 eV below the Fermi energy, and would imply that the work needed to compress the γ into the α phase would be around two orders of magnitude higher than the measured value.

1.4.2 MOTT TRANSITION

A *localization-delocalization* model that does not require a change in the number of f electrons was suggested in 1974 by Johansson [1]. According to the Johansson, the behavior of the f electrons in cerium could be associated to that of the valence electrons in a Mott metal-insulator transition [73, 74]. The transition would take place as follows. In the high volume, low pressure γ phase the f electrons feel an inter-site Coulomb repulsion due to their localized nature, sit close to the nuclei and

display a magnetic moment. Upon compression the energy cost of on-site double occupation due to the Coulomb interaction is compensated by the gain in kinetic energy by the formation of a conduction band. The f states subsequently hybridize with each other and the system relaxes into a state of lower volume and vanishing local spin moment.

This mechanism was formulated mathematically by Hubbard in 1963 [75] for interacting particles on a lattice. The so called *Hubbard model* (expressed in second quantization) reads as follows

$$H = -t \sum_{ij,\sigma} (c_{i,\sigma}^\dagger c_{j,\sigma} + h.c.) + U \sum_i n_{i,\uparrow} n_{i,\downarrow} \quad (1.5)$$

where i and j are nearest neighbors of an N site lattice, $c_{i,\sigma}^\dagger$ and $c_{i,\sigma}$ the creation and annihilation operators, $n_{i,\sigma}$ the density operator, t the hopping coefficient and U the on-site repulsion term. Each site can be empty, singly occupied or doubly occupied. The Hamiltonian therefore has two main features: a kinetic term that describes the hopping of particles from one site to the other, with probability proportional to the coefficient t , and an on-site repulsion term that accounts for the energy cost of double occupation U . The physics of the problem is dictated by the balance between U and t , the latter being proportional to the bandwidth W . In the infinite separation limit, the energy levels of a single site are simply ϵ and $\epsilon + U$, representing single and double occupation. When the sites are brought together, as atoms in a solid for instance, the two energy levels form distinct bands, that are commonly called *lower* and *upper* Hubbard bands. Upon compression the bandwidth W increases, and the on-site U shrinks, the two Hubbard bands come closer and eventually overlap. The usual band model is then recovered and the equivalent of a Mott metal-insulator transition is realized.

According to the Mott transition model, the $4f$ orbitals are slightly localized at well separated lattice sites in the γ phase, and in the α phase they form delocalized bands. In the first case, magnetic states emerge, while in the second the system follows a Pauli paramagnetic behavior, as is observed in experiment. In the work by Johansson, the estimated Coulomb interaction produced a bandwidth that was too small compared to the experimental photoemission bandwidth. However, practical

calculations for cerium are complicated by the presence of a conduction band already filled with three $6s5d$ electrons in both phases and close in energy to the $4f$ states. The presence of the $6s5d$ electrons could reduce the intra-atomic repulsion U due to screening effects, and also affect the $4f$ wave functions radial distribution. The interplay between the two effects would then be very difficult to describe. In other lanthanides the screening of outer electrons has already been proven to drive the *lanthanide contraction* (see Section 1.1). The idea of Johansson was adopted and developed in a number of theoretical papers, some of which have calculated the P - T phase diagram explicitly [76, 77, 78], with satisfactory agreement with experimental data.

1.4.3 KONDO VOLUME COLLAPSE

In 1964 Jun Kondo introduced a model to explain the minimum in the resistivity-temperature curve observed experimentally in several dilute magnetic alloys [79]. He associated the behavior of the resistivity with the presence of localized magnetic moments of impurity atoms and formulated a theory in terms of the scattering probability for the spin of conduction electrons and impurities. The outcome was a temperature dependent resistivity with an attractive interaction between the conduction and localized electrons, favoring antiparallel spins. The model predicts a logarithmic dependence of the resistivity on temperature, which originates in the dynamical character of the localized spin system.

The *Kondo physics* can be approximated by the periodic Anderson model [80]. The Hamiltonian is similar to the Hubbard model

$$H = \sum_{k,\sigma} \varepsilon_k c_{k,\sigma}^\dagger c_{k,\sigma} + V \sum_{i,\sigma} (c_{i,\sigma}^\dagger f_{i,\sigma} + h.c.) + U \sum_{i \in \{f\}}^N n_{i,\uparrow} n_{i,\downarrow} \quad (1.6)$$

but now the kinetic energy has two contributions: one from the localized f and the other from the conduction electrons c . f and conduction electrons hybridize with a strength proportional to V . The periodic Anderson model connects Mott-like problems to a band of itinerant electrons.

The idea of Kondo was taken and adapted to the case of cerium by Allen and

Martin, and Lavagna *et al.* in 1982 [2, 81, 3], who formulated what is now known as *Kondo volume collapse* (KVC). In the KVC model the localized states are identified with the $4f$ orbitals, and the itinerant ones with the conduction sd electrons. The α - γ phase transition is then explained by a rapid change of the Kondo temperature (T_K) of the system. The Kondo temperature is the critical parameter of the model. Above T_K the hybridization between the localized states and the conduction band is small. It is dictated by scattering processes and the conductivity displays a strong logarithmic temperature dependence. Below T_K , the localized magnetic moments become completely screened by the delocalized states and *Kondo singlets* (couples of one spin up and one spin down electrons) are formed. According to the model, a rapid variation of the hybridization between the f and sd wave functions under pressure (or decreasing temperature) would cause the Kondo temperature of cerium to change from $T_K \approx 70$ K in the γ phase to $T_K \approx 1700$ K in the α phase [82]. Around ambient conditions the material would be unstable with respect to the formation of Kondo singlets: while in the γ phase it would lie well above its Kondo temperature, the opposite would happen in the α phase. By temperature decrease, the sudden formation of *Kondo singlets* would remove the contribution of spin fluctuations to the entropy, causing the free energy to decrease abruptly with the subsequent volume collapse. The main argument in favor of the KVC model comes from spectroscopy experiments [83, 84, 46]. The increased spectral weight just above the Fermi level (the *Kondo peak*), that is observed in photoemission in the α phase and not in the γ phase, would be the signal of a typical *Kondo resonance* of virtually bound f and sd electrons.

1.4.4 MOTT TRANSITION VERSUS KONDO VOLUME COLLAPSE

The main difference between the Mott transition and the Kondo volume collapse is that in the Mott picture the $4f$ electrons are localized in the γ phase and delocalized in the α phase, while in the KVC the f states remain localized in both phases, and only contribute to cohesion through the interaction with the conduction electrons.

Johansson [76] has criticized the Kondo volume collapse model because the transition line in the P - T phase diagram bends upward, in contrast to the linearity that has been observed experimentally [9] and that is obtained in the framework of

the Mott transition. The Mott picture, on the other hand, suffers from inconsistent energy scales. The delocalization of f orbitals would require energy changes across the transition on the order of the Coulomb repulsion U , that is estimated from photoemission experiments to be about two orders of magnitude greater than the free energy change.

The Kondo scenario, while being motivated and supported by the interpretation of several spectroscopic data sets [54, 52, 46], was criticized in subsequent photoemission studies which revealed discrepancies between the data and the fitting procedures [45, 85, 86]⁷. Probing heavy-fermion compounds containing cerium –which are believed to approximate cerium metal reasonably well and for which the different phases can be explored in wider temperature ranges–, Joyce *et al.* in 1992 [45] performed measurements on the *localized* phase at lower temperatures than the ones available for γ -Ce and observed that the spectral weight of the feature near E_F , the *Kondo resonance*, does not scale with T_K as expected. However, the conclusions from the authors were criticized by Patthey *et al.* [88] in 1993, who suggested agreement of the same data with the KVC. The temperature invariance of photoemission spectra was also observed in Yb-based Ce compounds [89]. As evidenced by Andrew *et al.* [85], against the KVC also stands the amplitude variation with momentum k in the $4f$ bands, because, within the impurity model, the Kondo peak has no k dependence by construction [85]. The k -dependence of the $4f$ bands can instead be explained by a Mott-like interpretation of the α - γ transition [90, 91, 92]. In 1998 a study by Wesche *et al.* [47] further complicated the situation, showing that, at low temperatures, the photoemission spectra of Ce, characterized by the peak at the Fermi energy, is very similar to that of lanthanum, that has no $4f$ electrons.

Despite the numerous attempts to support one or the other model, it appears that a conclusive interpretation of the results has not yet been achieved. The last diatribe on the analysis of the same set of data is recent and dates back to 2009. Lipp *et al.* [58] and subsequently Johansson *et al.* [93] were able to reproduce the same P - T phase diagram and the same temperature dependence of the bulk modulus as derived from X-ray diffraction for both the Kondo volume collapse and the Mott transition model.

⁷We refer to [87] for a review of successes and failures of the KVC in describing photoemission experiments.

The Mott and Kondo volume collapse models have always been considered mutually exclusive, but in the last ten years the opinion has slightly changed. For instance, numerical results from dynamical mean field theory (DMFT)⁸ have revealed strong analogies between the Hubbard and the periodic Anderson model [94], see Figure 1.10. In 2010, Streltsov *et al.* [95] remarked on the importance of the inclusion of inter-site f - f Hubbard-like hybridization in the Anderson impurity calculations for cerium. They argued that, while for cerium containing heavy fermion compounds, such as CeCu₂Si₂, the f - f hybridization can be neglected and the periodic Anderson model gives reasonable results, for cerium metal the f - f hybridization, introduced by the kinetic hopping term of Equation 1.5, is comparable to the hybridization between $4f$ and conduction band electrons. They therefore remarked that the best way of approaching cerium would be through the most general Hamiltonian combining both the Hubbard and the Anderson model.

1.4.5 QUANTUM CHARGE DENSITY FLUCTUATIONS

Based on the observation that electron interactions of quadrupolar origin drive symmetry lowering phase transitions in many lanthanide and actinide compounds [96], and following an idea of Eliasbergh and Capellmann [97], Nikolaev and Michel suggested a new driving mechanism for the α - γ phase transition in a series of works [4, 62, 63]. Eliasbergh and Capellmann initially pointed out that a first order phase transition should imply a symmetry change according to Landau theory. This would be connected to a not yet observed change in lattice structure from fcc to distorted-fcc between the two phases of cerium. However, X-ray diffraction measurements did not provide evidence for such a symmetry breaking, and, in 2008, this hypothesis was excluded by Lipp *et al.* [58]. Nikolaev and Michel then suggested that the phase transition could be accompanied by a special symmetry change from the $Fm\bar{3}m$ to the $Pa\bar{3}$ space group. According to the authors, the atomic centers of mass remain in the fcc structure in both phases, while the symmetry of the electron density changes across the transition. As depicted in Figure 1.11, the orientational order is of a quadrupolar nature, where α -Ce represents the ordered phase. While in γ -Ce the quantum oscillations between degenerate localized f states lead to charge density

⁸Refer to Section 2.5.3 for an introduction to DMFT.

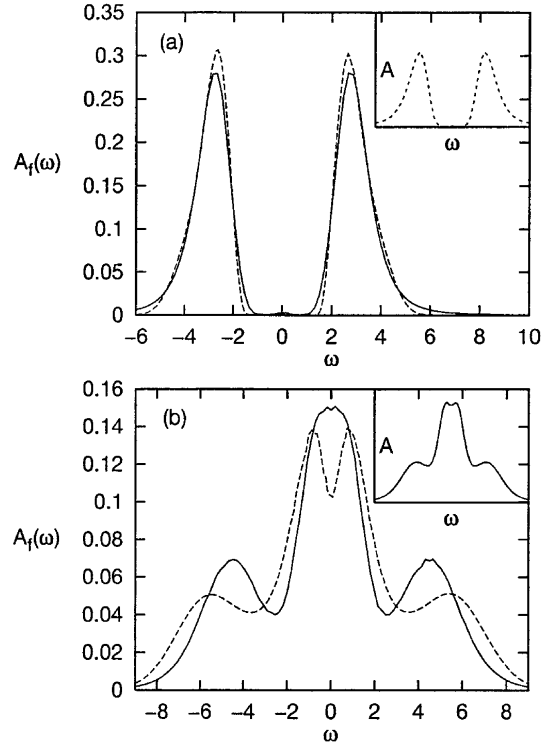


Figure 1.10: Spectral function of the periodic Anderson model according to DMFT calculations (solid line) in the (a) *localized* and (b) *delocalized* regime. Dashed lines are results from quantum Monte Carlo simulations. In the inset the results for the Hubbard Hamiltonian for the same parameters are reported. The similarities between the two models are remarkable. From Ref. [94].

fluctuations, which manifest as a repulsive Coulomb interaction. In the α phase the repulsive contribution suddenly drops because of the charge alignment, and the volume of the fcc crystal consequently collapses.

This mechanism would predict a linear increase of the transition temperature with pressure, fixing for instance one of the failures of the Kondo volume collapse model. However, while presenting an attractive alternative to the Mott and Kondo models, the symmetry change alone would estimate the transition energy to be two orders of magnitude smaller than the observed experimental one [62]. Nikolaev and Michel therefore refined the theory, adding an on-site Hubbard-like repulsion term for the f electrons and hybridization between f and conduction states in the spirit of the Anderson impurity Hamiltonian [62, 63]. They suggested that the change in

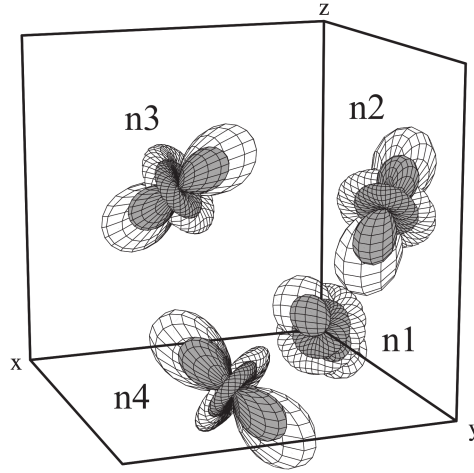


Figure 1.11: The $Pa\bar{3}$ fcc structure of the ordered α phase which gives rise to four distinct sub-lattices (n1-n4). Grey dark quadrupoles correspond to inner $4f$ electron densities and white quadrupoles to outer conduction electron densities with opposite sign. From Ref. [62].

symmetry could be the “real” driving force of a further energetic stabilization coming from Mott-KVC contributions. The model found partial support in the experiments of Tsvyashchenko *et al.* in 2010 [64], who measured the value of the electron field gradient in the α phase to be four time larger than the one in the γ phase⁹.

Still there is no consensus about which of the scenarios discussed above is the one that fully describes the α - γ phase transition. It could be that the complete explanation of the volume collapse would require ingredients from all of the approaches.

1.5 CERIUUM CLUSTERS

The importance of understanding the behavior of f electrons and their role in the α - γ phase transition has been stressed in the previous sections. It has also been pointed out that cerium, with its single $4f$ electron, is the easiest system for studying the behavior of f electrons. An interesting question to ask in this context is then if the phase transition persist on the nanoscale, i.e., for cerium clusters.

⁹Refer to Section 1.3, “Symmetry change”, for more details.

By studying clusters instead of bulk, the role of $4f$ electrons in the formation of chemical bonds could become clearer, for better understanding of bond formation in the solid. Although experimental studies on lanthanide and actinides clusters are scarce, due to the difficulties in the synthesis of these elements, some investigations can be found in the literature [98]. They are mainly focused on the simplest system: the dimer.

The cerium dimer has been studied by resonance Raman spectroscopy in an Ar matrix [99] and ionization potentials and spectroscopic data were collected. A stretching frequency of $\omega_c = 245.4 \pm 4.2 \text{ cm}^{-1}$ was reported, but no further extensive investigations were performed. The topic was addressed with theoretical methods only in recent years, and some proposals on the structure and nature of the bonding were provided by quantum chemical calculations [100, 101]. In 2010, Nikolaev *et al.* [102] attempted an analytical solution in a valence bond model with two $4f$ electrons localized at two cerium sites. The authors mainly confirmed the outcome of previous calculations, assuming a triple chemical bond of the $6s$ and $5d$ states in a $(6s\sigma_g)^2(5d\pi_u)^4$ configuration, and several almost degenerate states available to the localized f electrons.

The study of *rare earth* clusters constitutes a new interesting challenge for both experiment and theory. In particular for cerium, it would be of great interest to know whether the volume collapse is an intrinsic property of electron bonding, that carries from the dimer to the bulk, or, for example, is caused by collective phenomena, like the interaction between the electronic structure and the vibrational degrees of freedom of the lattice.

An eventual volume-collapse at the nano-scale would also be a great finding *per se*. It could open the way for new and unique nano tools. Cerium clusters assembled as nano-towers could become, for example, optically switchable length actors or grouped as rings around nano-capillaries they could act as optically activated valves.

1.6 SUMMARY

Rare earth are heavy elements characterized by the presence of f electrons. Despite their historic name, they are abundant in the earth crust and increasingly used for practical applications. Their properties and their physical behavior are not yet well understood, and subject of intensive research from both the experimental and the theoretical point of view.

Among the features that characterize *rare earth* metals, the presence of a phase transition accompanied by a volume collapse is surely one of the most intriguing. Most notably, in cerium the transition involves two phases that share the same crystal structure. The cerium isostructural α - γ *phase transition* is accompanied by a volume collapse of around 15% at room temperature and a change in the magnetic properties of the material. Experimental characterizations of the α - γ phase transition have been carried out for many decades now, but only partial consensus on the physical properties of the two phases has been reached. In this context a large debate concerns the interpretation of photoemission data. This hinders a complete understanding of the phase transition. Different theoretical models were proposed to address the driving mechanism of the volume collapse, and are found in agreement with one or the other experimental evidence. The Mott transition and the Kondo volume collapse are the most popular models and underlined the role of f electrons. However, these models contain adjustable parameters, and only describe the physical phenomena that are explicitly included in the theory.

Nevertheless, an ongoing discussion on which theory would better describe the differences between the α and γ phases makes cerium one of the most studied elements among the *rare earth*. Calculations that do not rely on model assumptions and are based on a description of the system from the *first-principles* of quantum mechanics also tried to address the problem. An additional advantage of *first-principles* methods over theoretical models is that they are transferable. If they work for cerium, for instance, other lanthanides can be studied with the same approach. As it will be shown in the next chapters, this thesis intends to contribute further in this direction.

2 THEORETICAL METHODS FOR ELECTRONIC STRUCTURE CALCULATIONS

2.1 THE MANY-BODY PROBLEM

Any relevant physical property of real materials can in principle be described *ab initio* by the laws of quantum mechanics. In a non-relativistic regime the behavior of any system of interest is governed by a Hamilton operator (\hat{H}) and a wave function (Φ) that, entering the corresponding Schrödinger equation, represent “the problem to be solved”. The Schrödinger equation is a complex differential equation that leads to the energy (E) and the spatial probability distribution ($|\Phi|^2$) of the ensemble of electrons and nuclei in a given system. Neglecting the spin of electrons and nuclei it assumes the general form

$$\hat{H}\Phi(\{\mathbf{R}_\alpha\}, \{\mathbf{r}_i\}) = E_{tot}\Phi(\{\mathbf{R}_\alpha\}, \{\mathbf{r}_i\}) \quad (2.1)$$

where Φ is the many body wave function that depends on the spatial coordinates of the nuclei ($\{\mathbf{R}_\alpha\}$, $\alpha = 1, \dots, M$ for M atoms in the system) and of the electrons ($\{\mathbf{r}_i\}$, $i = 1, \dots, N$, with N being the total number of electrons).

The Hamilton operator in the absence of external fields¹ is

$$\begin{aligned} \hat{H} = & - \sum_{i=1}^N \frac{1}{2} \nabla_i^2 - \sum_{\alpha=1}^M \frac{1}{2M_\alpha} \nabla_\alpha^2 + \frac{1}{2} \sum_{i \neq j}^N \sum_j^N \frac{1}{|\mathbf{r}_i - \mathbf{r}_j|} + \frac{1}{2} \sum_{\alpha \neq \beta}^M \sum_\beta^M \frac{Z_\alpha Z_\beta}{|\mathbf{R}_\alpha - \mathbf{R}_\beta|} \\ & - \sum_i^N \sum_\alpha^M \frac{Z_\alpha}{|\mathbf{r}_i - \mathbf{R}_\alpha|} \end{aligned} \quad (2.2)$$

where M_α is the mass of nucleus α and the first two terms represent the kinetic energy of electrons and nuclei, respectively. The third term is the Coulomb interaction between electrons, the fourth the Coulomb interaction between the nuclei and the last term the electron-nuclei interaction.

The Schrödinger Equation 2.1 with the Hamiltonian 2.2 is actually impossible to solve exactly for most of systems of interest. A series of approximations and methods were therefore developed in the past to reduce the complexity of the problem. This chapter summarizes those approaches that proved to be useful in the course of this thesis.

The contribution of non-adiabatic coupling to the electronic properties is neglected in what follows. Considering that the nuclei are much heavier than the electrons –the proton mass is approximately 2000 times larger than the electron mass– the motion of electrons and their response to excitations is a few orders of magnitudes faster than that of the nuclei. Therefore, a simplification to the problem is to assume that it is possible to decouple the dynamics of electrons and nuclei. This assumption is referred to as *Born-Oppenheimer approximation* [103]. The original Schrödinger equation can hence be separated into two coupled equations

$$\hat{H}'(\mathbf{r}, \mathbf{R})\Psi(\mathbf{r}, \mathbf{R}) = E_{\mathbf{R}}\Psi(\mathbf{r}, \mathbf{R}) \quad (2.3)$$

$$\left[\hat{H}_N(\mathbf{R}) + E_{\mathbf{R}} \right] \Gamma(\mathbf{R}) = E_{tot}\Gamma(\mathbf{R}). \quad (2.4)$$

The ionic potential occurs only parametrically in the first equation, that describes the motion of electrons in an external field generated by frozen nuclei, and the electronic contribution in Equation 2.4 is the *adiabatic* term $E_{\mathbf{R}}$, which acts as an attractive

¹And in atomic units $\hbar = m_e = e^2 = 1$, $\varepsilon_0 = 1/4\pi$.

potential on the lattice of ions.

Equations 2.3 and 2.4 do not always apply. For example they are not satisfied in a metal-superconductor phase transition, where electrons form Cooper pairs due to the interaction between electrons and lattice vibrations. Superconductivity is a well known phenomena in which the electron-phonon coupling becomes important and the Born-Oppenheimer approximation breaks down. However, for many systems of interest, the Born-Oppenheimer approximation works, and evaluating Equations 2.3 and 2.4 produces meaningful physical results.

In condensed matter physics Equation 2.4 is usually rewritten in a classical flavor, because the De Broglie wave length associated to nuclei is much smaller than the inter-atomic distances. Equation 2.3 then becomes “the problem to be solved” in cases where the electronic behavior is crucial for the understanding of the system’s properties, as in the case for instance in cerium and the α - γ phase transition. It is still a very complicated expression, where the term describing the interaction between electrons would require the knowledge of 3^N variables for a system of N electrons. Handling such a vast number of variables explicitly for real systems is computationally not tractable and approximated methods have been introduced to deal with the problem. The most important and also more relevant for this work will be discussed in the next Sections.

In general, these methods are build on the *independent particle* approximation, in which the electronic Hamiltonian takes the form

$$\hat{H}' = \sum_i \hat{H}_i \quad (2.5)$$

and the electrons wave function can be written as products of single particle wave functions. This leads to a separation similar to the one already achieved between electrons and nuclei. To perform such a separation, the initial Hamiltonian

$$\begin{aligned} \hat{H}' &= - \sum_{i=1}^N \frac{1}{2} \nabla_i^2 - \sum_i^N \sum_{\alpha}^M \frac{Z_{\alpha}}{|\mathbf{r}_i - \mathbf{R}_{\alpha}|} + \frac{1}{2} \sum_{i \neq j}^N \sum_j^N \frac{1}{|\mathbf{r}_i - \mathbf{r}_j|} \\ &= \hat{T}_e + \hat{V}^{\text{ext}} + \frac{1}{2} \sum_{i \neq j} v_{ij}(|\mathbf{r}_i - \mathbf{r}_j|) \end{aligned} \quad (2.6)$$

is reformulated in terms of an additional one-body potential Ω_i such that

$$\begin{aligned}
 \hat{H}' &= \underbrace{\left(\hat{T}_e + \hat{V}^{\text{ext}} + \sum_i \Omega_i \right)}_{\hat{H}^0} + \underbrace{\left(\frac{1}{2} \sum_{i \neq j} v_{ij}(|\mathbf{r}_i - \mathbf{r}_j|) - \sum_i \Omega_i \right)}_{\hat{H}^{\text{res}}} \\
 &= \hat{H}^0 + \hat{H}^{\text{res}} \\
 &= \sum_i \hat{H}_i^0 + \hat{H}^{\text{res}}
 \end{aligned} \tag{2.7}$$

where a convenient choice of Ω_i can provide a small \hat{H}^{res} , that can be treated as a perturbation or neglected.

2.2 HARTREE-FOCK THEORY

The fermionic nature of the electrons imposes the Pauli exclusion principle as an additional constraint. One possible way that automatically produces a Hamiltonian of the form 2.7, is to construct the many-body wave function in an anti-symmetric fashion. This is achieved by writing the electronic wave function as a Slater determinant of single-particle wave functions

$$\Psi(\mathbf{r}_1, \mathbf{r}_2, \dots, \mathbf{r}_N) = \frac{1}{\sqrt{N!}} \begin{vmatrix} \psi_1(\mathbf{r}_1) & \psi_1(\mathbf{r}_2) & \dots & \psi_1(\mathbf{r}_N) \\ \psi_2(\mathbf{r}_1) & \psi_2(\mathbf{r}_2) & \dots & \psi_2(\mathbf{r}_N) \\ \vdots & & \ddots & \\ \psi_N(\mathbf{r}_1) & \dots & & \psi_N(\mathbf{r}_N) \end{vmatrix}. \tag{2.8}$$

Taking the expectation value of the Hamiltonian in Equation 2.6 with respect to the newly introduced wave function leads to an energy functional that can be minimized variationally. Additionally, constraining the single-particle orbitals to be normalized

(i.e. $\langle \psi_i(\mathbf{r}_i) | \psi_j(\mathbf{r}_j) \rangle = \delta_{ij}$) gives the single particle Hartree-Fock² (HF) Equations

$$\begin{aligned} \hat{H}_i^{\text{HF}} \psi_i(\mathbf{r}_i) &= \left[-\frac{\nabla^2}{2} + v^{\text{ext}}(\mathbf{r}_i) + v^{\text{H}}(\mathbf{r}_i) + \hat{v}^{\text{EX}}(\mathbf{r}_i) \right] \psi_i(\mathbf{r}_i) \\ &= \epsilon_i \psi_i(\mathbf{r}_i) \end{aligned} \quad (2.9)$$

where the kinetic energy term \hat{T}_e and the external potential \hat{V}^{ext} are unchanged from Equation 2.6, now just divided in the single particle contributions, with $\hat{V}^{\text{ext}} = \sum_{i=1}^N v^{\text{ext}}(\mathbf{r}_i)$. The third term in 2.6, the interaction among electrons, produces two additional operators v^{H} and \hat{v}^{EX} . The first is called the *Hartree potential* and reads

$$\begin{aligned} v^{\text{H}}(\mathbf{r}_i) &= \sum_{j=1}^N \int \frac{|\psi_j(\mathbf{r}_j)|^2}{|\mathbf{r}_i - \mathbf{r}_j|} d\mathbf{r}_j \\ &= \int \frac{n(\mathbf{r}_j)}{|\mathbf{r}_i - \mathbf{r}_j|} d\mathbf{r}_j, \end{aligned} \quad (2.10)$$

where

$$n(\mathbf{r}) = N \int d\mathbf{r}_2, \dots, d\mathbf{r}_N |\Psi^0(\mathbf{r}_1, \mathbf{r}_2, \dots, \mathbf{r}_N)|^2. \quad (2.11)$$

It takes account of the mean-field Coulomb interaction between the i^{th} electron and the total electron density $n(\mathbf{r})$ as defined in 2.10. The second can be written in its integral form

$$\hat{v}^{\text{EX}}(\mathbf{r}_i) \psi_i(\mathbf{r}_i) = \sum_{j=1}^N \int d\mathbf{r}_j \psi_j^*(\mathbf{r}_j) \frac{1}{|\mathbf{r}_i - \mathbf{r}_j|} \psi_j(\mathbf{r}_i) \psi_i(\mathbf{r}_j). \quad (2.12)$$

It is known as *exchange potential* and takes account of the antisymmetric nature of the total wave function. When two particles have the same coordinates the Hartree and exchange potential cancel each other, so that the spurious self-interaction, formally build into the Hartree potential by summing over all electrons, is eliminated.

The solution of the Hartree-Fock equation are the HF orbitals. However, the orbitals are also part of the equation and the problem must then be solved self-consistently. Starting from an initial guess for the orbitals the density and

²From Hartree [104], who first postulated the factorization of the wave function in single particle states in 1928, and Fock [105], who refined the method by introducing the Slater determinant.

the potentials are derived. The equation is solved, new orbitals and hence a new density are obtained, and the process is iterated until the latter do not vary anymore according to determined convergence criteria.

The exchange operator $\hat{v}^{\text{EX}}(\mathbf{r}_i)$ is usually referred to as a *non-local operator*, in view of the fact that calculating its mean value on a state $\psi_i(\mathbf{r}_i)$ requires the knowledge of ψ_i not only at position \mathbf{r}_i but throughout all space. Evaluating \hat{v}^{EX} is already a non trivial task but the HF equations approximate the full many-body electronic problem in a way that leaves out important contributions. What is not considered is usually referred to as *correlation* –that here represents \hat{H}^{res} of Equation 2.7– and, even if normally small compared to the total energy of the system, its contribution can be crucial for many of the systems. The *correlation* contribution to the Hamiltonian takes mainly account of the fact that one electron is screened by others from the interaction with the nuclei and more distant electrons. The HF method therefore is usually suitable for systems in which particles do not “feel” each other much, and they are quite separated in energy, like in atoms, molecules and insulators. HF performs badly when electrons are large in number and close in energy, like metals.

2.3 DENSITY-FUNCTIONAL THEORY

Another widely used way of approaching the problem presented in Section 2.1 is density-functional theory (DFT) [106, 107, 108]. As the name suggests it is a method in which the total energy of the system is written as a functional of the electronic density rather than the single particle states. A significant difference with respect to Hartree-Fock approach is that, while the HF Slater determinant is an approximate solution to the Schrödinger equation, DFT allows for an *exact* mapping of the full many-body Hamiltonian to single particle effective wave functions. The outcome is therefore not approximated, but drastically reduced in the number of variables to be handled. Approximations are of course entering the problem, but at a subsequent stage, as we will see in the next paragraphs.

2.3.1 THE HOHENBERG-KOHN THEOREM

Considering a system of N interacting, spinless, identical fermions, with a non-degenerated ground state Ψ^0 , the associated density is defined by Equation 2.11. The Hamiltonian \hat{H} of the system takes the form of Equation 2.6, switching the notation $\hat{H}' \rightarrow \hat{H}$,

$$\begin{aligned}\hat{H} &= \sum_i -\frac{1}{2}\nabla_i^2 + \sum_i v^{\text{ext}}(\mathbf{r}_i) + \frac{1}{2} \sum_{i \neq j} v_{ij}(|\mathbf{r}_i - \mathbf{r}_j|) \\ &= \hat{T} + \hat{V}^{\text{ext}} + \hat{V}\end{aligned}\tag{2.13}$$

where \hat{T} is the kinetic energy term, \hat{V}^{ext} the interaction with an external field, usually the potential due to the nuclei, and \hat{V} the full electron-electron interaction. For such a system Hohenberg and Kohn (HK) [109] established the following theorem:

1. There is a one-to-one correspondence between external potential $v^{\text{ext}}(\mathbf{r})$ and electron density $n(\mathbf{r})$.
2. Given an external potential, the ground state expectation value of any physical observable O of a many-electrons system is a unique functional of the electron density $n(\mathbf{r})$

$$\langle \Psi^0 | O | \Psi^0 \rangle = O[n]\tag{2.14}$$

where Ψ^0 is the many-body ground state wave function. In particular the total energy functional can be expressed in terms of a *universal functional* of the density

$$\begin{aligned}E[n] &= \langle \Psi | \hat{T} + \hat{V} | \Psi \rangle + \int d\mathbf{r} v^{\text{ext}}(\mathbf{r})n(\mathbf{r}) \\ &= F_{\text{HK}}[n] + \int d\mathbf{r} v^{\text{ext}}(\mathbf{r})n(\mathbf{r}),\end{aligned}\tag{2.15}$$

and $F_{\text{HK}}[n]$ has a minimum, with respect to the variation of the density, in correspondence with the ground state density.

The Hohenberg-Kohn theorem implies that $F_{\text{HK}}[n]$ does not depend on the external potential and

$$\min_{\Psi \in \Pi} \langle \Psi | \hat{T} + \hat{V}^{\text{ext}} + \hat{V} | \Psi \rangle = \langle \Psi^0 | \hat{H} | \Psi^0 \rangle = \min_{n \in \mathbf{N}} E[n]_{V^{\text{ext}}} \quad (2.16)$$

where Π represents the space of all wave functions and \mathbf{N} the ensemble of all electron densities. Equation 2.16 moves the minimization problem from the wave function to the density and holds for all those densities that are called *v-representable*, for which it is always possible to find a corresponding external potential. This is a non trivial requirement, as there is a wider class of densities that do not correspond to a unique external potential. The latter belong to the *N-representable* ensemble, which contains the *v-representable* one³. One should note that, when approaching practical calculations, a drawback emerges from the HK theorem. The theorem proves the existence of a universal functional, but the functional itself is unknown. This leads to the consequence that the minimization of the energy functional is in practice impossible. The HK theory was therefore reformulated by Kohn and Sham, who suggested an efficient scheme to apply the HK theorem in the spirit of the self-consistent approach already introduced for the Hartree-Fock equations in Section 2.2.

2.3.2 THE KOHN-SHAM METHOD

Kohn and Sham [111] suggested to reformulate the many-body problem by introducing an auxiliary system of non-interacting particle, whose ground state density would be the same as that of the interacting particles system. If such a system would exist it would be unique according to the HK theorem. The original and the auxiliary systems would then be described by the Hamiltonians

$$\hat{H} = \hat{T} + \hat{V}^{\text{ext}} + \hat{V}, \quad (2.17)$$

³More details about the *N-representable* functionals can be found in [110, 107]. The HK theorem has been extended subsequently to its formulation to a wider group of systems, such as *N-representable* functionals, degenerated ground state problems, bosons, spin-polarized systems, superconductors, relativistic systems, etc.

from Equation 2.13, and

$$\hat{H}' = \hat{T}' + \hat{V}^{\text{eff}} \quad (2.18)$$

where T' assumes the general form of the kinetic energy, and \hat{V}^{eff} , called Kohn-Sham (KS) potential, represents an effective potential for a single particle. The energy functionals for the two systems could then be written as

$$\begin{aligned} E[n] &= F_{\text{HK}}[n] + \int d\mathbf{r} v^{\text{ext}}(\mathbf{r})n(\mathbf{r}) \\ &= T[n] + V[n] + \int d\mathbf{r} v^{\text{ext}}(\mathbf{r})n(\mathbf{r}), \end{aligned} \quad (2.19)$$

and

$$E'[n] = T'[n] + \int d\mathbf{r} v^{\text{eff}}(\mathbf{r})n(\mathbf{r}) \quad (2.20)$$

where $T[n]$, $V[n]$ and $T'[n]$ are expectation values of the operators in Equation 2.17 and 2.18. The electron-electron interaction can be approximated by the Hartree potential of Equation 2.10. Adding and subtracting from Equation 2.19 the quantity

$$T'[n] + E^{\text{H}}[n], \quad (2.21)$$

where $E^{\text{H}}[n]$ is evaluated as

$$E^{\text{H}}[n(\mathbf{r})] = \langle \Psi | \hat{V}^{\text{H}}(\mathbf{r}) | \Psi \rangle, \quad (2.22)$$

one obtains the expression

$$E[n(\mathbf{r})] = T'[n] + \int d\mathbf{r} v^{\text{ext}}(\mathbf{r})n(\mathbf{r}) + E^{\text{H}}[n(\mathbf{r})] + E_{\text{xc}}[n(\mathbf{r})], \quad (2.23)$$

where

$$E_{\text{xc}}[n(\mathbf{r})] = T[n] - T'[n] + V[n] - E^{\text{H}}[n] \quad (2.24)$$

is called *exchange-correlation energy*. One can see that $E_{\text{ex}}[n]$ comprises two contributions. The first one is the difference in kinetic energy between the original many-body system and the the new auxiliary system of non-interacting particles, while the second takes all electronic exchange and correlation effects into account, which are not included in the Hartree term.

Imposing then the stationary condition $\delta E[n] = 0$ on Equation 2.23 and Equation 2.20 one obtains

$$\frac{\delta T'[n(\mathbf{r})]}{\delta n(\mathbf{r})} + \int d\mathbf{r} v^{\text{ext}}(\mathbf{r}) + \int d\mathbf{r} d\mathbf{r}' \frac{n(\mathbf{r}')}{|\mathbf{r} - \mathbf{r}'|} + \frac{\delta E_{\text{xc}}[n(\mathbf{r})]}{\delta n(\mathbf{r})} = 0 \quad (2.25)$$

where E^{H} has now been put into the integral form of eq 2.10 and

$$\frac{\delta T'[n(\mathbf{r})]}{\delta n(\mathbf{r})} = - \int d\mathbf{r} v^{\text{eff}}(\mathbf{r}). \quad (2.26)$$

Substituting Equation 2.25 in Equation 2.26 it is possible to finally obtain an expression for the KS potential

$$v^{\text{eff}}(\mathbf{r}) = v^{\text{ext}}(\mathbf{r}) + v^{\text{H}}(\mathbf{r}) + v_{\text{xc}}(\mathbf{r}) \quad (2.27)$$

where $v_{\text{xc}}[n(\mathbf{r})] = \delta E_{\text{xc}}[n(\mathbf{r})] / \delta n(\mathbf{r})$. According to Equation 2.20 one can now rewrite the problem in terms of N *exact* single particle Schrödinger-like equations

$$\left[-\frac{1}{2} \nabla_i^2 + v^{\text{eff}}(\mathbf{r}) \right] \psi_i(\mathbf{r}) = \epsilon_i \psi_i(\mathbf{r}) \quad (2.28)$$

$\{\psi_i\}$ being the set of one-electron orbitals that define the electronic density. Equations 2.26, 2.27 and 2.28 are known as the *Kohn-Sham equations*, and $\{\psi_i\}$ the *Kohn-Sham orbitals*. According to Equation 2.27, v^{eff} depends on $n(\mathbf{r})$. Therefore the KS equations must be solved self-consistently, like in Hartree-Fock. At the very last step the total energy can be calculated according to Equation 2.23

$$E = \sum_{i=1}^N \epsilon_i - \frac{1}{2} \int d\mathbf{r} d\mathbf{r}' \frac{n(\mathbf{r})n(\mathbf{r}')}{|\mathbf{r} - \mathbf{r}'|} + \int d\mathbf{r} v^{\text{ext}}(\mathbf{r})n(\mathbf{r}) - \int d\mathbf{r} v_{\text{xc}}(\mathbf{r})n(\mathbf{r}) \quad (2.29)$$

where the first term contains the kinetic energy and the second is the Hartree energy.

Finally one problem is left: the exchange-correlation (xc) functional E_{xc} . Finding suitable expressions for E_{xc} is the main challenge in DFT, and the next sections will provide an introduction to the problem.

2.4 EXCHANGE-CORRELATION FUNCTIONALS

Since the introduction of the Kohn-Sham method a great number of approximate exchange-correlation functionals have been introduced. Their quality depends on the problem at hand and, of course, their level of complexity. Sophisticated functionals are usually also very computationally demanding. For this reason a never ending search for the right balance between sophistication and tractability is being pursued.

A useful way of categorizing the numerous exchange-correlation functionals is the so called *Jacob's ladder*, introduced by John Perdew [112]. At each rung of the ladder sits a family of functionals. The different families are organized according to the level of approximation they introduce. The Hartree approach is on the ground and the exact xc functional “on heaven”. The functionals that belong to the first rungs of the ladder are quite simple, and the most used ones due to their low computational cost. They perform well in a wide range of situations, as explained in the next paragraphs.

2.4.1 LOCAL-DENSITY APPROXIMATION

Despite sitting on the first rung of the Jacob's ladder, the local-density approximation (LDA) [109] proved to be a very useful approximation to the xc-functional. LDA assumes that the functional dependence of E_{xc} on the density can be approximated by a local relation

$$E_{xc}^{\text{LDA}}[n] \simeq \int d\mathbf{r} n(\mathbf{r}) \varepsilon_{xc}^{\text{hom}}[n(\mathbf{r})] \quad (2.30)$$

where $\varepsilon_{xc}^{\text{hom}}[n(\mathbf{r})]$ is the *exchange-correlation* energy per electron in a homogeneous electrons gas of density $n(\mathbf{r})$. In the homogeneous electrons gas limit the *exchange* energy is known analytically and takes the form

$$\varepsilon_x^{\text{hom}}[n] = -\frac{3}{4} \left(\frac{3}{\pi} \right)^{\frac{1}{3}} \int d\mathbf{r} n^{4/3}(\mathbf{r}) \quad (2.31)$$

while the *correlation* energy $\varepsilon_c^{\text{hom}}[n(\mathbf{r})]$ can be fit to solutions of the many body problem or Quantum Monte Carlo (QMC) data. Among the commonly used LDA

functionals are the Perdew-Zunger (PZ) [113], which parametrizes the QMC results of Ceperley and Alder, the Perdew-Wang (PW) [114], used in this thesis, and the Vosko-Wilk-Nusair (VWN) [115].

Due to its construction, LDA is perfectly suited for systems in which the electron density has very small spatial variations and the electron-electron interaction is well screened. Its success, however, extends to systems, like atoms and molecules, much beyond the initial expectations. This is partially due to a fortuitous cancellation of errors between exchange and correlation [107], and due to the fact that E_{xc}^{LDA} satisfies the *xc-hole* sum rule [116]. The latter asserts that LDA can reproduce the spherical average of a *hole* (the depletion of charge caused by one electron at point \mathbf{r} on all other electrons at point \mathbf{r}') even if the exact hole is not well reproduced.

Various problems, however, still require different treatments of the exchange-correlation functional. For strongly inhomogeneous systems such as surfaces, interfaces and clusters, and for weakly bonded systems, for which Van der Waals forces become important, LDA gives unsatisfactory results.

2.4.2 GENERALIZED GRADIENT APPROXIMATION

After the introduction of the LDA approximation it was suggested that the gradient of the density could also be incorporated into the exchange-correlation functional in order to deal with situations in which the density changes more rapidly in space. An initial guess was to include gradient corrections following a power expansion $|\nabla n(\mathbf{r})|$, $|\nabla n(\mathbf{r})|^2$, $|\nabla^2 n(\mathbf{r})|$. This was called gradient-expansion approximation (GEA). It was readily seen that high order gradient contributions are too complicated to calculate, and the inclusion of only low order contributions did not improve the results with respect to LDA, and often made them worse [117].

Subsequently, an intensive search started, aimed at finding suitable functionals that would include the density gradient in a general form together with the density. The functionals would follow the general expression

$$E_{xc}^{\text{GGA}}[n] = \int d\mathbf{r} f^{\text{GGA}}[n(\mathbf{r}), \nabla n(\mathbf{r})] \quad (2.32)$$

where GGA labels the approach, that is commonly referred to as *generalized gradient approximation* [118, 119, 120]. In GGA the parameters can either be constructed to satisfy as many exact constraints as possible or are fit to experimental data. For these reasons a large number of possible formulations have been developed during the years. In general, the GGA *exchange* energy functional is expressed as

$$E_x^{\text{GGA}}[n] = \int d\mathbf{r} n(\mathbf{r}) \epsilon_x^{\text{hom}}[n] F_x^{\text{GGA}}(s) \quad (2.33)$$

where $\epsilon_x^{\text{hom}}[n]$ is the energy functional of Equation 2.31, and $F_x^{\text{GGA}}(s)$ is an enhancement factor for the exchange energy over the LDA value. The variable s is a reduced gradient of the form

$$s = \frac{|\nabla n(\mathbf{r})|}{2(3\pi^2)^{1/3} n(\mathbf{r})^{4/3}}. \quad (2.34)$$

A very popular approximation is to express $F_x^{\text{GGA}}(s)$ as

$$F_x^{\text{PBE}}(s) = 1 + \kappa - \frac{\kappa}{(1 + \mu s^2/\kappa)} \quad (2.35)$$

where κ and μ are parameters obtained from physical, non-empirical, considerations. Accordingly, also the *correlation* energy is then expressed as a function of s . This is the well known Perdew-Burke-Ernzerhof (PBE) approximation [121], after the name of the authors that introduced it.

GGAs belong to the second rung of the Perdew's ladder. They are usually referred to as *semi-local* approaches, because the evaluation of the energy gradient at a point \mathbf{r} in space requires the density at points in the immediate vicinity. Climbing to the third rung of the Perdew's ladder one then encounters the *meta-GGA* approaches. In the same spirit of the GGA methods, they incorporate also the second derivative of the density, and kinetic energy density contributions. They will not be presented here and we refer the reader to [122, 123, 124] for a general introduction.

2.4.3 SELF-INTERACTION ERROR

One of the major intrinsic drawbacks of LDA and GGA is the so called *self-interaction error* [113, 125]. In the Hartree energy the sum runs over all electrons, although

in principle it should only run over the $N - 1$ other electrons. This introduces a spurious self-interaction (SI). The exchange-correlation functional should cancel this term exactly. However, in practical applications of DFT which require approximated xc functionals, the cancellation is generally not exact, and problems are encountered for example in the estimation of dissociation limits, energy barriers to chemical reactions, long range interactions etc.

It is of interest for this thesis that local and semi-local functionals also encounter large problems in the description of electron localization effects. The SI tends in fact to delocalize electrons. For example the Mott transition, that has been suggested as driving mechanism of the α - γ phase transition –see Section 1.4.2–, is impossible to study within LDA and GGA.

A first step in the direction of correcting self-interaction requires of course a definition of it. This could be formulated in a simple fashion by making the correspondence between orbital-densities

$$n_{i\sigma} = f_{i\sigma} |\psi_{i\sigma}(\mathbf{r})|^2, \quad (2.36)$$

where $f_{i\sigma}$ are the occupation numbers⁴, and accordingly define an interaction energy for a single electron

$$\delta_{i\sigma} = E^{\text{H}}[n_{i\sigma}] + E_{\text{xc}}^{\text{KS}}[n_{i\sigma}, 0]. \quad (2.37)$$

$E_{\text{xc}}^{\text{KS}}[n_{i\uparrow}, n_{i\downarrow}]$ represents the approximate exchange-correlation functional.

While for the exact functional all $\delta_{i\sigma}$ would vanish, this is not necessarily true for approximate functionals. It is, however, possible to define a functional $E_{\text{xc}}^{\text{KS}}[n_{i\uparrow}, n_{i\downarrow}]$ free from the SI problem if it satisfies the more general condition

$$\sum_{i=1}^{N_{\sigma}} \sum_{\sigma=\uparrow,\downarrow} \delta_{i\sigma} = 0. \quad (2.38)$$

But such a definition raises a problem: In a many-electron system there is no unique

⁴Here a spin degeneracy for the orbital i has been introduced through the spin index σ . The local/semi-local approximated xc functional includes therefore the spin coordinate. For a generalization of the approaches introduced in Section 2.4 to spin-dependent systems the reader can refer to [115].

way of defining a density for a single electron [107]. A quantification of self-interaction in a many-electron system should be invariant under unitary transformation, i.e. a transformation that changes the individual orbital densities but leaves the total density unchanged. For common density functionals Equation 2.38 does not have this property [113]. An attempt to introduce a self-interaction correction according to Equation 2.38 was developed in the past, and proved to be useful in some cases. It is presented in the next Section.

2.5 ORBITAL-DEPENDENT APPROACHES

To extend the applicability of DFT, intensive research was carried out in the last decades towards new functionals that would cancel, or reduce, the self-interaction error. In the following, some important functionals that rely on orbital dependent contributions are presented. Even if they were not applied during the course of this thesis, they assumed an important role since the beginning of *ab initio* studies of cerium, and they are most useful in order to understand the problems that are hidden in the *f* electron behavior and how these difficulties were faced in the past.

2.5.1 SELF-INTERACTION CORRECTION - SIC

In 1981, Perdew and Zunger [113] suggested to add a self-interaction correction (SIC) to the local and semi-local energy functionals. The idea was to subtract the SI contribution, as defined in Equation 2.38, directly from the functional expression. The exchange-correlation functional would then become

$$\begin{aligned}
 E_{\text{xc}}^{\text{SIC}} &= E_{\text{xc}}^{\text{KS}} [n_{\uparrow}, n_{\downarrow}] - \sum_{i=1}^{N_{\sigma}} \sum_{\sigma=\uparrow,\downarrow} \delta_{i\sigma} \\
 &= E_{\text{xc}}^{\text{KS}} [n_{\uparrow}, n_{\downarrow}] - \sum_{i=1}^{N_{\sigma}} \sum_{\sigma=\uparrow,\downarrow} (E^{\text{H}} [n_{i\sigma}] + E_{\text{xc}} [n_{i\sigma}, 0])
 \end{aligned}
 \tag{2.39}$$

where $E_{\text{xc}} [n_{\uparrow}, n_{\downarrow}]$ is the usual xc functional in a local/semi-local approximation. The most obvious consequence of the approach is that the newly defined energy functional

depends explicitly on the orbital occupations rather than on the total density. This implies equations that are more complicated to solve and carries a problem: As common functionals are not invariant under unitary transformation there is no unique definition of E_{xc}^{SIC} for a given system. In addition, the usual procedure of minimizing the total energy with respect to the density cannot be applied.

Nevertheless Perdew and Zunger suggested a direct minimization with respect to the orbitals. Even if not formally correct in the Kohn-Sham sense, this is possible and leads to a single-particle equation

$$\left[-\frac{1}{2}\nabla^2 + v_{i\sigma}^{\text{eff}}(\mathbf{r}) \right] \psi_{i\sigma}^{\text{PZ}}(\mathbf{r}) = \epsilon_{i\sigma} \psi_{i\sigma}^{\text{PZ}}(\mathbf{r}), \quad (2.40)$$

with an effective potential

$$\begin{aligned} v_{i\sigma}^{\text{eff}} &= \left[v^{\text{ext}}[n] + v^{\text{H}}[n] + v_{xc,\sigma}[n_{\uparrow}, n_{\downarrow}] \right] - \left[v_{i\sigma}^{\text{H}}[n_{i\sigma}] + v_{xc,i\sigma}[n_{i\sigma}, 0] \right] \\ &= v_{\text{eff},\sigma}^{\text{KS}} - v_{\text{eff},i\sigma}^{\text{SIC}} \end{aligned} \quad (2.41)$$

that substitutes the one of Equation 2.27. Here $v_{\text{eff},\sigma}^{\text{KS}}$ is the standard effective potential in the LDA/GGA approximation and $v_{\text{eff},i\sigma}^{\text{SIC}}$ vanishes for extended states. If the KS equations are solved according to the definition of the new effective potential in Equation 2.41, then the set of KS orbitals also solve Equation 2.38, leading the newly defined energy functional $E^{\text{SIC}}[n_{i\sigma}(\mathbf{r})]$ to a local minimum. However, this does not exclude the existence of other sets of orbitals that would give lower total energies. This deficiency, related to the unitary invariance problem, has been the subject of recent studies by Kümmel *et al.*, who suggested alternative approaches based on the optimized effective potential [126].

The orbital dependence of the SIC method is computationally more costly than local/semi-local functionals. The usual practice is therefore to choose a subspace of relevant orbitals to which the self-interaction correction can be applied. The latter approach is also used in another method that will be presented in the next section, where computational effort is reduced at the cost of formal consistence.

2.5.2 DFT + U

A way to partially remove the self-interaction error in systems that are problematic in the local/semi-local approximation is to add an energetic contribution that is generally called *Hubbard- U repulsion energy*. The U term is borrowed from the Hubbard model introduced in Section 1.4.2, where the Hamiltonian describes particles moving on a discrete space. In the Hubbard Hamiltonian two terms with opposite effects contribute to the system energy. The first one is called *hopping term*. It represents the kinetic energy, and gives the probability that the particles would hop from one site of the lattice to another. The second is called *on-site repulsion*, and penalizes the particles for sitting on an already occupied site. The latter is, in fact, a coefficient, and is usually known as U .

The purpose of adding a U term to LDA/GGA approaches is to localize specific orbitals that are believed to be particularly affected by the self-interaction error. While retaining the orbital-independent one-electron potential for the *delocalized* orbitals, a repulsion term of the form⁵

$$E_U [n_i] = \frac{1}{2}U \sum_{i \neq j} n_i n_j \quad (2.42)$$

is added to a specific subset of pathological orbitals with occupancies n_i . One can now assume a total number $N_l = \sum n_i$ of *localized* electrons. The resulting DFT+ U energy functional is then expressed as

$$E^{\text{DFT}+U} [n_i] = E^{\text{DFT}} [n] - E^{\text{dc}} [n] + E_U [n_i]. \quad (2.43)$$

where the *double counting term* E^{dc} describes the contribution from Equation 2.42 that is already included in the DFT Hamiltonian, and has to be subtracted in order to avoid double counting. It can be evaluated by considering the sum in Equation 2.42 in a mean-field spirit similar to that of Kohn-Sham DFT. The energy expression then reads

$$E_U^{\text{meanfield}} [n] = E^{\text{dc}} [n] = \frac{1}{2}UN_l(N_l - 1). \quad (2.44)$$

⁵The expression for E_U can be obtained by treating the interaction among electrons in a Hartree-Fock-type fashion with an effective screened Coulomb interaction [127, 128].

E^{dc} is subtracted from the usual KS energy functional so that the contribution from Equation 2.42 can be introduced in its orbital dependent form. This is very similar to Equation 2.39, but now it is not the full Hartree term that is subtracted, but only a reduced contribution of it, estimated by the parameter U on the orbitals of interest. The orbital eigenvalues can be calculated from Equation 2.43 as

$$\epsilon_i = \frac{\partial E^{\text{DFT}+U}}{\partial f_i} = \epsilon_i^{\text{DFT}} + U \left(\frac{1}{2} - f_i \right). \quad (2.45)$$

If the double counting contribution is evaluated according to Equation 2.44, the above formula shifts the KS orbital energies by $-U/2$ for occupied states ($f_i = 1$), and by $+U/2$ for unoccupied states ($f_i = 0$). The result is the formation of the so-called *Hubbard bands* above and below the Fermi energy. As illustrated in Figure 2.1, the physics of particular systems, the Mott-Hubbard insulators for instance, can be qualitatively reproduced within the DFT+ U approach [129].

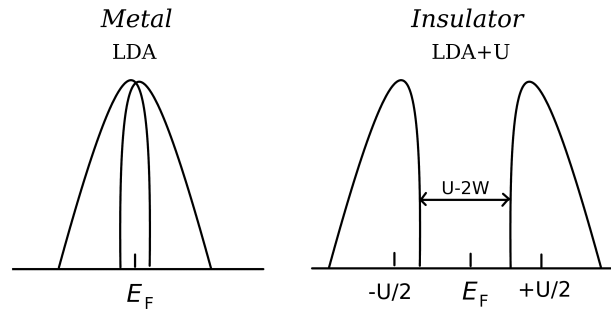


Figure 2.1: Schematic of the spectral function of a metal and a Mott insulator. In a metal the band crosses the Fermi level, the electrons are delocalized and usually local or semi-local functionals give a good description of the system. In a Mott insulator the band gap can be reproduced by adding a U contribution to the standard functionals and it becomes proportional to U and the band width W .

The parameter U has crucial importance for the method, and its determination has attracted growing interest in recent years. U can be treated as a coefficient and adjusted to the system under study in order to reach agreement with experimental data or it can be determined from *first principles*. In the latter case the most widely used approach is the constrained DFT formalism [130], but also approaches based on linear-response [131, 132] and the constrained random-phase approximation [133, 134] were suggested.

The DFT+ U scheme is, from a formal point of view, less sophisticated than SIC, as it does not take into account exchange and correlation in a consistent way. Nevertheless it proves very useful in practice.

2.5.3 DYNAMICAL MEAN FIELD THEORY - LDA+DMFT

The same many-body problem formulated in the DFT+ U (LDA+ U) approach – Equation 2.43 – can be solved with the LDA+DMFT method [135, 136, 137, 138], that combines LDA with dynamical mean field theory (DMFT). Both approaches augment the LDA Hamiltonian with local Coulomb correlation but, while LDA+ U solves the problem in a Hartree-Fock-type fashion without taking into account electronic correlations beyond HF, the LDA+DMFT approach relies on DMFT, as explained in the following paragraphs.

DMFT finds its roots in a concept introduced in 1989 by Metzner and Vollhardt [139] with reference to the Hubbard model in the limit of infinite dimensions. In the limit of infinite dimensions every site on a periodic lattice has an infinite number of neighboring lattice sites. The relation between kinetic energy and Coulomb interaction is maintained, but the momentum dependence drops, leading to considerably simplified calculations. As a consequence, the Coulomb interaction U yields a strictly local frequency-dependent (i.e. *dynamic*) interaction, while the non-local density-density interactions are reduced to the Hartree term, which is frequency-independent.

Georges and Kotliar [140] subsequently showed that a Hubbard-like Hamiltonian in the limit of infinite dimensions has local Feynman diagram contributions that are equivalent to the ones of an Anderson impurity model⁶. This means, a Hamiltonian like in Equation 1.5

$$\hat{H} = -t \sum_{ij,\sigma} (c_{i,\sigma}^\dagger c_{j,\sigma} + h.c.) + U \sum_i n_{i,\uparrow} n_{i,\downarrow} \quad (2.46)$$

can be mapped into an auxiliary Anderson impurity model –see Equation 1.6– in

⁶Provided that the on-site interaction has the same form as the original Hamiltonian. Refer to Section 1.4 for an introduction to the periodic Anderson model.

the infinite dimension limit:

$$\hat{H} = \sum_{\nu,\sigma} \varepsilon_{\nu}^{bath} n_{\nu,\sigma}^{bath} + \sum_{\sigma} \varepsilon_{0,\sigma} + U (n_{0,\uparrow} n_{0,\downarrow}) + V_{\nu} \sum_{\nu,\sigma} \left(f_{0,\sigma}^{\dagger} c_{\nu,\sigma}^{bath} + h.c. \right). \quad (2.47)$$

It describes an impurity with energy level $\varepsilon_{0,\sigma}$ in a bath of electrons with energy ε_{ν}^{bath} . The electrons can hop in and out the impurity via the hybridization V_{ν} . In Figure 2.2 a sketch of the DMFT mapping is shown.

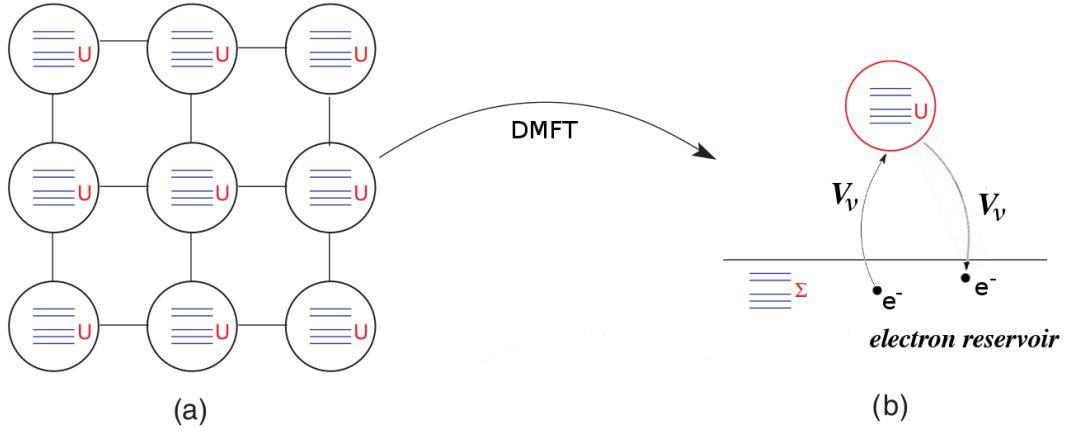


Figure 2.2: DMFT maps the lattice of atoms and electrons with in-site interaction U (a) into a single-site impurity that interacts with a bath of electrons (b). The bath electrons are dressed by the self-energy Σ and interact with the impurity via the hybridization coefficient V_{ν} . Adapted from Ref. [138].

The above considerations imply that the DFT+ U Hamiltonian of Equation 2.43 can be mapped onto an auxiliary Anderson impurity problem with the same Green function and self-energy. The parameters ε_{ν}^{bath} and V_{ν} can be combined in what is generally known as *hybridization function*,

$$\Delta(\omega) = \sum_{\nu} \frac{|V_{\nu}|^2}{\omega - \varepsilon_{\nu}^{bath}}, \quad (2.48)$$

which acts as a *dynamic mean field*. In this case the problem can be solved by guessing an hybridization function for the Anderson impurity model, that gives the

self-energy and the Green function according to the following expressions

$$\Sigma[\Delta(\omega)] = \Delta(\omega) - \frac{1}{G[\Delta(\omega)]} + \omega, \quad (2.49)$$

$$G[\Delta(\omega)] = \sum_{\mathbf{k}} (\omega - \Sigma[\Delta(\omega)] - t_{\mathbf{k}})^{-1}, \quad (2.50)$$

where the coefficient $t_{\mathbf{k}}$ represents the Fourier transform of the hopping matrix elements t_{ij} of the original system.

The essence of the DMFT method is the self-consistent determination of the hybridization function. After the initial guess, which leads to the self-energy and Green function of both original and auxiliary systems, the impurity model's *non-interacting* Green function is calculated according to

$$\mathcal{G}^0 = (G^{-1} + \Sigma^{-1})^{-1}. \quad (2.51)$$

The lattice problem is then reduced to a single-site problem with some effective parameters, and can be solved with a variety of analytic and numerical techniques, such as self-consistent perturbation theory [141], the non-crossing approximation [142, 143], quantum Monte Carlo [144, 145], exact diagonalization [146] and numerical renormalization groups [147]. A new hybridization function is then derived, the original self-energy and Green function are replaced, and the cycle is repeated until convergence is reached. The net result is a KS-type equation of the form

$$E^{\text{LDA+DMFT}}[n(\mathbf{r}), G] = T[n(\mathbf{r}), G] + E^{\text{ext}}[n(\mathbf{r})] + E^{\text{H}}[n(\mathbf{r})] + E_{\text{xc}}[n(\mathbf{r}), G] \quad (2.52)$$

where now the kinetic energy is no longer that of a free electron system because it involves the local Green function G .

With respect to DFT+ U , LDA+DMFT can account for local correlations. There are, however, some problems arising in practical calculations. A first one is intrinsic and is connected to the locality of the interaction that is taken into account: LDA+DMFT completely neglects the non-local part of the correlation. But there are also computational difficulties. The main one is that the approximated methods employed in solving the impurity problem are often very demanding and for this

reason, as for the case of Quantum Monte Carlo, restricted to the “high” temperature regime. This hinders the study of some interesting regions of the phase diagram, as for example for cerium.

A further development of the DMFT method is given by “cluster DMFT”. The Hubbard model can be mapped on a multi-site impurity (cluster) problem. This adds some spatial dependence to the impurity self-energy. Cluster DMFT is applied for example to non-trivial paramagnetic insulators (e.g. frustrated magnets), to preserve short range correlation (e.g. antiferromagnetic fluctuations), or to add systematic corrections beyond the mean field in Mott transitions.

2.6 HYBRID FUNCTIONALS

As the name suggests *hybrid functionals*, that sit on the fourth rung of the Jacob’s ladder, combine the local/semi-local treatment of exchange and correlation with a fraction of exact-exchange. In the simplest formulation, hybrid functionals are expressed as

$$E_{xc}^{\text{hyb}} = E_c^{\text{DFT}} + aE_x^{\text{EX}} + (1 - a)E_x^{\text{DFT}} \quad (2.53)$$

where correlation is retained at the level of KS-DFT and exchange is balanced between Hartree-Fock and standard xc functionals through the parameter a . The latter depends on the employed KS-functional and can be determined either from a fit to experimental data [148], from high-level quantum-chemistry results for molecules, or from considerations linked to the *adiabatic connection (AC) theorem* [149, 110, 150]. According to the AC theorem, an exchange-correlation functional can be expressed as an adiabatic connection between the fully interacting system and the non-interacting Kohn-Sham system. The Coulomb interaction between electrons is adiabatically switch on going from one system to the other and the two situations are linked to the extreme values of a coupling constant $0 \leq \lambda \leq 1$. In this picture, the HK functional of Equation 2.15 can be expressed as

$$F_\lambda[n] = \langle \psi_\lambda | T + \lambda V | \psi_\lambda \rangle \quad (2.54)$$

where V is the full many body electron-electron interaction and the ψ_λ are normalized, antisymmetric wave functions that minimize $F_\lambda[n]$. The coupling λ determines the percentage of electron-electron correlation that is included in the problem. Following Equation 2.24 the xc energy functional can then be written in terms of Equation 2.54 as

$$\begin{aligned} E_{\text{xc}}[n] &= F_1[n] - F_0[n] - E^{\text{H}}[n] \\ &= \int_0^1 \frac{\partial F_\lambda[n]}{\partial \lambda} d\lambda - E^{\text{H}}[n] \\ &= \int_0^1 E_{\text{xc},\lambda}[n] d\lambda, \end{aligned} \quad (2.55)$$

Equation 2.55 serves as a definition for a new density functional of a fictitious system with scaled Coulomb interaction

$$E_{\text{xc},\lambda}[n] = \langle \psi_\lambda | V | \psi_\lambda \rangle - E^{\text{H}}[n]. \quad (2.56)$$

Considering that HF provides an exact treatment of exchange, Becke [149] suggested in 1993 to approximate the integral according to the trapezoidal integration rule between $\lambda = 0$ and $\lambda = 1$, with exact exchange used to represent the first and LSDA⁷ the latter. The result reads

$$E_{\text{xc}} = 0.5E_x^{\text{EX}} + 0.5E_{\text{xc}}^{\text{LSDA}}[n]. \quad (2.57)$$

This approach did not considerably improve the description of systems over standard GGA functionals, but opened a way to explore a new class of methods in DFT. It was in fact discovered that it would help to separate the exchange and correlation parts in the form of Equation 2.53. In 1996, Perdew, Ernzerhof, and Burke suggested to express the integrand of Equation 2.55 as

$$E_{\text{xc},\lambda}^{\text{hyb}} = E_{\text{xc},\lambda}^{\text{KS}} + (E_x^{\text{EX}} - E_x^{\text{KS}})(1 - \lambda)^{n-1} \quad (2.58)$$

which lead to $a = 1/n$. They then suggested that an appropriate choice would be $n = 4$, as fourth order Møller-Plesset perturbation theory yields small atomization

⁷Local spin density approximation. Generalization of LDA to spin dependent systems [115].

errors for $n = 4$ [151]. The performance of this formulation was of course related to the GGA functional in use, but it turned out that for the PBE functional $a = 0.25$ was actually a very good estimation. The method, now labeled PBE0 [121], became very popular and largely contributed to improve results for a wide range of systems. For many materials, PBE0 improves the description of energetic and structural properties when compared to PBE [152]. As it will become clear in the second part of this thesis, PBE0 also proved to be a good choice for the description of cerium and the α - γ phase transition. This can be related to the fact that hybrid functionals, containing a fraction of exact exchange, often handle localized states well, despite the fact that they are not rigorously self-interaction-free [153, 154, 155].

The variety of hybrid xc approximations has grown considerably during time, and found application in a variety of problems. Further implementations of E_{xc}^{hyb} involve more than one parameter, the determination of which is usually deduced by fits to experimental data sets or high-level quantum-chemistry calculations. The most popular functionals of this group are the B3PW91 and B3LYP [156] functionals, and the meta-GGA based formulations MPWB1K [157] and PW6B95 [158]⁸. B3LYP, that is fit to the G1 data⁹, produces excellent results for a wide range of systems, and is nowadays the most widely used functional in chemistry.

Additional flexibility was introduced in hybrid functionals by the partition of the exchange term into short-range (SR) and long-range (LR) contributions. This lead to *screened hybrid functionals* of the form

$$\begin{aligned}
 E_{xc,\lambda}^{\text{hyb}} &= aE_x^{\text{SR,EX}} + (1 - a)E_x^{\text{SR,DFT}} \\
 &+ bE_x^{\text{LR,EX}} + (1 - b)E_x^{\text{LR,DFT}} \\
 &+ E_c^{\text{DFT}}.
 \end{aligned}
 \tag{2.59}$$

By setting $b = 0$ the long range part of exact exchange can be scaled down completely, leading to the approach that is generally known as HSE functional [161, 162, 163].

⁸The reader can refer to reference [125] for a review of the most used methods nowadays.

⁹Gaussian-1 database of Pople and co-workers [159, 160].

2.7 MANY-BODY PERTURBATION THEORY

Another rung in the Jacob's ladder is climbed when the description of physical systems is improved over the hybrid functional approach. The new approaches are based on many-body perturbation theory. The main characteristic of all these methods is that many-body contributions beyond the semi-local approximation apply not only to exchange, as in hybrid functionals, but also to correlation.

In the following some of the most popular methods, that were employed in this thesis, will be presented. As for the case of the random-phase approximation (RPA), adding many-body effects to the study of cerium turned out to be decisive for a better description of the system, as will be demonstrated in Chapter 5.

2.7.1 RANDOM-PHASE APPROXIMATION - RPA

The random-phase approximation was introduced already in the 50's, in the context of the homogeneous electron gas. In a series of papers published by Bohm and Pines [164, 165, 166, 167] it was suggested that a good estimation of correlation in the homogeneous electron gas could be obtained by separating the collective degrees of freedom from the single-particle degrees of freedom. This leads to an inclusion of the long-range Coulomb interaction in the collective behavior of the system, while the single-particle interaction is reduced to a short-range screened interaction. The RPA neglects the coupling between the collective and the single-particle degrees of freedom.

The idea has proved to be of great utility, and it led to a series of developments [168, 169, 170, 171, 172, 173]. In particular Gell-Mann and Brueckner noticed in 1957 that a sum of all Feynman ring diagrams in the perturbative expansion of the correlation energy would remove some divergence problems intrinsic to order-by-order expansions. The Gell-Mann and Brueckner result sets the foundation for modern applications of RPA, especially in the field of DFT, where it can be introduced in the framework of the adiabatic-connection fluctuation-dissipation theorem (ACFD) [174, 175, 176].

It can be shown¹⁰ that Equation 2.55 in Section 2.6 can be rewritten as

$$E_{\text{xc}} = \frac{1}{2} \int_0^1 d\lambda \int d\mathbf{r}d\mathbf{r}' \frac{n_{\text{xc}}^\lambda(\mathbf{r}, \mathbf{r}')n(\mathbf{r})}{|\mathbf{r} - \mathbf{r}'|} \quad (2.60)$$

where

$$n_{\text{xc}}^\lambda(\mathbf{r}, \mathbf{r}') = \frac{\langle \psi_\lambda | \delta \hat{n}(\mathbf{r}) \delta \hat{n}(\mathbf{r}') | \psi_\lambda \rangle}{n(\mathbf{r})} - \delta(\mathbf{r} - \mathbf{r}'), \quad (2.61)$$

$$\delta \hat{n}(\mathbf{r}) = \hat{n}(\mathbf{r}) - n(\mathbf{r}), \quad (2.62)$$

$$\hat{n}(\mathbf{r}) = \sum_{i=1}^N \delta(\mathbf{r} - \mathbf{r}'). \quad (2.63)$$

$n_{\text{xc}}^\lambda(\mathbf{r}, \mathbf{r}')$ is the so called *xc hole* at coupling strength λ . This is a less intuitive formulation, but it is useful to introduce the *fluctuation* $\delta \hat{n}(\mathbf{r})$ of the density operator $\hat{n}(\mathbf{r})$ around its expectation value $n(\mathbf{r})$. The density-density correlation of Equation 2.62 can then be linked to the response properties (dissipation) of the system through the zero-temperature *fluctuation-dissipation* theorem [178, 179]. The theorem states that the response of a system in thermodynamic equilibrium to a small external perturbation is the same as its response to the spontaneous internal fluctuations in the absence of the perturbation. It can be shown that the following relation holds

$$\langle \psi_\lambda | \delta \hat{n}(\mathbf{r}) \delta \hat{n}(\mathbf{r}') | \psi_\lambda \rangle = -\frac{1}{\pi} \int_0^\infty d\omega \text{Im} \chi^\lambda(\mathbf{r}, \mathbf{r}', \omega) \quad (2.64)$$

where $\chi^\lambda(\mathbf{r}, \mathbf{r}', \omega)$ is the density-response function of the system. Combining equations 2.60 and 2.64 one can obtain a new formulation for the exchange-correlation functional, with $v(\mathbf{r}, \mathbf{r}') = 1/|\mathbf{r} - \mathbf{r}'|$,

$$E_{\text{xc}} = \frac{1}{2} \int_0^1 d\lambda \int d\mathbf{r}d\mathbf{r}' v(\mathbf{r}, \mathbf{r}') \left[-\frac{1}{\pi} \int_0^\infty d\omega \chi^\lambda(\mathbf{r}, \mathbf{r}', i\omega) - \delta(\mathbf{r}, \mathbf{r}')n(\mathbf{r}) \right], \quad (2.65)$$

where now the problem of estimating the xc energy translates to the computation of the response function of the λ -interacting systems along the adiabatic-connection

¹⁰See Ren *et al.* [177] for a recent review on the RPA.

path. The RPA consists in approximating the response function as

$$\chi_{\text{RPA}}^\lambda(\mathbf{r}, \mathbf{r}', i\omega) = \chi^0(\mathbf{r}, \mathbf{r}', i\omega) + \int d\mathbf{r}_1 d\mathbf{r}_2 \chi^0(\mathbf{r}, \mathbf{r}_1, i\omega) \lambda v(\mathbf{r}_1 - \mathbf{r}_2) \chi_{\text{RPA}}^\lambda(\mathbf{r}_2, \mathbf{r}', i\omega) \quad (2.66)$$

with $\chi^0(\mathbf{r}, \mathbf{r}_1, i\omega)$ being the independent-particle response function of the KS reference system at $\lambda = 0$

$$\chi^0(\mathbf{r}, \mathbf{r}', i\omega) = \sum_{ij} \frac{(f_i - f_j) \psi_i^*(\mathbf{r}) \psi_j(\mathbf{r}) \psi_j^*(\mathbf{r}') \psi_i(\mathbf{r}')}{\epsilon_i - \epsilon_j - i\omega}. \quad (2.67)$$

A very insightful property of Equation 2.66 is that, when inserted into Equation 2.65, it produces two terms E_x^{EX} and E_c^{RPA} with:

$$E_{\text{xc}}^{\text{RPA}} = E_x^{\text{EX}} + E_c^{\text{RPA}}. \quad (2.68)$$

The explicit expression of the two contributions to the RPA xc energy is given by

$$\begin{aligned} E_x^{\text{EX}} &= \frac{1}{2} \int d\mathbf{r} d\mathbf{r}' v(\mathbf{r}, \mathbf{r}') \left[-\frac{1}{\pi} \int_0^\infty d\omega \chi^0(\mathbf{r}, \mathbf{r}', i\omega) - \delta(\mathbf{r}, \mathbf{r}') n(\mathbf{r}) \right] \\ &= - \sum_{ij} f_i f_j \int d\mathbf{r} d\mathbf{r}' \psi_i^*(\mathbf{r}) \psi_j(\mathbf{r}) v(\mathbf{r}, \mathbf{r}') \psi_j^*(\mathbf{r}') \psi_i(\mathbf{r}'), \end{aligned} \quad (2.69)$$

where in the last line the known formulation of $\chi^0(\mathbf{r}, \mathbf{r}', i\omega)$ in terms of the KS orbitals with occupation numbers f_i has been substituted, and

$$\begin{aligned} E_c^{\text{RPA}} &= \frac{1}{2\pi} \int d\mathbf{r} d\mathbf{r}' v(\mathbf{r}, \mathbf{r}') \int_0^\infty d\omega \left[\int_0^1 d\lambda \chi_{\text{RPA}}^\lambda(\mathbf{r}, \mathbf{r}', i\omega) - \chi^0(\mathbf{r}, \mathbf{r}', i\omega) \right] \\ &= \frac{1}{2\pi} \int_0^\infty d\omega \text{Tr} [\ln(1 - \chi^0(i\omega)v) + \chi^0(i\omega)v], \end{aligned} \quad (2.70)$$

where the following convention is used

$$\text{Tr}[AB] = \int \int d\mathbf{r} d\mathbf{r}' A(\mathbf{r}, \mathbf{r}') B(\mathbf{r}', \mathbf{r}). \quad (2.71)$$

In this expression for the E_{xc} functional the *exact-exchange* energy of Hartree-Fock theory is readily recognized in the first term E_x^{EX} , and the second term E_c^{RPA} can be

computed from the charge susceptibility.

Equation 2.68 has some great advantages over conventional ways of treating exchange and correlation in KS-DFT. The exact-exchange energy cancels the spurious self-interaction error present in the Hartree energy and the RPA correlation is fully non-local. In Figure 2.3 the RPA is illustrated in terms of Goldstone diagrams [180]. It can be shown that it takes the form of a sum of ring diagrams to infinite order. This selected summation to infinite order avoids divergences, which makes RPA applicable to small-gap or metallic systems where finite-order many-body perturbation theories break down.

The success of the random-phase approximation in DFT has been demonstrated in a series of works on e.g. molecular properties [181, 182, 183, 184], periodic systems [185, 186, 187], and adsorption problems [188, 189, 190, 191]. The RPA correction includes long-range van der Waals interactions automatically, so it improves the description of weakly bonded molecules substantially over conventional DFT and hybrid functionals [192, 193, 183]. For example, the performance of RPA on the S22 test set [192], which contains 22 weakly bound molecular complex of different size and bonding type, has been analyzed by Ren *et al.* [183], who reported a reduction of around 70% on the mean absolute error for the binding energy with respect to PBE. Likewise, RPA showed remarkable performance for the prediction of barrier heights in chemical reactions [194, 195], which are substantially underestimated by PBE. Concerning atomization energies instead, RPA does not improve considerably over PBE. The dissociation of H_2 in RPA, for example, preserves the positive “bump” at intermediate bond distances [177], typical of local/semi-local functionals. Several authors reported RPA calculations on crystalline solids (on e.g. Si [196, 197, 198], NaCl [197], rare-gas solids [187], graphite [186, 199]) reaching the general agreement that RPA performs better than LDA and PBE for the description of lattice constants and bulk moduli, while it can worsen results [185] for atomization energies, as for the case of molecules. It has been shown [186, 190], for example, that RPA can correct the known failure of LDA and GGA in predicting the right adsorption site for CO on Cu(111) surface.

The major drawback of the RPA approach remains, however, the high computational cost, that still hinders a widespread use. On the other hand several

improvements beyond the RPA have been proposed recently, which make RPA-based methods an active field of research. In the next paragraphs some of them will be presented.

2.7.2 SECOND ORDER SCREENED EXCHANGE - SOSEX

Recently, Ren *et al.* [195] demonstrated that an alternative derivation of the RPA is obtained by employing a perturbation theory on top of the non-interacting KS problem. This also automatically provides two further correction terms, called single excitations and second order screened exchange. The Hamiltonian of the system can be partitioned according to

$$\hat{H}(\lambda) = \hat{H}_0 + \lambda \hat{H}_1(\lambda) \quad (2.72)$$

where \hat{H}_0 is a mean-field Hamiltonian and $\hat{H}_1(\lambda)$ the rest. The total energy can then be expressed as

$$E = E_0 + \int_0^1 d\lambda \langle \psi_\lambda | \hat{H}_1 | \psi_\lambda \rangle. \quad (2.73)$$

Expanding Equation 2.73 according to second-order Rayleigh-Schrödinger perturbation theory, one obtains a first-order correction

$$\begin{aligned} E^{(1)} &= \int_0^1 d\lambda \langle \psi_0 | \hat{H}_1 | \psi_0 \rangle \\ &= E^{\text{H}} + E_{\text{x}}^{\text{EX}} - E^{\text{MF}} \end{aligned} \quad (2.74)$$

where the first two terms are known and $E^{\text{MF}} = \langle \psi_0 | v^{\text{MF}} | \psi_0 \rangle$ is a double-counting correction to the mean-field contributions included in \hat{H}^0 . If $\hat{H}^0 = \hat{H}^{\text{HF}}$ the sum $E_0 + E^{(1)}$ gives the Hartree-Fock energy, while if $\hat{H}^0 \neq \hat{H}^{\text{HF}}$ it adds exact-exchange contributions to the total energy. All higher order contributions take account of correlation in the system. For instance the second-order energy is given by

$$E^{(2)} = \sum_i^{\text{occ}} \sum_a^{\text{unocc}} \frac{|\langle \psi_0 | \hat{H}_1 | \psi_i^a \rangle|^2}{E_0 - E_{i,a}^{(0)}} + \sum_{ij}^{\text{occ}} \sum_{ab}^{\text{unocc}} \frac{|\langle \psi_0 | \hat{H}_1 | \psi_{ij}^{ab} \rangle|^2}{E_0 - E_{ij,ab}^{(0)}} \quad (2.75)$$

where the ψ_n correspond to the excited states of the system with energy $E_n^{(0)} = \langle \psi_n | \hat{H}_0 | \psi_n \rangle$. The wave functions ψ_n can be divided into single- and double-excited states, $\psi_{i,a}$ and $\psi_{ij,ab}$ respectively. Higher orders excitations do not contribute due to the nature of \hat{H}_1 , that contains only one- and two-particles operators.

The double-excitation contribution can be split into two terms, generally addressed as second-order *direct* and *exchange*. RPA corresponds to a renormalization of the direct term. As it turns out, one can apply the same renormalization also to the second order exchange term. The result is the inclusion of screened second-order exchange (SOSEX) processes [200, 201, 202] that takes the diagrammatic form in Figure 2.3.

$$E_c^{\text{RPA}} = \text{[Diagram 1]} + \text{[Diagram 2]} + \dots$$

$$E_c^{\text{SOSEX}} = \text{[Diagram 3]} + \text{[Diagram 4]} + \dots$$

Figure 2.3: Goldstone diagrams for the RPA and SOSEX correlation energy. Solid lines denote particle (up arrows) and hole (down arrows) states without frequency dependence. Dashed lines correspond to the bare Coulomb interaction v . From Ref. [177].

The combination of the RPA with SOSEX can perform better than the RPA alone in some cases. For example it has success for atomization energies. The improvement is however not systematic. This is the case for the dissociation of covalent diatomic molecules [202].

2.7.3 SINGLE-EXCITATIONS

Equation 2.75 also introduces the contribution of single excitations. It can be shown [177] that the single excitation energy can be expressed according to

$$\begin{aligned}
 E_c^{\text{SE}} &= \sum_i^{\text{occ}} \sum_a^{\text{unocc}} \frac{|\langle \psi_0 | \hat{H}_1 | \psi_i^a \rangle|^2}{E_0 - E_{i,a}^{(0)}} \\
 &= \sum_{ia} \frac{|\langle \psi_i | \hat{v}^{\text{HF}} - \hat{v}^{\text{MF}} | \psi_a \rangle|^2}{\epsilon_i - \epsilon_a},
 \end{aligned} \tag{2.76}$$

where \hat{v}^{HF} is the self-consistent Hartree-Fock potential and \hat{v}^{MF} is the mean field potential associated with the reference Hamiltonian. E_c^{SE} vanishes if \hat{H}_0 is the Hartree-Fock Hamiltonian. As for RPA and SOSEX, single-excitations can also be renormalized by a sum to infinite order –*renormalized single excitations* (rSE). The rSE contribution is illustrated in terms of Goldstone diagrams in figure 2.4, where the dashed lines denote the matrix elements $\Delta v_{pq} = \langle \psi_p | \hat{v}^{\text{HF}} - \hat{v}^{\text{MF}} | \psi_q \rangle$. The first diagram in Figure 2.4 represents the single-excitations..

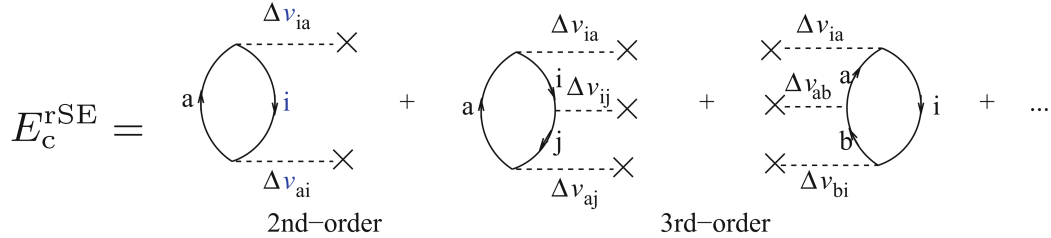


Figure 2.4: Goldstone diagrams for renormalized single-excitation contributions. From Ref. [177].

The combination of rSE, RPA and SOSEX is known as *renormalized second-order perturbation theory* (rPT2). rPT2 is a new method, but holds great promise. For example rSE improves the accuracy of weakly bonded molecules [183], as well as the atomization energies of covalent molecules and insulating solids [195], compared to RPA.

II *Ab initio* DESCRIPTION OF THE α - γ TRANSITION IN CERIUM

3 PREVIOUS *Ab initio* STUDIES OF THE α - γ TRANSITION

In Section 1.3.7 we have alluded to the fact that entropic effects are suspected to play a significant role in the α - γ phase transition. This motivated a number of authors to apply *first-principle* methods. The advantage of approaching complex problems, like the α - γ phase transition, with *ab initio* techniques is that no assumptions have to be made. However, *first-principles* DFT-based calculations for Ce have so far been unable to produce a double minimum in the total energy versus volume curve at zero temperature within a single theoretical framework. Such a double minimum would be a direct indication of the phase transition.

LDA and GGA¹ calculations of Ce were reported by various authors [203, 204, 205, 206]. An unchanged number of f electrons at the two experimental volumes for α and γ phases was reported by all authors, together with the observed experimental change in magnetic properties. However, no signature of the volume collapse was encountered in the total energy versus volume curve. Based on the *localization* vs. *delocalization* interpretation of the phase transition, the failure of LDA and GGA was mainly attributed to the well known *self-interaction problem* intrinsic in these theories –see Section 2.4.3. The self-interaction has a tendency to *delocalize* electrons. Local and semi-local approaches found a minimum in the cerium cohesive energy versus volume curve only in correspondence with the α phase, where the f electrons are believed to be delocalized, whereas no stable solution was found for the γ phase.

Following the failure of standard LDA and PBE approaches, a number of authors

¹Refer to Chapter 2 for an introduction of the different methods: LDA/GGA, Section 2.4; SIC-LSD, LDA+ U , LDA+DMFT Section 2.5.

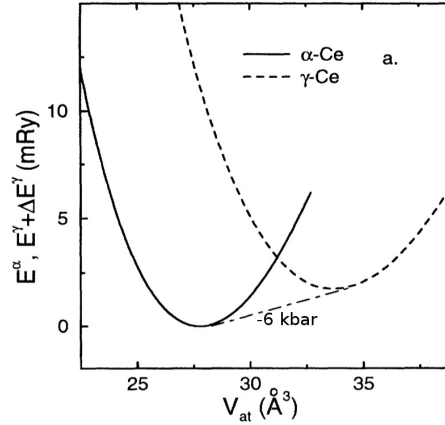


Figure 3.1: Cohesive energy versus volume curves of cerium α and γ phases according to the calculations by Johansson *et al.* [76].

employed *ab initio* methods. They assumed that the $4f$ electrons would be localized in γ -Ce, and delocalized in α -Ce [204, 207, 208, 76, 77, 78, 209, 210, 211, 212], following the Mott transition model suggested by Johansson [1]. In 1995, Johansson *et al.* [76] obtained two cohesive energy versus volume curves in GGA calculations. In one case the α -Ce $4f$ electrons were retained in the valence shell, while in the other case the γ -Ce $4f$ electrons were frozen in the core. The results by Johansson *et al.*, reported in Figure 3.1, are representative of most of the *ab initio* studies on cerium: two separated curves are obtained with different approaches.

The self-interaction corrected local spin density approximation (SIC-LSD), was applied in the same spirit. Good results for the γ phase were obtained by Szotek *et al.* [207] and Svane [208]. The downside of the approach is that SIC-LSD can only capture the *localized* phase. So the authors relied on LSD (the spin polarized variant of LDA) to describe α -Ce. Combining total energy curves from the two theories, Figure 3.2, produced a satisfactory estimation of the transition pressure with a difference between the two phases on the order of some meVs, as observed in experiment. Lüders *et al.*[209] further extended the SIC-LSD study of cerium by incorporating temperature effects through entropic contributions, and obtained a slope of the phase transition line in the P - T phase diagram in agreement with the experimental one.

LDA+ U calculations by Shick *et al.*[210] and Amadon *et al.*[211] also reproduced

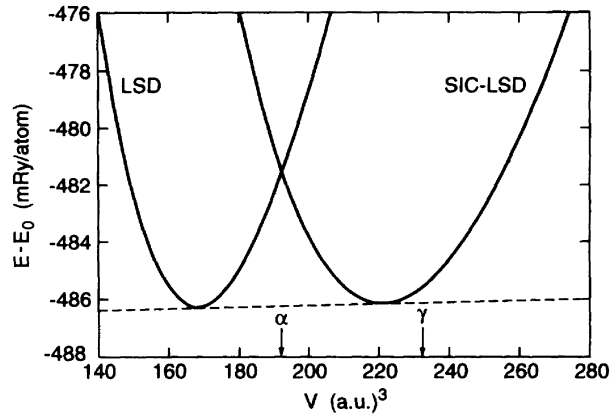


Figure 3.2: Cohesive energy versus volume curves of cerium α and γ phases according to LSD and SIC-LSD calculations. The arrows correspond to the position of the experimental volumes of the two phases. From [208].

the physical properties of the γ phase, by accounting for localization of the f electrons. They also predicted a magnetically polarized configuration of the system, in agreement with experiments, and a lattice constant close to the one of γ -Ce. Interestingly, during the search of the ground state, the authors found multiple metastable energy minima in the total energy versus volume curve. Multiple stable solutions also found in our work will be extensively discussed in the next chapters. Wang *et al.*[212] extended the previous LDA+ U studies. Following the SIC-LSD approach of Lüders *et al.*, they associated LDA and LDA+ U results to the α and γ phases, respectively, and added an estimation of the entropic contributions to reproduce the phase diagram of cerium. The outcome of their study, and the comparison with SIC-LSD results, will be discussed in Chapter 8 along with the results of this thesis.

LDA+DMFT offered a way to approach the problem from a different perspective. Also adding a *localizing* contribution for the f electrons to LDA, LDA+DMFT studies [214, 215, 213, 216, 217, 61, 218, 219] aimed to account for the description of both phases within a single level of theory. The main result of LDA+DMFT is the prediction of an increased spectral weight at the Fermi level going from the γ to the α phase. As discussed in Section 1.3.5, the photoemission spectrum of cerium shows, in the low-volume phase, a typical three-peak structure, which several authors considered as the proof for the presence of Kondo physics in the α - γ transition. SIC-LSD and LDA+ U cannot reproduce this three peak structure. LDA+DMFT

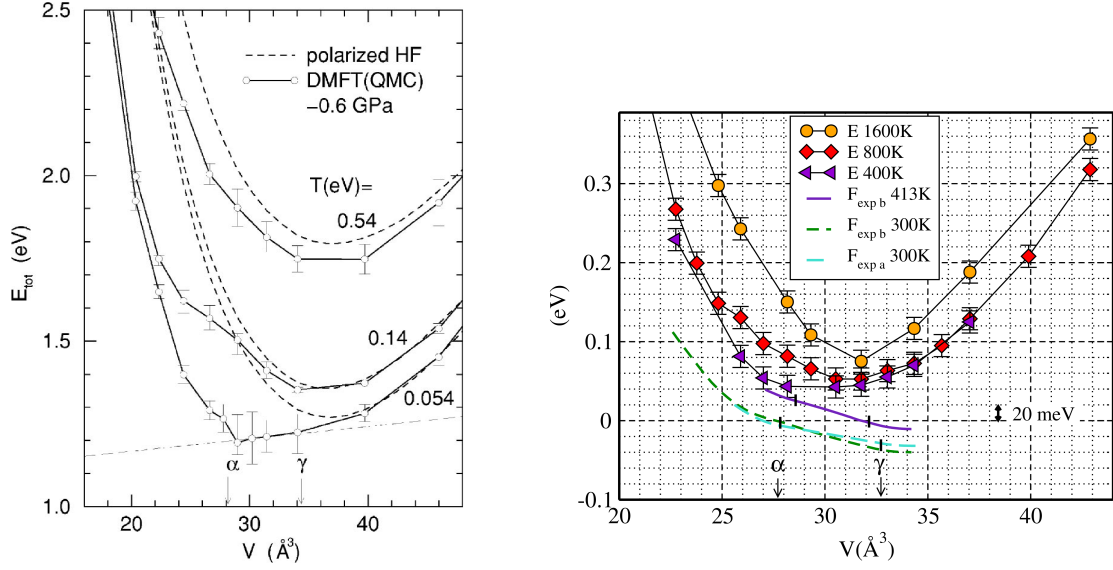


Figure 3.3: Left: total energy versus volume curve as obtained by Held *et al.* [213] in spin polarized Hartree-Fock and DMFT+LDA calculations at different temperatures ; a negative curvature appears in the LDA+DMFT curve in correspondence with the experimental α and γ volumes. Right: internal energy curve from Amadon *et al.*[61] where no negative curvature is observed at temperatures below the ones reached by Held at al. ($T = 0.054$ eV \approx 630 K); free energy curves derived from experiments are also reported in order to emphasize the role of entropy in the α - γ phase transition.

studies were able to obtain the three-peak structure in agreement with experiment, and supported, in this sense, the Kondo volume collapse mechanism. The nature of the three peaks and its link to the Kondo physics has been, however, a matter of everlasting controversy –see section 1.4.4 for a more detailed analysis of the topic.

The modern solvers that enter the DMFT scheme automatically include temperature effects (i.e. thermal broadening of the Fermi function) in the LDA+DMFT approach, and this provides direct access to the finite temperature phase diagram of the system. However, for the case of cerium, the temperatures that were usually reported were on the order of the critical temperature of the α - γ transition, or slightly lower. Low temperature calculations were hindered by computational requirements of the Quantum Monte Carlo solvers. As a consequence of this limitation, different authors reported different LDA+DMFT results. Held *et al.* [215] in 2001 reported a free energy curve with slight negative curvature. This would be a signature of the phase transition, but in 2006 Amadon *et al.* [61], with a different implementation

of the DMFT method, suggested that no negative curvature would emerge, even reaching temperatures below the ones reported in the previous study –Figure 3.3. As mentioned in Section 1.3.7 Amadon *et al.* subsequently claimed that the electronic degrees of freedom would not play a role in the phase transition.

4 *First principle* CALCULATIONS FOR CERIUM SYSTEMS

Motivated by the intriguing properties of cerium and by the apparent deficiencies of available *ab initio* approaches, one objective of this thesis was to test the performance of new *first-principle* approaches for f electron systems. The choice fell readily on hybrid functionals, which often handle localized states well, as stated in Section 2.6, despite the fact that they are not rigorously self-interaction-free. The self-interaction error has been pointed out as the main cause of the failure of DFT methods for cerium -Chapter 3. This chapter will describe how to overcome some of the computational difficulties that can be encountered in DFT and hybrid functional calculations for cerium. In the next chapters it will be shown how hybrid functionals may be able in fact to properly describe cerium systems, and to ultimately capture the physics of both the α and γ phases of cerium at zero temperature within a single approach.

4.1 COMPUTATIONAL SETTINGS

All calculations presented here were performed with the all-electron code FHI-aims (Fritz-Haber-Institut ab initio molecular simulations) [220, 221]. If not otherwise specified, the calculations were carried out with a tier 3 numeric atom-centered orbitals basis –see Appendix B.1. Relativistic effects were treated at the level of the scaled zero-order regular approximation (ZORA)¹.

¹Details about the scaled ZORA can be found in Ref. [222]. For a description of the implementation in FHI-aims and on the performance of the method refer to Ref. [220].

For periodic systems and hybrid functionals we employed tier 1 basis functions. All calculations were carried out with a $6 \times 6 \times 6$ k point sampling of the Brillouin zone, which gives energies that are converged to within 5 meV². We considered fcc crystal structures throughout and magnetic effects were taken into consideration in a ferromagnetic arrangement.

4.2 CONVERGENCE OF THE SCF CYCLE

In cerium the large number of almost degenerate low-lying states makes the ground state assignment difficult, and the convergence of the self-consistent field (SCF) cycle can be difficult to achieve. During this thesis a significant amount of time was spent on producing converged calculations. Special care was devoted to hybrid functionals. Unlike LDA and PBE, they exhibit several local minima that are difficult to converge. In the following paragraphs we will describe how to aid the convergence of the SCF cycle for f electron systems, and in the next Section we will show how to obtain multiple solutions within hybrid-functional calculations.

The difficult convergence of the SCF can be partially avoided with appropriate computational techniques. The optimal parameters involved in the calculations depend strongly on the system under study, nevertheless the following consideration may help.

- The settings for the electron density mixing algorithm have to be chosen carefully. In the FHI-aims code the default and most robust mixing scheme is the *Pulay mixer*. The two parameters that determine the behavior of the mixer are the number of past iterations that are kept in memory, and the linear factor. The product of the latter with the density change determines the new density.³ Increasing the number of past iterations over, e.g., 10 and reduce the linear factor below, e.g., 0.05 can greatly help the convergence of the SCF cycle. However, if the parameters are too large in the first case and too small in the second –this depend on the system– the number of SCF cycles increases

²We refer the reader to Appendix B.3 and B.5 for a detailed description of the convergence tests on the basis functions and the on k meshes.

³See [220] for further references and for the exact mathematical details.

dramatically.

- Especially for periodic systems, a *preconditioner* may help. The Kerker preconditioner [223, 220], which damps long range oscillations in the mixing procedure stronger than short ranged ones, is the preconditioner of choice in the FHI-aims code.
- Introducing a finite electronic temperature increases the stability in systems with a large number of available states close to the Fermi level –like metals or cerium clusters. In this thesis a Gaussian broadening scheme was applied [224]. It turned out to be crucial for the convergence of the SCF. The effect of the broadening will be more extensively discussed in the next Section.
- Hybrid-functional calculations achieve much faster convergence if they are restarted from previous PBE results. The multi-solution behavior –see Section 4.3– combined with the convergence problems is difficult to handle in practical calculations. PBE can serve as starting point for other methods.
- In extreme cases, especially if the density mixer has been set to follow a safe but slow convergence, it is useful to restart the same calculations several times from previously computed electronic structures. This helps if the system is already heading toward convergence. In this case, the history of the density mixer can be the source of problems. The restart clears all past configurations in the Pulay mixer and speeds up the convergence process.

4.2.1 Simulated annealing

In Kohn-Sham calculations with (nearly) degenerate ground states, a finite electronic temperature is usually introduced to accelerate the convergence of the electronic minimizer. In cerium however, the large number of almost degenerate states near the Fermi energy causes instabilities in the SCF cycle. Increasing the electronic temperature helps the convergence, but too high temperatures produce a too large contribution of the electronic entropy. Therefore, the recipe that was applied in this thesis was to initialize the calculations at a given bond distance with a high electronic temperature ($T \approx 1000$ K) and to subsequently reduce it. The initial broadening

of the one-electron energy levels allows the valence electrons to populate all the low lying excited electronic states. In subsequent calculations for the same bond distance, the temperature is gradually reduced until the ground-state is stabilized at $T = 0$ K. This procedure facilitates an initial sampling of all almost degenerate configurations, and a final choice of only the most stable ones. This approach is reminiscent of the *generalized simulated annealing* [225] techniques used in several fields of research, from thermodynamics [226] to genetics [227], to fitting procedures [228], to optimization of molecular geometries [229].

In this thesis we employed a Gaussian occupation function [224] of the form

$$f_l = 0.5 \left[1 - \operatorname{erf} \left(\frac{\epsilon_l - \epsilon_F}{w} \right) \right], \quad (4.1)$$

where ϵ_l are the KS eigenvalues, ϵ_F is the Fermi level, and f_l are the occupation numbers of the KS states. w is a rational number. In calculations for cerium systems, the value of w should be in the range 0.05-0.1, depending on the system. These values are still large enough to allow convergence of the SCF, and only introduce an electronic entropy on the order of 10^{-3} eV or smaller.

In Figure 4.1 the total energy of the cerium dimer is reported as a function of bond distance for different values of the broadening at the Fermi level. The calculations are done within PBE, a polarization of one, a tier 1 basis set, and default settings for the density mixer. The SCF limit was set to a maximum of 100 iterations, with convergence thresholds of 10^{-6} for the charge density change, 10^{-4} for the change of the sum of eigenvalues, and 10^{-6} for the total energy change –see [220] for more details about the convergence criteria.

The curves in panel (a) correspond to direct calculations, i.e. they are not restarted from previous results. The SCF convergence is reached for large values of w . For large distances and small broadening the total energy can be subject to serious instabilities.

Panel (b) of Figure 4.1 exemplifies the *simulated annealing* approach. All calculations for $w < 0.6$ are restarted from previous calculations. From $w = 0.6$ the value of the broadening is reduced in several steps. At each step the calculations are initialized with the electronic structure of the previous step. The outcome is a

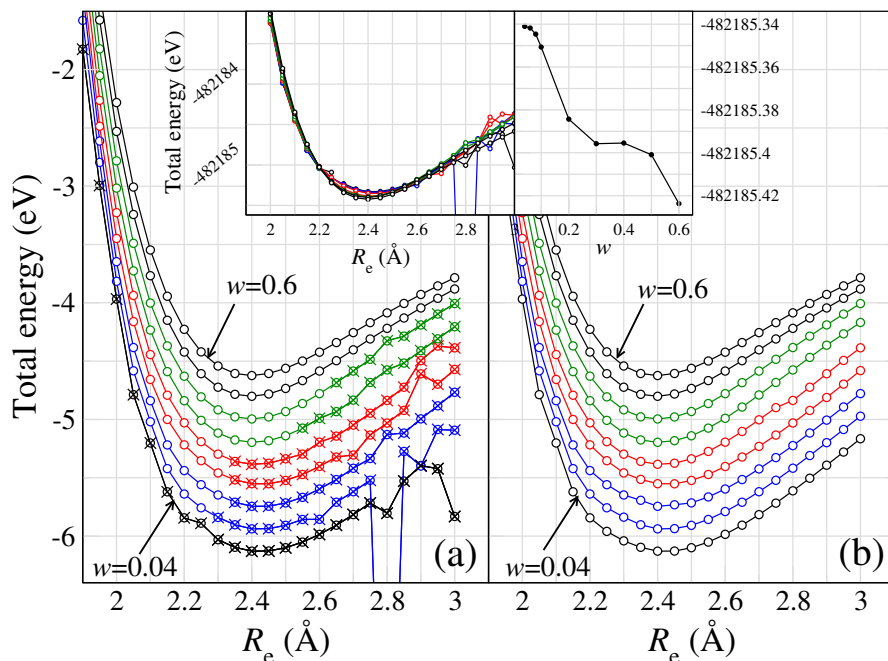


Figure 4.1: PBE total energy of the cerium dimer. Spin polarization is taken into account, restricted to one. A tier 1 basis set and default settings for the Pulay mixer are employed. Curves are shifted in energy for readability, while raw data –i.e. not shifted– are reported in the inset. Not converged calculations are marked with “x”. Panel (a): direct calculations for values of the broadening w (from top to bottom): 0.6, 0.5, 0.4, 0.3, 0.2, 0.1, 0.08, 0.06, 0.04. Panel (b): starting from $w = 0.6$ the broadening is gradually reduced, and at each step the SCF is restarted from the electronic structure of the previous result. Inset: raw total energy data for the direct calculations, and dependence of the total energy with w at 2.4 Å.

considerably improved convergence of the SCF and the curves are smooth.

4.3 MULTIPLE SOLUTIONS

More than one stable solution is found in hybrid functional PBE0 and HSE06 calculations for cerium systems. The *multi-solution* behavior is a known phenomenon when electronic configurations are close in energy [230]. This is often the case for open shell systems. Approaches that are based on the density matrix rather than the density are more susceptible to local minima in the potential-energy landscape of the electrons. If the orbital symmetry is broken the system initialization can

bias the outcome of the SCF cycle: filled orbitals are energetically favored over empty ones, they are pushed down in energy, and it is energetically beneficial for the system to keep the initial orbital occupations. This is a known issue in Hartree-Fock calculations [230], and is generally found in all approaches that create orbital anisotropy, like DFT+ U [210, 231] and SIC-LSD [209]. It was reported [232] that also hybrid functionals exhibit this behavior. We will show in the remainder of the thesis that the presence of multi-solutions in hybrid functionals turned out to be decisive for the study of the α - γ phase transition.

Some authors have employed simulated annealing techniques to locate the multiple SCF solutions in HF calculations [233, 234, 235]. Our approach of gradually reducing the electronic temperature follows the same spirit. For a given distance between the atoms, the calculations are initialized at a high temperature, and subsequently restarted at lower temperatures with the previously obtained electronic structure. At different distances the system is initialized in different configurations, that the Hartree-Fock exchange potential tends to preserve. The sampling happens therefore not on all available states, as in simulated annealing, but only on those configurations that are similar to the initial electronic structure. As a consequence, the system can fall into several different solutions when scanning a range of distances. In our calculations an additional random sampling that comes from the change of the distance between the atoms –i.e. the initialization of the electronic configuration– is introduced with respect to the simulated annealing technique. The different solutions are energetically stable, so we can restart calculations at neighbouring distances with the previously computed electronic structures and generate full curves. This combined approach provides an assessment of multiple solutions but it does not guarantee in general that the real ground state of the system is reached.

An exemplification of the procedure is presented in Figure 4.2 for the dimer. Spin polarized PBE0 calculations were performed with a tier 3 basis set, keeping ten iterations in the Pulay density mixer and performing 200 SCF cycles. The data corresponding to the highest value of the Gaussian broadening are obtained directly. All other calculations are restarted from previous results as explained in Section 4.2.1.

At small bond distances the SCF convergence is achieved for all values of w ,

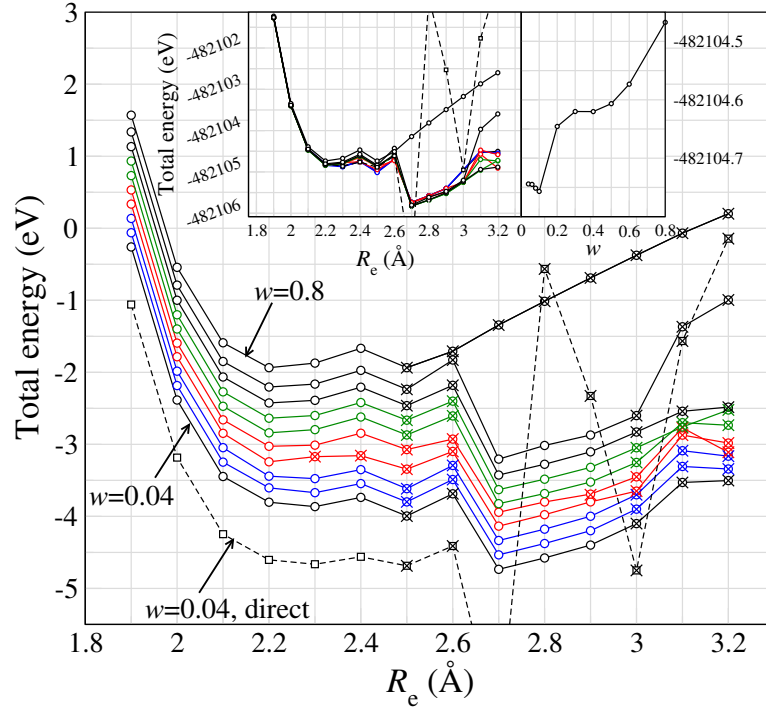


Figure 4.2: PBE0 total energy of the cerium dimer. Spin polarization is taken into account, restricted to one. A tier 3 basis set is employed and 10 iterations are kept in the Pulay mixer history. Curves are shifted in energy for readability, original data are reported in the inset. The curves correspond to values of the broadening w (from top to bottom): 0.8, 0.6, 0.5, 0.4, 0.3, 0.2, 0.1, 0.08, 0.06, 0.04. The lowest curve is generated with direct calculations with $w = 0.04$ for comparison. Inset: raw total energy data and dependence of the total energy with w at 2.2 Å.

while large distances are more problematic. Decreasing w from 0.8 helps to stabilize the calculations at 2.7, 2.8, and 2.9 Å, but no stable configuration can be reached at other bond lengths. Finally, for $w = 0.04$, two solutions emerge, corresponding to the converged points. From those data, restarting the calculations at nearest distances generates full cohesive energy curves. The full curves are displayed in Figure 5.5, Section 5.4.

The importance of the simulated annealing procedure becomes clear when looking at the lowest curve in figure 4.2. The curve corresponds to direct calculations with $w = 0.04$. Although convergence is achieved for small distances, and results coincide with the “annealed” solution, large bond lengths are extremely pathological and lead to unreliable binding energies.

5 CERIUM DIMER

In this thesis we employed LDA, PBE, and hybrid PBE0 and HSE06 functionals, and higher level EX+cRPA, rPT2 corrections for the study of cerium. We started from the dimer, and we increased the dimension of the system to larger clusters, and, at last, to cerium bulk.

In cerium, the radial distribution of the valence electrons, combined with their energetic proximity, creates an interplay between different contributions. As discussed in Section 1.2, the $4f$ states lie in the vicinity of the Fermi level but, being close to the nucleus, they shield other valence electrons from the interaction with the inner charge of the atom and at the same time they are shielded from the environment. As a result, it is not clear how much they contribute to the cohesive properties of cerium metal, and if they remain localized in an atomic-like configuration. It will be shown in the remainder of this thesis that already from the dimer it is possible to obtain meaningful results about the behavior of the f electrons in the metal.

Not many studies are available for the cerium dimer. Shen *et al.* [99] performed resonant Raman spectroscopy and reported a vibrational frequency of $\omega_e = 245.4 \pm 4.2 \text{ cm}^{-1}$. They calculated the dissociation energy with the third law method, and found $D_e = 2.57 \text{ eV}$. In 2003 Cao and Dolg [100] carried out calculations at the level of the complete active space self-consistent field (CASSCF) and multireference configuration interaction (MRCI). CASSCF/MRCI found a ground-state that corresponds to a $4f^1 4f^1 (6s\sigma_g)^2 (5d\pi_u)^4$ configuration in a possible spin singlet or spin triplet alignment, attributing therefore a core-like nature to the f states. The authors reported $R_e = 2.62 \pm 0.02 \text{ \AA}$ for the equilibrium distance, $D_e = 1.73 \pm 0.4 \text{ eV}$ for the bonding energy and $\omega_e = 201 \pm 13 \text{ cm}^{-1}$ for the vibrational frequency. Subsequently Roos *et al.* [101] used a multiconfigurational wave function approach with dynamic correlation

included using second-order perturbation theory (CASSCF/CASPT2). They found six different almost degenerate configurations with the s and d orbitals forming the bonding states $(6s\sigma_g)^2(5d\pi_u)^4$ and the f electrons being core-like or lying in possible $(4f\phi_g)^2$, $(4f\phi_g)(4f\phi_u)$, $(4f\phi_u)^2$ molecular orbitals. They found similar equilibrium distance, bonding energy and vibrational frequency for all configurations: $R_e = 2.63 - 2.66 \text{ \AA}$, $D_e = 2.61 - 2.68 \text{ eV}$, $\omega_e = 166 - 189 \text{ cm}^{-1}$. Nikolaev *et al.* [102] suggested in 2011 an analytical solution in a valence bond model with two $4f$ electrons localized at two cerium sites. The authors mainly confirmed the outcome of previous calculations, assuming a triple chemical bond of the $6s$ and $5d$ states in a $(6s\sigma_g)^2(5d\pi_u)^4$ configuration, and several almost degenerate states available to the localized f electrons.

5.1 LOCAL AND SEMI-LOCAL FUNCTIONALS: LDA AND PBE

LDA and PBE calculations with the FHI-aims code for the cerium dimer are reported in Figure 5.1. The calculations were performed with spin polarization taken into account. In both LDA and PBE the system takes a value of the spin $S=1$, as found by Roos *et al.* within high level quantum chemistry calculations. The spin is constant with respect to the change in the bond distance.

The results show a smooth behavior for the binding energy curves with respect to the distance between the two atoms. The binding energy is evaluated as $D_e = 2E_a - E_{tot}$, where E_a is the atomic reference and E_{tot} is the total energy of the dimer. The binding energy and bond distance for the LDA spin triplet configuration are $R_e = 2.35 \text{ \AA}$ and $D_e = 3.75 \text{ eV}$ respectively, while in PBE the values are $R_e = 2.40 \text{ \AA}$ and $D_e = 2.51 \text{ eV}$. The results are summarized in Table 5.1.

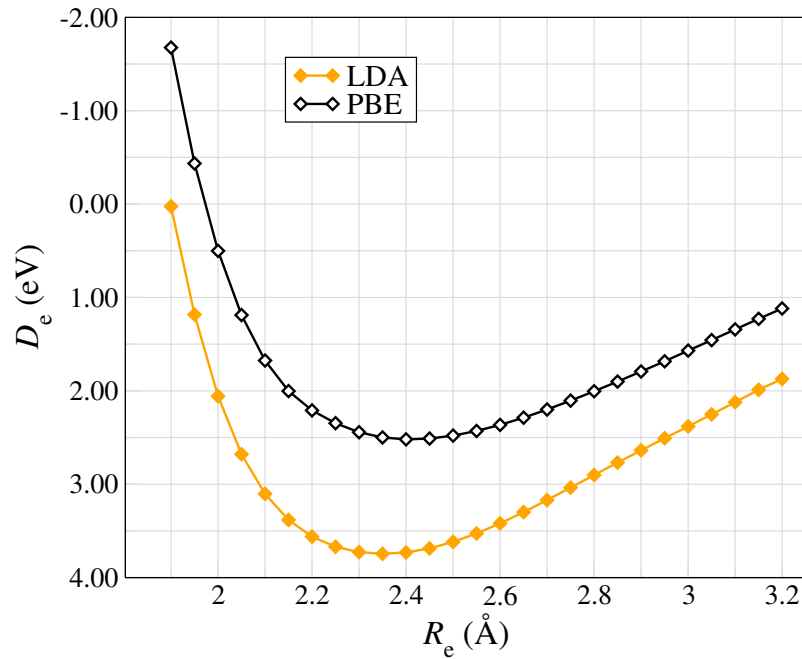


Figure 5.1: LDA and PBE results for the cerium dimer. The dimer has in both cases a spin $S=1$. The spin is constant with respect to the distance between the atoms.

Table 5.1: Equilibrium distance, bonding energy and vibrational frequency for the cerium dimer as obtained from different level of theories and experiments discussed in the main text. R_e represents the bond distance, D_e the binding energy and ω_e the vibrational frequency.

	R_e (Å)	D_e (eV)	ω_e (cm ⁻¹)
LDA (This work)	2.35	3.75	234
PBE (This work)	2.40	2.51	208
CASSCF/MRCI ^a	2.62	1.73	201
CASSCF/CASPT2 ^b	2.63/2.66	2.61/2.68	166/189
Exp. ^c	–	2.57	245.4

^aReference [100].

^bReference [101].

^cReference [99].

5.2 (EX+cRPA)@PBE

Exact-exchange plus correlation in the random-phase approximation –see Section 2.7.1– has been applied to cerium systems as a post processing correction. The EX+cRPA correction is based on the Kohn-Sham orbitals as output of PBE results, therefore all computational specification for the method that goes under the abbreviation (EX+cRPA)@PBE were unchanged with respect to PBE calculations. An additional parameter that enters the evaluation of cRPA, the number of frequency points, was involved in the accuracy of the calculations as described in Appendix B.4. For methods that involve a large number of states –i.e. empty states– expressing the basis functions in terms of atom centered orbitals leads to a large basis set superposition error (BSSE) –see Appendix B.2. Therefore, a counterpoise correction was always considered in the evaluation of the cohesive properties in (EX+cRPA)@PBE.

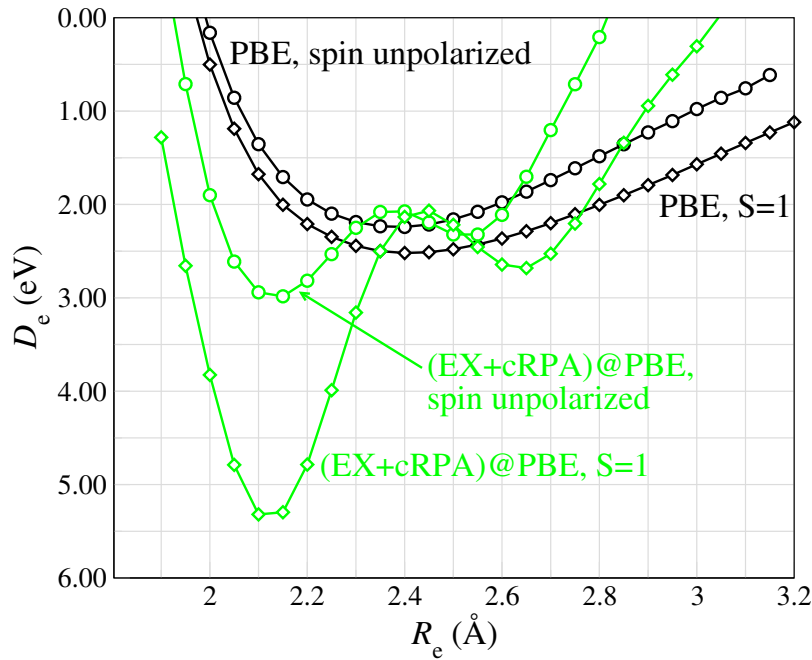


Figure 5.2: PBE (black) and (EX+cRPA)@PBE (green) calculations for the cerium dimer. Both spin unpolarized and spin S=1 configurations are reported.

In Figure 5.2 the (EX+cRPA)@PBE cohesive energy of the dimer is reported for the spin unpolarized –i.e. where the spin component is not taken into account– and spin S=1 configurations. (EX+cRPA)@PBE shows a characteristic double minimum

behavior between 2.1 and 2.7 Å. For both spin configurations, the binding energy of the minimum at small bond distance is higher than the one at large bond length—which would be closer to the experimental bond length. The vibrational frequencies of both solutions are distant from the experimental values.

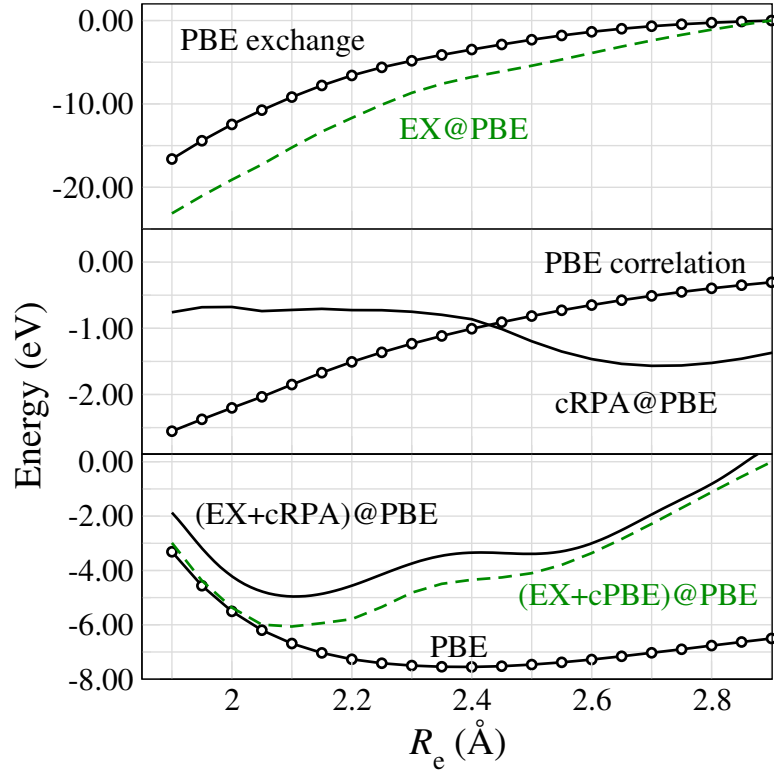


Figure 5.3: $(EX+cRPA)@PBE$ spin unpolarized calculations for the cerium dimer. All contributions are appropriately shifted in energy to facilitate a comparison.

The spin unpolarized results clarify that the appearance of the double minimum is not related to spin effects. For the dimer case, the introduction of the spin component only accentuates the distinctive features of the spin unpolarized binding curve. The double minimum can be traced back to a change in the exact-exchange contribution to $(EX+cRPA)@PBE$. The change in EX and the different contributions to the $(EX+cRPA)@PBE$ spin unpolarized results are addressed in Figure 5.3. The correlation energy varies with the distance between the atoms. It is almost constant at small distances and lowers by around 0.5 eV after 2.4 Å. The exact-exchange contribution has a bump between 2.35 and 2.6 Å, that strongly influences the $(EX+cRPA)@PBE$ energy. In fact, substituting EX for PBE exchange already

produces the double-well behavior that characterizes the (EX+cRPA)@PBE results.

The presence of the double-well in (EX+cRPA)@PBE reflects a change in the binding properties of the dimer. It signals a readjustment of the electronic states when the atoms are pulled apart. EX+cRPA is able to capture changes in the wave functions and occupations of the orbitals even if they do not manifest in the PBE cohesive energy. This means that the effects of the interplay between f and valence band electrons are already present in PBE, but they are hidden. The analysis in this Section illustrates that EX+cRPA has a non-trivial effect on the electronic structure of the dimer. This is indicative of the fact that perturbation theory is breaking down. Ideally EX+cRPA should be applied self-consistently. However, this is unfortunately not possible in FHI-aims at the moment. Since the EX contribution is at least an order of magnitude larger than cRPA, it will likely be the driving force. We will thus apply exchange self-consistently. We will show in the next Sections that hybrid functionals provide a remarkable description of the cerium dimer and larger cerium systems.

5.3 HARTREE-FOCK

Hartree-Fock calculations were performed as a first step toward hybrid functionals. The technique of gradually decreasing the electronic temperature, that resulted in smooth curves for LDA and PBE, was also applied to HF. However, the result was significantly different. As introduced in Section 4.3 and shown in Figure 5.4, gradually reducing the fractional occupation for the KS orbitals indeed favors the convergence of the SCF, but the converged results fall on *multiple solutions*.

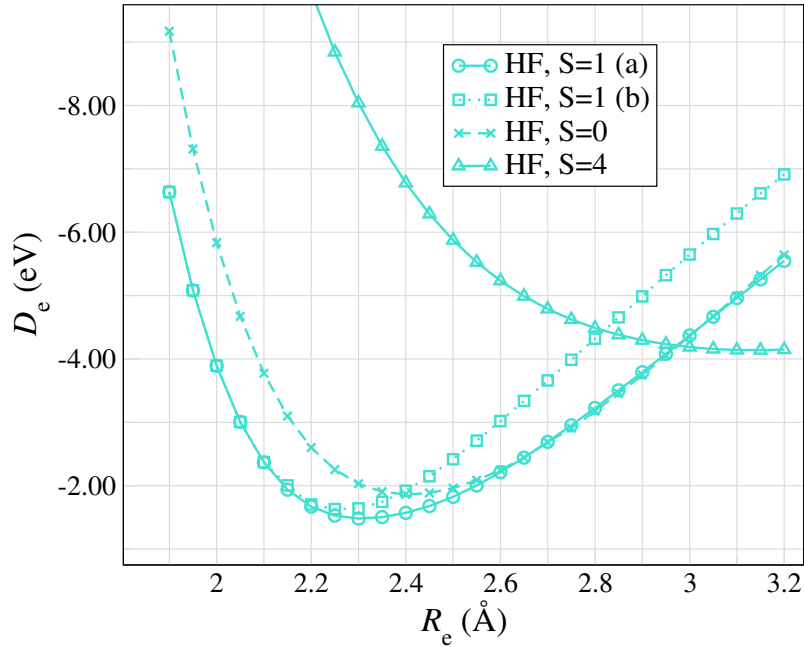


Figure 5.4: Hartree-Fock results for the cerium dimer. Different solutions are stabilized through the SCF cycle at different distances. They can correspond to equal or different spin configurations.

The different solutions correspond to different spin states and occupation of the valence orbitals. One $S=1$ solution is characterized by a $6s^15d^64f^1$ valence occupation, and the other by $6s^25d^54f^1$ valence occupation. The $S=0$ solution has $6s^25d^54f^1$ occupation and the $S=4$ curve lies in a $6s^25d^24f^4$ configuration. All solutions find that the dimer is not bound.

5.4 HYBRID FUNCTIONALS: PBE0

The presence of *multi-solutions* in hybrid functional calculations is an important outcome of our study. Also in PBE0 the cerium dimer displays the multi-solution behavior encountered in Hartree-Fock. However, the result is considerably different, as reported in Figure 5.5. In PBE0 the system relaxes into two low-lying solutions for each spin configuration and, while in HF the dimer is not bound, the dimer is actually stable. The binding energy of the lowest solution is close to the PBE one and to experiment one. Table 5.2 also compares the PBE0 results to accurate quantum chemistry methods. While PBE leads to a slightly better agreement for the binding energy, the 25% exact-exchange in PBE0 improves the bond length.

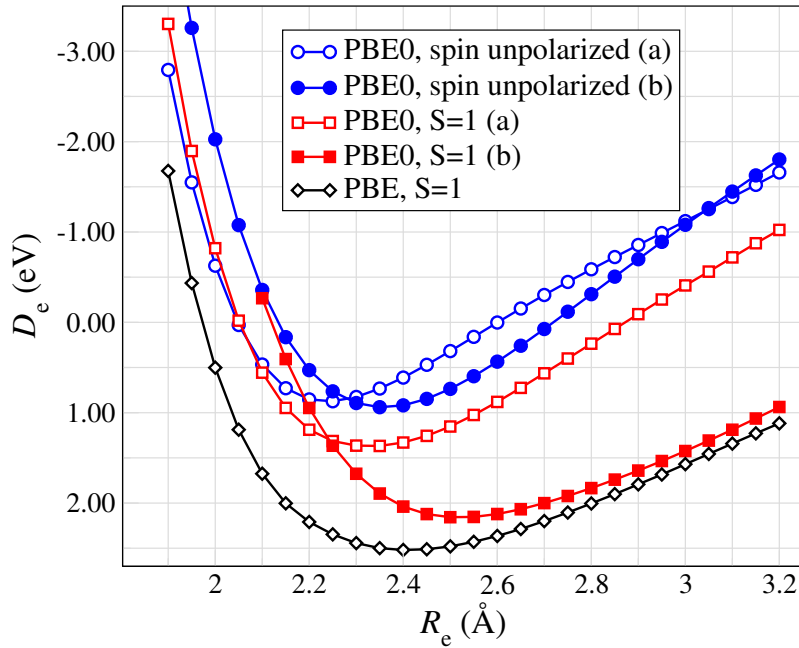


Figure 5.5: PBE0 results for the cerium dimer. Two stable solutions appear for each spin configuration.

The vibrational frequencies in Table 5.2 were obtained from a fit to the potential energy curve, without taking anharmonicity into account. The fit is done with a quadratic polynomial in a range of approximately 0.2 Å around the equilibrium distances. The contribution of anharmonicities will be investigated in future studies in the context of molecular dynamics simulations and experiment.

Table 5.2: Equilibrium distance, bonding energy and vibrational frequency for the cerium dimer as obtained from different level of theories and experiments discussed in the main text. R_e represents the bond distance, D_e the binding energy and ω_e the vibrational frequency.

	R_e (Å)	D_e (eV)	ω_e (cm ⁻¹)
PBE (This work)	2.40	2.51	208
PBE0 (b) (This work)	2.54	2.18	212
CASSCF/MRCI ^a	2.62	1.73	201
CASSCF/CASPT2 ^b	2.63/2.66	2.61/2.68	166/189
Exp. ^c	–	2.57	245.4

^aReference [100].

^bReference [101].

^cReference [99].

The fact that two solutions are present in both spin configurations implies that there is indeed a difference between their electronic structure, and the multiple solutions do not emerge from a change in the magnetic properties of the dimer. The spin unpolarized solutions (a) and (b) correspond to the occupations $6s^15d^54f^2$ and $6s^25d^44f^2$ respectively. While the S=1 PBE0 curves have both a $6s^25d^44f^2$ configuration. Spin polarization further stabilizes the energy of the spin unpolarized dimer. This will become more clear when we analyze the bulk system in Section 7.2.

The difference of the two S=1 solutions in Figure 5.5 can be understood by plotting the density of the highest occupied KS-orbitals. The left column of Figure 5.6 contains the spin up orbital densities of the (a) solution in Figure 5.5. The orbitals are listed according to their binding energy, with the highest occupied molecular orbital (HOMO) at the top. Similarly the right column corresponds to the (b) curve in Figure 5.5. For both solutions the difference between spin up and spin down states is the presence of the $4f$ orbitals. The (b) solution is in agreement with the results reported from CASSCF/MRCI and CASSCF/CASPT2 calculations: the $6s$ and $5d$ orbitals participate in the bonding and give rise to the $(6s\sigma_g)^2(5d\pi_u)^4$ configuration while the $4f$ states remain localized near the core. This is a noticeable achievement for hybrid functionals. While in quantum chemistry calculations the $4f$ electrons are manually placed in several orbital arrangements, in this thesis the arrangement is an outcome of the simulated annealing approach. The orbital arrangement of

the (a) solution is different from the (b) solution and has not previously been studied in quantum chemistry calculations. Its orbital structure corresponds to a $(6s\sigma_u)^2(5d\pi_u)^4(4f\delta_g)^1(4f\sigma_g)^1$ configuration¹. Going from (b) to (a) the $6s\sigma$ state remains the HOMO but changes its nature from bonding to antibonding. The $5d\pi$ molecular orbitals are instead unchanged. Finally one $4f\sigma_u$ molecular orbital changes its nature going from anti-bonding to bonding ($4f\delta_g$), partially compensating the loss of binding energy arising from the change in the $6s$ states.

¹The $6s\sigma$ orbital is *ungerade* because the sign of the wave function giving rise to the orbital density is not symmetric for reflection with respect to all coordinates.

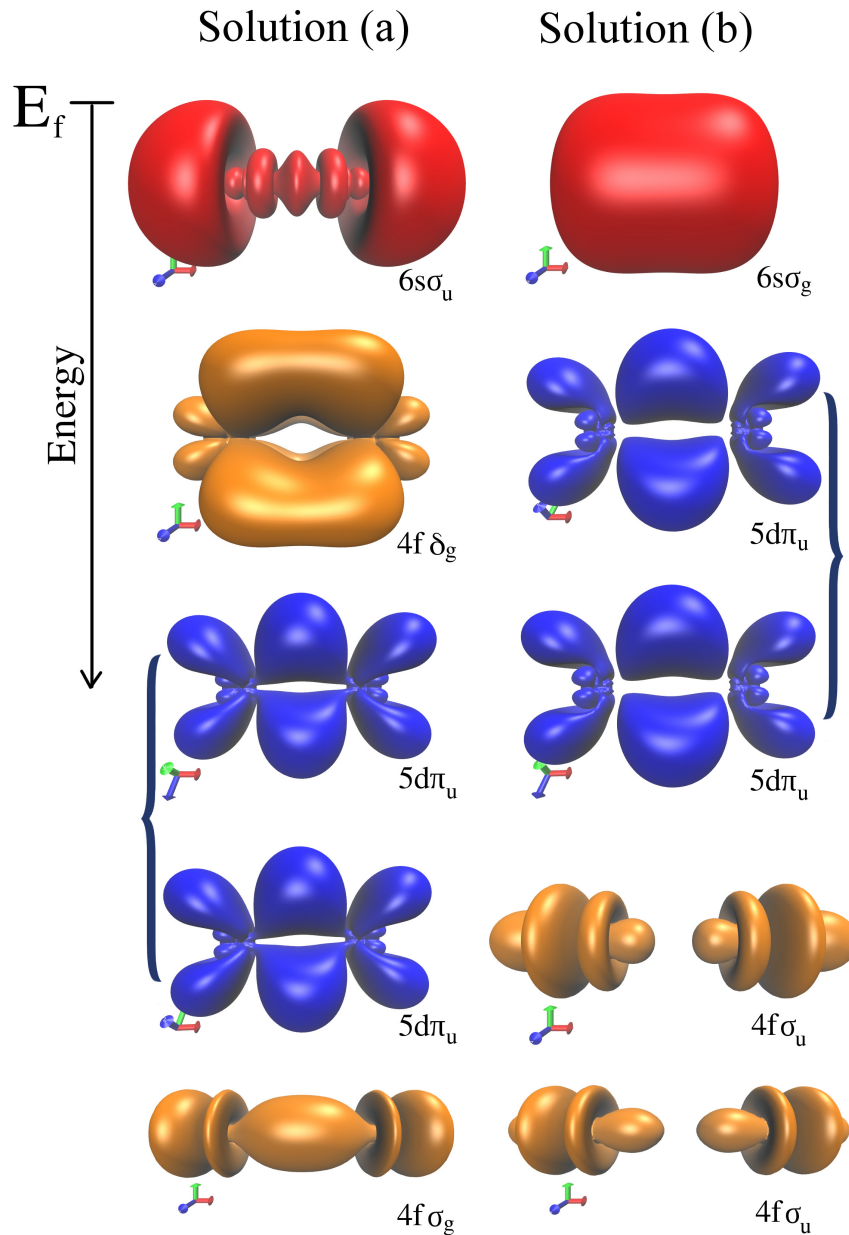


Figure 5.6: PBE0 electronic densities of the five spin up occupied orbitals closest to the Fermi level for solution (a) –left–, and solution (b) –right–, of Figure 5.5. Each orbital accommodates one electron. The energies of the orbitals for solution (a) are: $6s_u$ -2.51 eV; $4f\delta_g$ -3.14 eV; $5d\pi_u$ -3.62 eV (the two $5d\pi_u$ have the same energy); $4f\sigma_g$ -3.88 eV. The spin down valence configuration –not shown– of solution (a) is $(6s_u)^1(5d\pi_u)^2$, with energies: $6s_u$ -4.25 eV; $5d\pi_u$ -4.50 eV. The energies of the orbitals for solution (b) are: $6s_g$ -3.32 eV; $5d\pi_u$ -3.62 eV; $4f\sigma_u$ -4.19 eV; $4f\sigma_u$ -5.05 eV. The spin down valence configuration of solution (b) is $(6s_g)^1(5d\pi_u)^2$, with energies: $6s_g$ -3.35 eV; $5d\pi_u$ -3.51 eV.

gives a binding energy of 2.46 eV, and $a = 0.4$ gives a binding energy of 2.64 eV. Both energies are closer to the experimental value 2.57 eV than the PBE0 energy. However, avoiding adjustable parameters is one of the main purposes of this thesis. The mixing factor in the hybrid functionals that controls the fraction of exact exchange may be regarded as a simplified screening function, which is replaced by a physical and system-dependent screening in EX+cRPA. We decided therefore to proceed in a more rigorous way, and we applied the EX+cRPA correction to PBE0 –Section 5.6.

5.6 (EX+cRPA)@PBE0

Having seen that PBE0 qualitatively changes the electronic structure of the Ce dimer, we will now apply EX+cRPA again. In Figure 5.8 we show the PBE0 and (EX+cRPA)@PBE0 results for the cerium dimer with spin $S = 1$.

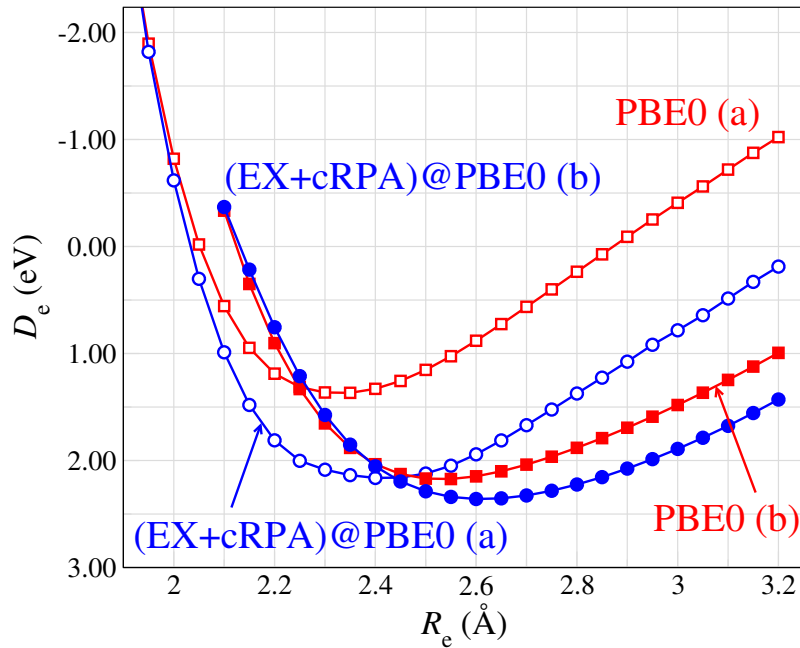


Figure 5.8: PBE0 and (EX+cRPA)@PBE0 calculations for the cerium dimer in the spin polarized configuration. Both (a) and (b) solutions have total spin $S = 1$.

The EX+cRPA correction lowers the PBE0 cohesive energy curves. As summarized in Table 5.3, solution (a) changes its binding energy from 1.40 to 2.18 eV

while solution (b) moves from 2.18 to 2.39 eV. At the same time also the bond distance is changed, by 0.09 Å for (a) and 0.07 Å for (b). This brings the equilibrium distance, bonding energy and vibrational frequency of the most stable solution into a remarkable agreement with quantum chemistry calculations. In particular the bond length is very close to the CASSCF/MRCI results of Cao and Dolg [100] and to the CASSCF/CASPT2 results by Roos *et al* [101]. The binding energy is underestimated with respect to experiment by only 0.18 eV. On the other hand, all values for the vibrational frequencies are underestimated as in previous calculations. The vibrational frequency of the (EX+cRPA)@PBE0 (b) configuration is again very close to the one reported by Roos *et al.* [101]. The similar binding energy, bond distance, and molecular orbital arrangement strengthen the accuracy of the (EX+cRPA)@PBE0 approach. And the fact that EX+cRPA does not bring significant changes to the (b) solution with respect to PBE0 is an indication that the underlying physics of the cerium dimer can already be captured by PBE0 –as also evidenced in Section 5.4.

Table 5.3: Equilibrium distance, bonding energy and vibrational frequency for the cerium dimer obtained from different levels of theory and from experiment. R_e represents the bond distance, D_e the binding energy and ω_e the vibrational frequency.

	R_e (Å)	D_e (eV)	ω_e (cm ⁻¹)
PBE0 (a) ^a	2.32	1.40	255
PBE0 (b) ^a	2.54	2.18	212
(EX+cRPA)@PBE0 (a) ^a	2.41	2.17	220
(EX+cRPA)@PBE0 (b) ^a	2.61	2.39	192
CASSCF/MRCI ^b	2.62	1.73	201
CASSCF/CASPT2 ^c	2.63/2.66	2.61/2.68	166/189
Exp. ^d	–	2.57	245.4

^aThis work.

^bReference [100].

^cReference [101].

^dReference [99].

The (EX+cRPA)@PBE0 results of Figure 5.8 are compared in Figure 5.9 to the spin unpolarized results. EX+cRPA lowers the spin unpolarized PBE0 cohesive energy by around 1 eV, and the curves are close to the (EX+cRPA)@PBE0 spin polarized cohesive energy curve of solution (a), as it was also found for PBE0.

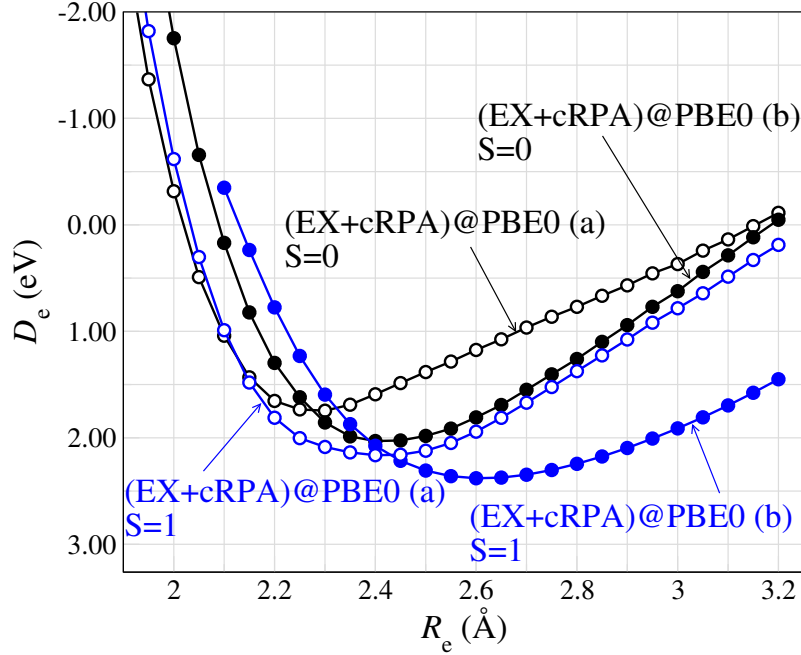


Figure 5.9: (EX+cRPA)@PBE0 calculations for the cerium dimer in the spin unpolarized (black) and polarized (blue) configuration.

Similarly to PBE0, spin polarization provides a stabilization of the dimer electronic structure for (EX+cRPA)@PBE0, giving the lowest cohesive energy –solution (b).

It has been suggested that the PBE0 α solution has delocalized f electrons with respect to the γ solution in the periodic system, with higher charge density in the interstitial region. In the same way the PBE0 (a) configuration for the dimer arrange the two f electrons in a bonding state, whereas a $4f$ antibonding orbital is formed in the (b) configuration. This signals the possibility of tracing the α - γ phase transition back to the dimer size. The (EX+cRPA)@PBE0 solutions for the dimer are very close in energy, as expected for the α and γ phases, and they are characterized by a different configuration of the f electrons, as it is believed to be for the α - γ phase transition. This provides an indication that the α - γ phase transition might be directly linked to the change in the $4f$ wave functions.

The dimer solution that is found at small bond distances actually represents a stable state, Figure 5.10, and has not been observed in any of the previous theoretical and experimental works. But the accuracy with which the most stable solution –i.e. solution (b)– has been reproduced with respect to quantum chemistry calculations

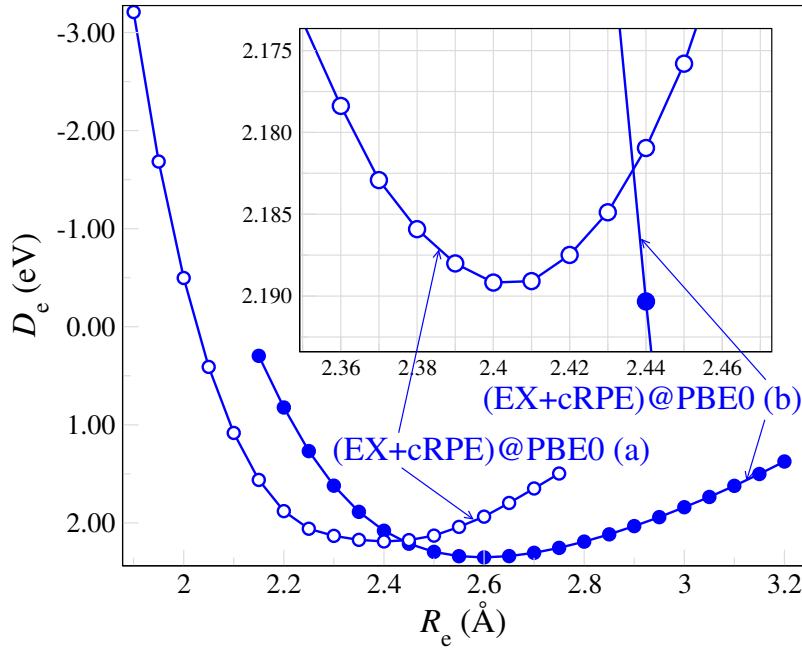


Figure 5.10: (EX+cRPA)@PBE0 data of Figure 5.8. The inset reports the range of stability of the (a) solution in a small energy scale. The cohesive energy is calculated for both (a) and (b) solutions with respect to the bond distance in steps of 0.01 Å. A stable state is confirmed for the (a) configuration.

suggests that (EX+cRPA)@PBE0 is a reliable approach. The reason why solution (a) has not been observed until present is probably related to the subspace of orbitals that is normally included in quantum chemistry calculations. The experimental confirmation of the existence of solution (a) would be a success for electronic structure methods, and, as described more extensively in the Outlook of this thesis, motivated a collaboration with the research group Prof. Wöste at the Freie Universität Berlin and the submission of a DFG joint research project on this topic.

5.7 BEYOND RPA METHODS

Before proceeding to the results for clusters, we will briefly address beyond RPA schemes. At the time of this thesis, the beyond RPA schemes second order screened exchange and single excitation corrections (SOSEX+rSE) [177] have appeared as promising beyond RPA methods². Due to the high computational requirements, the cerium dimer was the only system to which a post-processing SOSEX correction could be applied. The results are reported in Figure 5.11.

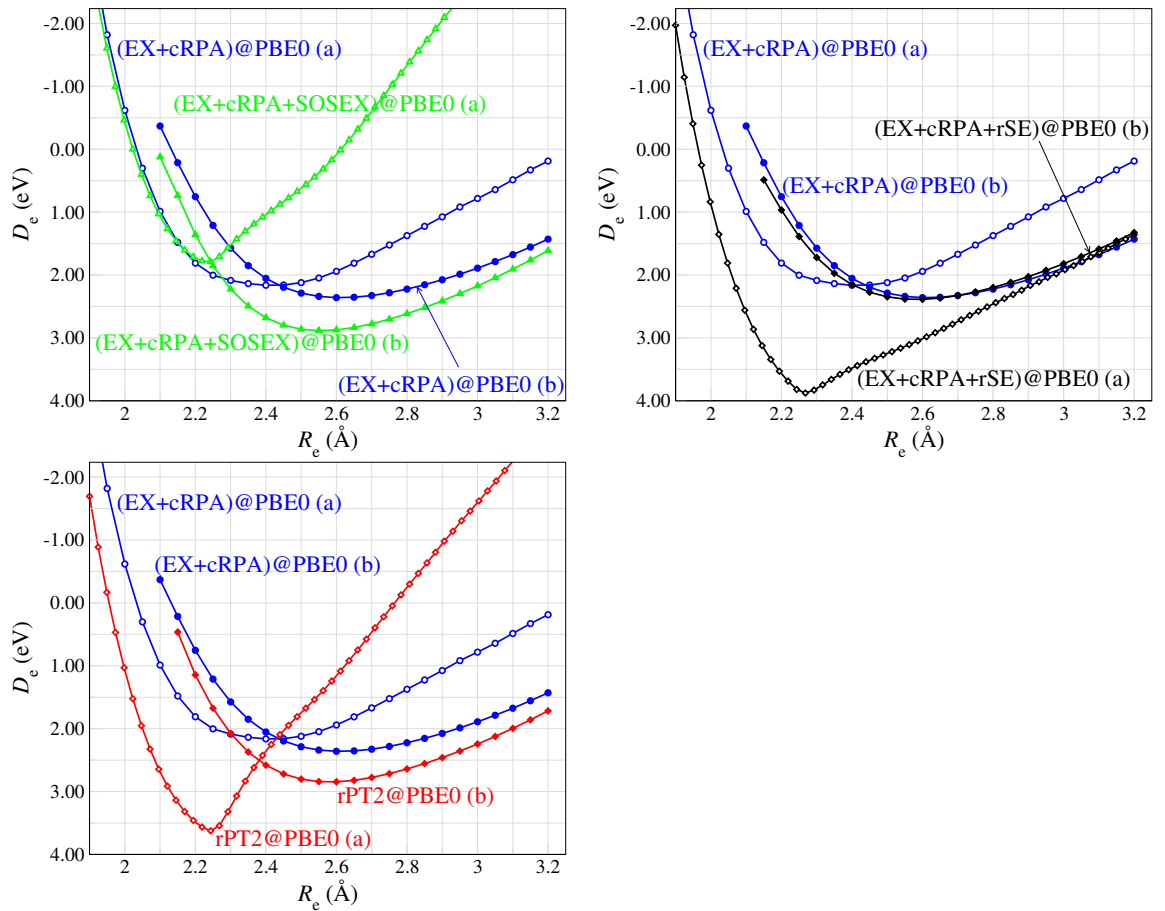


Figure 5.11: (EX+cRPA)@PBE0 cohesive energy for the (a) and (b) solutions compared to (EX+cRPA+SOSEX)@PBE0, (EX+cRPA+rSE)@PBE0 and rPT2@PBE0 results.

As for EX+cRPA, also SOSEX and rSE change the energy of the two so-

²Refer to Section 2.7.2 and 2.7.3 for a brief introduction to the beyond-RPA schemes.

lutions by a different amount. Adding only the SOSEX correction reduces the (EX+cRPA)@PBE0 cohesive energy by around 0.5 eV in solution (b) and increases the cohesive energy of solution (a) by around 0.2 eV. On the contrary, (EX+cRPA+rSE)@PBE0 stabilizes the (a) configuration by around 1.4 eV, while curve (b) is left almost unchanged. The net effect is that SOSEX causes the energy shift in solution (b) while rSE is responsible for the energy shift of solution (a). The energy contributions are summarized in Table 5.4. A noticeable feature of SOSEX+rSE is a strong stiffening of the vibrational frequency of solution (a), that is accompanied by an anomalous bump between 2.3 and 2.5 Å. This is not observed for solution (b) and could be an non-physical phenomena connected to computational issues. As mentioned above, the SOSEX+rSE correction is in active development and accurate tests, especially on metallic and f electron systems, are required in the future.

Table 5.4: Equilibrium distance, bonding energy and vibrational frequency for the cerium dimer obtained from different levels of theory and from experiment. R_e represents the bond distance, D_e the binding energy and ω_e the vibrational frequency.

	R_e (Å)	D_e (eV)	ω_e (cm ⁻¹)
PBE0 (a) ^a	2.32	1.40	255
PBE0 (b) ^a	2.54	2.18	212
(EX+cRPA)@PBE0 (a) ^a	2.41	2.17	220
(EX+cRPA)@PBE0 (b) ^a	2.61	2.39	192
(EX+cRPA+SOSEX)@PBE0 (a) ^a	2.23	1.81	598
(EX+cRPA+SOSEX)@PBE0 (b) ^a	2.58	2.88	219
(EX+cRPA+rSE)@PBE0 (a) ^a	2.26	3.88	698
(EX+cRPA+rSE)@PBE0 (b) ^a	2.6	2.40	190
rPT2@PBE0 (a) ^a	2.24	3.64	765
rPT2@PBE0 (b) ^a	2.59	2.85	198
CASSCF/MRCI ^b	2.62	1.73	201
CASSCF/CASPT2 ^c	2.63/2.66	2.61/2.68	166/189
Exp. ^d	–	2.57	245.4

^aThis work.

^bReference [100].

^cReference [101].

^dReference [99].

5.8 SUMMARY

In this chapter we have reported calculations for the cerium dimer with the LDA, PBE and PBE0 functionals, and we have added to PBE and PBE0 the EX+cRPA correction. The importance of the EX+cRPA approach is proved by the dramatic change in the (EX+cRPA)@PBE binding curve with respect to the PBE one. The (EX+cRPA)@PBE result is however not satisfactory, and suggests that exact-exchange should be included in a self-consistent way. This is done in PBE0, even if EX is included only for one fourth in the exchange part. PBE0 produces two binding curves, that correspond to different stable configurations of the dimer. The PBE0 and (EX+cRPA)@PBE0 results for the dimer are in good agreement with experiment and quantum chemistry calculations.

6 CERIUM CLUSTERS

Proceeding towards the study of cerium metal, we considered cerium clusters of increasing size with the PBE and PBE0 functionals, and EX+cRPA corrections. The clusters were cut from the face-centered cubic crystal structure, which characterizes both α and γ phases, in order to mimic the periodic environment. They were built with one atom in the center surrounded by shells of first, second and third nearest neighbors. This procedure leads to configurations of thirteen, nineteen and forty-three atom clusters as illustrated in Figure 6.1. The fcc structure and the configuration with one atom in the central position were preferred over other possible ones –for instance the one cut from the fcc structure with a first tetrahedral shell and a total of fourteen atoms– in order to recreate the bulk system environment on the central atom.

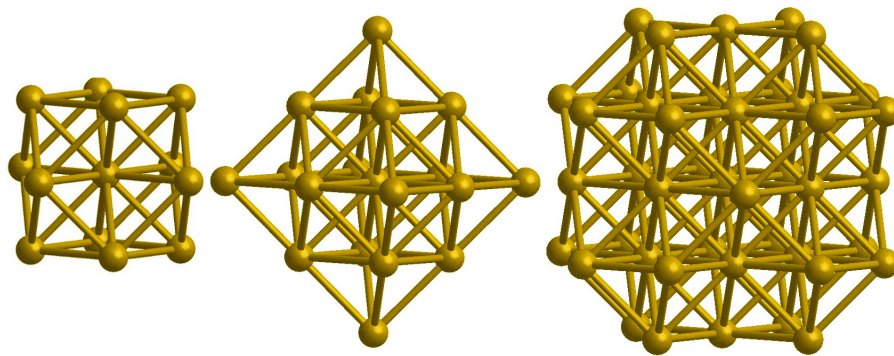


Figure 6.1: Cerium clusters cut from the fcc crystal structure with a total number of, going from left to right, 13, 19 and 43 atoms.

In order to reduce edge effects the expression for evaluating the effective cohesive energy of clusters was used [237, 238]. The formula assigns a weight –the second

term in Equation 6.1– to each atom depending on the number of nearest neighbors. Atoms that are in the inner region of the cluster are more important. The central atom for instance, for which the shell of first nearest neighbors is complete, has weight one. All other atoms have a weight smaller than one. The cohesive energy can then be expressed as¹

$$E_{\text{coh}} = - \left[E - \sum_{c=1}^{12} (N_c E_c^{\text{atom}}) \right] \left(\sum_{c=1}^{12} N_c \sqrt{\frac{c}{12}} \right)^{-1} \quad (6.1)$$

where E is the total energy, N_c the number of atoms in the cluster with c nearest neighbors, and E_c^{atom} the atomic total energy for a c -fold-coordinated atom².

6.1 PBE AND PBE0

In clusters, the assignment of a spin constraint can be difficult and sometimes misleading. Edge effects play an important role and atoms in different positions can display a completely different magnetic behavior. We decided therefore to perform unrestricted spin polarized calculations, which means that the system had no constraint on the spin value. This approach, combined with the simulated annealing technique, guarantees that the systems relaxes into one of the lowest –if not *the lowest*– states, with the corresponding optimal spin configuration. Concerning all other specifications the calculations were carried out following the procedures already used for the dimer and described in the previous section. The outcome for the cohesive energy is reported in Figure 6.2, 6.3 and 6.4. The energy is plotted with respect to the distance between the atoms that would correspond to the lattice constant (a_0) in an fcc environment.

All three clusters show similar features. The PBE functional gives a smooth curve for the cohesive energy. The magnetic moment of the central atom is zero

¹Note that the sum runs from 1 to 12, as 12 is the maximum number of nearest neighbors for an atom in the fcc environment.

²For the PBE and PBE0 functional, for which the BSSE –see Appendix B.2– can be neglected, E_c^{atom} is always the energy of the free atom. For (EX+cRPA)@PBE/PBE0 the atomic reference must be calculated explicitly at each atom position.

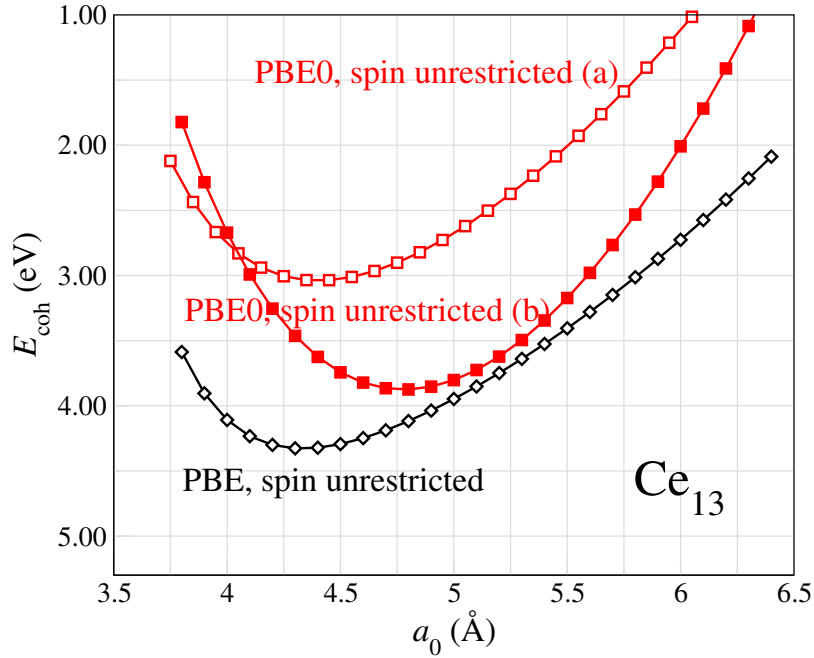


Figure 6.2: PBE and PBE0 cohesive energy for the cerium cluster of thirteen atoms.

around the equilibrium position and increases with increasing lattice constant³. Similar to the dimer, PBE0 results instead give two stable configurations. They both lie at higher energies compared to the PBE curve and they are separated by approximately 1 eV. Curve (a) is stable at a lattice constant that is close to the PBE one and has the same magnetic properties⁴. At the equilibrium position the spin value of solution (a) is almost zero. The minimum of solution (b) is found at a larger distance, and the spin of the central atom approaches one half⁵.

An analysis of the PBE and PBE0 solutions reveals that the different functionals preserve specific trademarks of the electronic structure in all clusters. In Figure 6.5 and 6.6 the density of Kohn-Sham states projected onto the central atom is plotted, for PBE and PBE0 respectively, with respect to the energy for all clusters. The density of states (DOS) for negative energies represents occupied levels, zero

³A similar change of the magnetic moment with the lattice constant is found for cerium bulk. See Figure 6.7 for the explicit volume dependence of the spin.

⁴For a summary of lattice constant, cohesive energy and magnetic moment values for the different clusters and a comparison with experiment refer to Figure 8.1 and 8.2 in Section 8.1.

⁵The spin on each atom is calculated according to the Mulliken charge partitioning scheme [239].

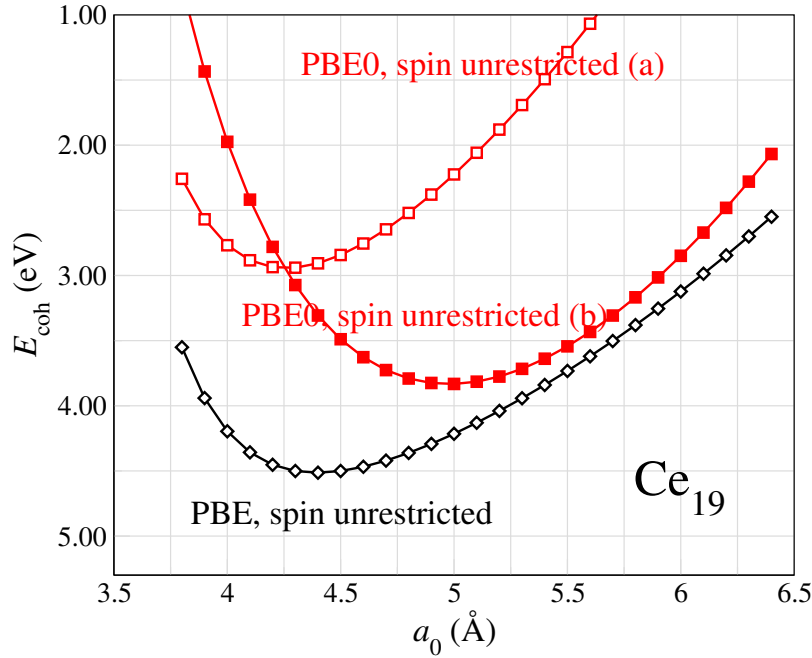


Figure 6.3: PBE and PBE0 cohesive energy for the cerium cluster of nineteen atoms.

corresponds to the Fermi energy (E_F), and the empty states are found at positive energies. The DOS in the plots is the sum of the spin up and spin down DOS. A Gaussian smearing⁶ of 0.2 is applied to the KS-DOS. For PBE0, all states below -4 eV are identical in both solutions.

A characteristic that emerges from Figure 6.5 and Figure 6.6 is the presence of a prominent peak in the unoccupied states—a comparison with photoemission experiments will follow, in the next Chapter, for bulk cerium. For all cluster sizes, the peak of PBE and the PBE0 (a) solution lies between 1 and 2 eV whereas in solution (b) it is moved to around 4 eV. In both cases it arises from a clear contribution of the 4*f* states. The number of electrons resolved for orbital components and projected on the central atom is reported for all the clusters in Table 6.1.

In both PBE and PBE0 the similarities between Ce₁₉ and Ce₄₃ are remarkable. The spectra is dominated by the *d* and *f* states. In PBE and the PBE0 (a) solution the 5*d* levels have peaks mainly around -2 and -3 eV and just above the Fermi energy. In the PBE0 (b) solution the 5*d* states, occupied and empty, are close to E_F . The

⁶See Section 4.2.1, Equation 4.1, for the definition of Gaussian smearing.

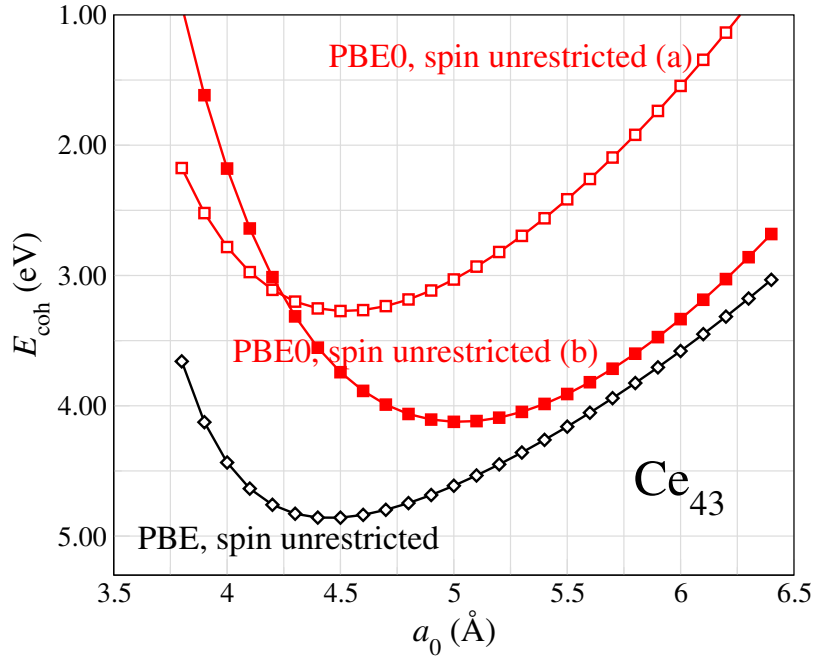


Figure 6.4: PBE and PBE0 cohesive energy for the cerium cluster of forty-three atoms.

position of the occupied and empty $4f$ states is similar between the PBE and PBE0 (a) solutions, where the empty $4f$ states are close to E_F . In PBE0 (b) instead, the empty states lie at higher energies –around 4 eV. A closer look around the Fermi energy reveals that there is a removal of f spectral weight from E_F going from PBE, PBE0 (a) to PBE0 (b). The f levels are pushed away from the Fermi level, while the occupied and empty d states come closer. The change in electronic structure arises therefore from the interplay between the $5d$ and $4f$ states.

Because of the similarity of the two solutions in the clusters –reflected in e.g. the equilibrium lattice constant, magnetic moment and density of KS-state– with the two phases of cerium –see Section 8.1–, the two hybrid functional solutions will be labeled with the letters “ α ” and “ γ ” in the remainder of this thesis to simplify the notation.

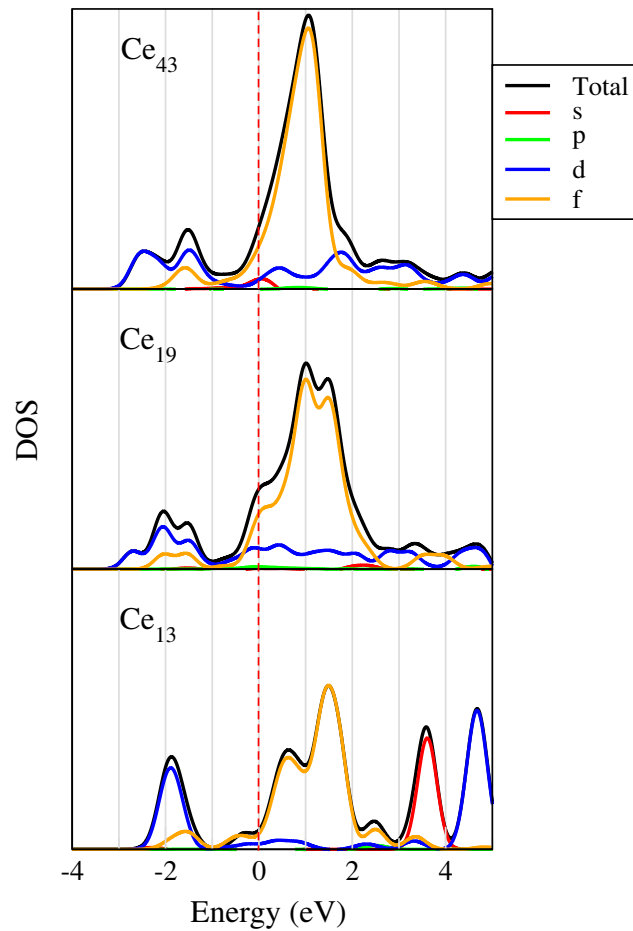


Figure 6.5: PBE density of Kohn-Sham states (sum of spin up and down DOS) of the cluster results of Figure 6.2, 6.3 and 6.4. Zero is the Fermi energy. The DOS is plotted at the equilibrium distances. The different colors label total (black), *s* (red), *p* (green), *d* (blue) and *f* (orange) DOS.

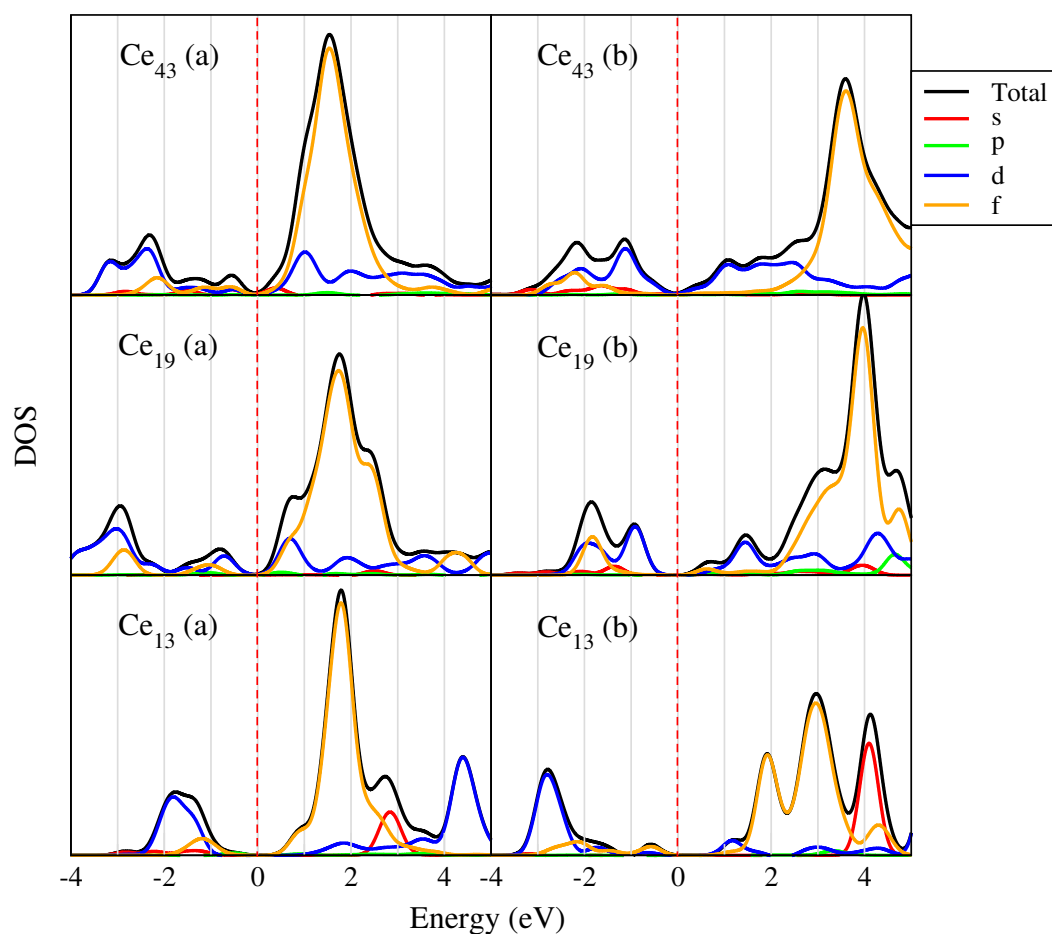


Figure 6.6: PBE0 density of Kohn-Sham states (sum of spin up and down DOS) of the (a) and (b) solution at the equilibrium distances. They correspond to the cluster results of Figure 6.2, 6.3 and 6.4. The different colors label total (black), *s* (red), *p* (green), *d* (blue) and *f* (orange) DOS.

Table 6.1: Number of electrons –orbital resolved– of the central atom of the Ce₁₃, Ce₁₉, Ce₄₃ clusters. The orbital components of the electronic density are calculated according to the Mulliken charge analysis [239].

	$a_0 = 4 \text{ \AA}$						$a_0 = 6 \text{ \AA}$					
	<i>Total</i>	<i>s</i>	<i>p</i>	<i>d</i>	<i>f</i>	<i>Total</i>	<i>s</i>	<i>p</i>	<i>d</i>	<i>f</i>		
Ce ₁₃	PBE	58.2	9.5	23.8	23.4	1.5	57.9	10.8	24.1	21.7	1.3	
	PBE0 (a)	58.4	9.5	23.8	23.7	1.3	58.0	10.9	24.2	22.0	0.9	
	PBE0 (b)	58.3	10.3	23.9	23.3	0.8	57.9	10.9	24.2	21.8	1.0	
Ce ₁₉	PBE	58.5	10.1	23.4	23.2	1.7	58.3	10.8	24.4	21.7	1.4	
	PBE0 (a)	58.7	10.1	23.4	23.7	1.5	58.0	10.8	24.5	21.6	1.1	
	PBE0 (b)	58.3	10.3	23.8	23.2	1.0	57.9	10.8	24.5	21.5	1.1	
Ce ₄₃	PBE	58.3	9.9	23.7	22.9	1.6	58.1	10.9	24.2	21.9	1.2	
	PBE0 (a)	58.5	10.0	23.7	23.3	1.4	58.1	10.7	24.1	22.4	0.9	
	PBE0 (b)	58.2	10.4	23.9	22.7	1.2	58.1	10.9	24.2	22.0	1.0	

6.2 EX+cRPA: THE α - γ PHASE TRANSITION

In this Section it will be shown that hybrid functionals combined with quantum many-body perturbation techniques are in fact a promising choice for the description of the α - γ transition. Our results not only constitute the first investigation of the phase change without adjustable parameters, but also provide insight on the nature of the phase transition.

We first discuss (EX+cRPA)@PBE results. In Figure 6.7 the (EX+cRPA)@PBE cohesive energy of Ce₁₉ is reported. The nineteen-atom cluster is the biggest one that could be study with high level quantum many body techniques. The restriction comes from the computational cost of computing RPA.

For both spin unpolarized and spin unrestricted PBE calculations the EX+cRPA correction causes a shift by around 4.5 eV to lower energies. At the same time the bulk modulus is considerably increased, as it was also observed for the vibrational frequency in the dimer. On the other hand the equilibrium lattice constants are close to the PBE values, 4.35 and 4.30 Å for the PBE and (EX+cRPA)@PBE spin unpolarized results respectively, and 4.40 and 4.26 Å for spin unrestricted results. In the same Figure the magnetic moment of spin unrestricted calculation is also plotted along with its $4f$ component. The spin component of the system is mainly dictated by the f electrons. For spin unpolarized results the EX+cRPA cohesive energy display a smooth behavior with distance. Instead, (EX+cRPA)@PBE for the spin unrestricted results display a region of negative curvature in correspondence with a change in magnetic properties.

Ce₁₉ is representative of the other clusters –see e.g. the density of KS-states in Figure 6.5. However, the PBE description of Ce₁₉ is not representative of the PBE bulk results reported in Section 7.1. This will be analyzed in Section 8.1 with a comparison of cluster and bulk properties. Although, one could associate the two minima with the α and γ phases of cerium, we will show that this is not the case. In Section 5.2 and 7.2 we show that the double minimum and the volume collapse is accompanied, but not driven, by a change in the magnetic properties. The absence of a double minimum or kink in the spin unpolarized (EX+cRPA)@PBE indicates that the wave functions do not change appreciably. In other words, there is no signature

of f -electron localization with increasing lattice constant. The structure in the spin polarized (EX+cRPA)@PBE curve therefore arises from the strange behavior of the magnetic moment in PBE and only coincidentally produces a double minimum.

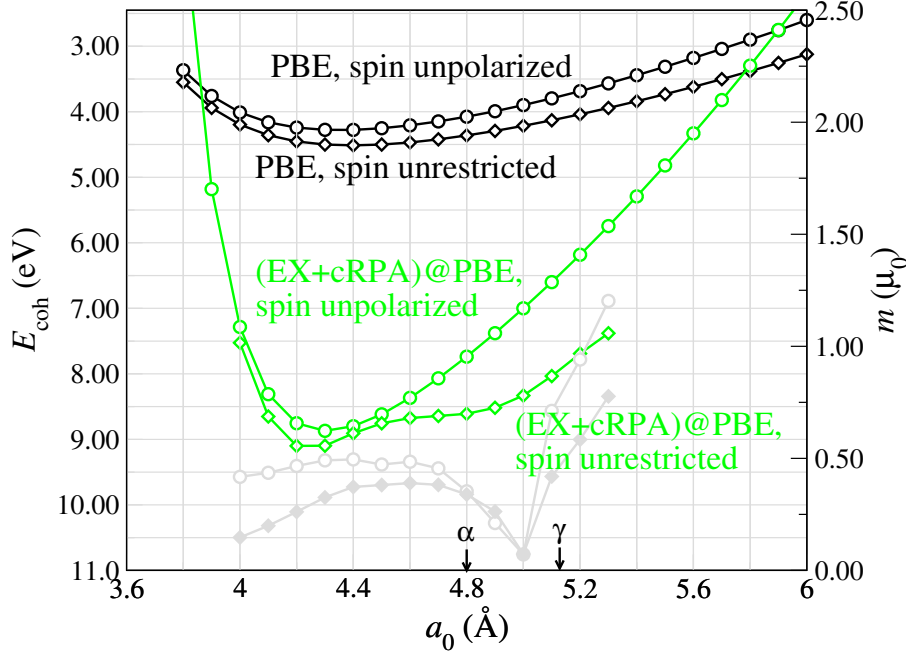


Figure 6.7: PBE (black) and (EX+cRPA)@PBE (green) cohesive energy for the 19-atom fcc-cerium cluster as a function of the lattice constant. Both the spin unrestricted and the spin unpolarized configurations are reported. The total magnetic moment (gray curve, open circles) and the $4f$ contribution to the magnetic moment (gray curve, filled diamonds) is shown for the spin unrestricted data and refers to the axes on the right.

(EX+cRPA)@PBE suggests that PBE is not a good starting point for higher level methods for cerium. This was also concluded from the cerium dimer results, and in the next paragraphs we will show that PBE0 constitutes instead a good ground to describe the α - γ phase transition.

The (EX+cRPA)@PBE0 cohesive energy for Ce_{19} is reported in Figure 6.8. It will be explained in Section 8.1 that Ce_{19} is representative of the PBE0 bulk result. It is therefore one of the main achievements of this thesis that EX+cRPA reverts the energetic ordering of the two PBE0 solutions, and brings the difference in energy between the PBE0 α and γ phases in agreement with experiment. At variance with PBE, PBE0 spin unpolarized calculations capture a change of the system properties with distance. We refer the reader to the bulk calculations of Section 7.2 for a

discussion of this result.

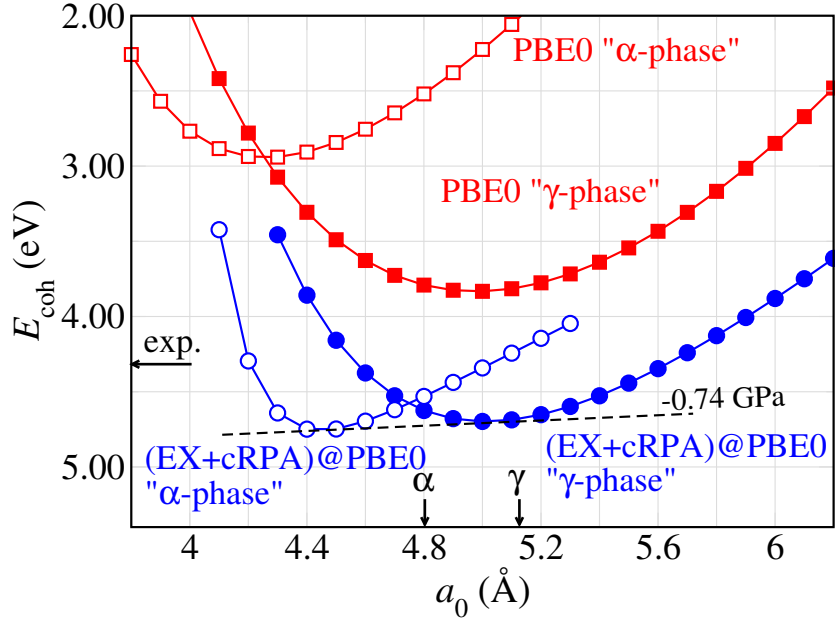


Figure 6.8: Calculated (EX+cRPA)@PBE0 cohesive energy for the 19-atom fcc-cerium cluster as a function of the lattice constant. The dashed line illustrates the Gibbs construction for the transition pressure in good agreement with the extrapolated experimental $P_t \simeq -0.8$ GPa [59]. Arrows on the energy axes: experimental cohesive energy from reference [240].

The EX+cRPA corrections to the PBE0 results are similar to those observed for the dimer, but the effect on the cohesive energy is more pronounced. The γ -like (EX+cRPA)@PBE0 solution is moved down in energy with respect to PBE0 by 0.8 eV, while the α -like solution lowers by as much as 1.8 eV. The energy shifts can be ascribed to the improved description of screening effects in the RPA correction. The α phase is more affected by the cRPA correction as the screening is higher for delocalized electrons⁷. It can also now be linked more directly to the KS density of states reported in Figure 6.6. The low-volume phase is shifted more in energy because the number of states near the Fermi level is higher in the α phase with respect to the γ phase. This cause the contribution from the polarizability –Equation

⁷Refer to Chapter 7 for a discussion of localization/delocalization in hybrid functional results for cerium. Note that the density difference plot reported in Figure 7.6 –which provides an indication of the delocalization of f electrons in the α -like phase with respect to the γ phase– displays the same characteristic when obtained from the densities of the two Ce₁₉ solutions.

2.67, Chapter 2– to grow, with a subsequent increase in the RPA energy –Equation 2.70.

According to the extrapolation of experimental data to zero temperature [61, 59], the difference in internal energy (ΔU) between the two phases should lie between 20 and 30 meV, while the (EX+cRPA)@PBE0 value for Ce₁₉ amounts to $\Delta U \simeq 45$ meV. Although the difference is larger than the experimental estimation of the maximum energy difference between the two phases, it is comparable to the experimental findings –see Figure 1.9, Chapter 1. This leaves room for the estimated entropy contribution $T\Delta S$ to play a role in the phase transition. The calculated lattice constants for the α - and γ -like phases are 4.45 and 5.03 Å, respectively. In other words the lattice constant of the α phase is underestimated (4.83 Å at 77 K), but the agreement with the experimental value for the γ phase is good (5.16 Å at room temperature). Consequently, the estimated volume collapse is $\simeq 30\%$ at zero temperature, instead of the 15% observed experimentally at ambient conditions [9]. The common tangent to the (EX+cRPA)@PBE0 cohesive energy curves leads, through the Gibbs construction, to a transition pressure of $P_t \simeq -0.74$ GPa at zero temperature. This is in good agreement with the extrapolated experimental $P_t \simeq -0.8$ GPa.

6.3 SUMMARY

Proceeding toward the study of cerium bulk, PBE, PBE0 and high level EX+cRPA calculations were performed on cerium clusters cut from the fcc crystal structure. The occurrence of two distinct solutions in PBE0, that was seen for the cerium dimer, is also confirmed for larger clusters. The two solutions preserve distinctive features –i.e. equilibrium lattice constant, magnetic moment, density of KS-states– along all the clusters, and can be associated to the α and γ phases of cerium.

Signatures of the two phases can eventually be found already in PBE. The spin unrestricted PBE cohesive energy curve for the nineteen atom cluster, for example, is smooth, but the magnetic moment changes around the experimental lattice constant of the α and γ phases. The (EX+cRPA)@PBE cohesive energy is largely affected by this change, leading to the characteristic double-well behavior sought in the *ab initio* study of the phase transition.

As for the dimer, PBE0 seems however to provide a better starting point for EX+cRPA and the two solutions are preserved also in (EX+cRPA)@PBE0 calculations. The cohesive energy of the most stable solution in, e.g., Ce₁₉ changes by 0.8 eV from PBE0 to (EX+cRPA)@PBE0 –to be compared with 4.5 eV from PBE to (EX+cRPA)@PBE–, and, most notably, the energy hierarchy is reversed: the solution compatible with the α phase is moved to lower energy and the α - γ transition pressure becomes in remarkable agreement with the extrapolated transition pressure to zero temperature.

7 CERIUM BULK

7.1 HYBRID FUNCTIONALS AND THE α AND γ PHASES

After the interesting results obtained for the clusters, the cerium atom was placed in a periodic environment¹. It is one of the main achievements of this thesis that, as reported in Figure 7.1, the presence of the two hybrid-functional solutions was confirmed in cerium bulk.

In Figure 7.1 the cohesive energy (E_{coh}) obtained from LDA, PBE, PBE0, and HSE06 are presented as a function of the lattice constant. The experimental lattice constants of the α and γ phases of cerium, at 77 and 273 K, are also reported. The LDA and PBE results are in agreement with previous calculations [76, 77, 209, 211, 212] and exhibit only one minimum. The associated volume is consistent with the α phase, although the actual value is underestimated. In contrast, in PBE0 and HSE06 two stable solutions are found. One solution has a minimum approximately coinciding with the LDA or PBE minimum, while the second reaches its equilibrium position at a much larger lattice constant, consistent with the one of the γ phase. The magnitude of the cohesive energy systematically reduces from LDA to PBE, and from PBE to PBE0. PBE0 and HSE06 results are almost identical, and will be considered as equivalent for the remainder of the Chapter and of the thesis. In Table 7.1 the values for the equilibrium lattice constant, cohesive energy, bulk modulus and magnetic moment are reported for bulk PBE and PBE0 calculations together with experimental reference values and previous calculations.

In LDA and PBE the system does not show a magnetic moment at the equi-

¹Refer to Section 4.1 for the computational details.

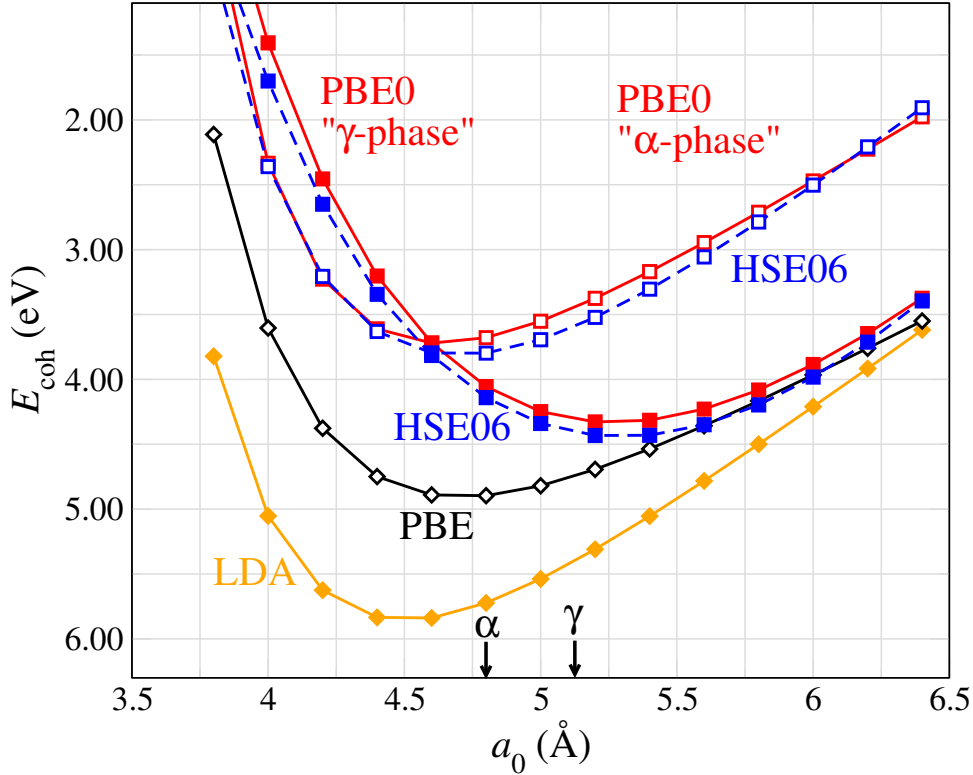


Figure 7.1: Cohesive energy [$E_{\text{coh}} = -(E - \sum E^{\text{atom}})$] of cerium for spin unrestricted calculations as a function of the lattice constant (a_0). Dashed lines show HSE06 results. The spin moment increases with volume for the LDA and PBE solutions, while in PBE0 and HSE06 it remains approximately constant at zero and one-half for the α - and γ -like solutions, respectively. Experimental lattice parameters for the two phases at finite temperature [9] are marked by black arrows.

librium lattice constant. A finite value for the spin only develops when the lattice constant is increased –Figure 7.12, 7.13. One should remember that the γ phase of cerium metal –see Section 1.3.2– displays localized magnetic moments but does not assume ferromagnetic order. In this sense the spin component present in our calculations only approximates the real behavior of the system. We believe the approximation to be reasonable, as it can be deduced from the negligible energetic difference –at the equilibrium lattice constant– between ferromagnetic and antiferromagnetic calculations, Figure 7.13.

The two PBE0 solutions differ in their electronic structure as reflected in the density of states, in Figure 7.2, and the magnetic moment (m), see Section 8.1. m of

Table 7.1: Comparison of the computed equilibrium lattice constants, bulk moduli and cohesive energies for the α and γ phases with those of other calculations and experiments. In reference [76], LDA and GGA (Becke-Perdew gradient correction) calculations for the α and γ phases were modeled by retaining the f electrons in valence shell – α phase– and inert core – γ phase–. In the SIC-LSD and LDA+ U the α phase results refer to LDA and LSD calculations.

Method	α -Ce			γ -Ce		
	a_0 (Å)	E_{coh} (eV)	B (GPa)	a_0 (Å)	E_{coh} (eV)	B (GPa)
LDA (This work)	4.50	5.84	64.1	–	–	–
PBE (This work)	4.68	4.93	36.6	–	–	–
PBE0 (This work)	4.63	3.76	50.5	5.22	4.35	28.3
LDA ^a	4.61	–	47.7	5.12	–	31.2
GGA ^b	4.80	–	39.1	5.30	–	28.8
SIC-LSD ^b	4.69	–	44.3	5.14	–	34
LDA+ U ^c	4.52	–	59	5.04	–	34
Expt. ^d	4.83	4.3	27	5.16	–	19

^aReference [76]

^bReference [77].

^cReference [211].

^dReference [10, 240, 66].

the low volume phase lies around $0.2 \mu_0$, while in the high volume phase m is close to one². Also the number of f electrons is approximately one in both phases, as suggested by positron annihilation experiments –Section 1.3.1.

The density of states is plotted in Figure 7.2 at the equilibrium distances of the two phases and it is reminiscent of the cluster DOS reported in Figure 6.6. The reported DOS is the sum of the spin up and spin down DOS. Direct and inverse photoemission data are also shown for comparison. The PBE0 γ phase displays some peaks below the Fermi energy, of which the peak around -3 eV arises mainly from an f contribution and the others accommodate d electrons. The region of the empty states is instead dominated by a major peak between 3 and 4 eV. The α -like phase is characterized by a strong peak between 1 and 2 eV. Also the PBE DOS is reported. PBE reproduces the experimental central peak. Going from PBE to the PBE0 α phase solution the spectral weight is shifted away from E_F : the occupied orbitals are

²The spin is calculated according to the Mulliken charge partitioning scheme [239].

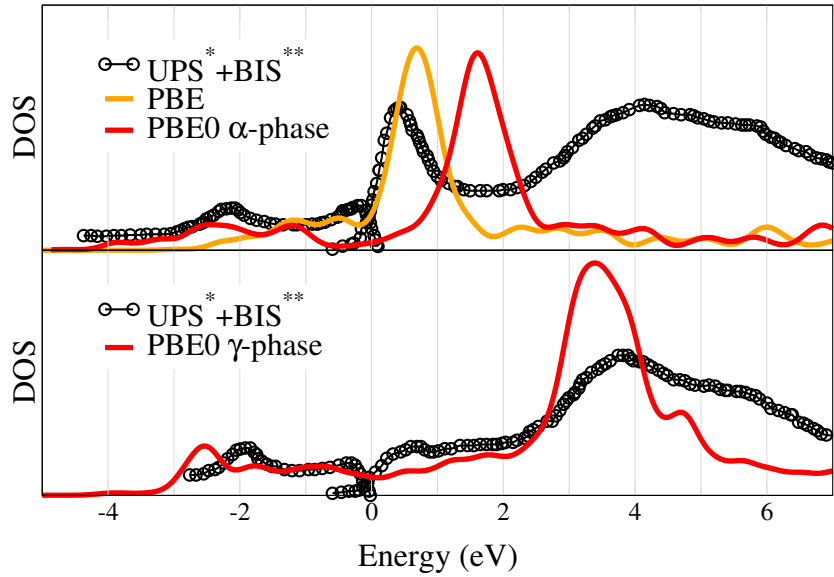


Figure 7.2: Density of Kohn-Sham states of the α - and γ -like solutions of Figure 7.1. Zero is the Fermi energy. Direct (*) and inverse (**) photoemission experiments are taken from reference [42] and [52] respectively.

moved to lower energy, the empty ones to higher energy.

As described in Section 1.3.4, for a long time the experimental spectrum of the α phase has been a matter of controversy. In particular, the characteristic three-peak structure has been observed in all measures, but the nature of the peaks –if they are of an f nature or not– remained uncertain. Moreover, in cerium the surface contributions play an important role and the surface is believed to preserve γ -like features also in the α phase. Consequently, the peak at around 4 eV could belong to the γ -like surface. From the theoretical point of view, both the Mott transition and the Kondo volume collapse models predict a three-peak structure in the intermediate temperature regime, but result in a broad central peak at the Fermi level at zero temperature –see Figure 1.10. It is therefore not certain whether the PBE and PBE0 α -like density of states are missing some features or they describe the cerium spectra as they would be if measured at 0 K without surface effects.

In this regard, one should therefore consider that the functionals that were employed in the calculations are derived from ground state theories, and that the KS eigenvalues enter the SCF cycle only as Lagrange multipliers. DFT is a ground state theory that can in principle be exact, but this does not mean that the Kohn-Sham

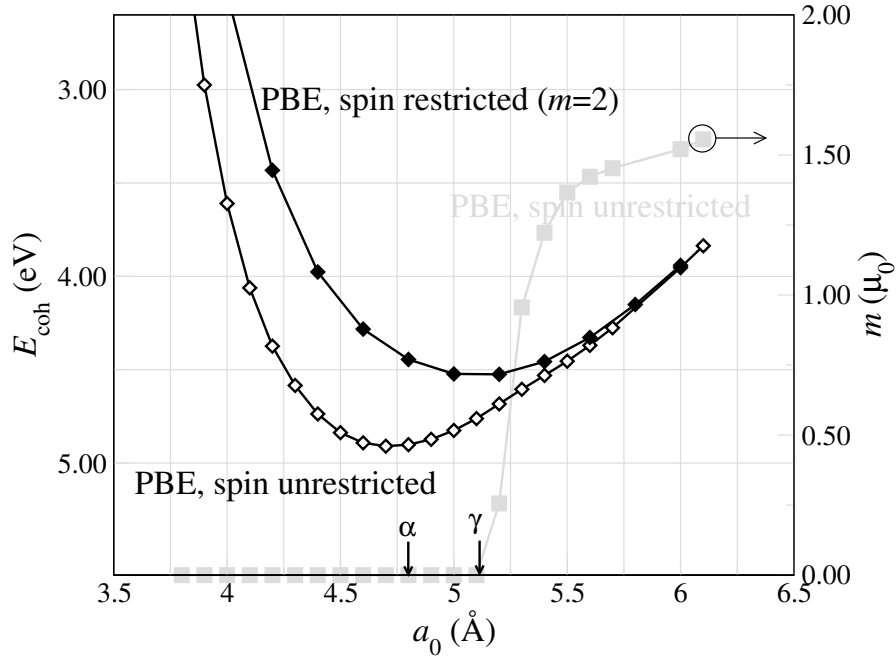


Figure 7.3: Cohesive energy of cerium bulk within PBE spin unrestricted and restricted calculations. Experimental lattice parameters for the two phases at finite temperature [9] are marked by black arrows. The gray line represents the magnetic moment of the unrestricted solution are refers to the scale on the right.

spectrum has to agree with the photoemission spectrum. As a consequence, the usual practice of comparing the KS spectra with the experimental one, even if it often proves useful, is not formally justified and the cohesive properties of a system can in principle be correctly described within KS-DFT even if the spectral function is not.

The fact that the two hybrid functional solutions display a different magnetic moment, that remains constant as the volume changes, would suggest that also the PBE functional would give rise to two distinct solutions if the s.c.f. cycle would be constrained into local minima by fixing the spin value. This is in fact the case, and the result of spin constrained PBE calculations is reported in Figure 7.3.

The spin unrestricted curve is the same as in Figure 7.1. The gray curve, on the other hand, represents the change of magnetic moment of the spin unrestricted solution with respect to the lattice constant. The abrupt emergence of a magnetic moment around the experimental lattice constant of the γ phase is representative of

the observed change in magnetic properties along the α - γ phase transition and was already observed in earlier DFT studies [203]. A different curve can be generated by constraining the spin of the system to the extreme case in which both the magnetic moments of the $4f$ and the $5d$ electrons are aligned, $m = 2 \mu_0$. The two PBE solutions now have lattice constants and magnetic properties that are compatible with the experimental values for the α and γ phases, respectively. Eriksson *et al.*, however, already pointed out that this approach to describe both phases and the phase transition within LDA/GGA fails for the energy of the system [204]. Johansson *et al.* [76] managed to produce two different solutions in LDA or GGA calculations by freezing or unfreezing the f electrons in the core. This is in practice similar to imposing a finite value of the spin to the system. However the authors had to apply an arbitrary shift to the curves in order to obtain a reasonable transition pressure. Also in the present calculations the energy of the solutions is an issue. With 0.5 eV the energy difference is more than an order of magnitude larger than what has been measured in experiment. In view of the (EX+cRPA)@PBE cluster results of Chapter 6, one can now state that PBE does not represent a good starting point for the description of the α - γ phase transition even if it is able to capture some features of the phase change, as e.g. the change in the magnetic properties.

The band energy of the PBE spin unrestricted and restricted solutions is presented in Figure 7.4 along the main directions through the Brillouin zone of the fcc structure. The bands are generated at the equilibrium lattice constants of 4.6 and 5.2 Å, respectively. Only the spin up component of the bands is reported. In PBE spin unrestricted calculations the magnetic moment at the equilibrium position is zero, so the spin up and down bands are equivalent. For spin restricted calculations the spin down bands correspond to a rigid upward shift of the spin up bands and are therefore omitted from the discussion.

The comparison between the two sets of bands evidences the similarities between the two types of calculations. In both cases the two bands below the Fermi level –of mixed d and f character– show a large dispersion, and they strongly hybridize around the X point and along the Δ and Z directions. At and above the Fermi level lie a number of dispersionless f bands. Their band width is smaller in restricted calculations, but this is also observed for unrestricted calculations by

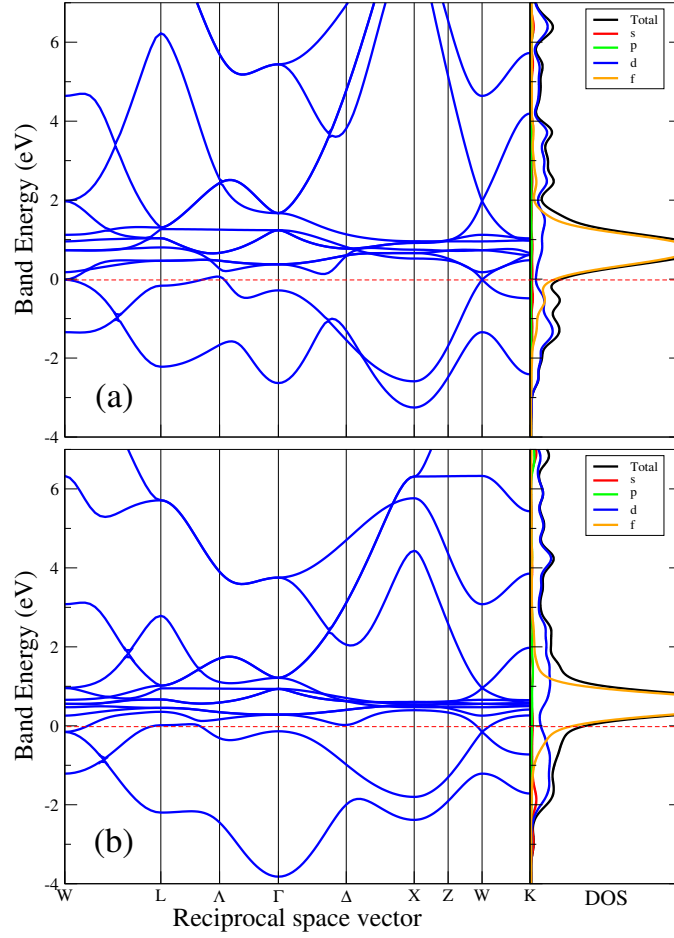


Figure 7.4: PBE band structure for spin unrestricted (a) and restricted (b) calculations. The band structure refers to the spin up component and it is taken at 4.6 in (a) and 5.2 Å in (b). Zero is the Fermi energy. The DOS is reported in the right panel.

increasing the lattice constant. The overall agreement with previously computed bands [241, 242, 209] is good.

The band structure of the PBE0 solutions is reported in Figure 7.5. Only the spin up component is shown. The spin down bands of the α phase solution are like the spin up bands, but shifted up by a small amount. In the α phase the two occupied bands hybridize strongly around the X point and along the Δ and Z directions, similarly to what was observed in PBE, while the unoccupied f bands are moved to higher energies by around 1 eV with respect to PBE. In the PBE0 γ phase the dispersionless empty bands are shifted by around 3 eV with respect to PBE.

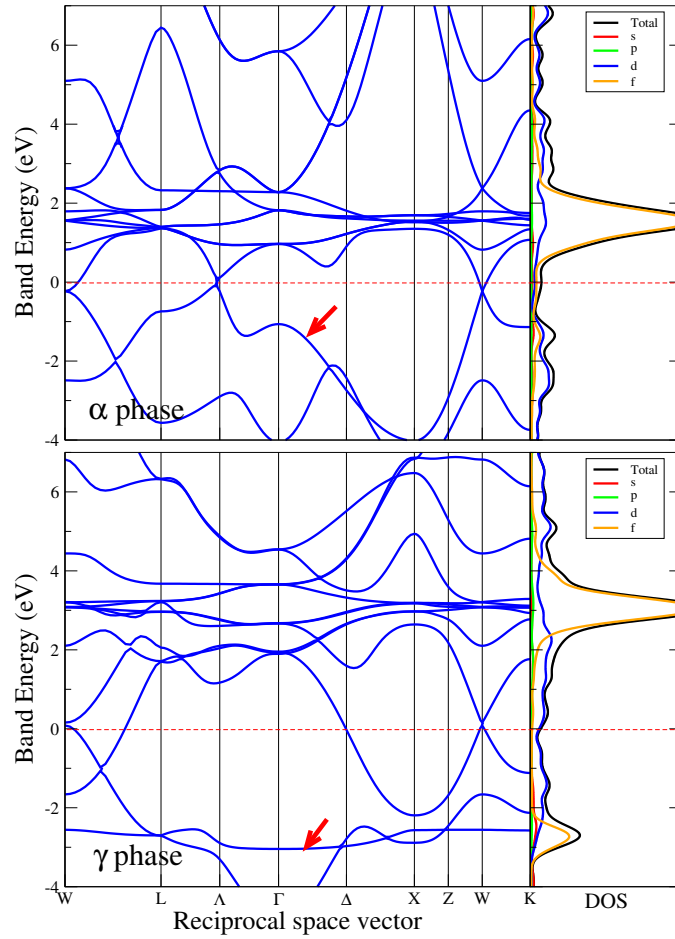


Figure 7.5: PBE0 band structure for spin unrestricted (a) and restricted (b) calculations. The band structure refers to the spin up component and it is taken at 4.6 in α and 5.3 Å in γ . Zero is the Fermi energy. Red arrows indicate the band that becomes dispersionless and occupied in γ . The DOS is also reported on the right panel.

However, major differences are observed for the occupied states. A flat band of f character is occupied at around 3 eV below E_F . The spin down bands for the γ phase are similar to the spin up ones, but the flat f band is shifted to around 4 eV above E_F . The band indicated by the red arrows in Figure 7.5 becomes dispersionless and fully populated going from the α to the γ phase. A $4f$ peak in the DOS appears for the occupied states in correspondence to the flat band. This feature is also observed in the SIC-LSD calculations of Lüders *et al.* [209]. It emerges in correspondence to the appearance of a magnetic moment close to one in the γ phase, and can be associated to the localization of one $4f$ electron when going from the α to the γ

PBE0 solution. The $4f$ peak in the occupied states is characteristic of photoemission studies –Figure 7.2– and it can not be reproduced within PBE.

The number of electrons per atom, resolved for orbital components, and the respective magnetic moments are reported in Table 7.2 for the PBE and PBE0 bulk calculations.

Table 7.2: Number of electrons –resolved for angular momentum– and magnetic moment for periodic PBE and PBE0 calculations calculated at the equilibrium lattice constants of 4.6 Å for PBE unrestricted, 5.2 Å for PBE restricted, 4.6 Å for PBE0 α phase and 5.3 Å for PBE0 γ phase. The atomic orbital components and magnetic moments of the electronic density are calculated according to the Mulliken charge analysis [239].

		Electron number					m (μ_0)				
		<i>Total</i> s	p	d	f	<i>Total</i> s	p	d	f		
PBE	unrestricted	58.0	10.2	23.9	22.7	1.2	0.0	0.0	0.0	0.0	0.0
	restricted	58.0	10.5	24.0	22.2	1.2	2.0	0.1	0.0	0.8	1.1
PBE0	α phase	58.0	10.3	23.8	23.0	0.9	0.2	0.0	0.0	0.0	0.2
	γ phase	58.0	10.6	24.1	22.3	1.0	1.1	0.0	0.0	0.1	1.0

The f electron localization process in hybrid functionals can be visualized in a more pictorial way by plotting the difference between the electron density of the PBE0 α - and the γ -like solutions, $n_\alpha(\mathbf{r}) - n_\gamma(\mathbf{r})$, shown in Figure 7.6.

The density difference is projected onto the [100] plane –but it is equivalent for the [010], [001] planes– at the lattice constant of 4.6 Å, where the two solutions have almost equal cohesive energy. The green ball marks the Ce atom in the unit cell. Blue colors indicate a surplus of electron density in the α phase and red in the γ phase. The plot shows that the interstitial region between the cerium atoms in the periodic environment is colored in blue, while the red color resides mainly on lobes around the atomic sites. This implies that the α -like phase has a higher density in the interstitial region with respect to the γ phase solution. This result provides an indication that the degree of electron localization/delocalization in the two phases is significantly different.

Furthermore, by plotting a three-dimensional isosurface with a cutoff at negative values of the density difference (i.e. where the γ -like phase has a larger number of

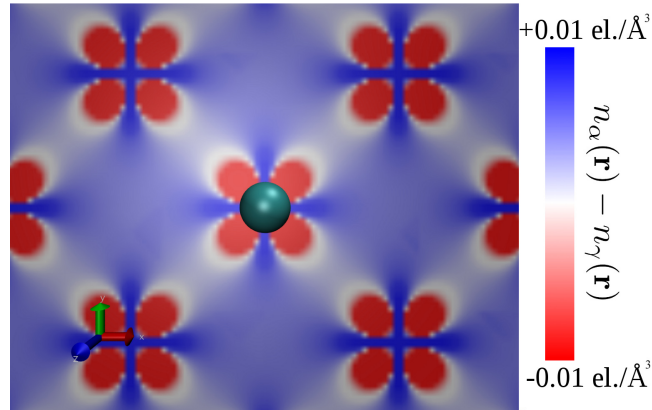


Figure 7.6: Difference between the bulk Ce electron densities of the α and γ phases at the same lattice constant of 4.6 Å, at which both phases have the same energy. The density difference is projected onto the [100] plane –the [010], [001] planes are equivalent. The α phase has a larger contribution in the interstitial region, whereas the γ phase density is more localized around the nuclei. The green ball marks the position of a Ce atom.

electrons with respect to the α -like phase) one obtains a surface with the shape of an f orbital of xyz or $z(x^2 - y^2)$ symmetry. This provides a strong indication that the delocalized electrons in the interstitial region are actually $4f$ in nature, and that it is the balance between localization and delocalization of the f electrons that plays a key role in the emergence of the double minimum in the cohesive energy curve³. This observation supports the picture that the driving mechanism of the α - γ phase transition is connected to a change in the behavior of the $4f$ electrons, that would participate in the bonding in α -Ce and would not in γ -Ce. This is also what was assumed in previous calculations on cerium by means of SIC-LSD and LDA+ U . In our study however it appears not as an *a priori* constraint of the system, but it arises naturally from calculations in which all electrons have been treated on the same quantum mechanical level.

³In section 7.2 we will show that the different magnetic properties of the two phases only stabilize an underlying difference in the electron wave function.

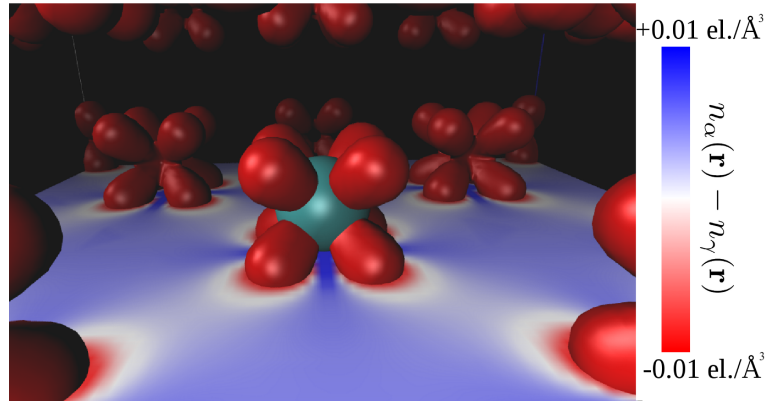


Figure 7.7: Isosurface with negative cutoff on the density difference between the α - and γ -like phases. The isosurface resembles an f orbital of $xyz, z(x^2 - y^2)$ symmetry. The projection onto the $[100]$ plane of Figure 7.6 is also reported.

7.2 SPIN UNPOLARIZED RESULTS

Regarding our results for the cohesive energy, DOS, and electron density, it seems quite plausible to associate the two PBE0 solutions to the α and γ phases of cerium. But some uncertainty remains on whether this achievement is due to an increased sophistication of the hybrid functional method with respect to local or semi-local functional or it is an artifact of the multi-solution behavior in Hartree-Fock. A main concern, for example, is that the system could be trapped in the two solutions due to the different spin values, and that the electronic structures would just correspond to a relaxation of the orbitals with respect to the different magnetic alignments. For this reason it proved useful to perform spin unpolarized calculations, and in Figure 7.8 the HSE06 results of Figure 7.1 are reported along with spin unpolarized calculations.

The spin unpolarized HSE06 direct calculations display a discontinuity between 5.3 and 5.5 Å in the cohesive energy curve. However, the two branches of the curve are not as stable as the spin polarized solutions. Restarting the calculations from large to small lattice constants with the previously calculated electronic structure produces a continuous curve, that overlaps with the original one around the equilibrium position. Nevertheless, the net result is that the cohesive energy of the spin unpolarized hybrid functional, even if it does not show a double minimum, exhibit a region of negative

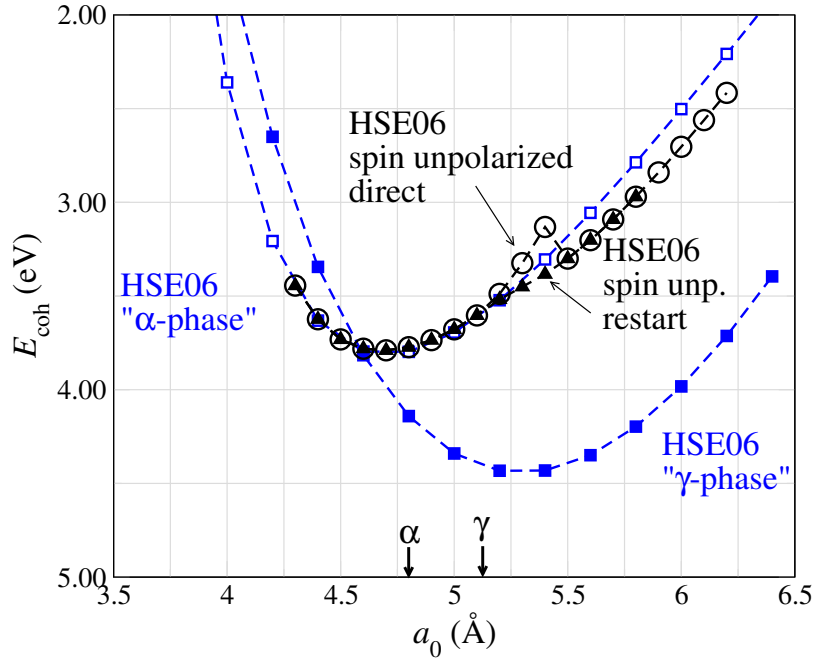


Figure 7.8: HSE06 cohesive energy curves for the spin polarized (blue) and unpolarized (black) solutions.

curvature⁴.

More insight is gained by plotting the density of KS states for the direct and restarted calculations at different values of the lattice constant, see Figure 7.9. For lattice constants of up to 5.1 Å the DOS of the two curves overlaps, which means that the restarted solution really falls onto the original one when decreasing the volume of the fcc unit cell. At 5.2 Å the system's total and orbital resolved density of states are slightly different in the two cases, but in both situations a small peak of mixed f and d contribution crosses the Fermi level and the main f peak lies just 1 eV above E_F . By further increasing the lattice constant, however, the f contribution differs in the two situations: direct calculations display a main peak that moves toward the Fermi energy and incorporates the small peak at E_F , while the restarted solution leaves the mixed f/d state unchanged at E_F , and shifts the large f spectral weight towards 2 eV. At 5.5 Å the direct calculations experience the discontinuity.

⁴Here HSE06 results are reported, but a similar picture can be eventually reproduced in the PBE0 framework, see Section 7.3. In addition, it was found that also spin unpolarized PBE0 calculations for cerium clusters display a region of negative curvature in the cohesive energy curve.

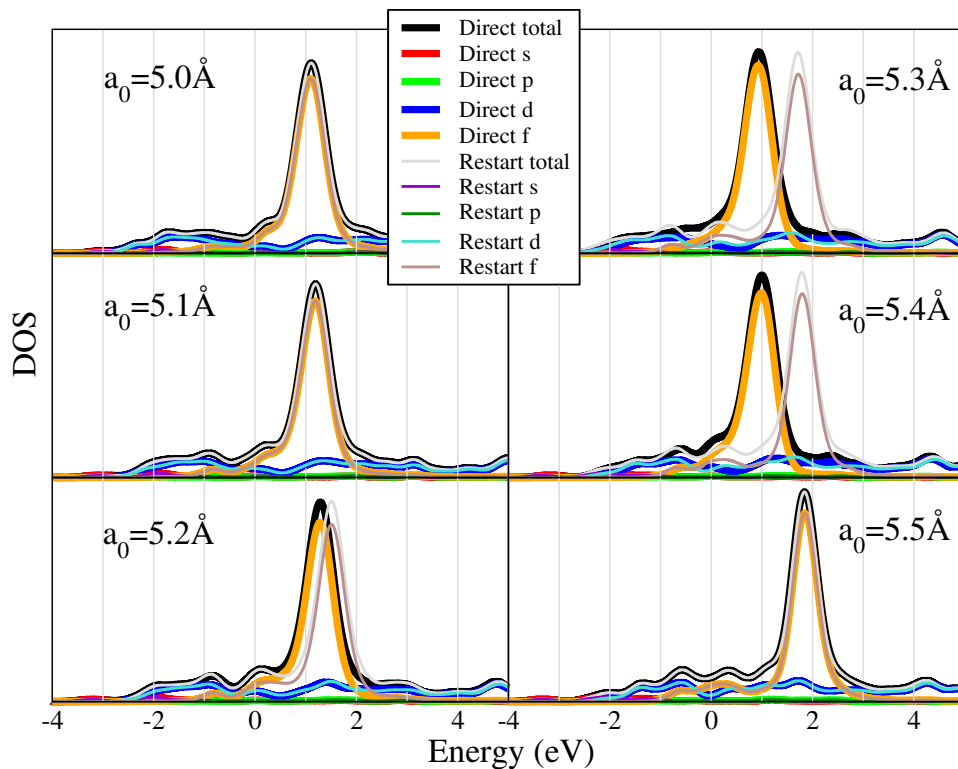


Figure 7.9: Density of KS states of the direct and restarted spin unpolarized calculations of Figure 7.8. The plots report the total and the orbital resolved DOS at different values of the lattice constant.

This is the point at which the other solution is then restarted. The two DOS are therefore identical by construction.

Figure 7.9 shows that from one original electronic configuration a different behavior of the system can be derived by smoothly varying the arrangement of the f states. The underlying s , p and d structure is very similar in both situations, but the f states can be accommodated in different ways. This is further seen in the band structure of the two HSE06 solutions, see Figure 7.10. The two sets of bands are similar, but some differences are present in the f bands above the Fermi energy. The empty f states are shifted to higher energy by around 1 eV in the restarted solution. The band that is flat and fully occupied in the PBE0 γ phase does not show the same properties for unpolarized calculations. However, we will show in the next paragraphs that trademarks of the γ phase are present in the restarted calculations.

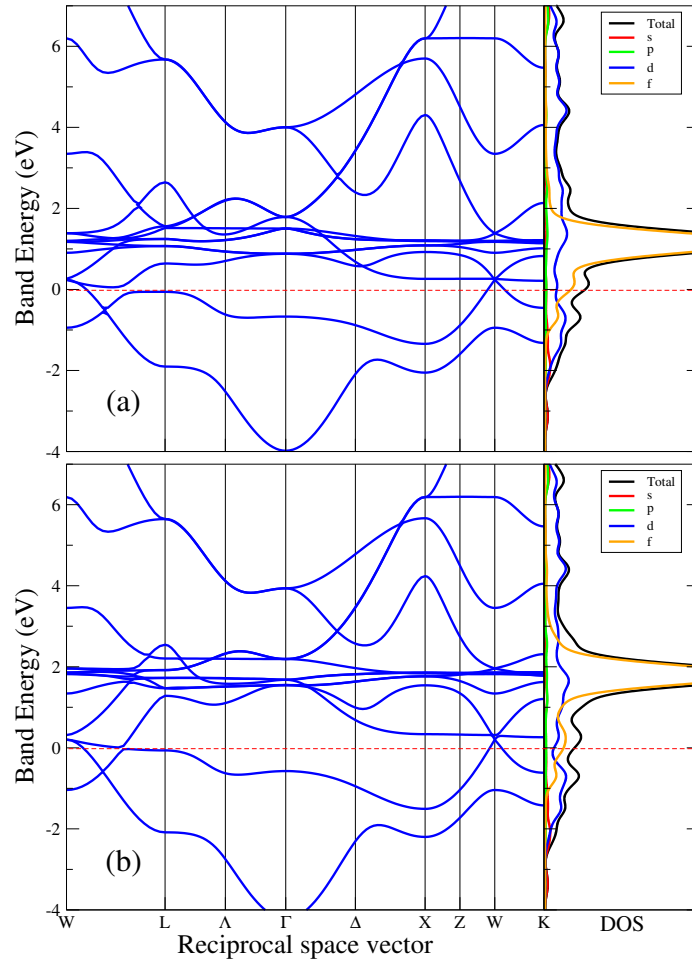


Figure 7.10: HSE06 band structure for spin unpolarized (a) and spin unpolarized restart (b) calculations. The band structure is taken at 5.4 \AA . Zero is the Fermi energy. The DOS is also reported in the right panel.

Figure 7.11 exemplifies the differences between the two HSE06 spin unpolarized solutions. In the first row of Figure 7.11 the density difference between the HSE06 direct and restarted calculations in the spin unpolarized configuration is projected onto a volume slice –parallel to the $[100]$ plane– that is approaching the cerium atom –green ball– from behind. The volume slice is moved, going from left to right, from the center of the f -shaped lobes to a position closer to the atom. Similarly, in the second row the difference is taken, at the same lattice constant and steps for the volume slice, between the HSE06 direct spin unpolarized solution and the ferromagnetic γ -like HSE06 solution of Figure 7.8.

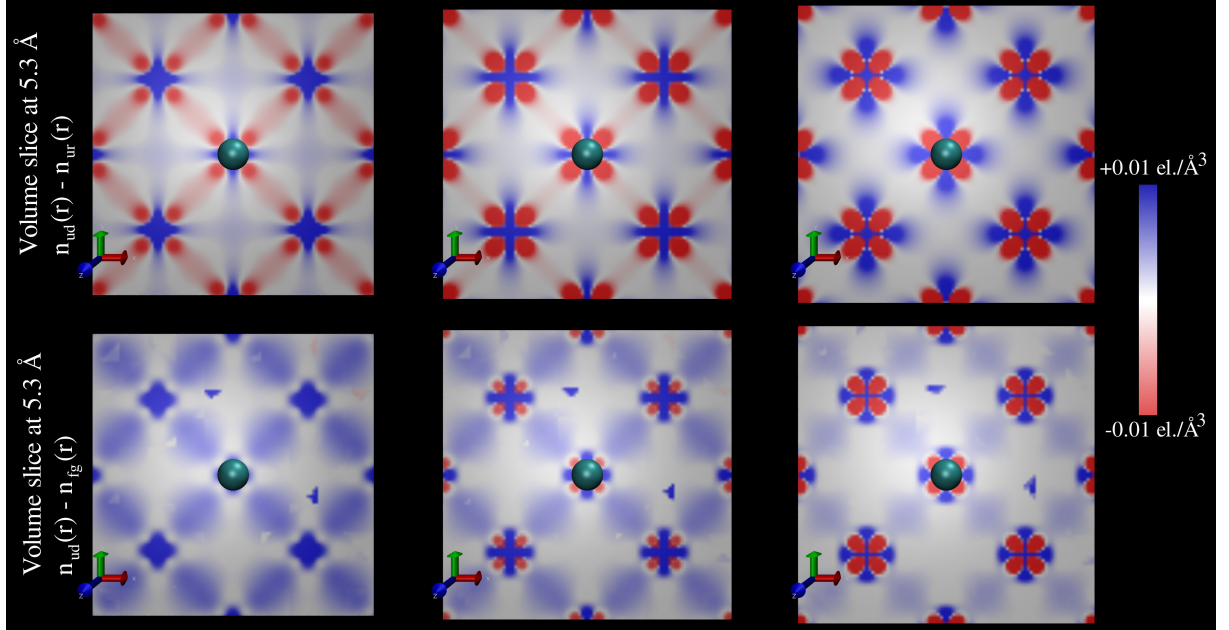


Figure 7.11: Volume slices –parallel to the $[100]$ plane– at a lattice constant of 5.3 \AA of the density difference between: direct (ud) and restarted (ur) spin unpolarized solutions (upper panels), direct spin unpolarized (ud) and γ -like spin polarized (fg) solutions (lower panels). Going from left to right the volume slice is approaching the cerium atom from behind: in the first column the slice is placed at 0.6 \AA behind the atom position, in the second column 0.5 \AA and in the third column 0.4 \AA .

In the top-right figure the density difference between the two unpolarized solutions displays similar features to the bottom right figure and to the spin polarized density difference of Figure 7.6. It also shares with the spin polarized PBE0 results the same three-dimensional f -shaped isosurface for negative values of the cutoff (not shown here). This confirms that a wave function change must happen when going from one spin unpolarized solution to the other. We can then conclude that exact-exchange provides wave functions that are suitable for the description of the α and γ phases, and that the spin polarization only stabilizes the solutions energetically.

Another element that provides insights to the results arises from the top-left panel, from which it becomes more clear that, in the two HSE06 spin unpolarized configurations, the spatial arrangement of the electrons – f electrons according to the isosurface plots– follows a different symmetry. In that figure a discrimination between localization and delocalization becomes more difficult and it is instead more

interesting to focus on the change in the preferred directions along which the f electrons are arranged. This change could be linked to the symmetry lowering, going from the γ to the α phase, suggested by Nikolaev and Michel –see Section 1.4.5– as a mechanism for the phase transition. As discussed in the Outlook of this thesis, a study of such a symmetry change will be the subject of future work.

By comparing the two rows in Figure 7.11 one can finally conclude that the magnetic degrees of freedom help stabilizing the solutions that are already inherent in spin unpolarized calculations. Going from left to right the volume slice approaches the atomic centers from behind. This evidences that the red lobes have reduced spatial extension in the second row, even if they share the same characteristics in both sets of plots. When a finite value of the magnetic moment is allowed, the electronic configuration of the α and γ phases relaxes: the α solution is stable with respect to the introduction of the spin component, but the magnetic moment greatly favors localization of the f states in the γ phase, and the red regions collapse towards the atomic centers.

7.3 MAGNETIC PROPERTIES

During this thesis the fcc crystal structure of cerium was studied in different magnetic configurations. The motivation was to address the change in the magnetic ordering –see Section 1.3.2– that the system undergoes across the α - γ phase transition.

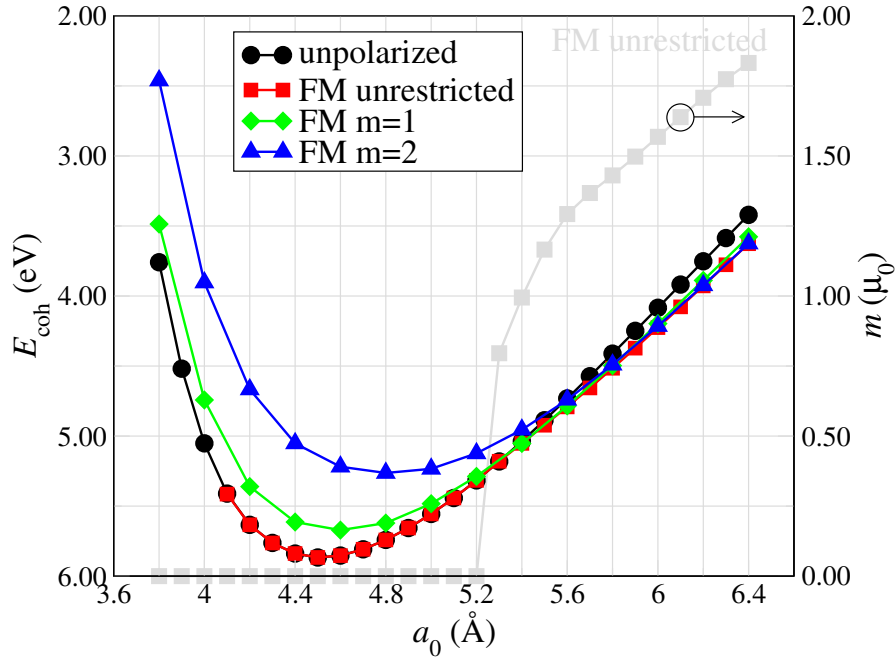


Figure 7.12: LDA cohesive energy of cerium bulk. The different curves correspond to the different spin alignments: *unpolarized*, calculations performed ignoring the spin component; *FM unrestricted*, the spin component is taken into account in a ferromagnetic alignment but the system is free to relax to the most stable spin value; *FM $m = 1$* , ferromagnetic alignment and total magnetic moment constrained to one; *FM $m = 2$* , ferromagnetic alignment and total magnetic moment constrained to two. The gray curve refers to the axis on the right and represents the magnetic moment of the *FM unrestricted* calculations.

In LDA and PBE spin unrestricted calculations the cohesive energy does not show the double-well behavior characteristic of an isostructural volume collapse, Figure 7.12-7.13, and the curves are smooth. Nevertheless a finite value for the magnetic moment m appears for large lattice constants. In particular, around the experimental equilibrium volume of the γ phase, LDA and PBE display a magnetic moment in agreement with the observed experimental spin configuration. The spin unrestricted calculations for the local and semi-local functionals always result in

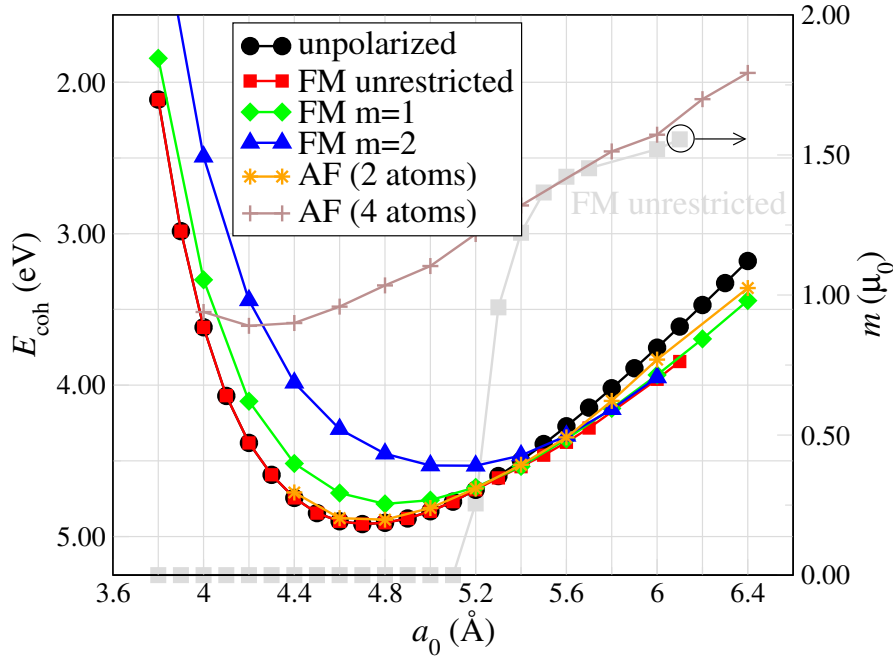


Figure 7.13: PBE cohesive energy of cerium bulk. For an explanation of the magnetic configurations see caption of Figure 7.12. *AF* stands for anti-ferromagnetic alignment. As for the fcc crystal structure antiferromagnetism can be implemented in two configurations, the curves for the two and four atoms arrangements are reported. The gray curve refers to the axis on the right and represents the magnetic moment of the *FM unrestricted* calculations.

a magnetic configuration that is the most stable one at a given lattice constant. Nevertheless different curves can be obtained imposing spin constraints, as discussed in Section 7.1.

In all calculations that develop a magnetic moment, the magnetic alignment was considered as ferromagnetic (FM). This was dictated by computational constraints and seemed to be a reasonable approximation, even if not correctly simulating the observed disordered local moments in γ -Ce. As another possibility also anti-ferromagnetic (AF) configurations were tested within PBE and HSE06. The outcome, in Figure 7.13 and 7.15, suggested no significant differences between the FM and the stable AF configuration. The AF constraint is also a test for the structural properties of the β -phase within PBE and HSE06. In view of the vicinity between the γ and β phases in the cerium phase diagram and the similarities between the two closed packed structures double-hcp (β -Ce) and fcc (γ -Ce), AF calculations

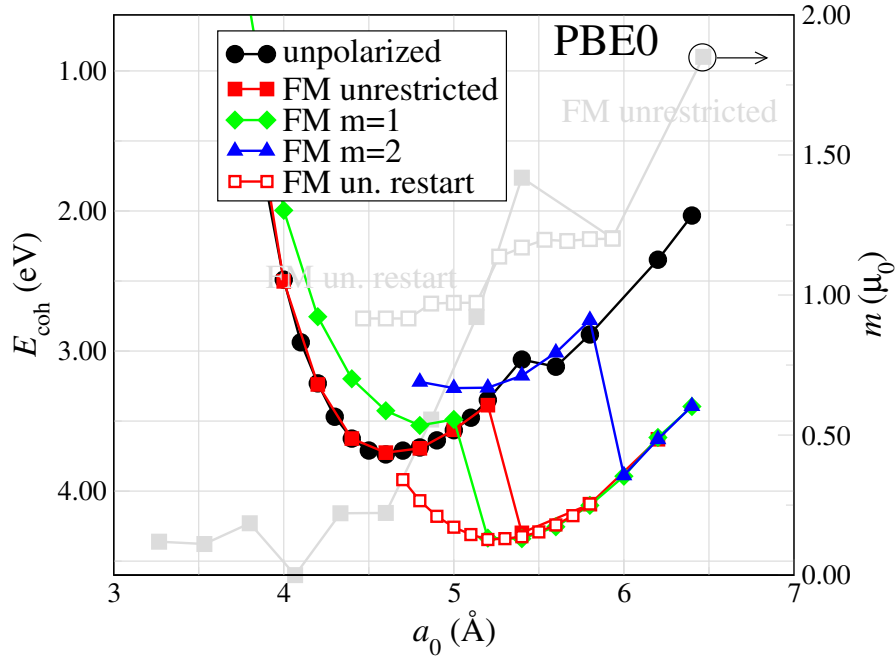


Figure 7.14: PBE0 Cohesive energy of cerium bulk. For an explanation of the magnetic configurations see caption of Figure 7.12. *FM un. restart* means that the electronic structure of the *FM unrestricted* solution at lattice constant 5.8 Å is used to restart calculations at left nearest neighbour lattice constants. Calculations are initialized with the suggested electronic structure but follow an independent SCF cycle.

on the fcc crystal structure could be representative, to first approximation, of the β -phase. The outcome however did not provide evidence for a stabilization of the antiferromagnetic structure with respect to the fcc one.

Hybrid functional calculations on the fcc structure are subject to the multi-solution behavior. Figure 7.14 illustrates how an instability region around $a_0 = 5.2$ Å emerges in unrestricted spin-polarized calculations. For smaller lattice constants the magnetic moment is close to zero (see gray curves) but when the system develops a finite value of the spin with increasing volume, the cohesive energy lowers considerably. For small lattice constants, where the system spontaneously chooses a paramagnetic-like behavior, it is possible to calculate the cohesive energy with the initial electronic structure obtained for large volumes. As the system is stable enough, the SCF preserves the electronic properties, and this leads to the appearance of more than one solution. Different solutions are also obtained if the spin is restricted to a finite value. The curves with spin constraints show the same discontinuity as the spin

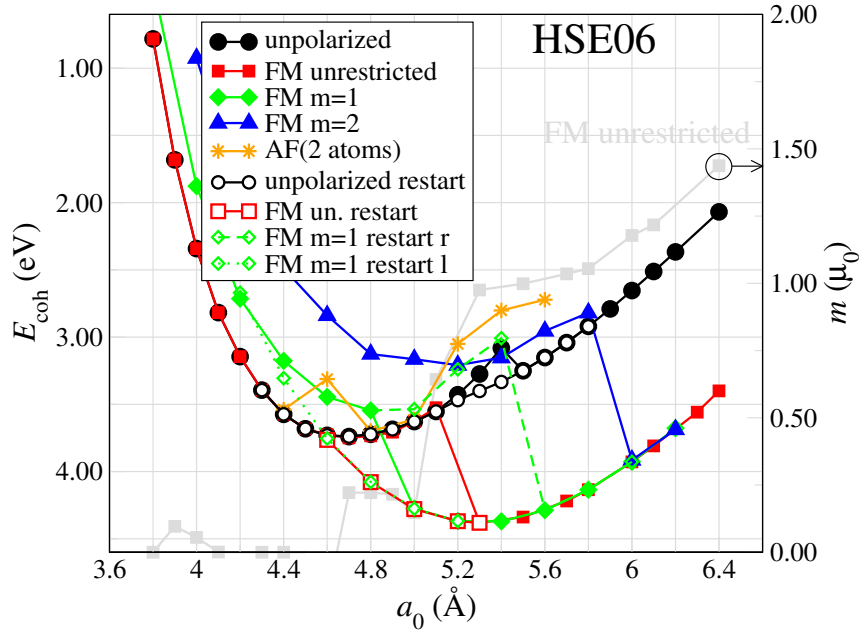


Figure 7.15: HSE06 Cohesive energy of cerium bulk. For an explanation of the magnetic configurations see caption of Figure 7.12 and 7.14. The curves *unpolarized restart*, *FM m=1 restart r* and *FM m=1 restart l* are obtained as described for the *FM un. restart* calculations. *r* and *l* refer to the right and left nearest neighbours to which the electronic structure has been passed. *AF* results only partially satisfy the convergence criterion imposed by the SCF cycle.

unrestricted solution. Therefore, the magnetic moment does not appear to be the driving mechanism of the multi-solution behavior, as argued in Section 7.2. PBE0 and HSE06 results of Figure 7.14 and 7.15 prove that there is indeed a change in the wave functions under variation of the lattice constant of the fcc crystal. The freedom of assuming a finite spin value only allows the system to relax in the most stable state at each lattice constant.

7.4 ROLE OF EXACT-EXCHANGE

The idea of applying hybrid functionals to cerium systems came from previous work –Chapter 3– which suggested that the failure of LDA and GGA in describing the α - γ phase transition would be closely related to the self-interaction error. This was then supported by the dimer and cluster results of Chapter 5 and 6. (EX+cRPA)@PBE results suggest that at least a fraction of exact-exchange should be included in a self-consistent way in the calculations. We have shown in this and previous Chapters that the outcome of PBE0 and HSE06 calculations confirms this assumption. Not only hybrid functionals provide better agreement with experiment than local/semi-local functionals in some cases –i.e. for the dimer and the bulk–, but also the α and γ phases can be reproduced within a single level of theory, and (EX+cRPA)@PBE0 gives remarkable agreement with experimental findings.

Supported by the charge density analysis of Section 7.1, the appearance of two phases in hybrid functionals can be interpreted in terms of *localization-delocalization* of the f electrons. Within LDA/GGA the intrinsic self-interaction error is not corrected, and valence electrons are therefore delocalized. In PBE0/HSE06 the self-interaction error is partially corrected. The fraction of exact-exchange –see Section 2.6– that is introduced brings the system into an intermediate regime in which the valence s and d electrons still form a conduction band and the f states can change their nature from delocalized to localized without changing the energy of the systems significantly. The amount of EX therefore acts as “localizing” factor, but how much EX should be included? The question was already raised in Section 5.5, and to address this problem further we report in Figure 7.16 the variation of the cohesive energy with respect to the amount of exchange (in terms of the parameter a). As in Section 5.5, all calculations that include a percentage of EX different than 0.25 –the PBE0 value– are restarted from the two initial PBE0 solutions. For $a = 0$ the curves correspond to PBE. However, $a = 1$ does not correspond to Hartree-Fock, because correlation is still retained at the PBE level. The discovery of two solutions would not be guaranteed without restarting the calculations from the PBE0 solutions.

The variation of a affects the α phase to a greater extent than the γ phase. The cohesive energy of α -Ce changes by more than 1.5 eV, around double of what is

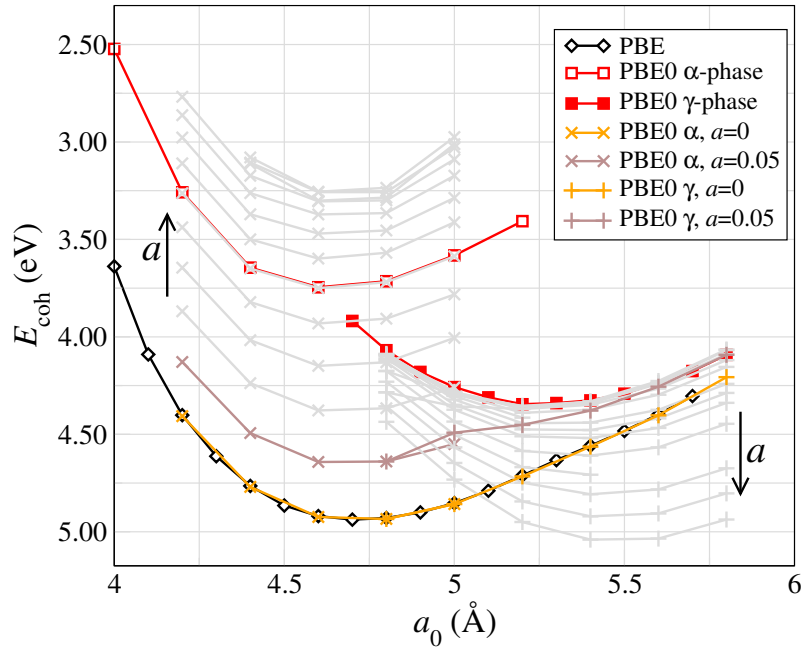


Figure 7.16: Variation of the cohesive energy for the α and γ phases of Ce with respect to the change in the fraction of exact-exchange a included in the PBE0 functional. a varies in steps of 0.05 for $0 \leq a \leq 0.25$ (0.25 corresponds to PBE0) and in steps of 0.1 for $0.25 \leq a \leq 1$.

found for γ -Ce, between $a = 0$ and $a = 1$. Increasing a from the original PBE0 value of $1/4$ shifts the α solution to lower energies, while decreasing it moves the curves to higher energy, until the PBE solution is recovered for $a = 0$. The opposite is true for the γ solution. Values larger than $1/4$ cause the cohesive energy to increase. For smaller values the cohesive energy does not change appreciably. Exceptions are $a = 0$ and $a = 0.05$, for which the trend in the cohesive energy is reversed. The γ solution is lowered with respect to PBE0, until a perfect agreement with PBE results is again reached.

One would be tempted to think that the α - γ transition could be described considering an amount of EX of 0.05. However, manually changing a in order to recover the correct transition is not a proper theoretical approach and also introduces arbitrariness and loss of predictive power. A more rigorous theoretical approach should be used to make robust conclusions. This is provided by higher level theories as the EX+cRPA correction. At the time being RPA cannot be computed for periodic systems in the FHI-aims code, but in the next Chapter we will show

that one can rely on the (EX+cRPA)@PBE0 results for the nineteen-atom cluster to produce a finite temperature phase diagram of cerium in fair agreement with experiment.

7.5 SUMMARY

The description of the volume collapse in cerium poses a great challenge to density-functional theory since local/semi-local functionals fail to produce the associated α - γ phase transition. Methods that introduce orbital dependent corrections have been applied to cerium in the past in order to overcome this failure. However, approaches like SIC-LSD or LDA+ U have only been able to describe the structural properties of the γ phase, and they have accounted for the α phase only within LDA/GGA. No study has reported a double minimum in the total energy versus volume curve at zero temperature, that would be a signature of the volume collapse, within a single theoretical framework. DMFT calculations reproduce the experimentally observed three-peak structure in photoemission spectra, but the results remained limited to high temperatures, and an ongoing debate between different studies remains whether the spectral properties manifest on two minima in the total energy curve or not. Based on the DMFT results, some authors emphasize the importance of including dynamical correlation in order to face the cerium problem.

In this chapter the cerium challenge was approached in a periodic environment by treating all electrons on the same quantum mechanical level (including the f electrons) using LDA, PBE and the hybrid functionals PBE0 and HSE06. PBE0 and HSE06 exhibit a multi-solution behavior and two distinct solutions are always obtained. Based on their magnetic, spectral and structural properties it seems reasonable to associate them with the α and γ phases of cerium. An analysis of the band structure and the electronic density distribution of the two solutions for different magnetic configurations proved that hybrid functional can indeed capture a change in the f wave functions around the region of the experimental α and γ lattice constants.

It is one of the main achievements of this thesis that both phases can be reproduced, at zero temperature, within a single theoretical framework. A first consequence of this result is that the debate whether the α - γ phase transition would survive at low temperature or not could be resolved in favor of the former hypothesis.

Even if potentially accounting for the volume collapse, the hybrid functional description of the two phases however provide a wrong energetic order of the two

solutions compared to the experimental phase diagram. It will be shown in Chapter 8 that the EX+cRPA approach is then essential to rectify this failure, and with the aid of cluster results it is possible to achieve good agreement with the experimental phase diagram at finite temperature.

8 PHASE DIAGRAM FOR THE α - γ TRANSITION

Hybrid functional calculations on cerium provide a new perspective for DFT methods in the description of the α - γ phase transition. In both PBE0 and HSE06 two solutions are found for clusters and the bulk. The double well observed in the cohesive energy versus volume curve shows the occurrence of a $T = 0$ K phase transition accompanied by a volume collapse that has not been obtained before in *ab initio* calculations. The two solutions display specific characteristics of the α and γ phases, including a good description of the change in magnetic and structural properties associated with the volume collapse. They also support the already suggested *localization-delocalization* process as a mechanism for the phase transition. However, the relative energetic order differs from what is expected according to the extrapolated experimental phase diagram at zero temperature, Section 1.3.

In Chapter 6 it was shown that already for cerium clusters cut from the fcc structure PBE0 produces two distinct solutions that can be associated with the α and γ phases. Exemplified by the case of the nineteen-atom cluster we showed that the EX+cRPA correction to hybrid functional brings the two solutions close in energy and recovers the right energetic order of the two solutions. This provides agreement between the calculated transition pressure and the experimental data extrapolated to zero temperature. In this Chapter we will show that relying on the cluster results –at the time being RPA is not available in the FHI-aims code for periodic systems– and adding entropic contributions, the temperature-pressure phase diagram of cerium can be reproduced with satisfactory accuracy.

8.1 TOWARD THE BULK

Looking at the electronic properties of the clusters –e.g. reflected in the density of states–, we realized that cerium clusters cut from the fcc crystal structure can describe cerium bulk. The PBE DOS of the central atom converges to the PBE bulk DOS with increasing cluster size –Figure 6.5 and 7.2. The same happens in PBE0, where the two phases maintain their distinctive features for all the clusters –Figure 6.6–, and the cluster DOS projected on the central atom is representative of the bulk DOS –Figure 7.2–. From Figure 8.1 and 8.2 it becomes clear that there is indeed a trend in the physical observables of the two solutions when increasing the dimension of the system.

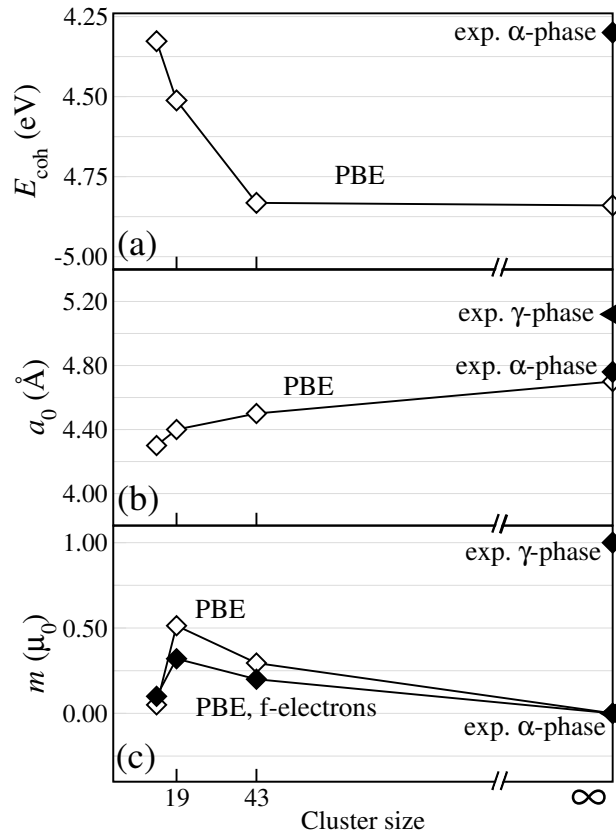


Figure 8.1: PBE results for cerium clusters and corresponding bulk values for (a) the cohesive energy E_{coh} , (b) the lattice constant a_0 , and (c) the magnetic moment on the central atom m . Experimental results marked on the right axis are taken from Ref. [9] and [240].

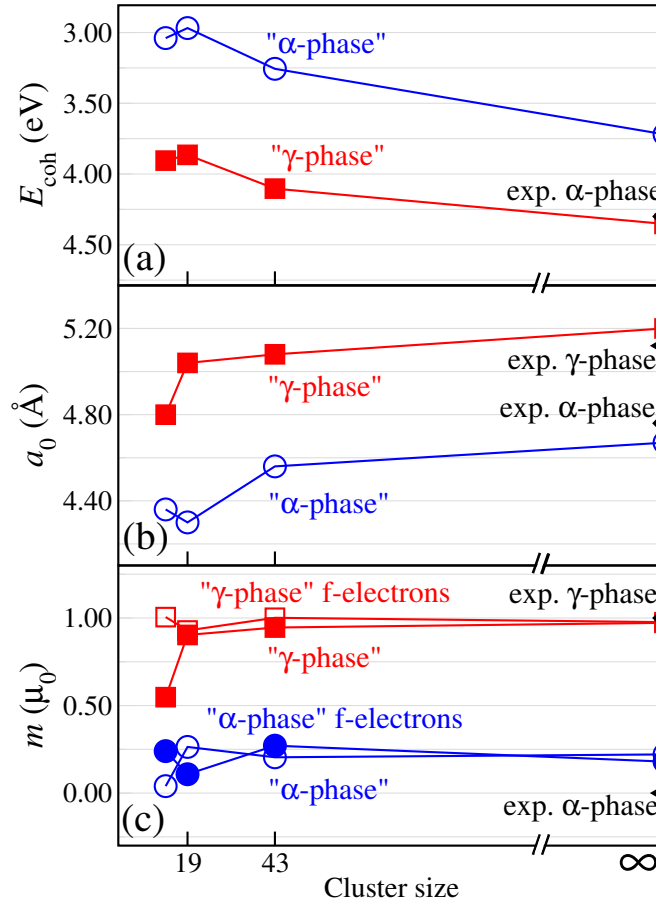


Figure 8.2: PBE0 results for cerium clusters and corresponding bulk values for (a) the cohesive energy E_{coh} , (b) the lattice constant a_0 , and (c) the magnetic moment on the central atom m . All clusters exhibit two solutions that converge to the calculated bulk limit. Experimental results marked on the right axis are taken from Ref. [9] and [240].

Figure 8.1 and 8.2 report the values of the cohesive energy, the equilibrium lattice constant, and the magnetic moment (on the central atom) for all clusters and the bulk. Experimental data are also included for comparison. In PBE and PBE0, all properties move towards the bulk limit with increasing cluster size. The bulk PBE lattice constant and magnetic moment approximate the measured values for the α phase well, even if the cohesive energy is overestimated. The two PBE0 solutions for the bulk are in agreement with the experimental lattice constant and magnetic moments of the α and γ phases. It is also evident from Figure 8.1 (c) and 8.2 (c) that in both PBE and PBE0 the spin component of the system mainly arises from the f electrons. In Section 6.2 we evidenced that PBE calculations for the nineteen

atom cluster are not representative of PBE bulk results. However, it can be stated that PBE0 captures for Ce_{19} the essential physics of the two bulk phases, and that, as a consequence, (EX+cRPA)@PBE0 results for Ce_{19} would be representative of the periodic system. We therefore based our finite temperature analysis of the phase transition on the (EX+cRPA)@PBE0 calculations for Ce_{19} . The result is presented in the next Section.

8.2 FINITE TEMPERATURE

In Section 6.2 a pressure induced phase transition at zero temperature was related to the (EX+cRPA)@PBE0 calculations for the nineteen-atom cluster. Here we extend the results to finite temperature by adding entropic effects to the ground state energy [76, 77, 206, 209, 212]. The first entropic contribution is configurational entropy. This is based on the assumption that the phase that is metastable at a given volume and pressure may become thermally populated as temperature is increased. We therefore adopt a “pseudo-alloy” model for the transition [76], where the α and γ phases coexist with concentrations x^α and x^γ but do not interact¹.

In order to obtain a description of the system at finite temperature the total Helmholtz free energy

$$F(V, T) = U(V) - TS \quad (8.1)$$

is required, where U is the internal energy, T the temperature, V the volume of the unit cell and S the entropy. The free energy can be obtained from the partition function, that is an additive quantity for all the non-interacting components of the system, for which the following relation holds

$$Z = e^{-\beta F(V, T)} = \sum_{\sigma} Z^{\sigma} = \sum_{\sigma} e^{-\beta F^{\sigma}(V, T)}, \quad (8.2)$$

where $\beta = 1/(k_B T)$, k_B is the Boltzmann constant, $\sigma = \{\alpha, \gamma\}$, and F^{σ} is the free

¹A coexistence of the two phases is generally observed in experiments, see e.g. Decremps *et al.* [59].

energy of the α or γ phase. One can now define two quantities

$$x^\sigma = \frac{Z_\sigma}{Z} \quad (8.3)$$

in order to rewrite the free energy as

$$\begin{aligned} F(V, T, x^\sigma) &= -k_B T \ln Z \\ &= -k_B T \sum_\sigma \frac{Z_\sigma}{Z} \ln Z^\sigma + k_B T \sum_\sigma \frac{Z_\sigma}{Z} \ln Z^\sigma - k_B T \sum_\sigma \frac{Z_\sigma}{Z} \ln Z \\ &= \sum_\sigma x^\sigma F^\sigma + k_B T \sum_\sigma x^\sigma \ln x^\sigma \\ &= \sum_\sigma x^\sigma F^\sigma - T S_{conf}. \end{aligned} \quad (8.4)$$

The quantity x^σ represents the contribution of one or the other phase to a determined state of the system and $S_{conf} = -\sum_\sigma x^\sigma \ln x^\sigma$ is the entropic contribution that arises from the coexistence of the two phases.

The free energy of a single phase can then be computed from

$$F^\sigma(V, T) = U^\sigma(V) - T(S_{el}^\sigma + S_{mag}^\sigma + S_{vib}^\sigma) \quad (8.5)$$

where U^σ is the internal energy, S_{el}^σ is the entropy arising from electronic degrees of freedom, S_{mag}^σ is the entropic contribution of the magnetic moment at each cerium site, and S_{vib}^σ is the entropy associated with lattice vibrations. The (EX+cRPA)@PBE0 calculations reported in the previous section proved to be a reasonable estimation of the two contributions U^α and U^γ according to the extrapolation of experimental data to zero temperature. Consequently, in the following analysis $U^\sigma(V)$ will be associated to $-E_{coh}^\sigma(V)$, with the latter obtained from a fit of the (EX+cRPA)@PBE0 results to the Birch-Murnaghan equation of state [243]

$$E_{coh}^\sigma(V) = E_0^\sigma + \frac{B_0^\sigma V}{B_0'^\sigma} \left(\frac{(V_0^\sigma/V)^{B_0'^\sigma}}{B_0'^\sigma - 1} + 1 \right) - \frac{B_0^\sigma V_0^\sigma}{B_0'^\sigma - 1}, \quad (8.6)$$

where E_0^σ is the energy at equilibrium, V_0^σ the equilibrium volume, B_0^σ the bulk modulus and $B_0'^\sigma$ the derivative of the bulk modulus. As it turned out in the

present study, the bulk modulus of the nineteen-atoms cluster, according to the Birch-Murnaghan fit, largely overestimates the experimental reported values. This is probably due to the still too small dimension of the system and affects the estimation of the α - γ phase diagram considerably. Instead, periodic PBE0 calculations produce values of the bulk modulus close to the experimental findings. It was therefore assumed that the bulk modulus B_0^σ , derived from a fit to Equation 8.6, would represent the physical situation better than the cluster B_0^σ . For this reason, we replace B_0^σ in Equation 8.5 by the PBE0 bulk value, but we leave all other variables at their (EX+cRPA)@PBE0 values.

In principle, the contribution S_{el}^σ can be calculated by either integrating over the $T = 0$ K Kohn-Sham DOS following the Fermi-Dirac distribution, or by introducing electronic temperature effects directly in (EX+cRPA)@PBE0. However, in the temperature range of interest –i.e. $T < 2000$ K– none of the two approaches produce a noticeable change of the results. The electronic degrees of freedom were therefore neglected in the present analysis, as also suggested by other authors [76, 77, 209].

Concerning the entropy arising from the magnetic moment of the cerium atoms, a state with total angular momentum J adds an entropic contribution to the free energy

$$S_{mag}^\sigma = k_B \ln(2J + 1). \quad (8.7)$$

assuming that for the temperatures of interest only the ground state multiplet is populated. The (EX+cRPA)@PBE0 α phase displays no magnetic moment, and the γ phase has a spin component arising from a localized $4f$ state, i.e. $J = 5/2$. So Equation 8.7 results in $S_{mag}^\alpha = 0$ and $S_{mag}^\gamma = k_B \ln 6$. However, based on crystal field splitting considerations, Lüders *et al.* [209] suggested that $S_{mag}^\gamma = k_B \ln 8$ would be more appropriate to describe the localized f states, and the latter assumption was also adopted in the present study.

The contribution of lattice vibrations to the total free energy has minor effects at the temperatures of interest so it has been generally neglected in previous studies. However, estimates have been provided by some authors, for example by considering the Debye-Grüneisen model [76] or by fitting to experimental data [77]. In this thesis the vibrational entropy as calculated from phonon theory by Wang *et al.* [212] was included in terms of the difference between the two phases. The authors reported a

temperature-independent difference between the phononic contributions of the two phases. So the vibrational entropy was considered to be

$$\Delta S_{vib} = 0.94k_B. \quad (8.8)$$

Finally, considering that only two phases are present in the system, and that therefore their concentrations can be expressed as relative percentages $x^\gamma = x_{eq}$ and $x^\alpha = (1 - x_{eq})$, Equation 8.1 can be evaluated as follows

$$\begin{aligned} F(V, T, x_{eq}) &= (1 - x_{eq})U^\alpha(V) + x_{eq}U^\gamma(V) - x_{eq}T(S_{mag}^\gamma + S_{vib}^\gamma) - TS_{conf} \\ &= (1 - x_{eq})U^\alpha(V) + xU^\gamma(V) \\ &\quad - k_B T [x_{eq} \ln 8 + 0.94x_{eq} - (1 - x_{eq}) \ln(1 - x_{eq}) - x_{eq} \ln x_{eq}]. \end{aligned} \quad (8.9)$$

The quantity x_{eq} in Equation 8.3, that represents the relative percentage of the two phases at equilibrium for a given volume and temperature, can also be obtained [76, 77, 209] by making the substitution $x_{eq} \rightarrow x$ in Equation 8.9 with $0 \leq x \leq 1$, and minimizing the free energy with respect to x . In Figure 8.3 the Helmholtz free energy of cerium as calculated by adding entropic contributions to the (EX+cRPA)@PBE0 results of Ce₁₉ is reported as a function of volume and relative concentration x of the α and γ phases for six temperatures of interest. For each panel also the value x_{eq} is reported as a function of volume. The value of x that minimizes the free energy is in fact x_{eq} . As reported in Figure 8.3, at $T = 0$ K the entropic contribution is zero and the free energy is minimized at each volume by the α and γ internal energies in their range of stability. Consequently, x_{eq} is flattened to zero for small volumes and approaches one at larger volumes. As the temperature grows, a mixing of the two phases starts to take place in the region between the two equilibrium lattice constants. The relative concentration x_{eq} moves to intermediate values until at high enough temperatures there is no volume for which the system is in a pure α phase.

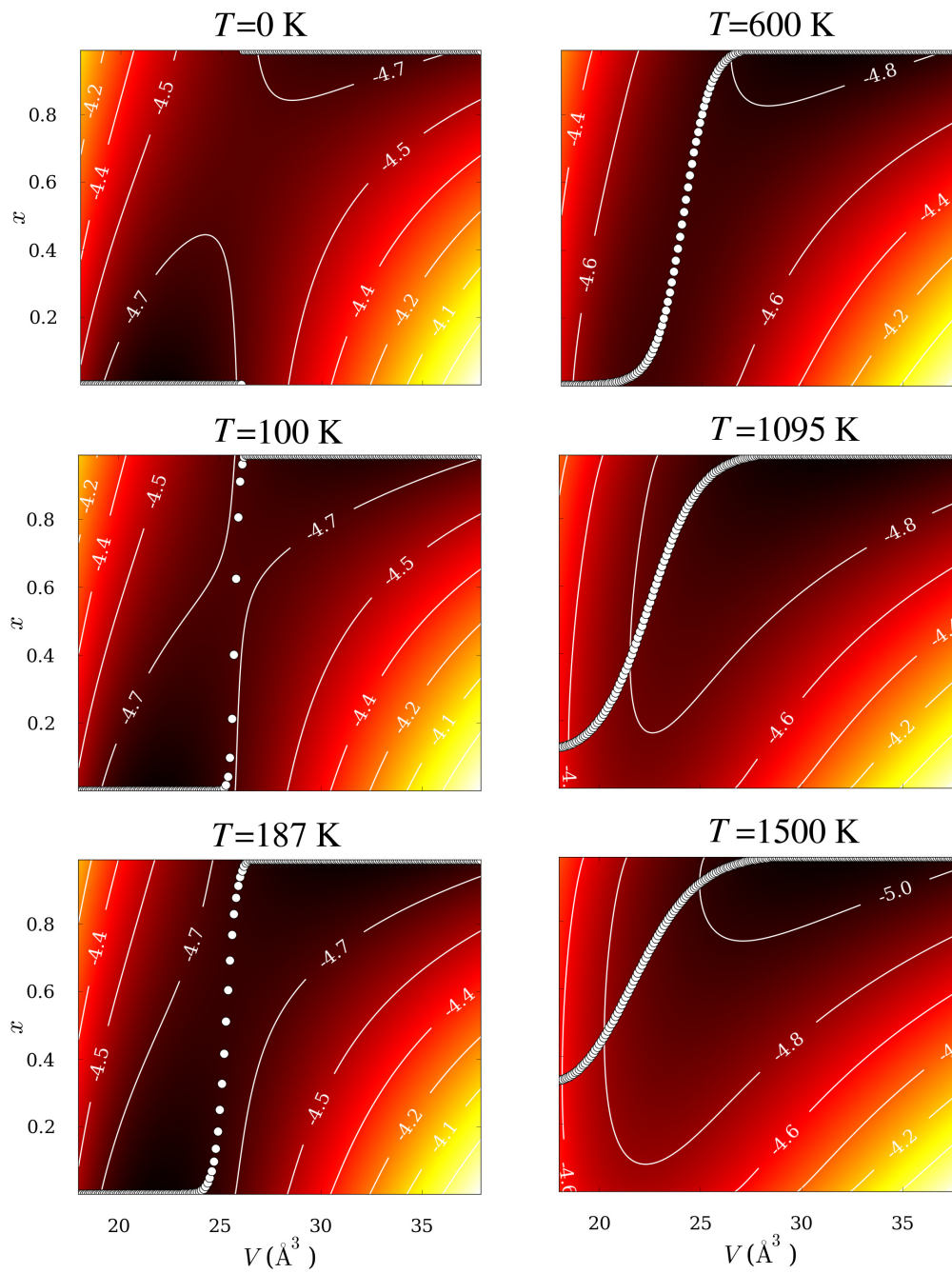


Figure 8.3: Calculated Helmholtz free energy as a function of volume and relative concentration of the α and γ phases at six temperatures of interest. For each panel also the equilibrium concentration x_{eq} is plotted as a function of volume. x_{eq} corresponds to the minimum of the free energy.

Following Equation 8.9, in Figure 8.4 the free energy of the pseudo-alloy is plotted as a function of volume for different values of the temperature. At $T = 0$ K the free energy coincides with the curves in Figure 6.8, except that here the values of the bulk modulus are taken from periodic PBE0 calculations. This produces a slightly different transition pressure –obtained from the double tangent to the curve– of -0.79 GPa, still close to the previous value, and in better agreement with the experimental extrapolation to zero temperature $P_t \simeq -0.8$ GPa.

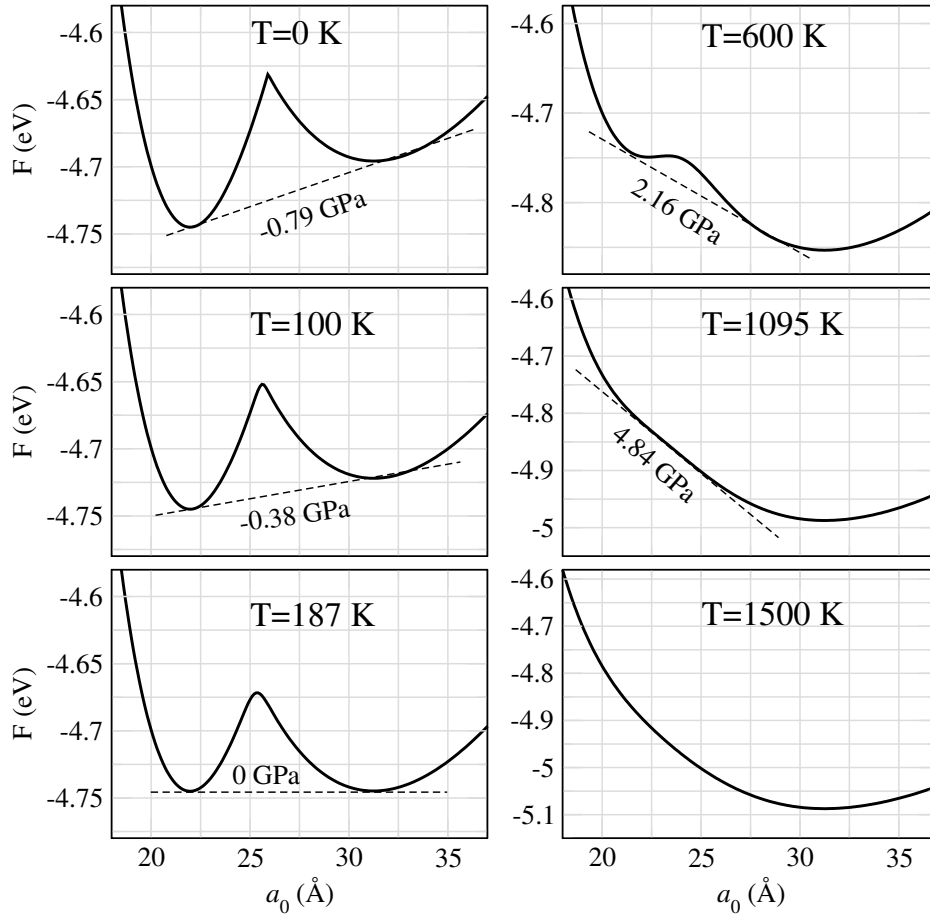


Figure 8.4: Calculated Helmholtz free energy as a function of volume for six temperatures of interest and relative equilibrium concentration x_{eq} . In each panel the transition pressure as obtained by the Gibbs construction is also reported. The double tangent to the curves is present until $T_c = 1095$ K. Above that temperature no volume collapse is registered. $T_c = 1095$ K, $P_c = 4.84$, GPa represents the critical point.

As the temperature grows, the transition pressure moves towards positive

values, until at $T = 187$ K it equals zero. The transition temperature at $P_t = 0$ GPa is a quantity of interest, as it represents the lowest point at which direct experimental estimates are available. As discussed in Chapter 1, it was observed that hysteresis effects play an important role in the α - γ phase transition. Moreover, the presence of the β phase further complicates the landscape. Nevertheless, considering the similarities between the γ and β phases, and that the γ - β transition involves a structural change that is generally understood in terms of the d electrons rearrangement [9], the β - α transition temperature at 0 GPa is accepted as a reasonable estimation for the α - γ phase diagram. As summarized in Table 8.1, $T_0 = 187$ K is not far from the experimental estimation $T_0 = 141$ K [9].

The inclusion of entropic effects in the free energy allows to make an estimate of the volume collapse associated with the α - γ phase transition at room temperature. As reported in Table 8.1, the approach followed in this thesis results in a 28 % volume collapse.

Table 8.1: Results from the present and previous theoretical works and experimental data for the α - γ phase transition. T_0 : transition temperature at 0 GPa. P_c : critical pressure. T_c : critical temperature. $\Delta V_{\gamma-\alpha}$: volume collapse associated with the transition at $T = 300$ K.

	Present work	Previous works	Experiments
T_0 (K)	187	135 ^a , 169 ^b	141±10 ^c
P_c (GPa)	4.84	3.86 ^a , 5.6 ^b , 4.7 ^d , 2.22 ^e	1.96±2 ^c , 1.8 ^f , 1.5 ^g , 1.44 ^h
T_c (K)	1095	980 ^a , 1377 ^b , 1300 ^d , 476 ^e	600±50 ^c , 485 ^f , 480 ^g , 460 ^h
$\Delta V_{\gamma-\alpha}$ (300 K) (%)	28	20 ^a , 20.5 ^b , 23.4 ^d , 16.5 ^e	14.7 ^f , 14 ^h

^aJohansson *et al.*, GGA [76]

^bLüders *et al.*, SIC-LSD [209]

^cKoskenmaki *et al.*, exp. [9]

^dSvane *et al.*, SIC-LSD [77]

^eWang *et al.*, LDA+ U [212]

^fSchiwek *et al.*, exp. [65]

^gLipp *et al.*, exp. [58]

^hDecremps *et al.*, exp. [59]

In the phase diagram of cerium the α - γ transition line terminates in the β phase

at low pressure and in a critical point (C.P.) at $T_c = 460$ K and $P_c = 1.44$ GPa [59]. Also in the present calculations a C.P. manifests. The critical temperature coincides with the disappearance of a negative curvature region in the free energy curve, that, from Figure 8.4, appears for $T_c = 1095$. The calculated critical pressure is $P_c = 4.84$ GPa. Previous analysis based on electronic structure theory also reported values close to the ones obtained in this thesis. Johansson *et al.* found $T_c = 980$ K and $P_c = 3.86$ GPa by means of GGA calculations in which the f electrons were retained in the valence shell in the α phase and in the inert core in the γ phase. Using SIC-LSD Svane *et al.* reported $T_c = 1300$ K and $P_c = 4.7$ GPa and Lüders *et al.* obtained $T_c = 1377$ K and $P_c = 5.6$ GPa. By means of LDA+ U calculations, Wang *et al.* found $T_c = 476$ K and $P_c = 2.22$ GPa, but the description of the γ phase was adjusted to the experimental reference through the tunable U parameter. Our approach differs from the previous ones by the starting point. In our calculations the internal energy at $T = 0$ K is obtained within a single level of theory and no adjustable parameters have been introduced. DMFT studies, which intrinsically include temperature effects, did not report a phase diagram for cerium.

From Equation 8.9 it is possible to obtain, at constant T and optimal mixing x_{eq} , the pressure dependence of the volume as

$$\begin{aligned} P(V, T, x_{eq}) &= -\frac{\partial F(V, T, x_{eq})}{\partial V} \\ &= -(1 - x_{eq}) \frac{\partial U^\alpha(V)}{\partial V} - (x_{eq}) \frac{\partial U^\alpha(V)}{\partial V}. \end{aligned} \quad (8.10)$$

By inserting Equation 8.6 in 8.10 through the equivalence $U^\sigma(V) = -E_{\text{coh}}^\sigma(V)$, one can further express the pressure explicitly in terms of the coefficients of the Birch-Murnaghan equation of state

$$P(V, T, x_{eq}) = (1 - x_{eq}) \frac{B_0^\alpha}{B_0'^\alpha} \left[\left(\frac{V_0}{V} \right)^{B_0'^\alpha} - 1 \right] + x_{eq} \frac{B_0^\gamma}{B_0'^\gamma} \left[\left(\frac{V_0}{V} \right)^{B_0'^\gamma} - 1 \right]. \quad (8.11)$$

The isotherms that correspond to Equation 8.11 are reported in Figure 8.5. At each temperature the transition pressure is estimated via the Gibbs construction as reported in Figure 8.4. The discontinuities in the $P - V$ curves are indicative of the volume collapse at different temperatures and delimit a region of instability generally

known as *miscibility gap*. The jump in volume between the two phases gradually shrinks with increasing temperature, until at $T_c = 1095$ K the isotherm becomes smooth and the volume varies continuously with pressure. This determines the critical point of the phase transition, at the associated transition pressure $P_c = 4.84$.

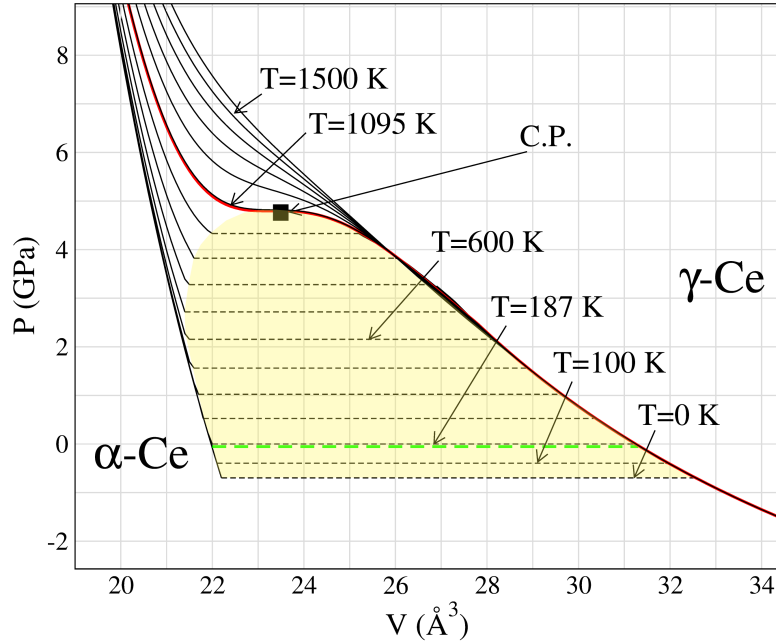


Figure 8.5: Pressure versus volume isotherms for temperatures between 0 K –lowest curve– and 1600 K, in steps of 100 K. The results for $T = 187$ K (in green) and $T = 1095$ K (red curve) are also reported as they represent the transition temperature at 0 GPa and the critical point temperature respectively. C.P. is the critical point.

Finally, by plotting the transition temperature as a function of pressure, the phase diagram of the α - γ phase transition can be drawn, Figure 8.6. With respect to the experimental phase diagram, the transition line is extended to negative pressures. This is a natural consequence of the fact that in our calculations the phase transition can be described at $T = 0$ K. Due to the lack of experimental references the survival of the phase transition in the negative pressure region has been a matter of debate. A first problematic aspect is the presence of the β phase. Based on the sequence of structural changes that is found in lanthanum, that has no f electrons, the crystal modification from fcc (γ phase) to dhcp (β phase) can be understood in terms of a rearrangement of d electrons. As discussed in Section 1.3, in this case one would think

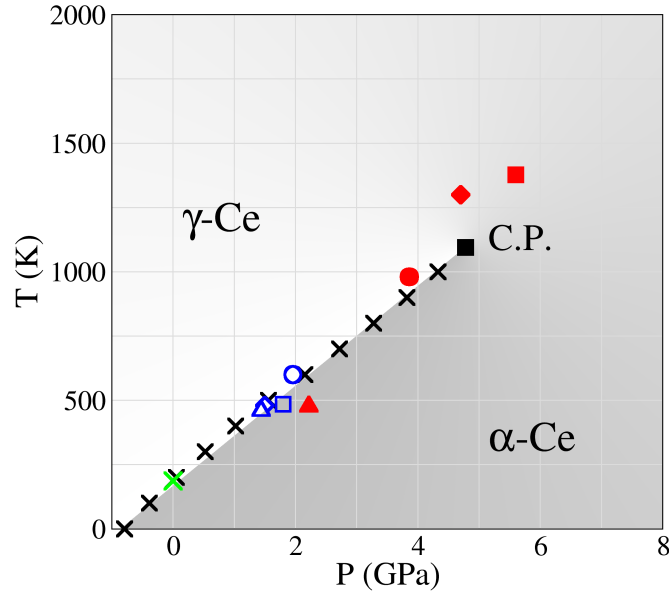


Figure 8.6: Temperature-pressure phase diagram of cerium (black crosses) as obtained by adding entropic contributions to the (EX+cRPA)@PBE0 results. C.P. is the calculated critical point (black square). The green cross indicates the transition temperature at $P_t = 0$. Experimental results for C.P., identified by the blue symbols, are from Koskenmaki *et al.* [9, 10] (open circle), Schiwiek *et al.* [65] (open square), Lipp *et al.*, Decremps *et al.* [59] (open triangle), [58] (open diamond, obscured by the triangle). Previous theoretical data are reported in red from Johansson *et al.* [76] (filled circle), Lüders *et al.* [209] (filled square), Svane *et al.* [77] (filled diamond), Wang *et al.* [212] (filled triangle).

of the f and d electrons as if they would act independently on the properties of the material, the d states not undergoing major changes across the α - γ , α - β transitions, but causing the structural change between the γ and β regions. The f electrons, on the other hand, remain localized in the γ and β phases and are delocalized in the α phase. However, in view of the mutual influence that f and d electrons have on each other –as discussed throughout the course of this thesis– the above considerations cannot be taken for granted. In addition, some authors suggested other possible reasons for the disappearance of the phase transition. De Medici *et al.* for example proposed that delocalization of f electrons via a Mott transition mechanism would be suppressed by Kondo screening at low enough temperatures [244]. The present calculations show, however, that a phase diagram can be produced in close resemblance to experiment by adding entropic contributions to the $T = 0$ K internal energy.

The estimated position of the C.P. is quite distant from the one reported in experiments. Nevertheless, it is a considerable achievement that the experimental critical points fall on the calculated transition line. This is also expected from the fact that the extrapolated transition pressure to zero temperature agrees well with the calculated one. We find that the transition line displays a linear behavior, which is also observed experimentally and constituted the main argument of Johansson *et al.* –see Section 1.4.4– against the Kondo volume collapse interpretation of the phase transition –as the KVC does not result in a linear dependence. In this sense the present outcome further strengthen the conclusion of Section 7.1 that the difference of the α phase with respect to the γ phase can be understood in terms of “direct” delocalization of f electrons.

8.3 SUMMARY

In Chapter 6 and 7 it was shown that hybrid functionals provide two solutions that can be associated with the α and γ phases of cerium. However, their relative energetic order is incorrect. In Chapter 6 we also showed that a proper description of the electronic screening among the electrons can in fact overcome this deficiencies of hybrid functionals. This is achieved through (EX+cRPA)@PBE0 calculations, which incorporate exact-exchange and correlation at the level of the random-phase approximation

At the time being, the RPA correction is not available in the FHI-aims code for periodic systems, but in this Chapter we showed that the main characteristic of hybrid functional calculations on cerium bulk are already present in cerium clusters cut from the fcc structure. In particular the nineteen-atom cluster provides a good foundation for reproducing the cerium phase diagram, that is obtained by adding entropic contributions and allowing the two phases to mix at finite temperature. The calculated finite temperature phase diagram is in reasonable agreement with experimental evidence.

9 BEYOND CERIUM

In the previous chapters we addressed the α - γ phase transition in cerium in detail. We explained the volume collapse in terms of localization versus delocalization of the $4f$ electrons. Subsequently, based on PBE0 results for cerium clusters, we reproduced the phase diagram of the α - γ phase transition, by applying a post-processing EX+cRPA correction to the PBE0 solutions, and including entropic effects in a pseudo-alloy model.

Our approach provides a consistent description of cerium metal, therefore it is fundamental to validate our methodology with calculations for other lanthanide elements. In order to address different scenarios we chose the cerium neighbours. Lanthanum is the first of the series, and has no f electrons. Cerium is the second, and its neighbour is praseodymium, which is characterized by the presence of three $4f$ electrons. Praseodymium, similar to cerium, also displays a first-order phase transition accompanied by a volume collapse. Unlike in cerium, The phase transition is not isostructural. Instead it occurs between a d-fcc and an orthorhombic α -U structure with a 9% volume change at room temperature¹. The fourth is neodymium, with four filled f states and no volume collapse. We point out that there is no element in the periodic table with two nominal $4f$ electrons. This anomaly is due to the presence of a $5d$ electron in La and Ce. After Ce the $5d$ electron is turned into a $4f$ one, and it reappears only in lutetium, which has a closed $4f$ shell.

Despite the presence or absence of a volume collapse, and the different number of f electrons, all four elements follow a general structural sequence under pressure,

¹Refer to Appendix A for an overview of the closed packed crystal structures that characterize lanthanide elements.

which goes from hcp to dhcp, to fcc (d-fcc), to orthorhombic². Because the sequence is found also in La and, for example, Y [245], which have no f electrons, the occurrence of the structural changes is interpreted to be independent from the f electrons [246, 247]. On the other hand, the volume collapse is characteristic of *rare earths*. This is in agreement with our findings that in cerium the f electrons drive the abrupt volume change.

Consequently, we decided to perform calculations for La, Pr and Nd only for the fcc crystal structure. The hcp, fcc and orthorhombic structures are all close packed, and are therefore quite similar. Assuming that the structural changes are not dictated by the f electrons, the effect of the crystal environment should be minor on the f electron properties. Considering only the fcc structures considerably simplifies periodic hybrid functional calculations, and also provides a consistent scenario to compare the response of the different lanthanides, in particular if there is a double minimum or not in the energy versus volume curves and a volume collapse (that could be accompanied by a structural transition, but might not be driven by it).

9.1 HYBRID FUNCTIONAL CALCULATIONS FOR LA, PR, AND ND

The study of La, Pr, and Nd bulk systems was carried out with the same computational details as for cerium metal –see Section 4.1. We performed PBE and HSE06 calculations in both the spin unpolarized and polarized configurations.

In Figure 9.1 the cohesive energy of lanthanum is reported with respect to the fcc lattice constant. The behavior of the system is unchanged whether or not spin polarization is taken into account. Spin unpolarized and polarized results almost coincide, and the value of the magnetic moment is always zero. The curves are smooth. In particular, HSE06 shows no signal for the multi-solution behavior that characterizes cerium. At room temperature La has a dhcp crystal structure, with lattice constant $a_0 = 3.773 \text{ \AA}$ and c/a_0 ratio of 3.201 [248]. The volume of the dhcp unit cell would approximately correspond to the volume of an fcc unit cell with

²We refer the reader to Section 1.2 and Figure 1.2 for more details about the structural changes.

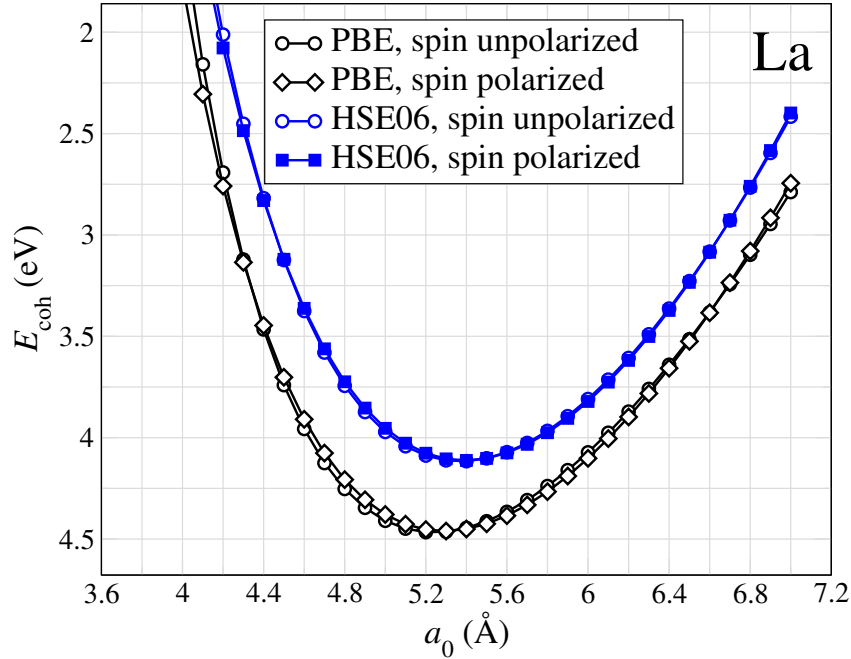


Figure 9.1: PBE and HSE06 cohesive energy of lanthanum. The calculations are performed both spin polarized and unpolarized. The results do not show a significant dependence in the spin configuration.

lattice constant 5.33 Å. PBE gives $a_0 = 5.3$ Å, and HSE06 gives $a_0 = 5.4$ Å. The cohesive energy is 4.46 eV and 4.11 eV, respectively. The bulk modulus is 28.3 GPa in PBE and 27.4 GPa in HSE06, to be compared with the experimental value 24.3 GPa [240].

The results for praseodymium, Figure 9.2, are reminiscent of those of cerium. In PBE the spin polarized solutions lies at lower energy with respect to the unpolarized one. The magnetic moment increases with lattice constant, and around the equilibrium distance lies between 2 and 3 μ_0 , consistent with an alignment of the three f electrons. It is a strong validation of the results presented in the previous chapters that HSE06 displays two stable solutions. As for cerium, one solution lies at high energy and is close to the spin unpolarized results. Here, however, solution (a) shares the magnetic behavior with solution (b). As for PBE, a finite value of the spin sets in with increasing lattice constant. The structural and energetic properties of the different calculations are summarized in Table 9.1.

The two HSE06 solutions are nested and have similar lattice constant, at

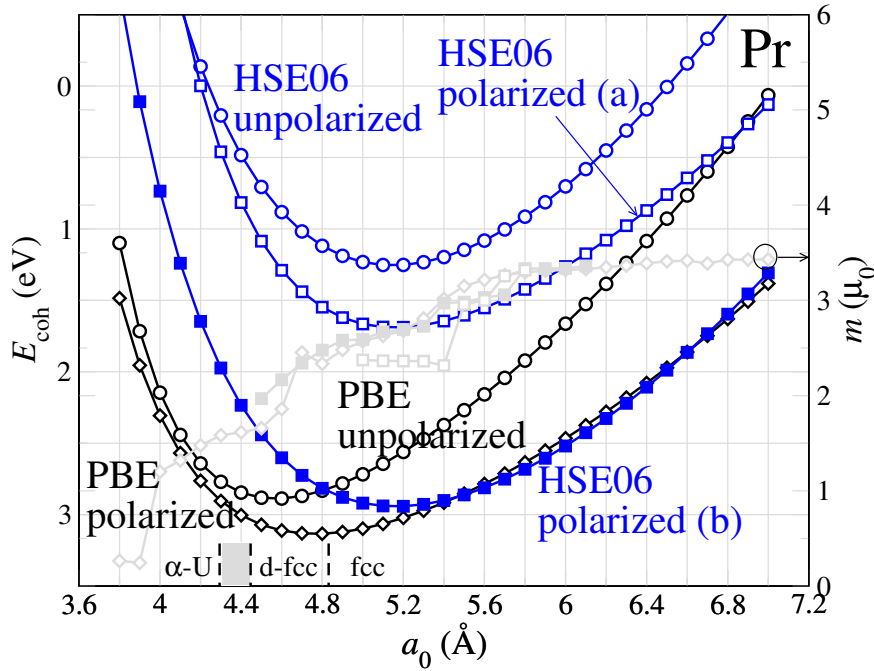


Figure 9.2: PBE and HSE06 cohesive energy for praseodymium. HSE06 spin polarized results are characterized by the presence of two solutions. Gray curves show the value of the magnetic moment for PBE (open diamonds), HSE06 (a) (open squares), and HSE06 (b) (filled squares) spin polarized solutions. Gray curves refer to the left axis. The dashed lines at the bottom mark the experimentally observed transitions. Shaded region: volume collapse.

variance with the hybrid functional calculations for cerium –see Figure 7.1. It means that no double tangent between the curves exists, and that no isostructural volume collapse is predicted. This agrees with the experimental observation that the volume collapse is linked to a structural change.

Next, the neodymium cohesive energy is reported in Figure 9.3. The overall behavior of the system reflects that of Pr, albeit with some differences. The spin unpolarized and polarized PBE curves are more distant in energy with respect to Pr. The magnetic moment around the equilibrium lattice constant is approximately $4 \mu_0$. The spin unpolarized HSE06 solution lies at very high energy, while the two polarized solution are now quite close. The system is then stable at different lattice constants, and a double tangent could be eventually drawn. Again, the two HSE06 solutions have similar magnetic properties. The structural and energetic properties of the different curves are summarized in Table 9.1.

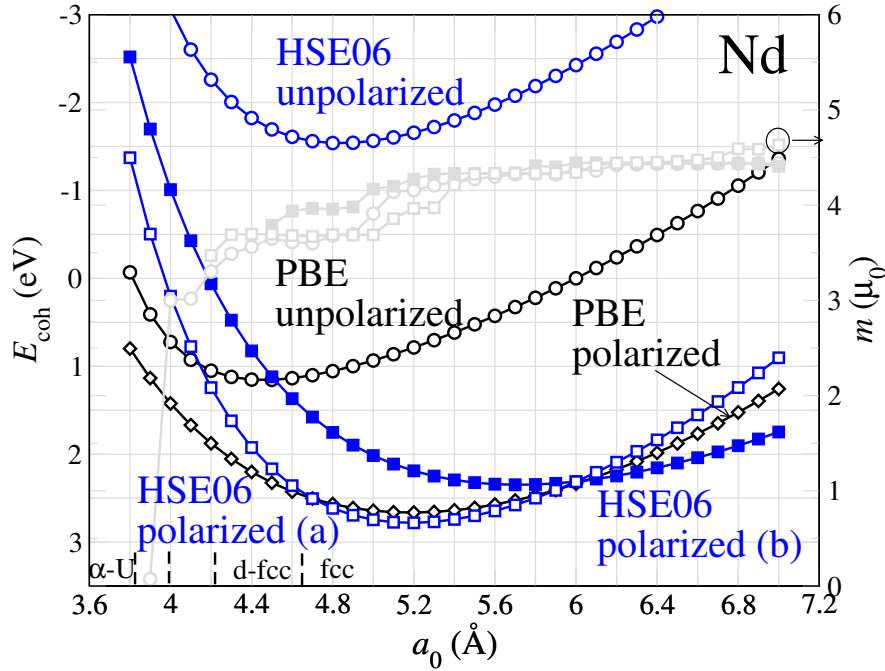


Figure 9.3: PBE and HSE06 cohesive energy for neodymium. HSE06 spin polarized results are characterized by the presence of two solutions. Gray curves represent the value of the magnetic moment for PBE (open diamonds), HSE06 (a) (open squares), and HSE06 (b) (filled squares) spin polarized solutions. Gray curves: are referred to the vertical left axis. The dashed lines at the bottom denote transitions.

In Nd no volume collapse is observed in experiment. However, our HSE06 results show that at least two configurations are close to the ground state. During this thesis, we showed the intrinsic complexity of the α - γ phase transition in cerium, and we discussed how different contributions could eventually cooperate. It is most likely that also in other f electron elements several factors may contribute to the structural properties of the system. In this context, our results suggest that the behavior of the f electrons may change with pressure—for example from localized to delocalized-, even if no volume collapse is observed. This supports recent findings for Nd, which suggest that the Nd α -U structure has delocalized f electrons, and is reached under pressure from the fcc structure (with localized electrons) in a relatively continuous fashion (through the d-fcc structure), without any phase transition [249].

Specific trademarks of the f electron behavior across the four elements become apparent from the density of states. In Figure 9.4 the DOS of spin polarized HSE06

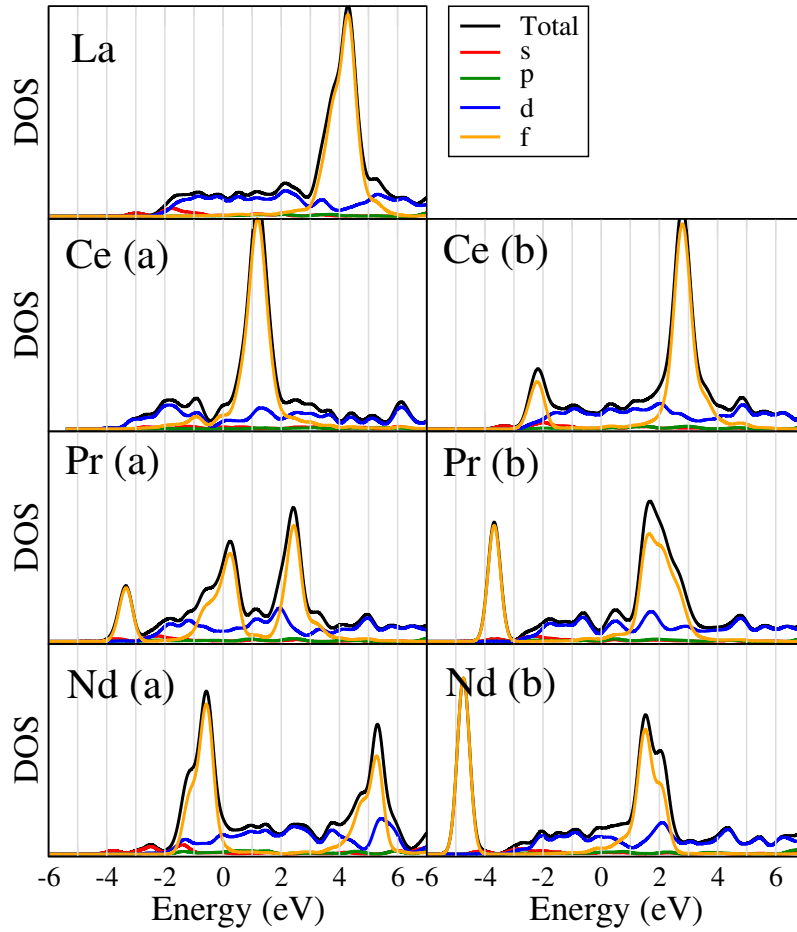


Figure 9.4: Density of states for La, Ce, Pr, Nd, obtained from HSE06 spin polarized calculations. The DOS is the sum of the spin up and down component and it is taken at the equilibrium lattice constant of each solution.

calculations are reported for La, Ce, Pr, and Nd. The DOS is the sum of the spin up and down components. Only one solution is found for lanthanum, so only one panel is presented. The other three elements display two solutions, and the DOS is taken at the equilibrium lattice constant of each solution.

In lanthanum the f states are empty, and lie well above the Fermi level (E_F , denoted by zero in Figure 9.4). The (a) and (b) solutions of cerium correspond to the α and γ phases of Figure 7.1, respectively. The important peak in the unoccupied f states moves towards the Fermi energy from La to the Ce (a) solution, where a small f contribution is also found below the Fermi level. Adding $4f$ electrons in

Pr –solution (a)– seems to cause a splitting of the large peak. Three contributions are distinguishable, of which one crosses E_F . In the Nd (a) solution the peak at lower energy is not present, but the two main peaks of Pr seem to be preserved. The contribution from occupied states is now pushed to lower energies and the one from empty states to higher.

The similarities among the (b) solutions of Ce, Pr, and Nd are even more apparent than for the (a) solutions. In all three elements there are two peaks, one below and one above E_F . The two spectral contributions are reminiscent of the *Hubbard bands* that describe the occurrence of localized states –we showed that this is in fact the case for the (b) solution of cerium. The spectral weight of the peak below E_F systematically increases with increasing number of $4f$ electrons, while the opposite is true for the peak in the unoccupied states. At the same time the two peaks are shifted simultaneously to lower energies going from Ce to Pr, to Nd.

Interestingly, cerium is the only element that does not show appreciable f -electron occupations in both solutions. In Ce only solution b) exhibits an f -peak below the Fermi level, but in Pr and Nd both solutions show large f state occupations. This difference could explain why the volume collapse is isostructural in Ce, but not in Pr and why it is not present in Nd at all. In Pr and Nd the f -electrons are more tightly bound than in Ce and therefore more localized from the outset. Delocalizing just one f -electron would thus not have such a drastic effect as it does in Ce. Moreover, unlike Ce, Pr and Nd have a high density of states at the Fermi level. In many other systems, the reduction of this density of states is a driving force for structural phase transitions. Which of these features is ultimately responsible for the different behaviors of the lanthanide elements will be investigated in future work.

Table 9.1: Comparison of the computed equilibrium lattice constants, bulk moduli and cohesive energies for La, Ce, Pr, Nd, with those of other calculations and experiments. The reported LDA calculations include effects for orbital polarization of the f states. LDA+DMFT results are obtained at 632 K.

	Method	a_0 (Å)	E_{coh} (eV)	B (GPa)
La	PBE (This work)	5.29	4.46	23.5
	HSE06 (This work)	5.39	4.11	24.1
	GGA ^a	5.34	–	24.3
	Expt. ^b	5.33	–	24
Ce	HSE06 (This work) α	4.63	3.76	50.5
	Expt. ^c	4.83	4.3	27
	HSE06 (This work) γ	5.22	4.35	28.3
	Expt. ^c	5.16	–	19
Pr	PBE (This work)	4.76	3.13	22.4
	HSE06 (This work) (a)	5.16	1.69	24.2
	HSE06 (This work) (b)	5.16	2.94	22.3
	LDA ^d (orb. pol.)	5.14	–	34.5
	LDA+DMFT ^e (632K)	5.16	–	31.0
	Expt. ^f	5.16	–	26-37
Nd	PBE (This work)	5.18	2.66	16.0
	HSE06 (This work) (a)	5.19	2.78	25.4
	HSE06 (This work) (b)	5.72	2.35	12.3
	LDA ^d (orb. pol.)	5.11	–	37.1
	LDA+DMFT ^e (632K)	5.09	–	32.9
	Expt. ^f	5.15	–	28-32

^aReference [250].

^bReference [248][240].

^cReference [10, 240, 66].

^dReference [204].

^eReference [216].

^fReference [251, 252].

9.2 MANY-BODY FUNCTIONAL CALCULATIONS OF THE DIMERS: La_2 , Pr_2 , AND Nd_2

As shown before, the calculations for cerium systems with many-body-based methods produces results in remarkable agreement with experiment. (EX+cRPA)@PBE0 for the nineteen atom cluster gives a transition pressure for the α - γ phase transition close to the extrapolated experimental value to zero temperature. Similarly, (EX+cRPA)@PBE0 produces an equilibrium distance, a bonding energy and a vibrational frequency in good agreement with experiment. It is important to address which is the impact of this finding to the smallest molecular unit, i.e. the dimer. Therefore we studied the La, Pr, and Nd dimers with the same approach.

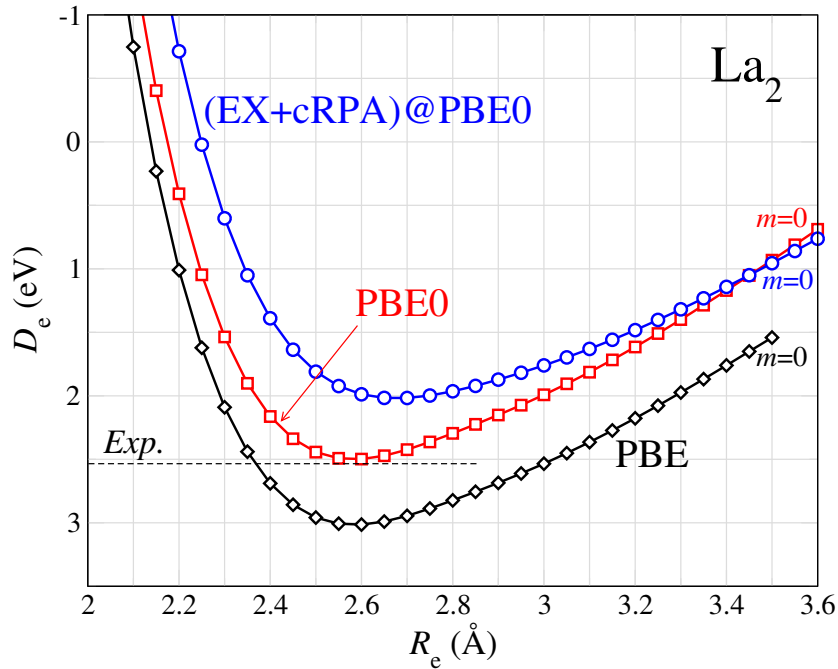


Figure 9.5: PBE, PBE0, and (EX+cRPA)@PBE0 binding energy, D_e , for La_2 . The magnetic moment is identified by m , and placed next to the curves (in units of μ_0).

In Figure 9.5 the binding energy curve of PBE, PBE0 and (EX+cRPA)@PBE0 is reported for the lanthanum dimer. The curves are smooth and they are all characterized by the absence of magnetic moment, even if the calculations include spin polarization. From all the three functionals we obtain similar equilibrium

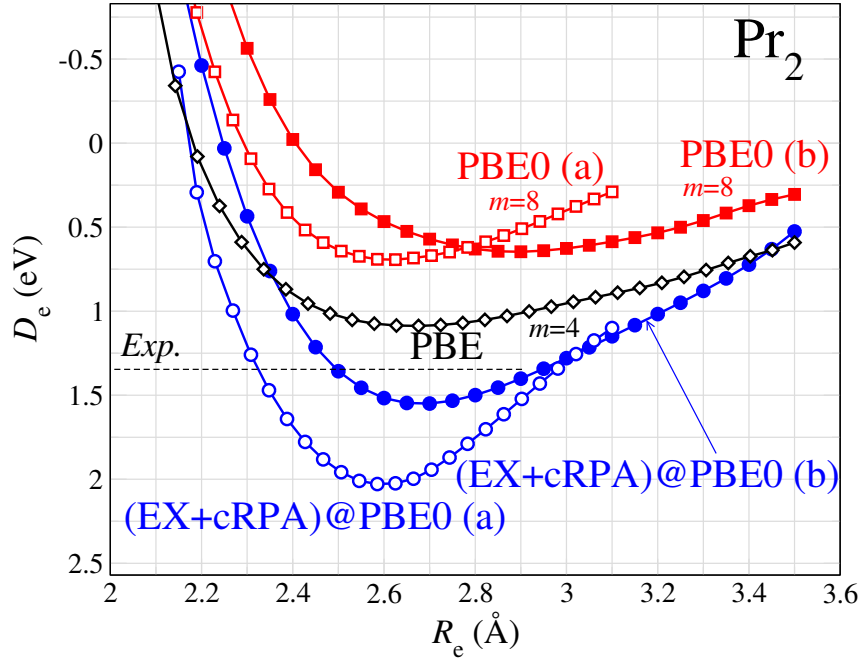


Figure 9.6: PBE, PBE0, and (EX+cRPA)@PBE0 binding energy, D_e , for Pr_2 . The magnetic moment is identified by m , and placed next to the curves (in units of μ_0). Two solutions are present in PBE0, denoted by (a) and (b).

distance, bonding energy and vibrational frequency, and PBE0 gives a D_e and a vibrational frequency in good agreement with experiment –Table 9.2. The EX+cRPA correction reduces the cohesive energy by 0.52 eV, on the other hand moves the bond length to 2.67 Å, closer to the value reported by quantum chemistry calculations –2.70 Å [100]–, the reference method in this case.

The calculations for the praseodymium dimer confirm the existence of multiple solutions for PBE0 in the presence of f electrons, Figure 9.6. Similarly to Ce_2 , the two solutions are stable at different bond lengths, and are close in energy. The magnetic moment is however considerably increased with respect to the cerium dimer. Also the effect of the EX+cRPA correction is sensibly increased. Both solutions have larger binding energy in (EX+cRPA)@PBE0 with respect to PBE0. This could be related to a not good description of the dimer structural properties in PBE0, Table 9.2. It is difficult to understand which of the two (EX+cRPA)@PBE0 solutions would correspond to the experimental configuration. The binding energy of solution (b), 1.56 eV, is in better agreement with the experimental 1.31 eV, however, solution

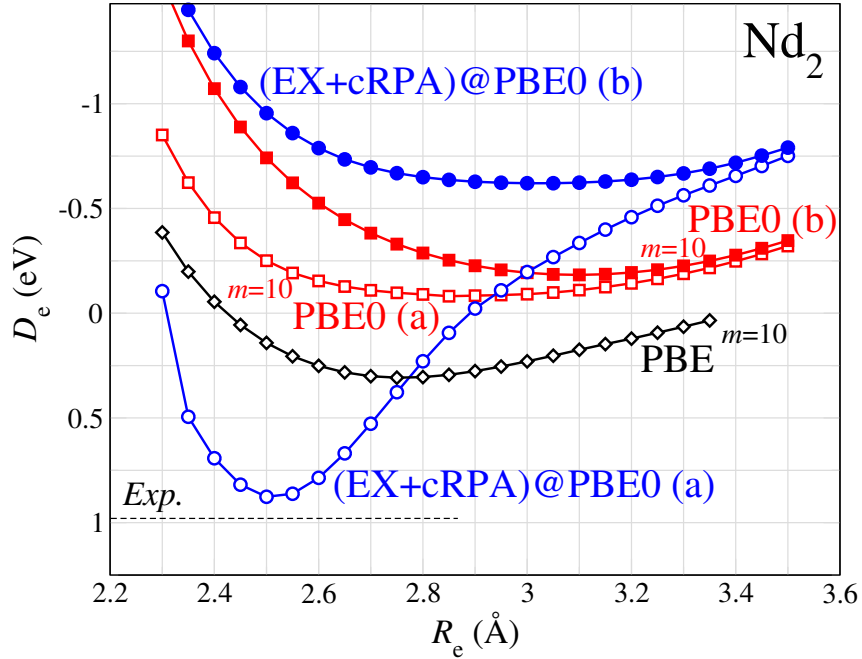


Figure 9.7: PBE, PBE0, and (EX+cRPA)@PBE0 binding energy, D_e , for Nd_2 . The magnetic moment is identified by m , and placed next to the curves (in units of μ_0). Two solutions are present in PBE0, denoted by (a) and (b).

(a) has a vibrational frequency -249 cm^{-1} that is closer to the observed 245 cm^{-1} .

PBE, PBE0, and (EX+cRPA)@PBE0 calculations on Nd_2 preserve previously observed features. PBE0 is characterized by two solutions which are stable at different bond lengths and are close in energy. All functionals produce small vibrational frequencies, in agreement with the softening of the vibrational modes observed in experiment, Table 9.2. Only exception is the (EX+cRPA)@PBE0 (a) solution. For Nd_2 , the difficulties of PBE0 and PBE in reproducing the correct equilibrium distance, bonding energy and vibrational frequency is probably further accentuated with respect to Pr_2 . The EX+cRPA correction tries to overcome this deficiency and results in a binding energy of 0.88 eV for solution (a), to be compared with the experimental 0.82 eV. However, this brings to a large vibrational frequency of 324 cm^{-1} , while the measured value is 93 cm^{-1} .

The PBE0 description of the dimer spectral constants worsens with increasing number of f electrons. However, the orbital charge density obtained from PBE0 preserve specific features across the elements. The charge density of the highest

occupied orbitals for La_2 , Pr_2 , and Nd_2 is reported in Figure 9.8. It refers to the spin up electrons. Each orbital is occupied by one electron. For all the three dimers the highest spin down orbitals are two $5d\pi_u$ and one $6s\sigma_g$ states. This means that the value of the magnetic moment for each configuration is obtained by subtracting three to the number of rows in Figure 9.8. By comparing Figure 9.8 with Figure 5.6 we note that the stable configuration for Ce_2 is that of La_2 plus two f -type orbitals. The $5d\pi_u$ orbitals are also maintained for all the other solutions of Pr_2 and Nd_2 .

Solution (a) of the praseodymium dimer closely resembles solution (a) of cerium. The relative ordering of the orbitals changes, but the highest occupied states share the same characteristics. The additional f electrons in Pr are placed at lower energy. Their charge density is localized at the atomic positions, and their orbital shape reminds of the $4f$ atomic orbitals. As for cerium, the most relevant change from the (b) to the (a) solution of Pr_2 is that an f molecular orbital goes from the $4f\delta_g$ bonding configuration to the $4f\sigma_u$ antibonding state. In Nd_2 there are no f bonding states. This explains the much reduced binding energy with respect to the other dimers.

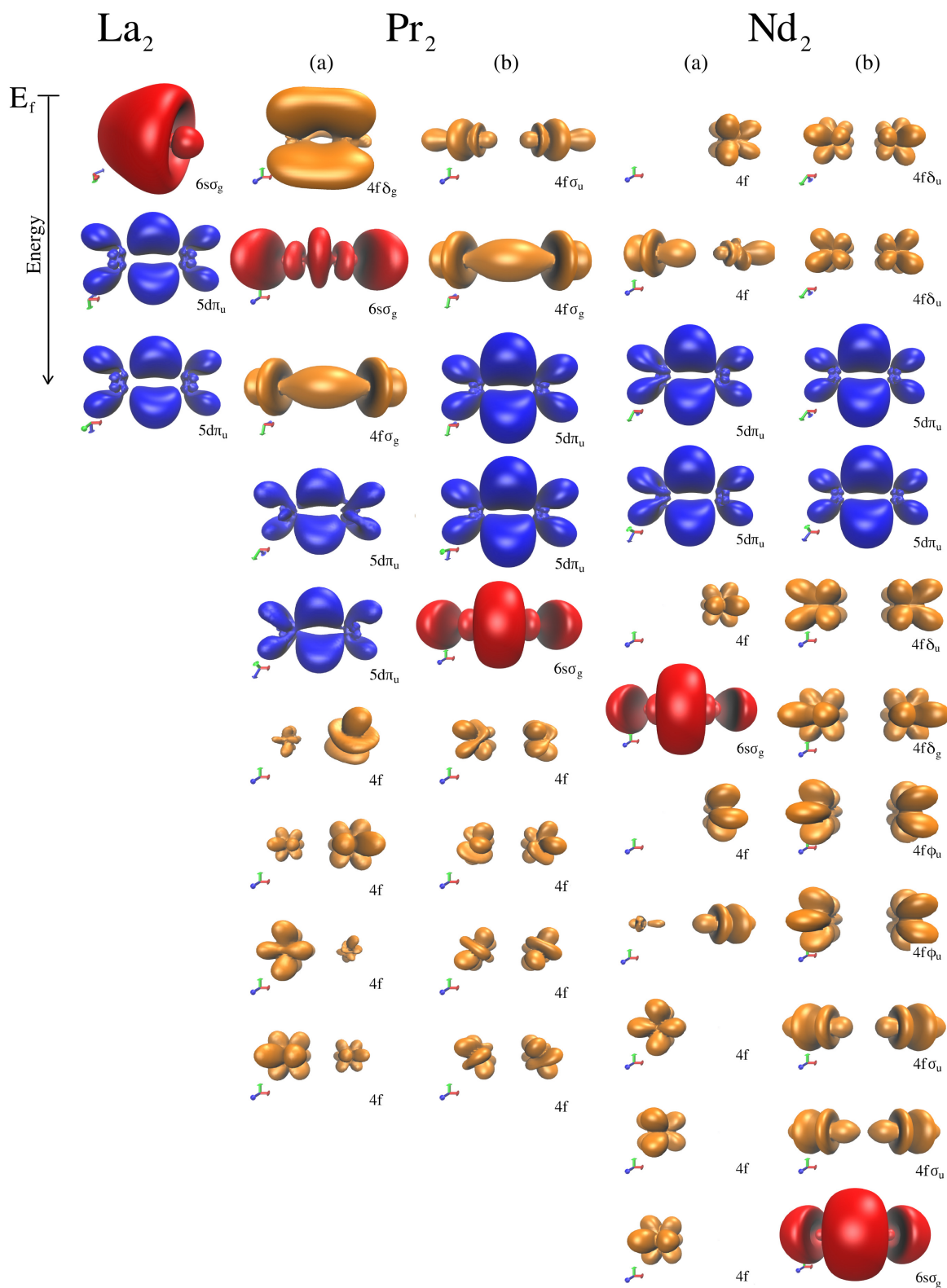


Figure 9.8: Charge density of the highest occupied spin up orbitals for the La, Pr, and Nd dimers.

Table 9.2: Equilibrium distance, bonding energy and vibrational frequency for the cerium dimer obtained from different levels of theory and from experiment. R_e represents the bond distance, D_e the binding energy and ω_e the vibrational frequency.

		R_e (Å)	D_e (eV)	ω_e (cm ⁻¹)
La ₂	PBE ^a	2.59	3.03	220
	PBE0 ^a	2.58	2.50	225
	(EX+cRPA)@PBE0 ^a	2.67	2.02	180
	B3LYP ^b	2.91	1.70	150
	CASSCF/MRCI ^c	2.70	2.31	186
	Exp. ^d	–	2.52	236
Pr ₂	PBE ^a	2.67	1.09	108
	PBE0 (a) ^a	2.61	0.70	153
	PBE0 (b) ^a	2.90	0.65	103
	(EX+cRPA)@PBE0 (a) ^a	2.61	2.03	249
	(EX+cRPA)@PBE0 (b) ^a	2.68	1.56	180
	CASSCF/MRCI ^c	2.55	1.19	213
	Exp. ^d	–	1.31	245
Nd ₂	PBE ^a	2.75	0.31	122
	PBE0 (a) ^a	2.87	-0.07	75
	PBE0 (b) ^a	3.11	-0.17	90
	(EX+cRPA)@PBE0 (a) ^a	2.51	0.88	324
	(EX+cRPA)@PBE0 (b) ^a	2.98	-0.61	73
	Exp. ^d	–	0.82	93

^aThis work.

^b[253]

^cReference [100].

^dReference [99].

9.3 SUMMARY

In this chapter we moved beyond cerium and we approached its neighbouring elements. We considered La, which has no f electrons, Pr, characterized by the presence of three $4f$ electrons and a volume collapse, and Nd, which has filled $4f$ states but does not undergo a phase transition.

For all the elements we performed the calculations in an fcc environment, that is believed to be representative of the various close packed structures in which the elements are found at different external conditions.

Hybrid functional calculations always predict the occurrence of multiple solutions in the presence of f electrons. The multiple solutions are a signal that the ground state assignment of the system can be difficult, and that the f electrons can arrange in several almost equivalent ways. Despite the presence of two stable configurations, no isostructural phase transition is found for Pr, in agreement with experiment. For Nd, instead, a double tangent can be traced between the two PBE0 solutions. At the level of HSE06 however, it is difficult to quantitatively examine the relative stability of the solutions. In this regard, we learned from cerium that the EX+cRPA correction is of crucial importance for a correct description of the energetic properties of the system. In addition, further calculations should be performed for the experimentally observed crystal structures. This constitutes a future step that we intend to accomplish.

Finally, we studied the La, Pr, and Nd dimers with (EX+cRPA)@PBE0. The multi-solution behavior is confirmed for Pr and Nd, but not for La. We note that the PBE0 description of the equilibrium distance, bonding energy and vibrational frequency progressively worsen with increasing number of f electrons. The EX+cRPA correction tends to overcome this deficiency, but the remarkable agreement of (EX+cRPA)@PBE0 with experiment that is found for the cerium dimer is not always reproduced in the other dimers. On the other hand, the electronic structure of the two solutions of Ce₂ finds specific trademarks in all other dimers, further proving the reliability of our approach.

10 SUMMARY AND OUTLOOK

10.1 THE α - γ PHASE TRANSITION

The presence of a phase transition accompanied by a volume collapse is one of the most intriguing features that characterizes rare earth metals. Due to its isostructural nature, the cerium α - γ phase transition is by far the most mysterious. Experimental characterizations of the α - γ phase transition have been carried out for many decades now, but only partial consensus on the physical properties of the two phases has been reached.

Different theoretical models have been proposed to address the driving mechanism of the volume collapse. The most notable are the Mott transition and the Kondo volume collapse, which highlight the role of f electrons. Recently, a symmetry breaking from the γ to the α phase has been suggested. This implies a quadrupolar alignment of the charge density from one phase to the other and does not exclude a change in hybridization of the f electrons suggested by the other models. However, all models only describe the physical phenomena that are explicitly included in the theory. Many studies approach the α - γ phase transition from *first principles*, avoiding *a priori* assumptions. These are mainly based on density-functional theory. Despite the effort, no study has been able to reproduce the structural properties of both the α and γ phases within a single theoretical framework and to understand the mechanism that dictates the volume collapse.

Motivated by the open challenge that the cerium α - γ phase transition poses to theoretical physicists, I approached the problem *ab initio*, in view of the newly-developed hybrid functionals PBE0 and HSE06 and many-body methods like EX+cRPA.

I studied cerium systems of increasing complexity, from the atom to bulk, and found that PBE0 and HSE06 always exhibit a multi-solution behavior. This behavior, a known feature of Hartree-Fock based calculations, has physical relevance for cerium, because the α and γ phases can be recognized in both bulk solutions. The analysis of the electronic density reveals, that hybrid functionals can indeed capture a change in the f electron wave functions around the region of the experimental α and γ lattice constants, and that it is not the only magnetic moment that discriminates the two solutions.

A proper description of the electronic screening among the electrons proved to be essential for a quantitative description of the phase transition. The already accurate description of the equilibrium distance, bonding energy and vibrational frequency for the cerium dimer is improved by incorporating exact-exchange and correlation at the level of the random-phase approximation. Likewise, EX+cRPA provides the correct energetic order for the two solutions in larger systems. Hybrid functional solutions show specific characteristics in all the systems under examination. I therefore performed (EX+cRPA)@PBE0 calculations for the Ce₁₉ cluster, because the higher-level, many-body methods are available in FHI-aims for finite systems. I found a transition pressure for the α - γ phase transition that is in agreement with the extrapolation of the experimental values to zero temperature. Based on my zero temperature results for the electronic structure I was able to reproduce the cerium phase diagram by adding entropic contributions in a pseudo-alloy model.

Due to the success with cerium, I tested this approach on other lanthanide elements with (La) and without (Pr, Nd) f electrons. The outcome of the calculations for the dimers and for bulk systems validated my results for cerium. The multi-solution behavior only appears in conjunction with the presence of f electrons. Moreover, hybrid functionals predict no isostructural phase transition for Pr and Nd, as observed experimentally.

Hybrid functional results appear consistent with a Mott transition scenario, in particular, with the Mott interpretation of localized and delocalized f states in the γ and α phases, respectively. However, we know that the transition is complex, and different mechanisms may cooperate. These results do not rule out the importance of Kondo physics at finite temperatures. They suggest, rather, that the driving

mechanism of the volume collapse should already occur at zero temperature, and therefore could be more directly related to the hybridization between f states. At the same time, these conclusions do not exclude a quadrupolar charge density alignment in the α phase. My work emphasizes the importance of *ab initio* methods. Models are important, as they can aid the interpretation of scientific results and suggest physical processes to include in our theories. However, to have an unbiased description of complex phenomena such as the α - γ phase transition, we need to start from *first principles*.

10.2 FUTURE DIRECTIONS

10.2.1 THE CERIUM DIMER

One unexpected result that emerged during the course of this thesis is the presence of a scale-spanning volume collapse – from the macroscale of bulk cerium to the nanoscale, in particular the cerium dimer. (EX+cRPA)@PBE0 calculations for the dimer produce an equilibrium distance, a bonding energy and a vibrational frequency for the ground state that are in agreement with experiment. This implies that my calculations predict that the cerium dimer should be stable in two different bond lengths at low enough temperatures. So far, this has not been observed experimentally nor have other theoretical studies addressed it. Similarly, the large Ce_{19} and Ce_{43} clusters that I investigate display similar characteristics. I did, however, constrain these two clusters to an fcc geometry, and it is not clear if the double minimum is still present after a full geometric relaxation. Thus, three important questions emerge. First, is the volume collapse present at the nanoscale, and second, can it be observed experimentally? Third, if the volume collapse cannot be found for the smallest clusters, at which cluster size approaching the macroscale will it set in?

To address these questions, we began a collaboration with Prof. Wöste's research group at the Freie Universität in Berlin. A joint funding project has been submitted to the German Science Foundation (DFG) and is currently under review. The first objective of the project is to map the potential energy surfaces of the cerium dimer experimentally and to test if two stable solutions (i.e., a bond-length

isomer) do indeed exist. For the experimental setup, the neutral as well as charged dimers are required to mass-select the dimers from the initial laser vaporization or sputtering source. My (EX+cRPA)@PBE0 calculations show that the ionic species also have two stable solutions (cf Fig. 10.1). The minima are deep enough to capture at least one vibrational mode and should therefore be stable enough for experimental detection. However, the barrier between the left and the right solution of the neutral dimer is relatively small. This might be an artifact of the (EX+cRPA)@PBE0 approach. To test this, higher-level theories should be applied to the ground state potential energy surface of the cerium dimer.

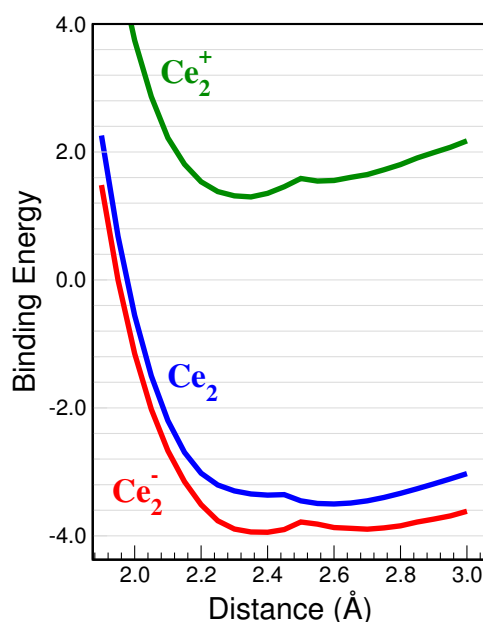


Figure 10.1: (EX+cRPA)@PBE0 binding energy of the cerium dimer in different charge states. The two bond-length isomers are conserved even when the dimer is positively or negatively charged (red and green curves).

A second goal of the proposed DFG project is to establish an optical link between the different bond-length isomers such that, depending on the irradiated light fields, the pathway can be switched toward one or the other bond-length isomer. This assumes that optically-excited states (gray curves in Figure 10.2 –only plotted as guides for the eye, not calculated) facilitate a transition from one minimum to another. To achieve the optical link, the anionic dimers would be irradiated with a series of electronic excitations, which could finally lead to the cationic electronic

ground state of the chosen isomer – Figure 10.2 a). Alternatively, the pathway to the desired isomer could also be directed to the electronic ground state of the corresponding neutral species, as shown in Figure 10.2 c).

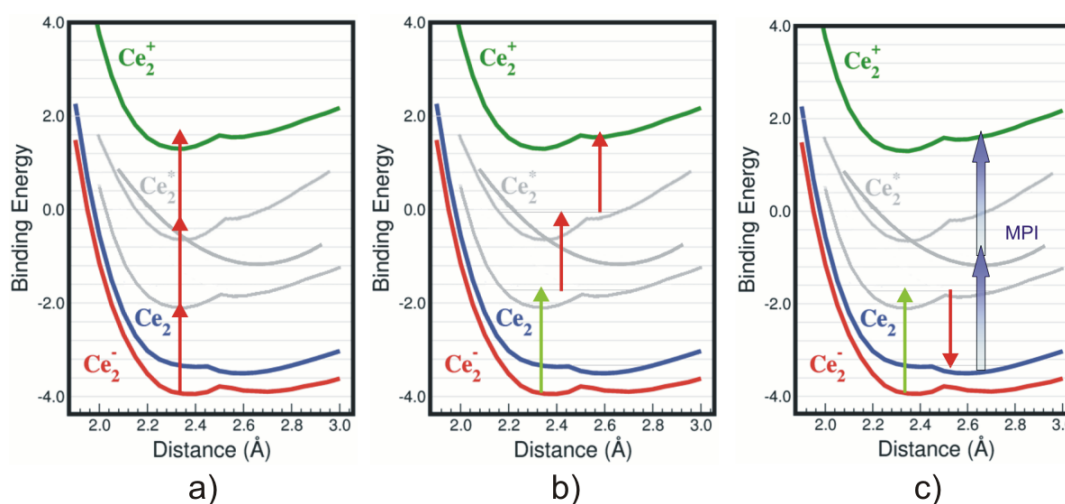


Figure 10.2: Experimental concept for connecting different bond-length isomers via sequenced electronic excitation by irradiating optimized pulse sequences: a) connects the isostructural transition from the anion to the cation vertically, b) connects one bond-length isomer of the anion to the other of the cation, c) connects one bond-length isomer of the anion to either one of the neutral ground states, which then is monitored by a multi-photon ionization (MPI) step to the cation. The gray curves are guides for the eye, not calculated.

If the first two goals can be accomplished, then larger clusters could be explored. Subsequently, the highly-reactive cerium clusters could be embedded within a flexible and transparent ligand shell that would passivate them without losing their optomechanical function. This would pave the way for new and unique nanotools. For example, optically-switchable length actors are conceivable if the passivated clusters could be assembled as nanotowers. If grouped as rings around nanocapillaries, they could act as optically-activated valves or peristaltic pumps.

10.2.2 THE VOLUME COLLAPSE

My spin unpolarized hybrid functional calculations for cerium bulk demonstrate that the emergence of the two solutions is connected to a change in the wave functions. In addition, the charge density difference between the solutions shows that there are

preferred directions along which the f electron density tends to align. One future goal is therefore to increase the dimension of the unit cell. This would allow the system to explore more degrees of freedom in the quantum mechanical calculations and might provide the first *ab initio* indication for the quadrupolar symmetry of the charge density suggested by Nikolaev *et al.* [62].

Further, whether other crystal structures of cerium, like double hcp, also exhibit a double minimum is an interesting area of research. This may reveal more about the behavior of f electrons in lanthanides. The relative stability of the β phase with respect to the α and γ phases also creates further benchmarking opportunities for our computational approaches. In my study, I assumed that the change from the γ to the β phase is mainly driven by the rearrangement of $5d$ electrons. Additional calculations could test this hypothesis.

10.2.3 OTHER LANTHANIDES

In the last part of my thesis, I present preliminary calculations for three other lanthanide elements. I chose lanthanum (no f electrons), praseodymium (3 f electrons) and neodymium (34 f electrons). For simplicity, I restricted my calculations to fcc structures and did not consider the other, close-packed crystal structures that these metals adopt. In principle, this should provide a reasonable first estimate, since fcc is itself close-packed, and the physics behind the f electrons should also be captured in a slightly different crystal environment. However, we know that several factors contribute to the structural properties of the system in lanthanide elements. A possible future step is therefore to perform hybrid functional and EX+cRPA calculations for other crystal structures. Then the study should be extended to the whole lanthanide series to develop a comprehensive picture of the $4f$ metals. An interesting remaining question is why some of the lanthanide elements display a volume collapse and others do not? *Ab initio* calculations across the lanthanide series could illuminate this fascinating problem.

Appendices

A CRYSTAL STRUCTURES

The *rare earth* metals are characterized by some complex crystal structures. Other than the fcc and hcp structures, the most relevant ones are double-hcp (dhcp), distorted fcc (d-fcc) and α uranium (α -U). As they do not belong to spacegroup representations, they are schematized in Figure A.1, A.2, A.3.

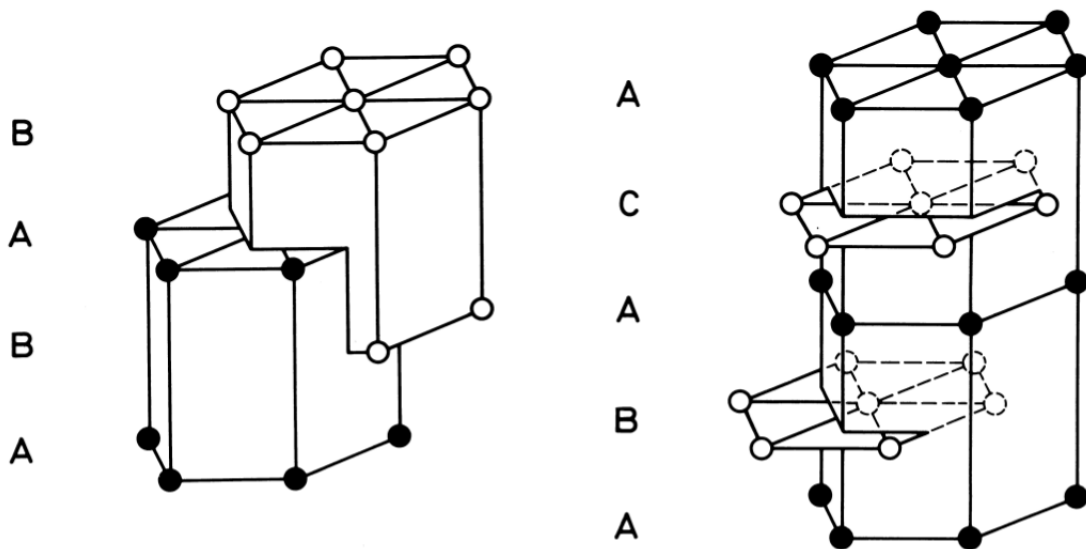


Figure A.1: The hcp and dhcp crystal structures. In the latter, the unit cell is doubled. The second *B* plane is rotated, and becomes a third *C* plane. From [254].

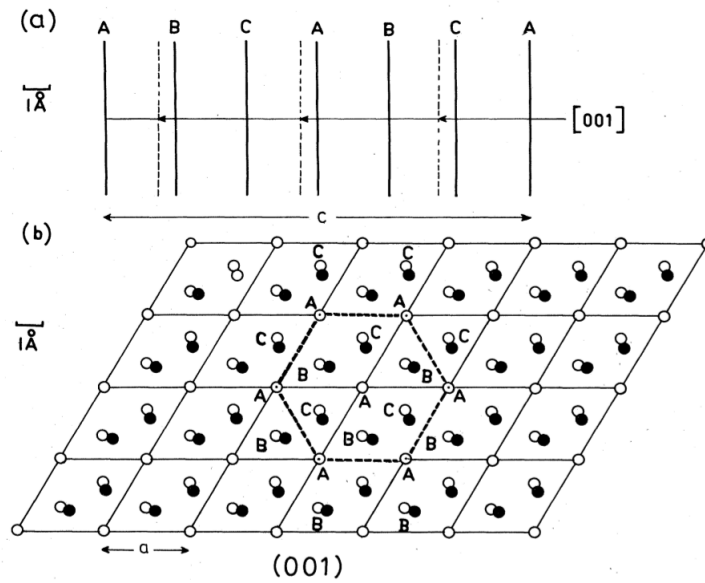


Figure A.2: The d-fcc structure is put in relation to the fcc structure by: a) Periodic modulation of the hexagonal layers along the c axis: dashed lines represent d-fcc positions. b) The relative shifts of the hexagonal layers in the basal plane. The B and C layers are sheared with respect to A layer, the dhcp atom positions are indicated by filled circles. From [255].

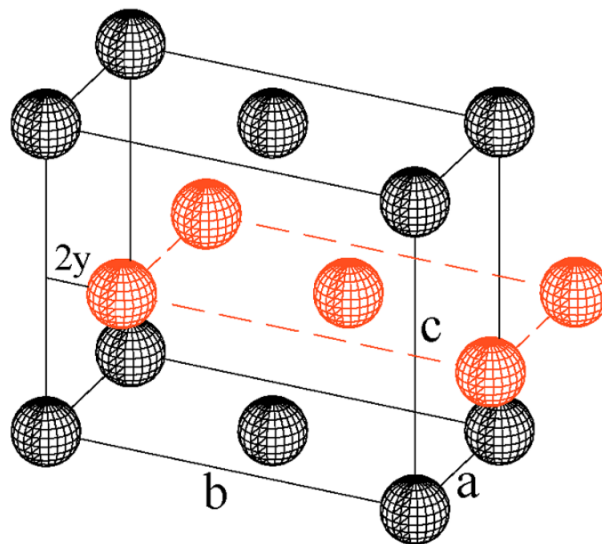


Figure A.3: The α -U structure is put in relation to the fcc structure by a distortion of the cubic environment and a shift of the plane containing the face-centered atoms. From [256].

B COMPUTATIONAL DETAILS

B.1 NUMERICAL ATOM CENTERED ORBITALS

All calculations in this thesis were performed with the all-electron code FHI-aims (Fritz-Haber-Institut ab initio molecular simulation) [220, 221], that is based on numeric atom-centered orbitals.

To solve the quantum mechanical equations numerically, a basis set has to be introduced. The optimal choice would be to work with a basis set that spans the full Hilbert space, but this is not possible in practice. Instead, in the FHI-aims package numeric atom centered orbitals are used as basis functions¹.

For better computing performances the FHI-aims code utilizes numerical atom centered orbitals (NAOs) of the form

$$\phi_n = \frac{u_n(r)}{r} Y_{lm}(\Omega) \quad (\text{B.1})$$

where the basis function ϕ_n consists of a radial part $u_n(r)$ and an angular part which is given by the spherical harmonics $Y_{lm}(\Omega)$. The functions $u_n(r)$ are obtained by a numerical solution of a one-dimensional radial Schrödinger equation

$$\left[-\frac{1}{2} \frac{d^2}{dr^2} + \frac{l(l+1)}{r^2} + v_{\text{shape}}(r) + v_{\text{cut}(r)} \right] u_n(r) = \epsilon_n U_n(r) \quad (\text{B.2})$$

where l is the angular quantum number. The potential v_{shape} determines the main shape of $u_n(r)$ and v_{cut} is a confining potential. The latter ensures that the wave

¹Refer to [257] for a review of different basis sets that can be employed in HF and KS-DFT.

function $u_n(r)$ smoothly decays to zero outside a defined region $r \geq r_{\text{cut}}$ and it can be expressed in the form

$$v_{\text{cut}}(r) = \begin{cases} 0 & r \leq r_{\text{onset}} \\ \frac{s}{(r-r_{\text{cut}})^2} e^{\frac{w}{r-r_{\text{onset}}}} & r_{\text{onset}} < r < r_{\text{cut}} \\ 0 & r \geq r_{\text{cut}} \end{cases} \quad (\text{B.3})$$

where s and w are global scaling parameters, and r_{onset} determines the onset of the exponential part of v_{cut} .

Systematic basis sets have been constructed according to equations B.2 and B.3 with the following procedure:

1. Constructing a functional dependent minimal basis for the free atom by setting v_{shape} to the self-consistent radial part of the KS potential².
2. Generating a pool of additional basis functions by solving Equation B.2 for various choices of v_{shape} . In FHI-aims these are hydrogen-like, atom-like or cation-like potentials.
3. From the generated pool of additional functions select the ones that contribute most to a pre-defined objective function. In FHI-aims the objective function is the LDA total energy of a di-atomic dimer for a given species.

The additional basis functions obtained in step 3 are grouped together in ‘‘tiers’’, that for the case of cerium, praseodymium, and neodymium are summarized in Table B.1. Once the radial part of the basis function is constructed, its three-dimensional form is obtained by multiplication of $2l + 1$ angular momentum functions, according to Equation B.1.

²See reference reference [221] for HF or hybrid functionals.

Table B.1: Standard radial basis functions for Ce, Pr, Nd. The minimal basis consists of free atom radial functions (notation: [noble gas configuration] + additional valence functions). The additional radial functions are of the form $H(nl, z)$ or $X^{2+}(nl)$. $H(nl, z)$ denotes a hydrogen-like radial function for the Coulomb potential $v_{\text{shape}}(r) = z/r$, in Equation B.2, with quantum numbers n and l . $X^{2+}(nl)$ labels the n, l function for the doubly positive charged ion X.

	Ce	Pr	Nd
minimal	[Xe]+6s5p5d4f	[Xe]+6s5p5d4f	[Xe]+6s5p5d4f
tier 1	H(4d, 4.8) H(5g, 11.2) H(4f, 7.6) H(2p, 1.8) H(3s, 2.7)	H(3d, 4.9) H(2p, 1.3) H(4f, 8) H(5g, 11.2) Pr ²⁺ (6s)	H(3d, 5) H(5g, 11.2) H(4f, 7.6) H(2p, 1.4) H(3s, 2.6)
tier 2	H(6h, 14.8) H(4f, 5.2) H(3d, 3) H(3d, 2.2) H(5g, 11.6) H(3p, 2.8) Ce ²⁺ (6s)	H(4f, 4) H(6h, 15.2) H(4d, 3.4) H(5g, 7.2) H(2p, 1.6) H(4s, 3.0)	H(4f, 4.3) H(6h, 15.6) H(3d, 3) H(2p, 2) H(5g, 8.6) H(4s, 3.6)
tier 3	H(6h, 15.2) H(4f, 8.2) H(5g, 30) H(6d, 16.4) H(5f, 15.6) H(5p, 17.6) H(4s, 7.2)	H(5d, 12) H(4f, 6.2) H(5g, 14.4) H(6h, 14.4) H(5p, 8.8) H(5s, 6.0)	H(4d, 14) H(6h, 12.4) H(4f, 6.6) H(5g, 24.8) Nd ²⁺ (6p) H(1s, 0.75)
tier 4	H(5g, 20) H(4f, 16.4) H(6d, 20) H(6p, 9.2) H(1s, 0.85) H(6h, 14)	H(5f, 15.6) H(4d, 19.2) H(5g, 36) H(3d, 1.5) Pr ²⁺ (4f) H(5g, 16.4) H(5f, 16.4) H(6p, 18)	H(6d, 18.8) H(5f, 16) H(4p, 6) H(5g, 4.9) H(3d, 4.2) H(6h, 16) H(5g, 12) H(4s, 6.8)

B.2 BASIS SET SUPERPOSITION ERROR

Localized basis functions such as NAOs are subject to a problem known as basis set superposition error (BSSE) [258]. When the atoms of a system approach each other their basis functions overlap. The result is that each atom feels a larger basis set than in the isolated configuration. This can be the source of several problems. For example for the cohesive energy versus volume curve the effective number of basis functions that are available to the atoms vary with the distance between them. Since the Hilbert space is not complete the denser basis functions lead to more negative total energies. Consequently obtaining reliable values for the total energy becomes difficult.

In the FHI-aims code, the BSSE is efficiently reduced for LDA/GGA and HF calculations [220], because the NAOs minimal basis is exact for the free atom for LDA/GGA functionals and it is nearly optimal for the description of the Kohn-Sham core orbitals. Only the contribution coming from the valence orbitals has to be compensated, but its effect is minimal on the total energy and the BSSE can be neglected. However, for methods that extensively involve a description of empty states, like RPA, rSE and SOSEX, the BSSE can be severe and needs to be properly taken into account.

In order to eliminate or partially remove the BSSE several methods have been developed. One that is computationally effective, and has been the method of choice in this thesis, is commonly referred to as counterpoise correction (CC). The CC was suggested by Boys and Bernardi [259] and amounts to an *a posteriori* BSSE correction. The reference atomic energies are computed in a basis set that corresponds to the one of the full system, so that the cohesive energy arises from a difference between total and reference atomic energies that are expressed in the same basis set. In practice the cohesive energy E_{coh}^{BSSE} is calculated according to the following expressions

$$E_{\text{coh}}^{BSSE} = E_{\text{coh}} + \Delta_{\text{CC}} \quad (\text{B.4})$$

where

$$E_{\text{coh}} = - \left[E^{\text{sys}}(\text{sys}) - \sum_{\text{atom}} E^{\text{atom}}(\text{atom}) \right] \quad (\text{B.5})$$

and

$$\Delta_{\text{CC}} = - \sum_{atom} [E^{atom}(atom) - E^{atom}(sys)]. \quad (\text{B.6})$$

Here $E^x(y)$ represents the total energy of system x in the basis set of y . sys and $atom$ represent the whole system and the single atoms, respectively. With the CC method the BSSE is avoided and the dependence of the results on the basis set only determines the overall accuracy of the calculations.

B.3 CONVERGENCE WITH RESPECT TO THE BASIS SET

In DFT and related methods using the largest basis set available is of course the desirable way of approximating the full Hilbert space. In practice, however, one has to carefully measure the computational resources (i.e. cpu time and memory requirements) dedicated to the calculations. In general a large basis set also implies large computational requirements and a balance between accuracy and computational constraints has to be found for each individual system. The usual way of proceeding is to systematically increase the number of basis functions until the quantities of interest do not vary any more.

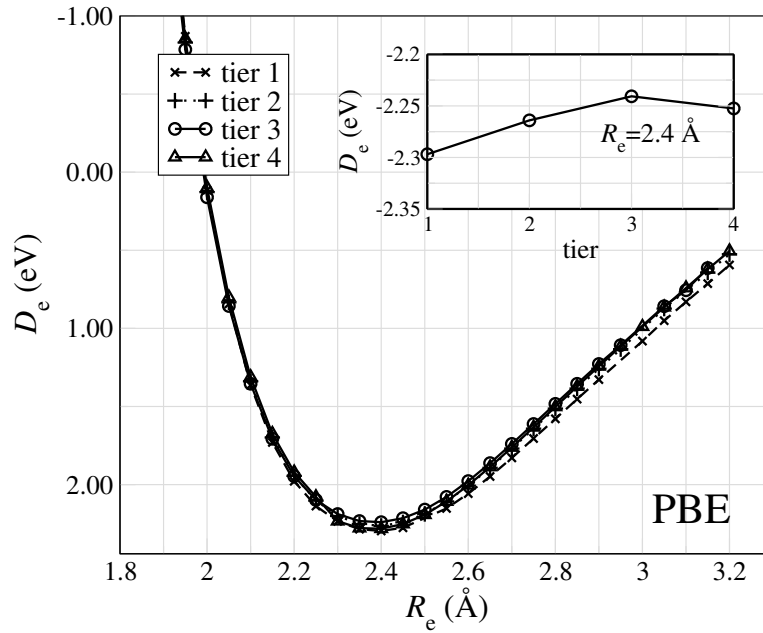


Figure B.1: Cohesive energy for the cerium dimer calculated with the PBE spin unpolarized approach.

For the case of a cerium dimer, Figure B.1, B.2, B.3, B.4 show the change in binding energy upon increasing the number of basis functions by adding subsequent tiers. The convergence tests are separately performed for different functionals and all refer to spin unpolarized calculations³.

³In RPA calculations a total of 100 frequency points for the Fourier transform are considered.

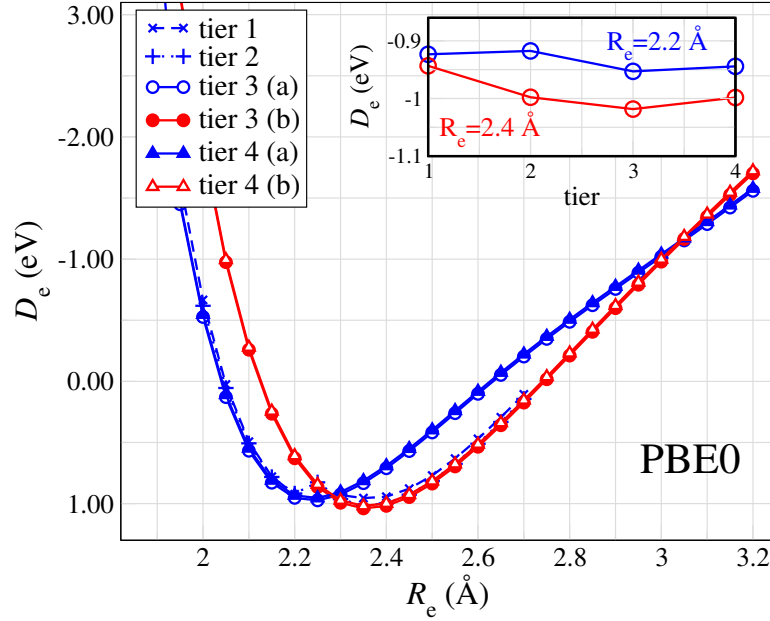


Figure B.2: Cohesive energy for the cerium dimer calculated with the PBE0 spin unpolarized approach.

As it shown in the plots, already the additional tier 1 basis set provide good convergence with respect to the basis functions, and adding tier 2 and tier 3 does not change appreciably the cohesive energy results for PBE and PBE0. In particular at tier 2 one could safely consider the calculations converged with respect to the basis set. A similar result is obtained when the EX+cRPA correction is applied on top of PBE0. For the case of (EX+cRPA)@PBE it would seem that for small distances the convergence with respect to the basis set has not yet been achieved, in view of the other results however it is more likely that other effects are entering the problem. As analyzed in Section 5.2 (EX+cRPA)@PBE calculations have, in fact, a singular outcome, and need caution in the interpretation.

Calculating the cohesive energy for other cerium clusters and for the bulk system with increasing number of basis functions confirms the results obtained for the dimer: the tier 1 additional basis set already provides a sufficient number of basis functions and at tier 2 the cohesive energy of the system is converged to within 30 meV.

See Section B.2 for an explanation of the frequency points usage.

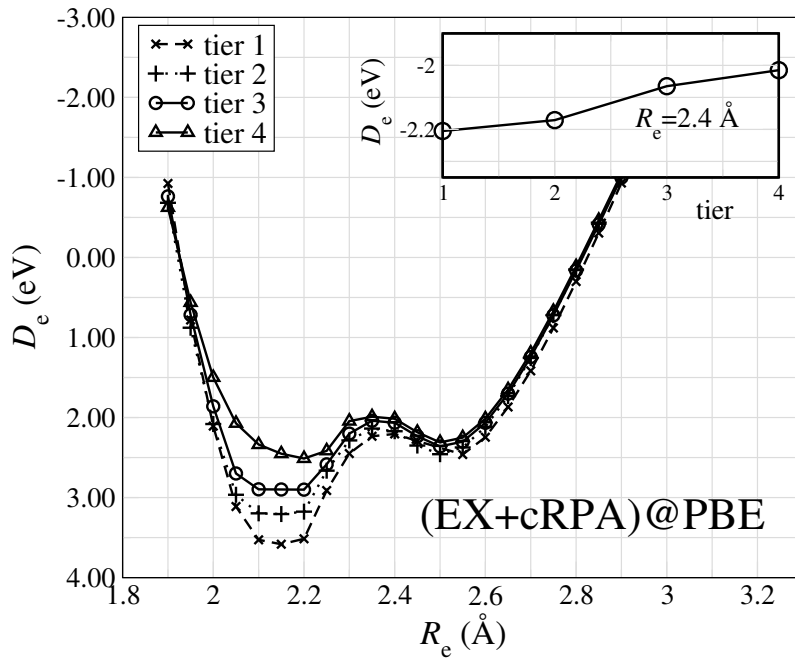


Figure B.3: Cohesive energy for the cerium dimer calculated with the (EX+cRPA)@PBE spin unpolarized approach.

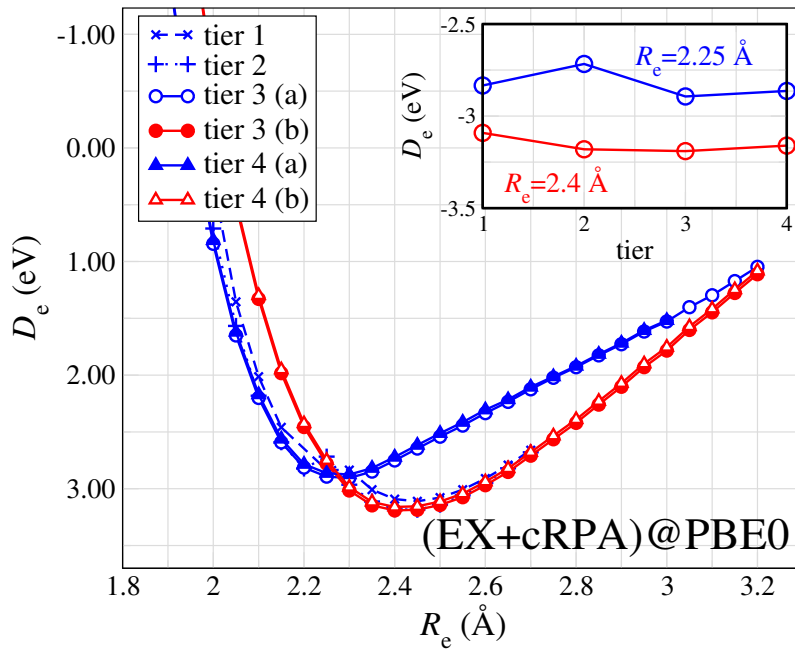


Figure B.4: Cohesive energy for the cerium dimer calculated with the (EX+cRPA)@PBE0 spin unpolarized approach.

B.4 CONVERGENCE WITH RESPECT TO THE FREQUENCY POINTS

The frequency integration in the EX+cRPA correction in Equation 2.64 is performed, in the FHI-aims code, on a Gauss-Legendre grid. As for the basis functions, a larger number of frequency points leads of course to more accurate results, but also to an increased computational cost.

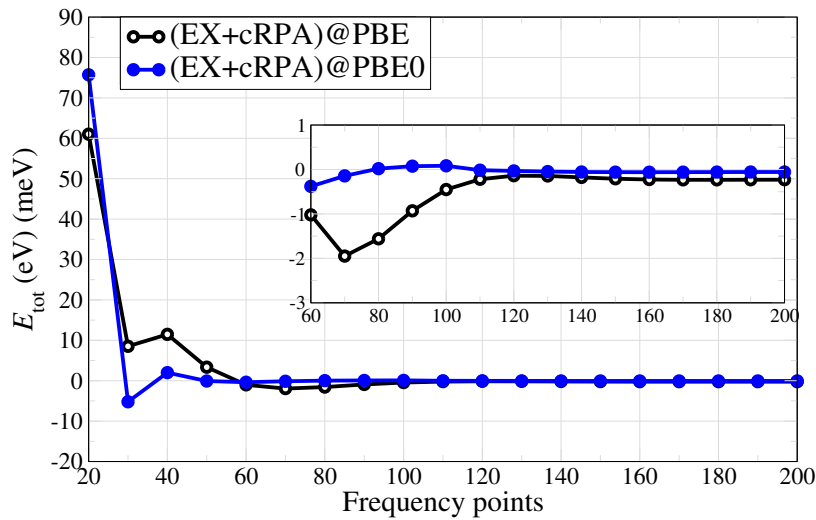


Figure B.5: Total energy as a function of the frequency points employed in the RPA frequency integration. The total energy is arbitrarily shifted to set the result for 200 points to zero. Inset: same plot with a higher resolution on the energy axis.

In Figure B.5 the convergence of the EX+cRPA correction with respect to the frequency points is reported for the cerium dimer. The spin is unpolarized, tier 3 basis functions are included, and the distance between the atoms is set to 2.4 Å, which is next to the minimum of the PBE0 (b) solution. Figure B.5 shows that 60 points are sufficient. At 60 points the (EX+cRPA)@PBE total energy is converged within 2 meV and the (EX+cRPA)@PBE0 total energy within 0.3 eV. The calculations reported in Section 5.2 and 5.6 for the dimer are performed at 100 frequency points, where (EX+cRPA)@PBE0 results are converged within 0.15 meV. For the case of the Ce₁₉ cluster, see Section 6.2, the number of points could not be increased above 40 due to computational reasons. While this value seems only

acceptable for the case of PBE, one should note that, for the dimer, the same value brings (EX+cRPA)@PBE0 results into a convergence window of 2 meV.

B.5 k -point CONVERGENCE

For periodic calculations one has also to converge the sampling of the first Brillouin zone in reciprocal space. Figure B.6 shows the convergence of the cohesive energy of bulk cerium with respect to the number of points that are considered along each of the three directions k_x , k_y , k_z of reciprocal space. Both PBE and HSE06 calculations are performed for a spin unpolarized configuration and at a lattice constant of 4.6 Å.

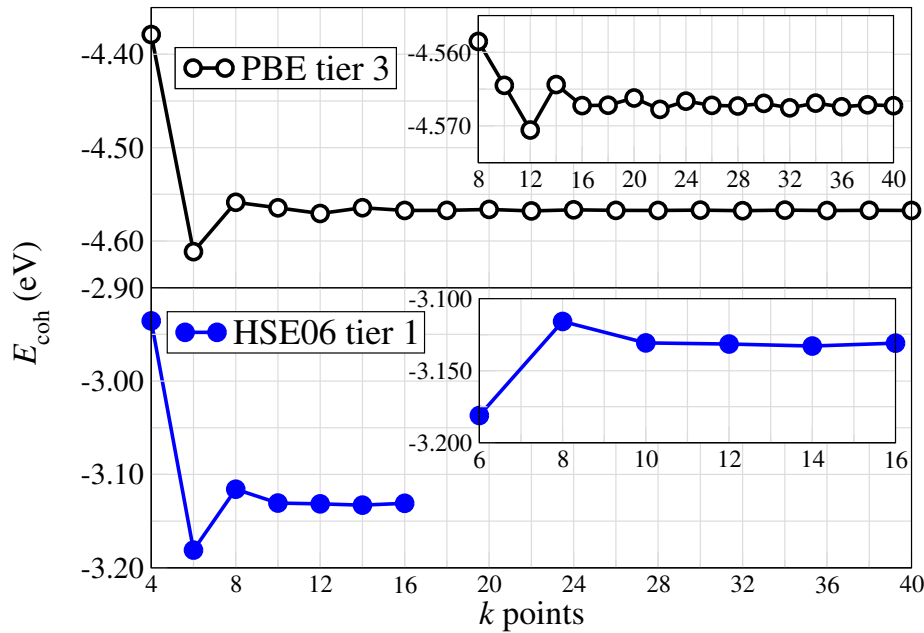


Figure B.6: Cohesive energy as a function of the k points employed to sample the first Brillouin zone. The number of k points refers to one direction in the reciprocal space. The total number of points is therefore k^3 . The insets report part of the curves with a higher resolution on the energy axis.

At $10 \times 10 \times 10$ k points PBE results are converged to within 10 meV, while the value of the cohesive energy in HSE06 does not vary by more than 2 meV if the k sampling is increased further to a $16 \times 16 \times 16$ mesh. Moreover, it is interesting to

note that the convergence with respect to the k sampling is largely determined by the PBE part of the calculations because, as depicted in Figure B.7, the Hartree-Fock exact exchange contribution that is introduced in the hybrid functional displays a very rapid convergence. From a $4 \times 4 \times 4$ to a $16 \times 16 \times 16$ sampling the HSE06 cohesive energy oscillates within a 15 meV range. For most of the calculations performed during this thesis a $6 \times 6 \times 6$ mesh was therefore chosen for both PBE and hybrid functional calculations.

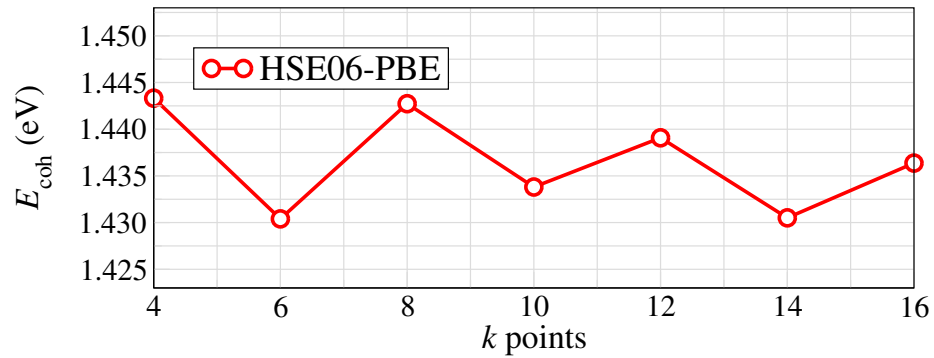


Figure B.7: Difference between the cohesive energy as calculated within PBE and HSE06 plotted with respect to the number of k points employed in the sampling of the first Brillouin zone.

PUBLICATIONS RELATED TO THIS THESIS

1. **Marco Casadei**, Xinguo Ren, Patrick Rinke, Angel Rubio, and Matthias Scheffler, *Density-Functional Theory for f -Electron Systems: The α - γ Phase Transition in Cerium*, Phys. Rev. Lett. **109**, 146402 (2012), [DOI](#).

CURRICULUM VITÆ

For reasons of data protection,
the curriculum vitae is not included in the online version

ACKNOWLEDGEMENTS

My biggest thanks to Prof. Matthias Scheffler for the great opportunity to work in his department. The years I spent at the FHI have been of great help for the development of my scientific and personal life. Many thanks to Prof. Angel Rubio, who guided me through the difficulties and supported me with his never ending ideas. Special thanks to Patrick Rinke for the careful and patient supervision, and to Xinguo Ren for his constructive help. I thank Joachim Paier for the sharp advice in crucial times, and Viktor Atalla for the unforgettable support during the writing of this manuscript. I thank my colleagues and friends who followed day by day the growth of this project. Thanks to: Andrea, Eli, Fabio, Mariana, Mathis, Matteo, Nicola, Oliver, Wael. Many thanks to the people from the ETSF and the San Sebastian group, who enriched this important experience with a productive and friendly environment. Sincere thanks to Prof. Armando Trottole and to Prof. Fabio Ortolani, without whom all of this would not have been possible. Thank to all the people that lived with me these Berlin years and that I will never forget, and to all those who have supported me from afar. Thank to my family. To Beatrice and Agata, who reminded me of the right way to go.

Grazie a tutti. Per davvero. Siamo alla fine. E ho perso l'inizio. Ma ho un senso in più.

BIBLIOGRAPHY

- [1] B. Johansson, “The α - γ transition in cerium is a Mott transition,” *Philos. Mag.*, vol. 30, pp. 469–482, Sept. 1974.
- [2] J. Allen and R. Martin, “Kondo Volume Collapse and the γ - α Transition in Cerium,” *Phys. Rev. Lett.*, vol. 49, pp. 1106–1110, Oct. 1982.
- [3] M. Lavagna, C. Lacroix, and M. Cyrot, “Volume collapse in the Kondo lattice,” *Phys. Lett. A*, vol. 90, pp. 210–212, July 1982.
- [4] a.V. Nikolaev and K. Michel, “Quantum charge density fluctuations and the phase transition in Ce,” *Europ. Phys. J. B*, vol. 9, pp. 619–634, July 1999.
- [5] A. K. McMahan, C. Huscroft, R. T. Scalettar, and E. L. Pollock, “Volume-collapse transitions in the rare earth metals,” *J. Comp.-Aid. Mat. Des.*, pp. 131–162, 1998.
- [6] G. Haxel, J. Hedrick, and G. Orris, “Rare Earth Elements: Critical Resources for High Technology,” *USGS Fact Sheet*, vol. 87, p. 2, 2012.
- [7] U. Benedict, “Pressure-induced phase transitions in 5f and 4f metals and compounds,” *J. Alloys Comp.*, vol. 193, pp. 88–93, 1993.
- [8] M. S. S. Brooks, B. Johansson, H. L. Skriver, A. J. Freeman, and G. H. Lander, *Handbook on the Physics and Chemistry of the Actinides*. North-Holland, Amsterdam, 1984.
- [9] D. C. Koskenmaki and K. A. Gschneidner, *Handbook on the Physics and Chemistry of Rare Earths*. North-Holland, 1978.
- [10] J. Olsen, L. Gerward, U. Benedict, and J. Itié, “The crystal structure and the equation of state of cerium metal in the pressure range 0–46 GPa,” *Physica B+C*, pp. 129–137, 1985.
- [11] H. K. Mao, “Evidence for 4f-shell delocalization in praseodymium under pressure,” *J. App. Phys.*, vol. 52, no. 7, p. 4572, 1981.

- [12] Y. Zhao and F. Porsch, “Determination of triple points in the phase diagram of praseodymium,” *Phys. Rev. B*, vol. 52, no. 1, pp. 134–137, 1995.
- [13] B. Baer, H. Cynn, V. Iota, C.-S. Yoo, and G. Shen, “Phase diagram and equation of state of praseodymium at high pressures and temperatures,” *Phys. Rev. B*, vol. 67, pp. 1–7, Apr. 2003.
- [14] H. Hua, Y. K. Vohra, J. Akella, S. T. Weir, R. Ahuja, and B. Johansson, “Theoretical and Experimental Studies on Gadolinium at Ultra High Pressure,” *Rev. High Press. Sci. Tech.*, vol. 7, p. 233, 1998.
- [15] R. Patterson, “Static high-pressure structural studies on Dy to 119 GPa,” *J. App. Phys.*, vol. 95, no. 10, p. 5443, 2004.
- [16] L. Pauling, “Atomic radii and interatomic distances in metals,” *J. Americ. Chem. Soc.*, vol. 69, no. 7, p. 542, 1947.
- [17] A. Lawson and T. Tang, “Concerning the High Pressure Allotropic Modification of Cerium,” *Phys. Rev.*, vol. 76, pp. 301–302, July 1949.
- [18] W. Holzapfel, “Structural systematics of 4f and 5f elements under pressure,” *J. All. Comp.*, vol. 223, pp. 170–173, June 1995.
- [19] M. Dolg, “Lanthanides and actinides,” *Chem. Rev.*, vol. 107, pp. 2592–614, June 2007.
- [20] A. V. Nikolaev and A. V. Tsvyashchenko, “The puzzle of the γ - α and other phase transitions in cerium,” *Phys.-Uspekhi*, vol. 55, pp. 657–680, July 2012.
- [21] M. K. Wilkinson, H. R. Child, C. J. McHargue, W. C. Koehler, and E. O. Wollan, “Neutron Diffraction Investigations of Metallic Cerium at Low Temperatures,” *Phys. Rev.*, vol. 122, pp. 1409–1413, June 1961.
- [22] D. Gustafson and A. Mackintosh, “Positron annihilation in rare-earth metals,” *J. Phys. Chem. Sol.*, vol. 25, pp. 389–394, Apr. 1964.
- [23] U. Kornstädt, R. Lässer, and B. Lengeler, “Investigation of the γ - α phase transition in cerium by Compton scattering,” *Phys. Rev. B*, vol. 21, pp. 1898–1901, Mar. 1980.

- [24] A. Murani, Z. Bowden, A. Taylor, R. Osborn, and W. Marshall, “Evidence for localized 4f states in α -Ce,” *Phys. Rev. B*, vol. 48, no. 18, pp. 13981–13984, 1993.
- [25] M. MacPherson, G. Everett, D. Wohlleben, and M. Maple, “Magnetic Susceptibility of Cerium Metal Under Pressure,” *Phys. Rev. Lett.*, vol. 26, pp. 20–23, Jan. 1971.
- [26] A. Grimberg, C. Schinkel, and A. Zandee, “The magnetic and electrical properties of pure α -cerium at atmospheric pressure,” *Solid State Comm.*, vol. 11, pp. 1579–1583, Dec. 1972.
- [27] D. Koskimaki and K. Gschneidner, “Heat capacity and magnetic susceptibility of single-phase α -cerium,” *Phys. Rev. B*, vol. 11, pp. 4463–4469, June 1975.
- [28] R. Colvin, S. Arajs, and J. Peck, “Paramagnetic Behavior of Metallic Cerium and Europium,” *Phys. Rev.*, vol. 122, pp. 14–18, Apr. 1961.
- [29] C. Burr and S. Ehara, “High-Temperature Magnetic Susceptibility of Lanthanum and Cerium Metals,” *Phys. Rev.*, vol. 149, pp. 551–555, Sept. 1966.
- [30] T. Naka and T. Matsumoto, “Magnetic states of α - and γ -Ce at high pressure,” *Physica B: Cond. Mat.*, vol. 205, pp. 121–126, 1995.
- [31] A. Murani, S. Levett, and J. Taylor, “Magnetic Form Factor of α -Ce: Towards Understanding the Magnetism of Cerium,” *Phys. Rev. Lett.*, vol. 95, pp. 3–6, Dec. 2005.
- [32] H. Katzman and J. Mydosh, “Electrical Resistivity of Exchange-Enhanced α -Cerium Under Pressure,” *Phys. Rev. Lett.*, vol. 29, pp. 998–1001, Oct. 1972.
- [33] M. Brodsky and R. Friddle, “Electrical Resistivity of α -Cerium,” *Phys. Rev. B*, vol. 7, pp. 3255–3260, Apr. 1973.
- [34] M. Nicolas-Francillon and D. Jerome, “Low temperature electrical resistivity of α -cerium under pressure,” *Solid State Comm.*, vol. 12, pp. 523–526, Mar. 1973.
- [35] J. Leger, “Electrical resistivity of α cerium under high pressure,” *Phys. Lett. A*, vol. 57, pp. 191–192, May 1976.

- [36] A. B. Kaiser and S. Doniach, “Temperature-dependent resistivity of dilute alloys with nearly magnetic impurities,” *Int. J. Mag.*, vol. 1, p. 11, 1970.
- [37] R. Jullien, M. Béal-Monod, and B. Coqblin, “Resistivity of nearly magnetic metals at high temperatures: Application to neptunium and plutonium,” *Phys. Rev. B*, vol. 9, pp. 1441–1457, Feb. 1974.
- [38] C. Probst and J. Witting, *Low Temperature Physics*, vol. 5. North-Holland, 1975.
- [39] K. A. Gschneidner, P. Burgardt, S. Legvold, J. O. Moorman, T. A. Vydrostek, and C. Stassis, “Kondo scattering in a pure metal β -cerium. I. Experimental,” *J. Phys. F: Met. Phys.*, vol. 6, pp. L49–L53, Feb. 1976.
- [40] P. Burgardt, K. Gschneidner, D. Koskenmaki, D. Finnemore, J. Moorman, S. Legvold, C. Stassis, and T. Vydrostek, “Electrical resistivity and magnetic susceptibility of β -cerium from 2 to 300 K,” *Phys. Rev. B*, vol. 14, pp. 2995–3006, Oct. 1976.
- [41] J. V. der Eb, A. Kuz’menko, and D. V. D. Marel, “Infrared and Optical Spectroscopy of α - and γ -Phase Cerium,” *Phys. Rev. Lett.*, vol. 86, pp. 3407–3410, Apr. 2001.
- [42] D. Wieliczka, C. Olson, and D. Lynch, “High-resolution photoemission study of γ - and α -cerium,” *Phys. Rev. B*, vol. 29, pp. 3028–3030, Mar. 1984.
- [43] F. Patthey, B. Delley, W. Schneider, and Y. Baer, “Low-Energy Excitations in α - and γ -Ce Observed by Photoemission,” *Phys. Rev. Lett.*, vol. 55, pp. 1518–1521, Sept. 1985.
- [44] E. Weschke, C. Laubschat, T. Simmons, M. Domke, O. Strebel, and G. Kaindl, “Surface and bulk electronic structure of Ce metal studied by high-resolution resonant photoemission,” *Phys. Rev. B*, vol. 44, no. 15, p. 8304, 1991.
- [45] J. Joyce, A. Arko, J. Lawrence, P. Canfield, Z. Fisk, R. Bartlett, and J. Thompson, “Temperature-invariant photoelectron spectra in cerium heavy-fermion compounds: Inconsistencies with the Kondo model,” *Phys. Rev. Lett.*, vol. 68, pp. 236–239, Jan. 1992.

- [46] L. Liu, J. Allen, O. Gunnarsson, N. Christensen, and O. Andersen, “ α - γ transition in Ce: A detailed analysis of electron spectroscopy,” *Phys. Rev. B*, vol. 45, pp. 8934–8941, Apr. 1992.
- [47] E. Weschke, G. Kaindl, and S. Molodtsov, “Surface electronic structure of epitaxial Ce and La films,” *Phys. Rev. B*, vol. 58, no. 7, pp. 3682–3689, 1998.
- [48] M. Higashiguchi, K. Shimada, T. Narimura, H. Namatame, and M. Taniguchi, “Temperature-dependent high-resolution resonant photoemission study of Ce,” *Physica B: Cond. Mat.*, vol. 351, pp. 256–258, Sept. 2004.
- [49] D. Wieliczka, J. J. Weaver, D. Lynch, and C. Olson, “Photoemission studies of the γ - α phase transition in Ce: Changes in 4f character,” *Phys. Rev. B*, vol. 26, pp. 7056–7059, Dec. 1982.
- [50] Y. Baer and G. Busch, “X-Ray Photoemission Study of Some Light Rare-Earth Metals,” *Phys. Rev. Lett.*, vol. 31, pp. 35–37, July 1973.
- [51] Y. Baer and G. Busch, “X-ray photoemission study of the outermost levels of the rare earth metals,” *J. Electr. Spectr. Relat. Phenom.*, vol. 5, pp. 611–626, Jan. 1974.
- [52] E. Wuilloud, H. Moser, W. Schneider, and Y. Baer, “Electronic structure of γ - and α -Ce,” *Phys. Rev. B*, vol. 28, pp. 7354–7357, Dec. 1983.
- [53] M. Grioni, P. Weibel, D. Malterre, Y. Baer, and L. Du’o, “Resonant inverse photoemission in cerium-based materials,” *Phys. Rev. B*, vol. 55, pp. 2056–2067, Jan. 1997.
- [54] J. Allen, S. Oh, O. Gunnarsson, K. Schönhammer, M. Maple, M. Torikachvili, and I. Lindau, “Electronic structure of cerium and light rare-earth intermetallics,” *Adv. Phys.*, vol. 35, pp. 275–316, Jan. 1986.
- [55] E. Jensen and D. Wieliczka, “Angle-resolved photoemission from γ -Ce: Distinguishing band peaks from f-electron emission,” *Phys. Rev. B*, vol. 30, pp. 7340–7342, Dec. 1984.

- [56] C. Dallera, M. Grioni, A. Palenzona, M. Taguchi, E. Annese, G. Ghiringhelli, A. Tagliaferri, N. Brookes, T. Neisius, and L. Braicovich, “ α - γ transition in metallic Ce studied by resonant x-ray spectroscopies,” *Phys. Rev. B*, vol. 70, pp. 3–10, Aug. 2004.
- [57] J.-P. Rueff, C. Hague, J.-M. Mariot, L. Journel, R. Delaunay, J.-P. Kappler, G. Schmerber, A. Derory, N. Jaouen, and G. Krill, “f-State Occupancy at the γ - α Phase Transition of Ce-Th and Ce-Sc Alloys,” *Phys. Rev. Lett.*, vol. 93, pp. 1–4, Aug. 2004.
- [58] M. Lipp, D. Jackson, H. Cynn, C. Aracne, W. Evans, and A. McMahan, “Thermal Signatures of the Kondo Volume Collapse in Cerium,” *Phys. Rev. Lett.*, vol. 101, pp. 15–18, Oct. 2008.
- [59] F. Decremps, L. Belhadi, D. Farber, K. Moore, F. Ocelli, M. Gauthier, A. Polian, D. Antonangeli, C. Aracne-Ruddle, and B. Amadon, “Diffusionless γ - α Phase Transition in Polycrystalline and Single-Crystal Cerium,” *Phys. Rev. Lett.*, vol. 106, pp. 1–4, Feb. 2011.
- [60] R. I. Beecroft and C. A. Swenson, “On the existence of a critical point for the phase transition in cerium,” *J. Phys. Solids*, vol. 15, 1960.
- [61] B. Amadon, S. Biermann, A. Georges, and F. Aryasetiawan, “The α - γ Transition of Cerium Is Entropy Driven,” *Phys. Rev. Lett.*, vol. 96, pp. 1–4, Feb. 2006.
- [62] A. Nikolaev, “Electric quadrupole interactions and the γ α phase transition in Ce : the role of conduction electrons,” *Eur. Phys. J. B*, vol. 17, pp. 15–32, 2000.
- [63] a. Nikolaev and K. Michel, “Intrasite 4f-5d electronic correlations in the quadrupolar model of the γ - α phase transition in Ce,” *Phys. Rev. B*, vol. 66, pp. 1–12, Aug. 2002.
- [64] A. Tsvyashchenko, A. Nikolaev, A. Velichkov, A. Salamatin, L. Fomicheva, G. Ryasny, A. Sorokin, O. Kochetov, M. Budzynski, and K. Michel, “Lowering

- of the spatial symmetry at the γ - α phase transition in cerium,” *Phys. Rev. B*, vol. 82, pp. 1–4, Sept. 2010.
- [65] A. Schiwiek, “High temperature - high pressure structural study of cerium,” *High Press. Res.*, vol. 22, p. 407, 2002.
- [66] I.-K. Jeong, T. Darling, M. Graf, T. Proffen, R. Heffner, Y. Lee, T. Vogt, and J. Jorgensen, “Role of the Lattice in the γ - α Phase Transition of Ce: A High-Pressure Neutron and X-Ray Diffraction Study,” *Phys. Rev. Lett.*, vol. 92, pp. 10–13, Mar. 2004.
- [67] M. Manley, R. McQueeney, B. Fultz, T. Swan-Wood, O. Delaire, E. Goremychkin, J. Cooley, W. Hulst, J. Lashley, R. Osborn, and J. Smith, “No role for phonon entropy in the fcc-fcc volume collapse transition in Ce_{0.9}Th_{0.1} at ambient pressure,” *Phys. Rev. B*, vol. 67, pp. 1–5, Jan. 2003.
- [68] F. Decremps, D. Antonangeli, B. Amadon, and G. Schmerber, “Role of the lattice in the two-step evolution of γ -cerium under pressure,” *Phys. Rev. B*, vol. 80, pp. 1–4, Oct. 2009.
- [69] B. P. B. D. Antonangeli, D. L. Farber, C. M. Aracne, D. G. Ruddle, J. Siebert, “Kinetics of the isostructural γ - α transition in cerium investigated by ultrasonics,” *High Press. Res.*, vol. 30, no. 1, pp. 151–158, 2010.
- [70] M. Krisch, D. L. Farber, R. Xu, D. Antonangeli, C. M. Aracne, A. Beraud, T.-C. Chiang, J. Zarestky, D. Y. Kim, E. I. Isaev, R. Ahuja, and B. Johansson, “Phonons of the anomalous element cerium,” *Proc. Nat. Ac. Sci. USA*, pp. 1–4, May 2011.
- [71] R. Ramirez and L. M. Falicov, “Theory of the α - γ Phase Transition in Metallic Cerium,” *Phys. Rev. B*, vol. 3, no. 8, p. 2425, 1971.
- [72] B. Coqblin and A. Blandin, “Advances in Physics Stabilité des Moments Magnétiques Localisés dans les Métaux,” *Adv. Phys.*, vol. 17, no. 67, pp. 281–366, 1968.
- [73] N. Mott, *Metal-Insulator Transitions*. Taylor & Francis Ltd., 1974.

- [74] M. Imada, A. Fujimori, and Y. Tokura, “Metal-insulator transitions,” *Rev. Mod. Phys.*, vol. 70, pp. 1039–1263, Oct. 1998.
- [75] J. Hubbard, “Electron Correlations in Narrow Energy Bands,” *Proc. Royal Soc. London*, vol. 276, no. 1365, pp. 238–257, 1963.
- [76] B. Johansson, I. Abrikosov, M. Aldén, A. Ruban, and H. Skriver, “Calculated Phase Diagram for the γ - α Transition in Ce,” *Phys. Rev. Lett.*, vol. 74, pp. 2335–2338, Mar. 1995.
- [77] A. Svane, “Electronic structure of cerium in the self-interaction-corrected local-spin-density approximation,” *Phys. Rev. B*, vol. 53, pp. 4275–4286, Feb. 1996.
- [78] J. Laegsgaard and A. Svane, “Theory of the α - γ phase transition in Ce,” *Phys. Rev. B*, vol. 59, pp. 3450–3459, Feb. 1999.
- [79] J. Kondo, “Resistance minimum in dilute magnetic alloys,” *Prog. Theor. Phys.*, vol. 32, no. 1, pp. 37–49, 1964.
- [80] P. Anderson, “Localized magnetic states in metals,” *Phys. Rev.*, vol. 124, no. 1, p. 41, 1961.
- [81] J. Allen and L. Liu, “ α - γ transition in Ce. II. A detailed analysis of the Kondo volume-collapse model,” *Phys. Rev. B*, vol. 46, pp. 5047–5054, Sept. 1992.
- [82] J.-P. Rueff, J.-P. Itié, M. Taguchi, C. Hague, J.-M. Mariot, R. Delaunay, J.-P. Kappler, and N. Jaouen, “Probing the γ - α Transition in Bulk Ce under Pressure: A Direct Investigation by Resonant Inelastic X-Ray Scattering,” *Phys. Rev. Lett.*, vol. 96, pp. 1–4, June 2006.
- [83] O. Gunnarsson and K. Schönhammer, “Photoemission from Ce compounds: exact model calculation in the limit of large degeneracy,” *Phys. Rev. Lett.*, vol. 50, no. 8, pp. 604–607, 1983.
- [84] O. Gunnarsson and K. Schönhammer, “Electron spectroscopies for Ce compounds in the impurity model,” *Phys. Rev. B*, vol. 28, pp. 4315–4341, Oct. 1983.

- [85] A. Andrews, J. Joyce, A. Arko, and J. Thompson, “Evidence for possible 4f bands at TTK in the heavy-fermion single crystal CePt_{2+x},” *Phys. Rev. B*, vol. 51, no. 5, pp. 3277–3280, 1995.
- [86] A. Arko, J. Joyce, A. Andrews, and J. Thompson, “Strongly correlated electron systems: Photoemission and the single-impurity model,” *Phys. Rev. B*, vol. 56, no. 12, pp. 7041–7044, 1997.
- [87] D. Malterre and M. Grioni, “Recent developments in high-energy spectroscopies of Kondo systems,” *Adv. Phys.*, no. July 2012, pp. 37–41, 1996.
- [88] F. Patthey, W. Schneider, M. Grioni, D. Malterre, Y. Baer, and B. Delley, “Comment on Temperature-invariant photoelectron spectra in cerium heavy-fermion compounds: Inconsistencies with the Kondo model,” *Phys. Rev. Lett.*, vol. 70, pp. 1179–1179, Feb. 1993.
- [89] J. Joyce, A. Andrews, A. Arko, R. Bartlett, R. Blythe, C. Olson, P. Benning, P. Canfield, and D. Poirier, “Photoelectron spectroscopy of strongly correlated Yb compounds,” *Phys. Rev. B*, vol. 54, pp. 17515–17535, Dec. 1996.
- [90] E. Weschke, C. Laubschat, and R. Ecker, “Bandlike character of 4f electrons in CeRh₃,” *Phys. Rev. Lett.*, vol. 69, no. 12, pp. 1792–1795, 1992.
- [91] A. Boring, R. Albers, and O. Eriksson, “Hubbard parameters for metallic Ce,” *Phys. Rev. Lett.*, vol. 68, no. 17, 1992.
- [92] S. Beiden, W. Temmerman, and Z. Szotek, “Self-Interaction Free Relativistic Local Spin Density Approximation: Equivalent of Hund’s Rules in γ -Ce,” *Phys. Rev. Lett.*, vol. 79, p. 3970, 1997.
- [93] B. Johansson, A. Ruban, and I. Abrikosov, “Comment on “Thermal Signatures of the Kondo Volume Collapse in Cerium”,” *Phys. Rev. Lett.*, vol. 102, pp. 189601–189601, May 2009.
- [94] K. Held, C. Huscroft, R. Scalettar, and A. McMahan, “Similarities between the Hubbard and Periodic Anderson Models at Finite Temperatures,” *Phys. Rev. Lett.*, vol. 85, pp. 373–6, July 2000.

- [95] S. V. Streltsov, a. O. Shorikov, and V. I. Anisimov, “Validity of the Anderson and Hubbard models for the description of metallic Ce and cerium heavy fermion compounds,” *JETP Letters*, vol. 92, pp. 543–546, Dec. 2010.
- [96] P. Morin and D. Schmitt, *Ferromagnetic Materials*. Amsterdam: North-Holland, 1990.
- [97] G. Eliashberg and H. Capellmann, “On the nature of the α - γ phase transition in cerium,” *JETP Letters*, vol. 67, p. 125, 1998.
- [98] X. Chen, L. Fang, X. Shen, and J. R. Lombardi, “Spectroscopy of mass-selected gadolinium dimers in argon matrices,” *J. Chem. Phys.*, vol. 112, no. 22, p. 9780, 2000.
- [99] X. Shen, L. Fang, X. Chen, and J. R. Lombardi, “Absorption , excitation , and resonance Raman spectra of Ce₂, Pr₂, and Nd₂,” *Chem. Phys.*, vol. 113, no. 6, 2000.
- [100] X. Cao and M. Dolg, “Electronic structure of lanthanide dimers,” *Mol. Phys.*, vol. 101, pp. 1967–1976, July 2003.
- [101] B. O. Roos, R. Lindh, P.-A. Malmqvist, V. Veryazov, P.-O. Widmark, and A. C. Borin, “New relativistic atomic natural orbital basis sets for lanthanide atoms with applications to the Ce diatom and LuF₃,” *J. Phys. Chem. A*, vol. 112, pp. 11431–5, Nov. 2008.
- [102] a. Nikolaev, “Low-lying energy spectrum of the cerium dimer,” *Phys. Rev. A*, vol. 84, pp. 1–9, July 2011.
- [103] M. Born and R. Oppenheimer, “Zur Quantentheorie der Molekeln,” *Ann. Phys.*, vol. 84, pp. 457–484, 1927.
- [104] D. R. Hartree, “The Wave Mechanics of an Atom with a Non-Coulomb Central Field. Part I. Theory and Methods,” *Mat. Proc. Cambridge Philos. Soc.*, vol. 24, p. 89, Oct. 1928.
- [105] V. Fock, “Bemerkung zur Quantelung des harmonischen Oszillators im Magnetfeld,” *Zeitschrift für Physik A Hadrons and Nuclei*, vol. 47, pp. 446–448, 1928.

- [106] R. G. Parr and W. Yang, *Density-Functional Theory of Atoms and Molecules*. New York: Oxford University Press, 1989.
- [107] M. R. Dreizler and E. K. U. Gross, *Density Functional Theory : An Approach to the Quantum Many-Body Problem*. Berlin: Springer, 1990.
- [108] J. M. Seminario, *Recent Developments and Applications of Modern Density Functional Theory*. Amsterdam: Elsevier, 1996.
- [109] P. Hohenberg and W. Kohn, “Inhomogeneous electron gas,” *Phys. Rev.*, vol. 136, no. 3B, p. B864, 1964.
- [110] M. Levy, “Electron densities in search of Hamiltonians,” *Phys. Rev. A*, vol. 26, no. 3, p. 1200, 1982.
- [111] W. Kohn, L. Sham, and Others, “Self-consistent equations including exchange and correlation effects,” *Phys. Rev.*, vol. 140, no. 4A, pp. A1133–A1138, 1965.
- [112] J. P. Perdew and K. Schmidt, “Density functional theory and its application to materials,” in *Density functional theory and its application to materials* (V. Van Doren, C. Van Alsenoy, and P. Geerlings, eds.), Melville, NY: AIP, 2001.
- [113] J. Perdew and A. Zunger, “Self-interaction correction to density-functional approximations for many-electron systems,” *Phys. Rev. B*, vol. 23, no. 10, p. 5048, 1981.
- [114] J. Perdew and Y. Wang, “Accurate and simple analytic representation of the electron-gas correlation energy,” *Phys. Rev. B*, vol. 45, no. 23, pp. 244–249, 1992.
- [115] S. H. Vosko, L. Wilk, and M. Nusair, “Accurate spin-dependent electron liquid correlation energies for local spin density calculations: a critical analysis,” *Canad. J. Phys.*, vol. 58, no. 8, pp. 1200–1211, 1980.
- [116] O. Gunnarsson, M. Jonson, and B. Lundqvist, “Descriptions of exchange and correlation effects in inhomogeneous electron systems,” *Phys. Rev. B*, vol. 20, no. 8, p. 3136, 1979.

- [117] K. Capelle, “A bird’s-eye view of density-functional theory,” *Braz. J. Phys.*, vol. 36, pp. 1318–1343, Dec. 2006.
- [118] D. Langreth and J. Perdew, “Theory of nonuniform electronic systems. I. Analysis of the gradient approximation and a generalization that works,” *Phys. Rev. B*, vol. 21, no. 12, p. 5469, 1980.
- [119] J. Perdew and W. Yue, “Accurate and simple density functional for the electronic exchange energy: Generalized gradient approximation,” *Phys. Rev. B*, vol. 33, no. 12, p. 8800, 1986.
- [120] J. Perdew, J. Chevary, and S. Vosko, “Atoms, molecules, solids, and surfaces: Applications of the generalized gradient approximation for exchange and correlation,” *Phys. Rev. B*, vol. 46, no. 11, p. 6671, 1992.
- [121] J. Perdew, K. Burke, and M. Ernzerhof, “Generalized Gradient Approximation Made Simple,” *Phys. Rev. Lett.*, vol. 77, pp. 3865–3868, Oct. 1996.
- [122] J. Perdew, S. Kurth, A. Zupan, and P. Blaha, “Accurate Density Functional with Correct Formal Properties: A Step Beyond the Generalized Gradient Approximation,” *Phys. Rev. Lett.*, vol. 82, pp. 2544–2547, Mar. 1999.
- [123] J. Perdew, S. Kurth, A. Zupan, and P. Blaha, “Erratum: Accurate Density Functional with Correct Formal Properties: A Step Beyond the Generalized Gradient Approximation [Phys. Rev. Lett. 82, 2544 (1999)],” *Phys. Rev. Lett.*, vol. 82, pp. 5179–5179, June 1999.
- [124] S. Kurth, J. P. Perdew, and P. Blaha, “Molecular and solid-state tests of density functional approximations: LSD, GGAs, and meta-GGAs,” *Int. J. Quant. Chem.*, vol. 75, no. 4-5, pp. 889–909, 1999.
- [125] S. Kümmel and L. Kronik, “Orbital-dependent density functionals: Theory and applications,” *Rev. Mod. Phys.*, vol. 80, pp. 3–60, Jan. 2008.
- [126] T. Körzdörfer, S. Kümmel, and M. Mundt, “Self-interaction correction and the optimized effective potential,” *J. Chem. Phys.*, vol. 129, p. 014110, July 2008.

- [127] A. I. Liechtenstein and J. Zaanen, “Density-functional theory and strong interactions: Orbital ordering in Mott-Hubbard insulators,” *Phys. Rev. B*, vol. 52, pp. R5467–R5470, Aug. 1995.
- [128] H. Jiang, R. Gomez-Abal, P. Rinke, and M. Scheffler, “First-principles modeling of localized d states with the GW@LDA+U approach,” *Phys. Rev. B*, vol. 82, pp. 1–16, July 2010.
- [129] V. I. Anisimov, F. Aryasetiawan, and A. I. Lichtenstein, “First-principles calculations of the electronic structure and spectra of strongly correlated systems : the LDA + U method,” *J. Phys.: Cond. Mat.*, vol. 9, pp. 767–808, 1997.
- [130] V. I. Anisimov and O. Gunnarsson, “Density-functional calculation of effective Coulomb interactions in metals,” *Phys. Rev. B*, vol. 43, pp. 7570–7574, Apr. 1991.
- [131] W. Pickett, S. Erwin, and E. Ethridge, “Reformulation of the LDA+U method for a local-orbital basis,” *Phys. Rev. B*, vol. 58, pp. 1201–1209, July 1998.
- [132] M. Cococcioni and S. de Gironcoli, “Linear response approach to the calculation of the effective interaction parameters in the LDA+U method,” *Phys. Rev. B*, vol. 71, pp. 035105–, Jan. 2005.
- [133] F. Aryasetiawan, K. Karlsson, O. Jepsen, and U. Schönberger, “Calculations of Hubbard U from first-principles,” *Phys. Rev. B*, vol. 74, p. 125106, Sept. 2006.
- [134] T. Miyake and F. Aryasetiawan, “Screened Coulomb interaction in the maximally localized Wannier basis,” *Phys. Rev. B*, vol. 77, pp. 085122–, Feb. 2008.
- [135] G. Kotliar and D. Vollhardt, “Strongly Correlated Materials: Insights From Dynamical Mean-Field Theory,” *Phys. Tod.*, vol. 57, no. 3, p. 53, 2004.
- [136] G. Kotliar, S. Savrasov, K. Haule, V. Oudovenko, O. Parcollet, and C. Marianetti, “Electronic structure calculations with dynamical mean-field theory,” *Rev. Mod. Phys.*, vol. 78, pp. 865–951, Aug. 2006.

- [137] K. Held, I. a. Nekrasov, G. Keller, V. Eyert, N. Blümer, a. K. McMahan, R. T. Scalettar, T. Pruschke, V. I. Anisimov, and D. Vollhardt, “Realistic investigations of correlated electron systems with LDA + DMFT,” *Physica Stat. Solid. (B)*, vol. 243, pp. 2599–2631, Sept. 2006.
- [138] K. Held, “Electronic structure calculations using dynamical mean field theory,” *Adv. Phys.*, vol. 56, no. 6, pp. 829–926, 2007.
- [139] W. Metzner and D. Vollhardt, “Correlated lattice fermions in $d=$ dimensions,” *Phys. Rev. Lett.*, vol. 62, no. 3, p. 324, 1989.
- [140] A. Georges and G. Kotliar, “Hubbard model in infinite dimensions,” *Phys. Rev. B*, vol. 45, no. 12, p. 6479, 1992.
- [141] E. Müller-Hartmann, “The Hubbard model at high dimensions: some exact results and weak coupling theory,” *Zeitschrift für Physik B Cond. Mat.*, vol. 7, pp. 2–8, 1989.
- [142] M. Jarrell and T. Pruschke, “Anomalous properties of the Hubbard model in infinite dimensions,” *Phys. Rev. B*, vol. 49, no. 2, pp. 1458–1461, 1994.
- [143] T. Pruschke, D. Cox, and M. Jarrell, “Hubbard model at infinite dimensions: Thermodynamic and transport properties,” *Phys. Rev. B*, vol. 47, no. 7, pp. 3553–3565, 1993.
- [144] M. Jarrell, “Hubbard model in infinite dimensions: A quantum Monte Carlo study,” *Phys. Rev. Lett.*, vol. 69, no. 1, pp. 168–171, 1992.
- [145] M. Rozenberg, X. Zhang, and G. Kotliar, “Mott-Hubbard transition in infinite dimensions,” *Phys. Rev. Lett.*, pp. 1236–1239, 1992.
- [146] M. Caffarel and W. Krauth, “Exact diagonalization approach to correlated fermions in infinite dimensions: Mott transition and superconductivity,” *Phys. Rev. Lett.*, vol. 72, no. 10, p. 1554, 1994.
- [147] R. Bulla, A. Hewson, and T. Pruschke, “Numerical renormalization group calculations for the self-energy of the impurity Anderson model,” *J. Phys.: Condens. Matter*, vol. 10, p. 8365, 1998.

- [148] A. D. Becke, "Density-functional thermochemistry. IV. A new dynamical correlation functional and implications for exact-exchange mixing," *J. Chem. Phys.*, vol. 104, no. 3, p. 1040, 1996.
- [149] A. D. Becke, "A new mixing of HartreeFock and local density-functional theories," *J. Chem. Phys.*, vol. 98, no. 2, p. 1372, 1993.
- [150] J. P. Perdew, M. Ernzerhof, and K. Burke, "Rationale for mixing exact exchange with density functional approximations," *J. Chem. Phys.*, vol. 105, no. 22, p. 9982, 1996.
- [151] P. Löwdin, "Correlation Problem in Many-Electron Quantum Mechanics* I. Review of Different Approaches and Discussion of Some Current Ideas," *Adv. Chem. Phys.*, vol. 2, p. 207, 1959.
- [152] J. Paier, R. Hirschl, M. Marsman, and G. Kresse, "The Perdew-Burke-Ernzerhof exchange-correlation functional applied to the G2-1 test set using a plane-wave basis set.," *J. Chem. Phys.*, vol. 122, p. 234102, June 2005.
- [153] K. Kudin, G. Scuseria, and R. Martin, "Hybrid Density-Functional Theory and the Insulating Gap of UO₂," *Phys. Rev. Lett.*, vol. 89, p. 266402, Dec. 2002.
- [154] J. E. Peralta, E. R. Batista, G. E. Scuseria, and R. L. Martin, "All-Electron Hybrid Density Functional Calculations on UF_n and UCl_n (n = 16)," *J. Chem. Theory Comput.*, vol. 1, pp. 612–616, July 2005.
- [155] P. J. Hay, R. L. Martin, J. Uddin, and G. E. Scuseria, "Theoretical study of CeO₂ and Ce₂O₃ using a screened hybrid density functional.," *J. Chem. Phys.*, vol. 125, p. 34712, July 2006.
- [156] A. D. Becke, "Density-functional thermochemistry. III. The role of exact exchange," *J. Chem. Phys.*, vol. 98, no. 7, p. 5648, 1993.
- [157] Y. Zhao and D. G. Truhlar, "Hybrid Meta Density Functional Theory Methods for Thermochemistry, Thermochemical Kinetics, and Noncovalent Interactions: The MPW1B95 and MPWB1K Models and Comparative Assessments for Hydrogen Bonding and van der Waals Interactions," *J. Phys. Chem. A*, vol. 108, pp. 6908–6918, Aug. 2004.

- [158] Y. Zhao and D. G. Truhlar, "Design of density functionals that are broadly accurate for thermochemistry, thermochemical kinetics, and nonbonded interactions.," *J. Phys. Chem. A*, vol. 109, pp. 5656–67, June 2005.
- [159] J. A. Pople, M. Head-Gordon, D. J. Fox, K. Raghavachari, and L. A. Curtiss, "Gaussian-1 theory: A general procedure for prediction of molecular energies," *J. Chem. Phys.*, vol. 90, p. 5622, May 1989.
- [160] L. A. Curtiss, C. Jones, G. W. Trucks, K. Raghavachari, and J. A. Pople, "Gaussian-1 theory of molecular energies for second-row compounds," *J. Chem. Phys.*, vol. 93, p. 2537, Aug. 1990.
- [161] J. Heyd and G. E. Scuseria, "Efficient hybrid density functional calculations in solids: assessment of the Heyd-Scuseria-Ernzerhof screened Coulomb hybrid functional.," *J. Chem. Phys.*, vol. 121, pp. 1187–92, July 2004.
- [162] J. Heyd and G. E. Scuseria, "Assessment and validation of a screened Coulomb hybrid density functional.," *J. Chem. Phys.*, vol. 120, pp. 7274–80, Apr. 2004.
- [163] J. Heyd, G. E. Scuseria, and M. Ernzerhof, "Hybrid functionals based on a screened Coulomb potential," *J. Chem. Phys.*, vol. 118, p. 8207, May 2003.
- [164] D. Bohm and D. Pines, "A Collective Description of Electron Interactions. I. Magnetic Interactions," *Phys. Rev.*, vol. 82, pp. 625–634, June 1951.
- [165] D. Pines and D. Bohm, "A Collective Description of Electron Interactions: II. Collective vs Individual Particle Aspects of the Interactions," *Phys. Rev.*, vol. 85, pp. 338–353, Jan. 1952.
- [166] D. Pines, "A Collective Description of Electron Interactions: IV. Electron Interaction in Metals," *Phys. Rev.*, vol. 92, pp. 626–636, Nov. 1953.
- [167] D. Bohm and D. Pines, "A Collective Description of Electron Interactions: III. Coulomb Interactions in a Degenerate Electron Gas," *Phys. Rev.*, vol. 92, pp. 609–625, Nov. 1953.
- [168] J. Hubbard, "The Dielectric Theory of Electronic Interactions in Solids," *Proc. Phys. Soc. A*, vol. 68, pp. 976–986, Nov. 1955.

- [169] J. Hubbard, “On the Interaction of Electrons in Metals,” *Proc. Phys. Soc. A*, vol. 68, pp. 441–443, May 1955.
- [170] H. Fröhlich and H. Pelzer, “Plasma Oscillations and Energy Loss of Charged Particles in Solids,” *Proc. Phys. Soc. A*, vol. 68, pp. 525–529, June 1955.
- [171] S.-i. Tomonaga, “Elementary Theory of Quantum-Mechanical Collective Motion of Particles, I,” *Prog. Theor. Phys.*, vol. 13, pp. 467–481, May 1955.
- [172] S.-i. Tomonaga, “Elementary Theory of Quantum-Mechanical Collective Motion of Particles, II,” *Prog. Theor. Phys.*, vol. 13, pp. 482–496, May 1955.
- [173] M. Gell-Mann and K. Brueckner, “Correlation Energy of an Electron Gas at High Density,” *Phys. Rev.*, vol. 106, pp. 364–368, Apr. 1957.
- [174] D. Langreth and J. Perdew, “The exchange-correlation energy of a metallic surface,” *Solid State Comm.*, vol. 17, pp. 1425–1429, Dec. 1975.
- [175] O. Gunnarsson and B. Lundqvist, “Exchange and correlation in atoms, molecules, and solids by the spin-density-functional formalism,” *Phys. Rev. B*, vol. 13, pp. 4274–4298, May 1976.
- [176] D. Langreth and J. Perdew, “Exchange-correlation energy of a metallic surface: Wave-vector analysis,” *Phys. Rev. B*, vol. 15, no. 6, p. 2884, 1977.
- [177] X. Ren, P. Rinke, C. Joas, and M. Scheffler, “Random-phase approximation and its applications in computational chemistry and materials science,” *J. Mat. Sci.*, vol. 47, pp. 7447–7471, June 2012.
- [178] R. Kubo, “The fluctuation-dissipation theorem,” *Rep. Prog. Phys.*, vol. 29, pp. 255–284, Jan. 1966.
- [179] P. Nozières and D. Pines, *The theory of quantum liquids*. New York: Benjamin, 1966.
- [180] J. Goldstone, “Derivation of the Brueckner Many-Body Theory,” *Proc. Royal Soc. A: Math., Phys. Eng. Sci.*, vol. 239, pp. 267–279, Feb. 1957.

- [181] J. Toulouse, I. Gerber, G. Jansen, A. Savin, and J. Ángyán, “Adiabatic-Connection Fluctuation-Dissipation Density-Functional Theory Based on Range Separation,” *Phys. Rev. Lett.*, vol. 102, Mar. 2009.
- [182] F. Furche and T. Van Voorhis, “Fluctuation-dissipation theorem density-functional theory,” *J. Chem. Phys.*, vol. 122, p. 164106, Apr. 2005.
- [183] X. Ren, A. Tkatchenko, P. Rinke, and M. Scheffler, “Beyond the Random-Phase Approximation for the Electron Correlation Energy: The Importance of Single Excitations,” *Phys. Rev. Lett.*, vol. 106, pp. 16–19, Apr. 2011.
- [184] H. Eshuis and F. Furche, “A Parameter-Free Density Functional That Works for Noncovalent Interactions,” *J. Phys. Chem. Lett.*, vol. 2, pp. 983–989, May 2011.
- [185] J. Harl, L. Schimka, and G. Kresse, “Assessing the quality of the random phase approximation for lattice constants and atomization energies of solids,” *Phys. Rev. B*, vol. 81, Mar. 2010.
- [186] J. Harl and G. Kresse, “Accurate Bulk Properties from Approximate Many-Body Techniques,” *Phys. Rev. Lett.*, vol. 103, pp. 4–7, July 2009.
- [187] J. Harl and G. Kresse, “Cohesive energy curves for noble gas solids calculated by adiabatic connection fluctuation-dissipation theory,” *Phys. Rev. B*, vol. 77, Jan. 2008.
- [188] H.-J. Kim, A. Tkatchenko, J.-H. Cho, and M. Scheffler, “Benzene adsorbed on Si(001): The role of electron correlation and finite temperature,” *Phys. Rev. B*, vol. 85, Jan. 2012.
- [189] J. Ma, “Adsorption and diffusion of water on graphene from first principles,” *Phys. Rev. B*, vol. 84, no. 3, 2011.
- [190] X. Ren, P. Rinke, and M. Scheffler, “Exploring the random phase approximation: Application to CO adsorbed on Cu(111),” *Phys. Rev. B*, vol. 80, pp. 1–8, July 2009.

- [191] M. Rohlfing and T. Bredow, “Binding Energy of Adsorbates on a Noble-Metal Surface: Exchange and Correlation Effects,” *Phys. Rev. Lett.*, vol. 101, Dec. 2008.
- [192] P. Jurecka, J. Sponer, J. Cerný, and P. Hobza, “Benchmark database of accurate (MP2 and CCSD(T) complete basis set limit) interaction energies of small model complexes, DNA base pairs, and amino acid pairs,” *Physical Chemistry Chem. Phys. : PCCP*, vol. 8, pp. 1985–93, May 2006.
- [193] W. Zhu, J. Toulouse, A. Savin, and J. G. Ángyán, “Range-separated density-functional theory with random phase approximation applied to noncovalent intermolecular interactions.,” *J. Chem. Phys.*, vol. 132, p. 244108, June 2010.
- [194] H. Eshuis, J. E. Bates, and F. Furche, “Electron correlation methods based on the random phase approximation,” *Theor. Chem. Acc.*, vol. 131, p. 1084, Jan. 2012.
- [195] J. Paier, X. Ren, P. Rinke, G. E. Scuseria, A. Grüneis, G. Kresse, and M. Scheffler, “Assessment of correlation energies based on the random-phase approximation,” *New J. Phys.*, vol. 14, p. 043002, Apr. 2012.
- [196] H.-V. Nguyen and S. de Gironcoli, “Efficient calculation of exact exchange and RPA correlation energies in the adiabatic-connection fluctuation-dissipation theory,” *Phys. Rev. B*, vol. 79, pp. 205114–, May 2009.
- [197] P. García-González, J. J. Fernández, A. Marini, and A. Rubio, “Advanced correlation functionals: application to bulk materials and localized systems.,” *J. Phys. Chem. A*, vol. 111, pp. 12458–65, Dec. 2007.
- [198] T. Miyake, F. Aryasetiawan, T. Kotani, M. van Schilfhaarde, M. Usuda, and K. Terakura, “Total energy of solids: An exchange and random-phase approximation correlation study,” *Phys. Rev. B*, vol. 66, p. 245103, Dec. 2002.
- [199] S. Lebègue, J. Harl, T. Gould, J. Ángyán, G. Kresse, and J. Dobson, “Cohesive Properties and Asymptotics of the Dispersion Interaction in Graphite by the Random Phase Approximation,” *Phys. Rev. Lett.*, vol. 105, pp. 196401–, Nov. 2010.

- [200] D. Freeman, “Coupled-cluster expansion applied to the electron gas: Inclusion of ring and exchange effects,” *Phys. Rev. B*, vol. 15, pp. 5512–5521, June 1977.
- [201] A. Grüneis, M. Marsman, J. Harl, L. Schimka, and G. Kresse, “Making the random phase approximation to electronic correlation accurate,” *J. Chem. Phys.*, vol. 131, p. 154115, Oct. 2009.
- [202] J. Paier, B. G. Janesko, T. M. Henderson, G. E. Scuseria, A. Grüneis, and G. Kresse, “Hybrid functionals including random phase approximation correlation and second-order screened exchange,” *J. Chem. Phys.*, vol. 132, p. 094103, Mar. 2010.
- [203] B. Min and H. Jansen, “Total-energy local-density studies of the α - γ phase transition in Ce,” *Phys. Rev. B*, vol. 34, p. 369, 1986.
- [204] O. Eriksson, M. Brooks, and B. Johansson, “Orbital polarization in narrow-band systems: Application to volume collapses in light lanthanides,” *Phys. Rev. B*, vol. 41, pp. 7311–7314, Apr. 1990.
- [205] P. Söderlind, O. Eriksson, B. Johansson, and J. Wills, “Electronic properties of f-electron metals using the generalized gradient approximation,” *Phys. Rev. B*, vol. 50, pp. 7291–7294, Sept. 1994.
- [206] T. Jarlborg, “ α - γ transition in Ce from temperature-dependent band-structure calculations,” *Phys. Rev. B*, vol. 55, no. 3, pp. 1288–1291, 1997.
- [207] Z. Szotek, W. Temmerman, and H. Winter, “Self-interaction corrected, local spin density description of the γ - α transition in Ce,” *Phys. Rev. Lett.*, vol. 72, pp. 1244–1247, Feb. 1994.
- [208] A. Svane, “Electronic structure of cerium in the self-interaction corrected local spin density approximation,” *Phys. Rev. Lett.*, vol. 72, pp. 1248–1251, Feb. 1994.
- [209] M. Lüders, A. Ernst, M. Däne, Z. Szotek, A. Svane, D. Ködderitzsch, W. Hergert, B. Györffy, and W. Temmerman, “Self-interaction correction in multiple scattering theory,” *Phys. Rev. B*, vol. 71, p. 205109, May 2005.

- [210] A. Shick, “Ground and metastable states in γ -Ce from correlated band theory,” *J. Elect. Spectr. Relat. Phenom.*, vol. 114-116, pp. 753–758, Mar. 2001.
- [211] B. Amadon, F. Jollet, and M. Torrent, “ γ and β cerium: LDA+U calculations of ground-state parameters,” *Phys. Rev. B*, vol. 77, pp. 1–10, Apr. 2008.
- [212] Y. Wang, L. Hector, H. Zhang, S. Shang, L. Chen, and Z. Liu, “Thermodynamics of the Ce γ - α transition: Density-functional study,” *Phys. Rev. B*, vol. 78, p. 104113, Sept. 2008.
- [213] A. McMahan, K. Held, and R. Scalettar, “Thermodynamic and spectral properties of compressed Ce calculated using a combined local-density approximation and dynamical mean-field theory,” *Phys. Rev. B*, vol. 67, pp. 1–18, Feb. 2003.
- [214] M. Zöfl, I. Nekrasov, T. Pruschke, V. Anisimov, and J. Keller, “Spectral and Magnetic Properties of α - and γ -Ce from Dynamical Mean-Field Theory and Local Density Approximation,” *Phys. Rev. Lett.*, vol. 87, pp. 1–4, Dec. 2001.
- [215] K. Held, A. McMahan, and R. Scalettar, “Cerium Volume Collapse: Results from the Merger of Dynamical Mean-Field Theory and Local Density Approximation,” *Phys. Rev. Lett.*, vol. 87, pp. 1–4, Dec. 2001.
- [216] A. McMahan, “Combined local-density and dynamical mean field theory calculations for the compressed lanthanides Ce, Pr, and Nd,” *Phys. Rev. B*, vol. 72, pp. 1–14, Sept. 2005.
- [217] K. Haule, V. Oudovenko, S. Savrasov, and G. Kotliar, “The α - γ Transition in Ce: A Theoretical View from Optical Spectroscopy,” *Phys. Rev. Lett.*, vol. 94, pp. 1–4, Jan. 2005.
- [218] A. K. McMahan, R. T. Scalettar, and M. Jarrell, “Screening of 4f moments and delocalization in the compressed light rare earths,” *Phys. Rev. B*, vol. 80, Dec. 2009.
- [219] S. Streltsov, E. Gull, A. Shorikov, M. Troyer, V. Anisimov, and P. Werner, “Magnetic susceptibility of cerium: An LDA+DMFT study,” *Phys. Rev. B*, vol. 85, pp. 1–5, May 2012.

- [220] V. Blum, R. Gehrke, F. Hanke, P. Havu, V. Havu, X. Ren, K. Reuter, and M. Scheffler, “Ab initio molecular simulations with numeric atom-centered orbitals,” *Comp. Phys. Comm.*, vol. 180, pp. 2175–2196, Nov. 2009.
- [221] X. Ren, P. Rinke, V. Blum, J. Wieferink, A. Tkatchenko, A. Sanfilippo, K. Reuter, and M. Scheffler, “Resolution-of-identity approach to HartreeFock, hybrid density functionals, RPA, MP2 and GW with numeric atom-centered orbital basis functions,” *New J. Phys.*, vol. 14, p. 053020, May 2012.
- [222] E. van Lenthe, E. J. Baerends, and J. G. Snijders, “Relativistic total energy using regular approximations,” *J. Chem. Phys.*, vol. 101, p. 9783, Dec. 1994.
- [223] G. Kerker, “Efficient iteration scheme for self-consistent pseudopotential calculations,” *Phys. Rev. B*, vol. 23, pp. 3082–3084, Mar. 1981.
- [224] C. Fu and K. Ho, “First-principles calculation of the equilibrium ground-state properties of transition metals: Applications to Nb and Mo,” *Phys. Rev. B*, vol. 28, pp. 5480–5486, Nov. 1983.
- [225] C. Tsallis and D. A. Stariolo, “Optimization by Simulated Annealing: Recent Progress,” in *Annual Reviews Of Computational Physics II* (D. Stauffer, ed.), vol. 11, Singapore: World Scientific, ii ed., 1995.
- [226] C. Tsallis, “Possible generalization of Boltzmann-Gibbs statistics,” *J. Stat. Phys.*, vol. 52, pp. 479–487, July 1988.
- [227] C. Miron, “Optimisation par Recuit Simulé Généralise,” *Report of Ecole Normale Supérieure de Lyon/France*, 1994.
- [228] T. J. P. Penna, “Fitting curves by simulated annealing,” *Computers Phys.*, vol. 9, 1995.
- [229] K. Mundim and C. Tsallis, “Geometry optimization and conformational analysis through generalized simulated annealing,” *Int. J. Quant. Chem.*, vol. 58, no. 4, pp. 373–381, 1996.
- [230] H. Fukutome, “Theory of the Unrestricted Hartree-Fock Equation and Its Solutions I,” *Prog. Theor. Phys.*, vol. 45, pp. 1382–1406, 1971.

- [231] B. Meredig, A. Thompson, H. Hansen, C. Wolverton, and A. van de Walle, “Method for locating low-energy solutions within DFT+U,” *Phys. Rev. B*, vol. 82, Nov. 2010.
- [232] F. Jollet, G. Jomard, and B. Amadon, “Hybrid functional for correlated electrons in the projector augmented-wave formalism: Study of multiple minima for actinide oxides,” *Phys. Rev. B*, vol. 80, pp. 1–8, Dec. 2009.
- [233] M. D. De Andrade, K. C. Mundim, and L. a. C. Malbouisson, “GSA algorithm applied to electronic structure: Hartree-Fock-GSA method,” *Int. J. Quant. Chem.*, vol. 103, no. 5, pp. 493–499, 2005.
- [234] M. D. D. Andrade and M. Nascimento, “GSA algorithm applied to electronic structure II: UHF-GSA method,” *Int. J. Quant. Chem.*, vol. 106, pp. 2700–2705, 2006.
- [235] A. Thom and M. Head-Gordon, “Locating Multiple Self-Consistent Field Solutions: An Approach Inspired by Metadynamics,” *Phys. Rev. Lett.*, vol. 101, pp. 1–4, Nov. 2008.
- [236] J. A. Connor, *Metal Clusters in Catalysis Vol. 29*. Amsterdam: Elsevier, 1986.
- [237] M. Scheffler and C. Stampfl, *Handbook of Surface Science Vol. 2*. Amsterdam: Elsevier, 2000.
- [238] Q.-M. Hu, K. Reuter, and M. Scheffler, “Towards an Exact Treatment of Exchange and Correlation in Materials: Application to the CO Adsorption Puzzle and Other Systems,” *Phys. Rev. Lett.*, vol. 98, pp. 1–4, Apr. 2007.
- [239] R. S. Mulliken, “Electronic Population Analysis on LCAO[Single Bond]MO Molecular Wave Functions. I,” *The Journal of Chemical Physics*, vol. 23, no. 10, p. 1833, 1955.
- [240] C. Kittel, *Introduction to Solid State Physics*. New York: Wiley, 7 ed., 1996.
- [241] R. Podloucky and D. Glözel, “Band structure, cohesive properties, and Compton profile of γ - and α -cerium,” *Physical Review B*, vol. 27, pp. 3390–3405, Mar. 1983.

- [242] W. Pickett, A. Freeman, and D. Koelling, “Local-density-functional approach to the isostructural γ - α transition in cerium using the self-consistent linearized-augmented-plane-wave method,” *Physical Review B*, vol. 23, no. 3, pp. 1266–1291, 1981.
- [243] F. D. Murnaghan, “The Compressibility of Media under Extreme Pressures,” *Proc. Nat. Ac. Sci. USA*, vol. 30, no. 9, pp. 244–247, 1944.
- [244] L. de Medici, A. Georges, G. Kotliar, and S. Biermann, “Mott Transition and Kondo Screening in f-Electron Metals,” *Phys. Rev. Lett.*, vol. 95, pp. 5–8, Aug. 2005.
- [245] Y. Vohra, H. Olijnik, W. Grosshans, and W. Holzapfel, “Structural Phase Transitions in Yttrium under Pressure,” *Phys. Rev. Lett.*, vol. 47, pp. 1065–1067, Oct. 1981.
- [246] J. Duthie and D. Pettifor, “Correlation between d-Band Occupancy and Crystal Structure in the Rare Earths,” *Phys. Rev. Lett.*, vol. 38, pp. 564–567, Mar. 1977.
- [247] F. P. Holzapfel and W. B., “Novel reentrant high pressure phase transition in lanthanum,” *Phys. Rev. Lett.*, vol. 70, no. 26, p. 4087, 1993.
- [248] K. Syassen and W. Holzapfel, “Compression of lanthanum to 120 kbar,” *Solid State Comm.*, vol. 16, pp. 533–536, Mar. 1975.
- [249] G. Chesnut and Y. Vohra, “ α -uranium phase in compressed neodymium metal,” *Phys. Rev. B*, vol. 61, pp. R3768–R3771, Feb. 2000.
- [250] L. Nixon, D. Papaconstantopoulos, and M. Mehl, “Electronic structure and superconducting properties of lanthanum,” *Phys. Rev. B*, vol. 78, p. 214510, Dec. 2008.
- [251] K. A. Gschneidner, “Physical properties of the rare earth metals,” *Bulletin of Alloy Phase Diagrams*, vol. 11, pp. 216–224, June 1990.
- [252] W. Grosshans and W. Holzapfel, “Atomic volumes of rare-earth metals under pressures to 40 GPa and above,” *Phys. Rev. B*, vol. 45, pp. 5171–5178, Mar. 1992.

- [253] Z. Wu, J. Shi, S. Zhang, and H. Zhang, “Density-functional study of lanthanum, ytterbium, and lutetium dimers,” *Phys. Rev. A*, vol. 69, pp. 1–4, June 2004.
- [254] J. Jensen and A. Mackintosh, *Rare earth magnetism*. Oxford: Clarendon Press, 1991.
- [255] Y. Vohra and V. Vijayakumar, “Structure of the distorted fcc high-pressure phase of the trivalent rare-earth metals,” *Physical Review B*, vol. 143, no. 400, pp. 6205–6207, 1984.
- [256] N. Stojic, J. Davenport, M. Komelj, and J. Glimm, “Prediction of a surface magnetic moment in alpha-uranium,” *arXiv preprint cond-mat/...*, no. 001, pp. 2–5, 2003.
- [257] K. B. Lipkowitz, D. B. Boyd, D. Feller, and E. R. Davidson, “Basis Set for Ab Initio Molecular Orbital Calculations and Intermolecular Interactions,” in *Reviews in Computational Chemistry* (K. B. Lipkowitz and D. B. Boyd, eds.), vol. 1 of *Reviews in Computational Chemistry*, ch. 1, pp. 1–43, Hoboken, NJ, USA: John Wiley & Sons, Inc., Jan. 2007.
- [258] F. B. van Duijneveldt, J. G. C. M. van Duijneveldt-van de Rijdt, and J. H. van Lenthe, “State of the Art in Counterpoise Theory,” *Chem. Rev.*, vol. 94, pp. 1873–1885, Nov. 1994.
- [259] S. Boys and F. Bernardi, “The calculation of small molecular interactions by the differences of separate total energies. Some procedures with reduced errors,” *Molec. Phys.*, vol. 19, pp. 553–566, Oct. 1970.

